



Swansea University
Prifysgol Abertawe



Swansea University E-Theses

Effect of plate characteristics on ink transfer in flexographic printing.

Hamblyn, Anja

How to cite:

Hamblyn, Anja (2015) *Effect of plate characteristics on ink transfer in flexographic printing..* thesis, Swansea University.

<http://cronfa.swan.ac.uk/Record/cronfa42827>

Use policy:

This item is brought to you by Swansea University. Any person downloading material is agreeing to abide by the terms of the repository licence: copies of full text items may be used or reproduced in any format or medium, without prior permission for personal research or study, educational or non-commercial purposes only. The copyright for any work remains with the original author unless otherwise specified. The full-text must not be sold in any format or medium without the formal permission of the copyright holder. Permission for multiple reproductions should be obtained from the original author.

Authors are personally responsible for adhering to copyright and publisher restrictions when uploading content to the repository.

Please link to the metadata record in the Swansea University repository, Cronfa (link given in the citation reference above.)

<http://www.swansea.ac.uk/library/researchsupport/ris-support/>



Swansea University
Prifysgol Abertawe

**Effect of Plate Characteristics on
Ink Transfer in Flexographic Printing**

Anja Hamblyn

Dipl.-Ing. (FH), MSc

Submitted to Swansea University in fulfilment of the
requirements for the Degree of Doctor of Philosophy

Swansea University

June 2015

ProQuest Number: 10821217

All rights reserved

INFORMATION TO ALL USERS

The quality of this reproduction is dependent upon the quality of the copy submitted.

In the unlikely event that the author did not send a complete manuscript and there are missing pages, these will be noted. Also, if material had to be removed, a note will indicate the deletion.



ProQuest 10821217

Published by ProQuest LLC (2018). Copyright of the Dissertation is held by the Author.

All rights reserved.

This work is protected against unauthorized copying under Title 17, United States Code
Microform Edition © ProQuest LLC.

ProQuest LLC.
789 East Eisenhower Parkway
P.O. Box 1346
Ann Arbor, MI 48106 – 1346



Summary

Flexography is gaining market share from other printing processes by continuously improving its performance through innovations of materials, technologies and processes. However, the exploitation of the new developments is restricted by a lack of knowledge of their underlying science. This research investigated the role of printing plate properties, namely feature geometries resulting from imaging technologies, surface texturing of printing areas and their combined effect, on ink transfer.

White light interferometry was used for the plate characterisation. New methods for the determination of top geometry and surface area of halftone dots were developed, the latter using post-processing with image analysis. Laboratory- and industrial-scale print trials investigated the effect of plate parameters on print quality, notably optical density, print uniformity and defects, under different process conditions.

The top geometry of halftone dots on the printing plate was found to be a material parameter and independent from imaging technology. This was the first time that the predominantly concave geometry has been quantified. Concavity together with a new dot deformation mechanisms were suggested as a cause for the printing defects of halos and partially unprinted areas in the halftone dot itself.

The ink transfer mechanisms for patterned printing areas were dependent on the ink type used. In conjunction with lower-viscosity water-based ink many surface patterns performed in an analogous manner to anilox cells and increased ink transfer to the prints. Higher-viscosity UV-curing ink remained atop pattern features and caused unprinted areas on the substrate. Micro-patterns imaged with “flat-top” imaging technology improved the ink laydown of halftones, but deteriorated solid prints compared to pattern patches imaged by standard digital technology.

The new understanding of ink transfer from different feature geometries and surface texturing gained through this research can be used as basis for simulations and optimise flexography as a mass-production process for high-quality applications.

Declaration and Statements

Declaration

This work has not previously been accepted in substance for any degree and is not being concurrently submitted in candidature for any degree.

Signed _____ (Anja Hamblyn)

Date 12/12/2015 /

Statement 1

This thesis is the result of my own investigations, except where otherwise stated. Other sources are acknowledged by explicit references. A bibliography is appended.

Signed _____ (Anja Hamblyn)

Date 12/12/2015 -

Statement 2

I give consent for the thesis, if accepted, to be available for photocopying, inter-library loan, electronic storage and distribution, and for the title and summary to be made available to outside organisations.

Signed _____ (Anja Hamblyn)

Date 12/12/2015 /

Acknowledgements

This research has been enabled by the Knowledge Economy Skills Scholarship (KESS), a pan-Wales higher level skills initiative led by Bangor University on behalf of the higher education sector in Wales. It was funded in parts by the Welsh Assembly Government's European Social Fund convergence programme for West Wales and the Valleys, and by Swansea Printing Technology as industrial partner. Thanks to the KESS teams in Swansea and Bangor, in particular Cassy Froment, Jane Kelly and Penny Dowdney who kept their cool despite all administrative resistance.

Generous and much appreciated support in form of materials was provided by Asahi Photoproducts, Innovia Films, SGS International and SunChemical. Thanks also for professional and light-hearted conversions to David Galton (Asahi), Wayne Peachey (SGS), Brian Crombie and Michael Simoni (SunChemical).

I would like to offer my special thanks to David Gethin for his ever calm, patient and positive influence, especially during the writing and correcting of this thesis. The reader is indebted to him for making this volume more palatable, and I myself for much more. Thanks to Tim Claypole for the opportunity to pursue a doctorate at the Welsh Centre for Printing and Coating (WCPC).

The help of Lorraine Leung (Swansea University), Justine Rexer and Sullivan Delanoë (Grenoble INP-PAGORA, Grenoble Institute of Technology, Grenoble, France) with the small-scale print trials, digitising and measuring of samples is very much appreciated. Thanks to Nick Croft, Dan Curtis, Peter Davies, Davide Deganello, Simon Hamblyn, Chris Phillips and Sam Rolland for the support with instruments and software.

A huge thank you to WCPC staff, home and visiting students – past and present – who sweetened the occasionally bitter pill of research: Bahar Aslan, Andreas von Berchem, David Beynon, Ben Clifford, Glyn Davies, Matt Everett, Sakulrat Foulston, Neil Graddage, Christine Hammett, Charles Jones, Tatyana Korochkina, Tim Mortensen, Ben Mogg, Adam Rees, and especially my fellow doctorate sufferers Alexandra Lyashenko, Fotios Pelesis and Ingmar Petersen.

I would like to thank the following people for their assistance in obtaining and translating relevant literature: J. Aspler (Canada), N. Bornemann and the staff at Universitätsbibliothek Potsdam (Germany), T. Gotsick and J. Seymour (USA), J. T. Guthrie (UK), J. Johnson (Sweden), M. Kaplanová (Czech Republic), S. Shilko (Belarus) and the staff at Converter E Cartotecnica (Italy).

Simon and Ava. Never ever again and at least three times more! I would not and could not have done it without you.

Contents

Summary	2
Declaration and Statements	3
Acknowledgements.....	4
Contents.....	5
List of Tables	8
List of Figures	9
Abbreviations and Symbols.....	15
Chapter 1 Introduction and Background	18
1.1 Aim and Motivation	18
1.2 Flexographic Printing Process	19
1.2.1 Printing Plates	19
1.2.1.1 Digital Flexo Plate Structure and Imaging Processes	19
1.2.1.2 Oxygen Inhibition of Imaging Process.....	23
1.2.2 Plate Image and Optical Density	26
1.2.3 Printing Unit.....	28
1.2.4 Ink Delivery System and Anilox Roll.....	29
1.2.5 Ink Composition and Drying Mechanisms	31
1.3 Objectives and Thesis Layout.....	32
Chapter 2 Literature Review	34
2.1 Ink Transfer	34
2.1.1 Wettability and Ink Transfer Mechanisms	34
2.1.2 Effect of Material Parameters on Ink Transfer	36
2.1.2.1 Printing Plate.....	36
2.1.2.2 Ink and Substrate	41
2.1.3 Effect of Process Parameters on Ink Transfer.....	42
2.2 Flexographic Printing Plates.....	44
2.2.1 Geometry of Dot Tops.....	44
2.2.1.1 Effect of Top Geometry on Ink Transfer	45
2.2.1.2 Related Publications.....	47
2.2.2 Texturing of Printing Surfaces.....	48
2.3 Print Characterisation	50
2.3.1 Introduction to Halftone Models	50
2.3.2 Printing Defects.....	52
2.3.2.1 Doughnuts and Halos	52
2.3.2.2 Uncovered Areas.....	54
2.3.2.3 Fingering Instabilities	55
2.4 Conclusions	57
Chapter 3 Methodology.....	60
3.1 Surface Profilometry	60
3.1.1 Determination of Feature Dimensions and Surface Roughness	61
3.1.2 Determination of Planar Surface Area of Printing Features	62
3.1.2.1 Planar Surface Area in Wyko Vision32	63
3.1.2.2 Planar Surface Area in ImageJ.....	66
3.2 Surface Energy	68
3.2.1 Steady-state Surface Tension.....	68
3.2.2 Steady-state Surface Energy	68
3.3 Rheology	70
3.4 Printing.....	71
3.4.1 Printing on Laboratory Printability Tester	71
3.4.2 Industrial-scale Printing	72

3.4.2.1	Setup of the T-Flex 508	73
3.4.2.2	Thin Film Pressure Sensors	74
3.4.2.3	Test for Cyclic Variations.....	75
3.5	Print Characterisation	75
3.5.1	Visual Inspection of Samples by Microscopy	76
3.5.2	Determination of Planar Surface Area and Volume of Printed Dots	76
3.5.3	Determination of Optical Density by Spectrophotometry.....	78
3.5.4	Digitisation of Prints by Scanning.....	79
3.5.5	Digital Image Analysis in ImageJ	80
3.5.5.1	Determination of Print Density	80
3.5.5.2	Determination of Print Uniformity	82
3.6	Design of Experiments	85
3.7	Closure	85
Chapter 4	Dot Top Geometry of Halftones.....	86
4.1	Materials – Plates, Substrate and Inks.....	86
4.2	Printing.....	92
4.2.1	Printing Conditions.....	92
4.2.2	Printing Force by Thin Film Sensor.....	93
4.3	Print Characterisation	95
4.3.1	Planar Surface Area and Volume of Printed Dots.....	95
4.3.2	Optical Density.....	97
4.4	Results and Discussions	98
4.4.1	Characteristics of Plate Features	98
4.4.1.1	Planar Surface Area of Plate Features	98
4.4.1.2	Geometry of Plate Features	102
4.4.2	Characteristics of Printed Features.....	107
4.4.2.1	Ink Distribution across Printed Features.....	107
4.4.2.2	Planar Surface Area of Printed Features.....	115
4.4.2.3	Volume of Printed Features.....	120
4.4.2.4	Optical Density of Printed Features	125
4.4.2.5	Applicability and Comparison of Halftone Models	127
4.4.3	Conclusions	137
4.5	Closure	138
Chapter 5	Meso-Patterns on Printing Plates	139
5.1	Meso-Pattern Effect using a Printability Tester	140
5.1.1	Materials – Plates, Substrates and Inks	140
5.1.2	Printing.....	144
5.1.3	Print Characterisation	145
5.1.3.1	Definition of Fingering Instabilities	145
5.1.3.2	Introduction to DoE Analysis Approach	147
5.1.4	Results and Discussions.....	149
5.1.4.1	Plate Characterisation.....	149
5.1.4.2	Effect of Ink Type	152
5.1.4.3	Effect of Substrate Type.....	152
5.1.4.4	Effect of Plate Material	153
5.1.4.5	Effect of Anilox Volume.....	157
5.1.4.6	Effect of Printing Force	157
5.1.4.7	Effect of Printing Speed	159
5.1.4.8	Effect of Surface Patterning	160
5.1.5	Conclusions	166
5.2	Meso-Pattern Effect using an Industrial Printing Press	167

5.2.1	Materials – Plate, Substrates and Ink	167
5.2.2	Printing and Print Characterisation.....	167
5.2.3	Results and Discussions.....	170
5.2.4	Conclusions	174
5.3	Closure	175
Chapter 6	Microcell Patterns on Printing Plates.....	176
6.1	Microcell Pattern Effect using a Printability Tester	177
6.1.1	Materials, Printing and Print Characterisation	177
6.1.2	Printing and Print Characterisation.....	179
6.1.3	Results and Discussions.....	180
6.1.3.1	Plate Characterisation.....	180
6.1.3.2	Effect of Plate Material and Imaging Technology	181
6.1.3.3	Effect of Microcell versus Meso-patterns.....	184
6.1.3.4	Effect of Pattern Scaling.....	191
6.1.4	Conclusions	194
6.2	Microcell Pattern Effect using an Industrial Printing Press.....	196
6.2.1	Materials, Printing and Print Characterisation	196
6.2.2	Results and Discussions.....	198
6.2.2.1	Plate Characterisation.....	198
6.2.2.2	Microcells on Solids.....	202
6.2.2.3	Microcells on Halftones	208
6.2.3	Conclusions	213
6.3	Closure	214
Chapter 7	Conclusions and Recommendations	215
7.1	Conclusions	215
7.2	Further Work.....	219
7.3	Industrial Recommendations.....	220
A	Appendix	222
A.1	Macros for ImageJ.....	222
A.2	Screening of Scanning Parameters	224
A.2.1	Selection of Scan Colour	224
A.2.2	Selection of Scan Resolution	225
A.2.3	Determination of Temporal Stability and Consistency	225
A.2.4	Determination of Linearity and Gamma Correction	229
A.2.5	Selection of File Format	231
A.2.6	Selection of ROI Size.....	232
A.3	Macro – Print Uniformity and Optical Density in ImageJ.....	233
A.4	Striation of Printing Plate Surface.....	233
A.5	Area Transfer Ratios.....	235
A.6	Volume Transfer Ratios.....	237
A.7	Plate Characterisation.....	239
A.8	Example of Full Data Set for Main Factor and Interaction Effects.....	242
A.9	Printing Defects of AFP-DSH Plate	242
A.10	Print Characterisation	245
Glossary	246
Bibliography	248

List of Tables

Table 3.1: Measurement parameters for Spectrolino with ColorScout A+ measurement table.....	79
Table 3.2: Scan parameters for digitisation of prints.....	80
Table 4.1: Parameter combinations for the generation of different feature geometries on printing plate	87
Table 4.2: Ink surface tension of SunChemical Solarflex Nova SL Pro DK03 series process colours	91
Table 4.3: Rheometer settings for ink pre-conditioning and measurement geometry (inks of industrial printing press studies)	91
Table 4.4: Rheometer settings for ink viscosity determination (inks of industrial printing press studies).....	91
Table 4.5: Combination of print parameters for dot geometry trial	92
Table 4.6: Anilox specifications for dot geometry trial.....	93
Table 4.7: Combinations of parameters for which planar surface area and volume of printed dots was determined	95
Table 4.8: Comparison of model errors for different halftone models at 100 lpi line ruling	129
Table 4.9: Comparison of model errors for Yule-Nielsen and Expanded Murray-Davies halftone models.....	133
Table 4.10: Comparison of model errors for different halftone models at 150 lpi line ruling	135
Table 5.1: Selected properties of plate materials used for meso-pattern study on the IGT-F1.....	140
Table 5.2: Specifications of meso-patterns.....	141
Table 5.3: Material properties of substrates used for surface patterning studies on the IGT-F1	142
Table 5.4: Rheometer settings for ink pre-conditioning and measurement geometry (inks for IGT-F1 studies).....	143
Table 5.5: Rheometer settings for ink viscosity determination (inks for IGT-F1 studies).....	143
Table 5.6: Parameter levels for experimental plan of meso-pattern study on the IGT-F1.....	144
Table 5.7: Parameter levels for experimental plan of meso-pattern trial on the T-Flex 508.....	169
Table 5.8: Volume specification of anilox bands	169
Table 5.9: Combination of print parameters for meso-pattern trial on the T-Flex 508	170
Table 6.1: Selected properties of plate material used for micro-pattern study on the IGT-F1.....	177
Table 6.2: Surface patterns of the three printing plates used for micro-pattern study on the IGT-F1	178
Table 6.3: Specifications of microcell patterns	179
Table A.1: Scan conditions for determination of scanner's temporal stability and consistency.....	227
Table A.2: Distance and depth of striae.....	235
Table A.3: Exemplary DoE data set of plain solid reference (meso-pattern trial on the IGT-F1)	242

List of Figures

Figure 1.1: Market shares won by flexography from other printing processes	18
Figure 1.2: Schematic of terminology referring to the structure and geometry of printing plates	20
Figure 1.3: Schematic of digital plate-making process.	20
Figure 1.4: Comparison of conventional Gaussian and SQUAREspot laser imaging technology.....	21
Figure 1.5: Effects of oxygen inhibition on feature geometry of curing halftone dots	23
Figure 1.6: Schematic of industrial solutions against oxygen inhibition.....	25
Figure 1.7: Typical image elements in functional printing and graphical printing	26
Figure 1.8: Representation of different tonal values by dots in the unit square	27
Figure 1.9: Schematic of physical and optical dot gain.....	28
Figure 1.10: Schematic of flexographic printing unit.....	28
Figure 1.11: Enclosed ink delivery system	29
Figure 1.12: Selected anilox engraving geometries	30
Figure 1.13: Schematic of interaction between plate feature and cell opening size	30
Figure 2.1: Contact angle θ at triple contact line of liquid, solid and vapour phase	35
Figure 2.2: Schematic of the pressure distribution in the printing nip and film splitting by the mechanisms of cavitation and filamentation	36
Figure 2.3: Mechanisms of plate deformation – top expansion and shoulder barrelling	37
Figure 2.4: Folding-over of model halftone dot under axial load	37
Figure 2.5: Flexographic process variables	42
Figure 2.6: Comparison of microphotographs of standard digital to “flat-topped” plate features and their resultant print quality.....	45
Figure 2.7: Microphotographs of halftone dots suggesting concave dot geometry on conventional and standard digital plate	45
Figure 2.8: Mechanisms of liquid pinning to sharp edge of conical frustum.....	47
Figure 2.9: Apparent liquid pinning to imperfect sharp edge	47
Figure 2.10: Secondary asperities on the sides of a conical frustum.....	48
Figure 2.11: Schematic of underlying assumptions for different halftone models.....	51
Figure 2.12: Printing defect of doughnut and halo.....	53
Figure 2.13: Schematic of potential cause for halo	54
Figure 2.14: Different manifestations of fingering instabilities in prints.....	56
Figure 2.15: Schematic of potential ink transfer mechanisms depending on dot geometry	58
Figure 2.16: Schematic of potential ink transfer mechanisms depending on surface patterning.....	59
Figure 3.1: False colour image of a chequer pattern on a printing plate	61
Figure 3.2: Display option “2D analysis” in WYKO Vision32 software.....	62
Figure 3.3: Challenge of determining the surface area for different feature geometries.....	63
Figure 3.4: Customised display option in WYKO Vision32 software for determination of planar surface area and volume.....	64
Figure 3.5: Comparison of 3-D appearance of halftone dot for different restoration and threshold sequences in Vision32.....	65
Figure 3.6: Image processing steps in ImageJ for determination of planar surface area of an isolated printing feature.....	67
Figure 3.7: Schematic viscosity-shear rate diagram illustrating Newtonian, shear-thinning and shear-thickening properties of fluids.....	70
Figure 3.8: Schematic of IGT-F1 printability tester.....	72
Figure 3.9: Schematic of T-Flex 508 printing unit with UV lamp	73
Figure 3.10: Temporal variation in solid optical density measured on consecutive sheets to test for cyclic variations.....	75
Figure 3.11: Microscopic image of printed dot showing irregular contour of the main ink volume and UCAs.....	76
Figure 3.12: Manual selection of ROI for determination of planar surface area and ink volume.....	77

Figure 3.13: Schematic of (natural) volume algorithm in Vision32 software and matching up of actual ink volume with algorithm by data inversion	78
Figure 3.14: Original image of prints versus positioning template for ColorScout A+	78
Figure 3.15: Example of GSL distribution in histogram for a printed and subsequently digitised sample.....	81
Figure 3.16: Correlation of optical density (spectrophotometry) and MGSL (ImageJ) for experimental and computed data pairs.....	82
Figure 3.17: Illustration of deficiency of Coefficient of Variation approach for print uniformity	83
Figure 3.18: Correlation of uniformity ranking obtained by visual judgement and uniformity parameter StDev obtained by image analysis software ImageJ.....	84
Figure 4.1: Image for print trial on dot geometry.....	88
Figure 4.2: Methodology for quantification of dot geometry	89
Figure 4.3: Location of WLI profiles along which the cup depth of the dot top was measured	89
Figure 4.4: Comparison of surface striation in halftone dots and solid for Asahi plate	89
Figure 4.5: Ink viscosity of SunChemical Solarflex Nova SL Pro DK03 series process colours	91
Figure 4.6: Possible locations along plate's bearer bars for force measurement using thin film sensor	93
Figure 4.7: Comparison of consistent setup of anilox-plate cylinder nip using anilox force	94
Figure 4.8: Comparison of consistent setup of printing nip using mean printing force	94
Figure 4.9: Comparison of ink transfer (planar surface area and volume of printed halftones) for different inks.....	96
Figure 4.10: WLI images showing printed dot shapes dependent on dot size and printing conditions	97
Figure 4.11: Plate gain for Asahi plate (standard digital imaging technology).....	99
Figure 4.12: Plate gain for MacDermid plate (standard digital imaging technology).....	99
Figure 4.13: Plate for MacDermid Lux plate (LUX "flat-top" imaging technology).....	100
Figure 4.14: Plate gain for Kodak plate (Flexcel NX "flat-top" imaging technology).....	100
Figure 4.15: Comparison of dot shape for different plate materials and imaging technologies.....	101
Figure 4.16: Profiles of 10% and 50% nominal area coverage dots at 100 lpi line ruling.....	102
Figure 4.17: Cup depth for Asahi plate (standard digital imaging technology)	103
Figure 4.18: Cup depth for MacDermid plate (standard digital imaging technology).....	103
Figure 4.19: Cup depth for MacDermid Lux plate (LUX "flat-top" imaging technology)	104
Figure 4.20: Cup depth for Kodak plate (Flexcel NX "flat-top" imaging technology)	104
Figure 4.21: Schematic of potential cause for cupping	105
Figure 4.22: Images of printed dots at 10% nominal area coverage and 100 lpi line ruling for different printing conditions showing the evolution of doughnut and halo defects	108
Figure 4.23: Comparison of printed halo with central diameter of dot cupping on printing plate....	109
Figure 4.24: Schematic of potential interaction of cupping and halo	109
Figure 4.25: Images of printed dots compared for different dot top geometries at 50% nominal area coverage and 100 lpi line ruling showing UCAs and ink residue around the printed dot edges.....	110
Figure 4.26: Schematic of the potential interaction of cupping and air entrapment.....	111
Figure 4.27: Potential modelling sequence for the future study of printing defects such as halos and UCAs.....	113
Figure 4.28: Comparison of ink residue around yellow and black dots showing varying amounts of pigments	114
Figure 4.29: ATRs for dots of 100 lpi line ruling (1 thou engagement).....	116
Figure 4.30: ATRs for dots of 100 lpi line ruling (4 thou engagement).....	116
Figure 4.31: ATRs under different printing conditions for 10% dots of 100 lpi line ruling.....	117
Figure 4.32: Comparison of magenta ink buildup on dots of 20% nominal area coverage at 100 lpi line ruling for two different plate materials	117
Figure 4.33: Comparison of ATRs for line rulings of 150 lpi and 100 lpi for Asahi plate	119

Figure 4.34: VTRs for dots of 100 lpi line ruling (150 ft/min, 4 thou engagement).....	121
Figure 4.35: VTRs for dots of 100 lpi line ruling (300 ft/min, 4 thou engagement).....	121
Figure 4.36: Relationship of ink volume transferred and planar surface area of printed dot at 100 lpi line ruling	122
Figure 4.37: Mean film thickness for dots of 100 lpi line ruling	122
Figure 4.38: Comparison of VTRs for line rulings of 150 lpi and 100 lpi for Asahi plate	123
Figure 4.39: Relationship of ink volume transferred and planar surface area of printed dots compared for 150 lpi and 100 lpi line ruling.....	124
Figure 4.40: Mean film thickness compared for dots of 150 lpi and 100 lpi line ruling	124
Figure 4.41: Comparison of cup geometry for similar dot sizes at different line rulings	125
Figure 4.42: Optical density under different printing conditions for 70% dots of 100 lpi line ruling.	126
Figure 4.43: Relationship of optical density and area coverage on print for dots of 100 lpi line ruling sorted by imaging technology.....	126
Figure 4.44: Relationship of optical density and area coverage on print compared for 150 lpi and 100 lpi line ruling.....	127
Figure 4.45: Comparison of actual and calculated reflectance at 100 lpi line ruling obtained from different halftone models.....	128
Figure 4.46: Comparison of print defects included in solids produced by different plate materials.	129
Figure 4.47: Comparison of actual and calculated reflectance obtained from Murray-Davies model for 100 lpi line ruling sorted by imaging technology	130
Figure 4.48: Comparison of actual and calculated reflectance obtained from Beer's Law for 100 lpi line ruling	131
Figure 4.49: Comparison of actual and calculated reflectance at 150 lpi line ruling obtained from different halftone models.....	134
Figure 4.50: Comparison of actual and calculated reflectance obtained from Beer's Law for 150 lpi line ruling	135
Figure 4.51: Printed dot structure of highlights, midtones and shadows in photo-engraving.....	136
Figure 5.1: Schematic comparison of scale between meso- and micro-patterns	139
Figure 5.2: Illustrations of the 12 meso-patterns and reference solid	141
Figure 5.3: Viscosity of the UV-curing and water-based inks used for surface patterning studies on the IGT-F1.....	143
Figure 5.4: Parameters and their potential interactions in meso-pattern study on the IGT-F1.....	144
Figure 5.5: Classes of fingering instabilities as observed in the meso-pattern trials	145
Figure 5.6: Revelation of fingering instabilities underneath bead pattern	147
Figure 5.7: Comparison of optical and histogram data for two print samples produced by checker pattern at 45° tilt	148
Figure 5.8: Actual area coverage of meso-patterns on printing plate and coverage loss compared to the artwork for the AFP-DSH plate	149
Figure 5.9: Actual area coverage of meso-patterns on printing plate and coverage loss compared to the artwork for the AWP-DEF plate	150
Figure 5.10: Comparison of nominal polka dot design and plate geometry captured by WLI.....	150
Figure 5.11: Main effect of ink type on MGSL and StDev compared for plain solid reference and all surface patterns.....	150
Figure 5.12: Nonuniformity of ink films printed with polka dot pattern using different inks and printing conditions (AFP-DSH plate, APCO substrate)	151
Figure 5.13: Main effect of substrate type on MGSL and StDev compared for plain solid reference and all surface patterns	152
Figure 5.14: Main effect of plate type on MGSL and StDev compared for plain solid reference and all surface patterns.....	153
Figure 5.15: Chequer pattern at 45° tilt on AWP-DEF plate material. Little change between fingering defect regimes with printing conditions observed for water-based ink on APCO substrate	155

Figure 5.16: Chequer pattern at 45° tilt on AWP-DEF plate material. Strong change between fingering defect regimes with printing conditions observed for water-based ink on APCO substrate	156
Figure 5.17: Main effect of anilox volume on MGSL and StDev compared for plain solid reference and all surface patterns	157
Figure 5.18: Main effect of printing force on MGSL and StDev compared for plain solid reference and all surface patterns	158
Figure 5.19: Main effect of printing speed on MGSL and StDev compared for plain solid reference and all surface patterns	159
Figure 5.20: Main effect of surface patterning on MGSL and StDev for all surface patterns compared to the plain solid reference.....	161
Figure 5.21: Effect of the meso-patterns on fingering demonstrated on the example of a single set of printing conditions (water-based ink on APCO substrate, AWP-DEF plate material)	164
Figure 5.22: Image for meso-pattern trial on the T-Flex 508	168
Figure 5.23: Parameters and their interactions of meso-pattern trial on the T-Flex 508	169
Figure 5.24: Mean optical densities for plain solid reference and all surface patterns in meso-pattern trial on the T-Flex 508	171
Figure 5.25: Comparison of printing defects (areas of missing ink) in meso-pattern trial on the T-Flex 508	171
Figure 5.26: The 15 largest main factor and interaction effects on optical density for the example of chequer pattern at 45° tilt on the T-Flex 508	172
Figure 6.1: Illustrations of microcell patterns.....	179
Figure 6.2: Parameters and their potential interactions in micro-pattern study on the IGT-F1	179
Figure 6.3: Actual area coverage on printing plate and coverage loss compared to the artwork for MacDermid Lux Plate 1	180
Figure 6.4: Actual area coverage on printing plate and coverage loss compared to the artwork for MacDermid Lux Plate 2	180
Figure 6.5: Actual area coverage on printing plate and coverage loss compared to the artwork for MacDermid Lux Plate 3	181
Figure 6.6: Comparison of mean MGSL for MacDermid Lux (Plate 1) and Asahi plates.....	181
Figure 6.7: Surface profile of negative hexagon pattern on different plate types	182
Figure 6.8: Comparison of mean StDev for MacDermid Lux (Plate 1) and Asahi plates.....	183
Figure 6.9: Effect of printing force on MGSL for MacDermid Lux (Plate 1) and Asahi plates.....	184
Figure 6.10: Effect of printing force on StDev for MacDermid Lux (Plate 1) and Asahi plates.....	184
Figure 6.11: Mean MGSL and mean StDev for plain solid reference and all surface patterns on MacDermid Lux (Plate 2).....	185
Figure 6.12: Main effect of surface patterning on MGSL and StDev for all surface patterns on MacDermid Lux (Plate 2).....	185
Figure 6.13: Correlation of area coverage on MacDermid Lux (Plate 2) with mean MGSL.....	186
Figure 6.14: Correlation of recess volume on MacDermid Lux (Plate 2) with mean MGSL for all surface patterns except V50/50, tiles and positive hexagons	187
Figure 6.15: Example profiles of selected microcell and meso-patterns featuring recesses	187
Figure 6.16: Lack of defects in prints made with UV-curing ink (APCO substrate, MacDermid Lux (Plate 2)).....	188
Figure 6.17: Correlation of area coverage on MacDermid Lux (Plate 2) with mean StDev	188
Figure 6.18: Correlation of recess volume on MacDermid Lux (Plate 2) with mean StDev for all surface patterns except V50/50, tiles and positive hexagons	189
Figure 6.19: Transition of fingering defect regimes with area coverage in descending order (water-based ink on APCO substrate, MacDermid Lux (Plate 2)).....	190
Figure 6.20: Scaling example of chequer meso-pattern designs	191
Figure 6.21: MGSL and StDev of entire experimental plan for plain solid reference and all surface patterns on MacDermid Lux (Plate 3)	192

Figure 6.22: Main factor effects of patterning on MGSL and StDev for different pattern scales on MacDermid Lux (Plate 3).....	192
Figure 6.23: Transition of printing defects with pattern scaling for chequer pattern at 45° tilt (APCO substrate).....	193
Figure 6.24: Samples indicating ink squeeze at high printing force (APCO substrate).....	193
Figure 6.25: Image for microcell trial on the T-Flex 508.....	197
Figure 6.26: Actual area coverage of micro- and meso-patterns on printing plates investigated on the T-Flex 508.....	198
Figure 6.27: Surface profile of solid superimposed with MC09P_L microcell pattern.....	199
Figure 6.28: Example of microcells superimposed on halftone dots of all three plate types.....	200
Figure 6.29: Effect of microcells on cup depth of halftone dots on plate.....	200
Figure 6.30: Area coverage of halftone dots with and without microcells based on dot edge.....	201
Figure 6.31: Area coverage of halftone dots with and without microcells based on actual data points on MacDermid Lux plates.....	201
Figure 6.32: Comparison of optical densities for plain solid reference and microcells patches for all plate materials.....	202
Figure 6.33: Difference in optical density between solids without and with microcells on Asahi plate for different printing conditions.....	203
Figure 6.34: Difference in optical density between solids without and with microcells on MacDermid plate for different printing conditions.....	203
Figure 6.35: Difference in optical density between solids without and with microcells on MacDermid Lux plate for different printing conditions.....	204
Figure 6.36: Correlation of actual area coverage and optical density for the microcell patterns for all plate materials.....	204
Figure 6.37: Printing defects (UCAs) in printed reference solids caused by air entrapment.....	205
Figure 6.38: Orientation of UCAs in prints along lines similar in frequency to striae on Asahi printing plate.....	206
Figure 6.39: Change of size and distribution of UCAs with increasing engagement (Asahi plate).....	207
Figure 6.40: Schematic of redistribution of entrapped air bubbles by microcells.....	207
Figure 6.41: Distribution of UCAs in relationship to microcell location on different printing plate materials (MC16P pattern).....	208
Figure 6.42: Difference in optical density between halftones without and with microcells (Asahi plate).....	209
Figure 6.43: Difference in optical density between halftones without and with microcells (MacDermid plate).....	209
Figure 6.44: Comparison of print uniformity produced by halftone dots imaged without and with microcells on Asahi and MacDermid plate materials.....	210
Figure 6.45: Difference in optical density between halftones without and with microcells (MacDermid Lux plate).....	211
Figure 6.46: Comparison of print uniformity produced by halftone dots without and with microcells on MacDermid Lux plate material.....	211
Figure 6.47: Optical densities of halftones without and with microcells for all plate materials.....	212
Figure A.1: Normalised histogram of GSL distribution for patch “reference solid” at different scan resolutions.....	226
Figure A.2: Water-based ink prints – MGSL and StDev of test scans in consecutive order.....	228
Figure A.3: UV-curing ink prints – MGSL and StDev of test scans in consecutive order.....	229
Figure A.4: Reference greyscale as part of the Color Checker Classic.....	230
Figure A.5: Comparison of normalised MGSL (determined by scanning) and normalised luminance (obtained by spectrophotometry) showing non-linear manipulation of scanner data using “no colour correction” option.....	230

Figure A.6: Normalised histogram of GSL distribution for patch “reference solid” at different ROI sizes.....	232
Figure A.7: Comparison of surface striation in halftone dots and solids on printing plates	233
Figure A.8: Comparison of ATRs for line rulings of 150 lpi and 100 lpi for Kodak plate	235
Figure A.9: Comparison of ATRs for line rulings of 150 lpi and 100 lpi for MacDermid plate	236
Figure A.10: Comparison of ATRs for line rulings of 150 lpi and 100 lpi for MacDermid Lux plate....	236
Figure A.11: Comparison of VTRs for line rulings of 150 lpi and 100 lpi for Kodak plate	237
Figure A.12: Comparison of VTRs for line rulings of 150 lpi and 100 lpi for MacDermid plate	237
Figure A.13: Comparison of VTRs for line rulings of 150 lpi and 100 lpi for MacDermid Lux plate....	238
Figure A.14: Nominal versus actual feature geometries of original image on printing plates for the meso-pattern trials on the IGT-F1	239
Figure A.15: Chequer pattern without tilt on AFP-DSH plate material. Strong change between fingering defect regimes with printing conditions observed for water-based ink on APCO substrate	243
Figure A.16: Polka dot pattern on AFP-DSH plate material. Strong change between fingering defect regimes with printing conditions observed for water-based ink on APCO substrate	244
Figure A.17: Failure of meso-patterns to produce closed ink films on the T-Flex 508.....	245

Abbreviations and Symbols

ABBREVIATIONS

2-D	two-dimensional	ISO	International Organization for Standardization
3-D	three-dimensional	IR	infrared
ANSI	American National Standards Institute	MGSL	mean greyscale level (histogram)
ATR	Area Transfer Ratio	lpi	lines per inch
BS	British Standard	LAMS	laser ablation mask system
CIE	Commission International de l'Éclairage (International Commission on Illumination)	OWRK	Owens, Wendt, Rabel and Kaelble (approach)
CMYK	cyan, magenta, yellow and black ("key") – the process colours	ROI	region of interest
CV	Coefficient of Variation	STC	Surface Tension Component (approach)
D50	standard illuminant (daylight)	StDev	standard deviation of mean greyscale level (histogram)
D65	standard illuminant (daylight – noon)	TIFF	Tagged Image File Format
DoE	Design of Experiments	thou	one thousands of an inch (25.4 μm)
dpi	dots per inch	UCA	uncovered area (printing defect)
DTP	dot top peak	UV	ultraviolet
ft	foot (0.3048 m)	VTR	Volume Transfer Ratio
FT	mean film thickness	WLI	white light interferometry
GSL	greyscale level (histogram)		

LATIN SYMBOLS

Symbol	Meaning	Unit
$A_{\%}$	area coverage	% (percent)
α	relative area (Noffke-Seymour equation)	-
ATR	Area Transfer Ratio	-
C^*	chroma (CIE $L^*C^*h^*$ colour space)	-
Ca	capillary number	-
CV	Coefficient of Variation	-
D	optical density	-
\bar{D}	mean optical density	-
E	effect (DoE)	[case dependent]
ΔE	uncertainty of effect (DoE)	[case dependent]
FT	mean film thickness	m
GSL	greyscale level	-
h	nip height	m
L^*	lightness (CIE $L^*C^*h^*$ colour space)	-
N	number of data points	-
n	n-value (Yule-Nielsen equation)	-
R R_a R_z	roughness average roughness (entire surface area) average roughness (10 greatest separations of surface points)	m
R^2	correlation coefficient	-
r	radius	m
t	film thickness	m
u	velocity	$m \cdot s^{-1}$
v	v power factor (Expanded Murray-Davies equation)	-
w	w power factor (Expanded Murray-Davies equation)	-
Y	relative linear luminance (CIE XYZ colour space)	-
z	adjustment parameter (viscous fingering equation)	-

GREEK SYMBOLS

Symbol	Meaning	Unit
β (beta)	reflectance factor	-
γ (gamma)	linearity correction factor	-
η (eta)	viscosity	Pa·s
θ (capital theta)	contact angle	° (degree)
θ_a	advancing contact angle	° (degree)
$\theta_{a,0}$	advancing contact angle on a flat, horizontal surface	° (degree)
σ (sigma)	standard deviation	[case dependent]
σ_s (sigma)	surface free energy of a solid	mN/m
σ_l	surface tension of a liquid	
σ_{sl}	interfacial tension between a solid and a liquid	
σ^d	dispersive component of surface free energy	
σ^p	polar component of surface free energy	
τ (tau)	transmission factor	-
φ (phi)	corner sharpness angle	° (degree)

Chapter 1 Introduction and Background

Traditionally printing processes are used for the production of graphical items such as books, magazines, calendars, wallpapers, laminates and packaging. Since printing is a fast, consistent and relatively cheap means of mass production (Hübler et al., 2002; Kempa et al., 2008), it also has potential to expand into the manufacture of functional devices, for example photovoltaics, light emitters, transistors, batteries and antibody sensors (Sauer, Bornemann and Dörsam, 2011; Hecker, 2013). For both, graphical and functional device printing, it is of the utmost importance to be able to predict the outcome of the printing process in order to achieve the target quality and avoid wasting resources during the printing. However, printers are continuously challenged by developments in the printing market such as new materials, technologies and processes. Their introduction by industry is often not accompanied by a good theoretical understanding of the impact on the underlying process mechanisms. Thus, technologies are not fully exploited due to a lack of knowledge about the process conditions that could lead to optimisation.

1.1 Aim and Motivation

Over the last two decades the flexographic printing process has gained importance within the printing market. It replaces other printing technologies, because it can achieve large volume production runs in short periods of time with ever improving quality and lower costs (Figure 1.1). The printing plate as the carrier of the actual image information stands at the heart of the printing process.

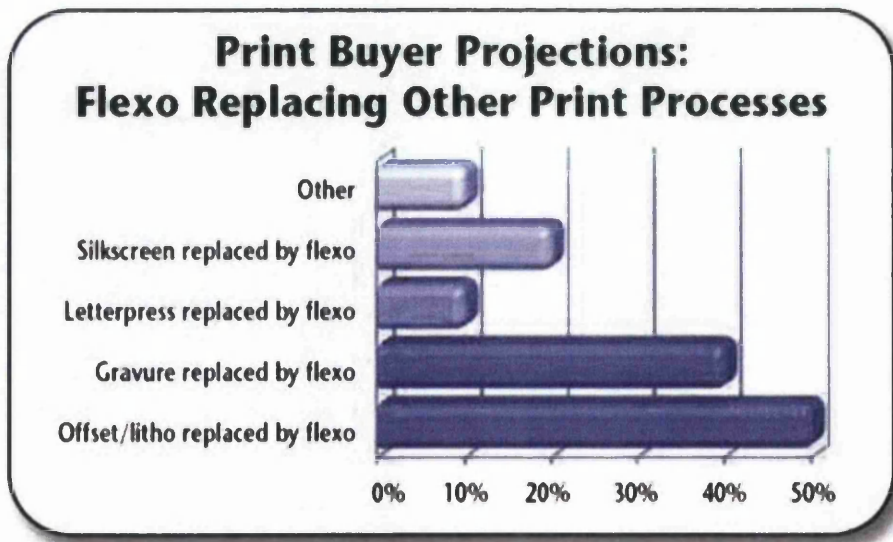


Figure 1.1: Market shares won by flexography from other printing processes (LPC, 2010)

Recent years have seen numerous commercial developments in flexographic printing plate technology including material properties, surface characteristics and imaging processes all of which claim to improve print quality and increase efficiency. Ink transfer mechanisms are proposed based on the outcomes of selected commercial print runs, which only serves to highlight inadequate insight into the underlying science. The research reported in this thesis focusses on developing the understanding of how the ink transfer from the printing plate is affected by plate properties, namely surface geometry and patterning. The next section will give an overview of the flexographic printing process, before discussing the research objectives and thesis structure in more detail.

1.2 Flexographic Printing Process

A summary of the current state of the flexographic printing process as relevant to this work is provided in the following section. Particular emphasis is placed on the printing plate, plate-making and -imaging. The second half of the section is concerned with the components of a flexographic printing press and the printing ink as significant material parameter.

1.2.1 Printing Plates

For this work only the digital plate-making process is of importance as it currently prevails on the market and has been employed to produce the plates used in this research project.

1.2.1.1 Digital Flexo Plate Structure and Imaging Processes

The general terminology used to describe the structure of the printing plate is provided in Figure 1.2. The image information is contained in the form of raised features, and the ink transferred from the image area at the top of these features. The creation of a digital printing plate for flexography involves six main steps: (Dykes, 1999; Liu and Guthrie, 2003; Birkenshaw, 2004)

- Imaging
- Back exposure
- Front exposure
- Washout
- Drying and stabilisation
- Finishing and post-exposure

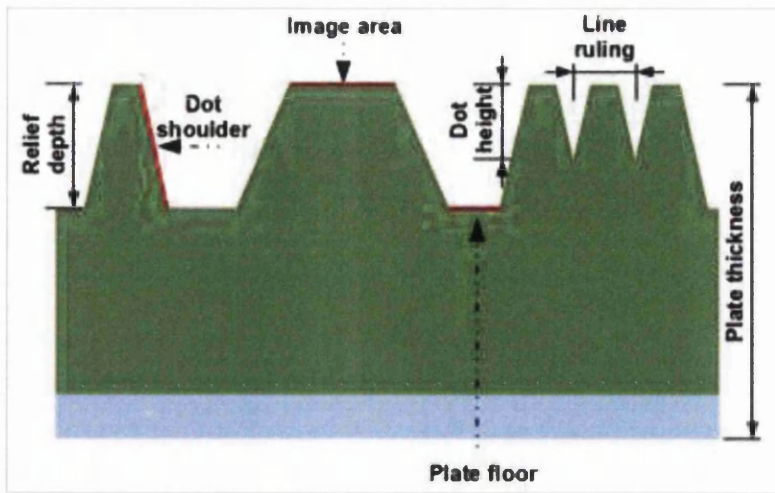


Figure 1.2: Schematic of terminology referring to the structure and geometry of printing plates
(adapted from S. Hamblyn, 2004)

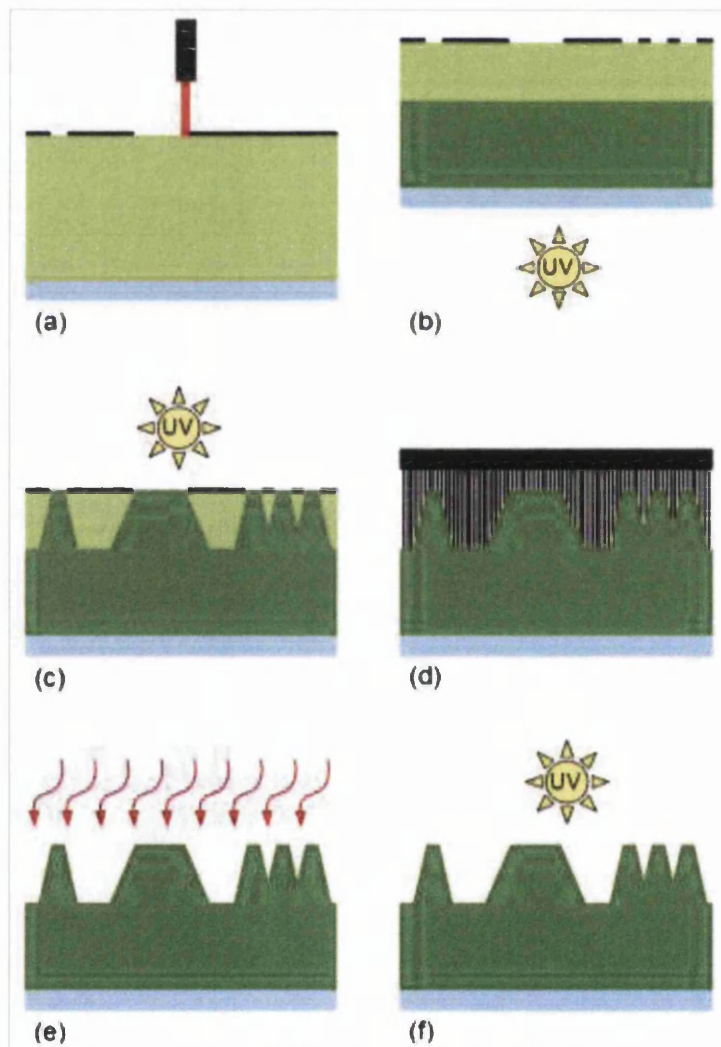


Figure 1.3: Schematic of digital plate-making process: During laser imaging the carbon mask layer is partially removed (a). Back exposure with UV-light cures the plate floor (b) to which the halftone dots, created by UV-light transmission through the mask layer, are anchored in the front exposure step (c). Uncured plate material is washed out using a suitable solvent and brushing (d). The solvent is then evaporated (e) and the plate surface finished under UV-light (f).

In its most simple form the digital printing plate consists of a photopolymer layer sandwiched between a form-stable polyester backing sheet and carbon mask layer. During the first step of the digital imaging process the image information is transferred directly from the artwork in the computer to the mask layer using laser ablation or sublimation (Figure 1.3a). In the case of laser ablation the mask layer is sensitive to infrared (IR) radiation and an IR-laser physically destroys the mask layer to reveal the photopolymer underneath. This method is referred to as laser ablation mask system (LAMS). Mask layers for laser sublimation are designed to change their chemical composition under laser exposure, while remaining intact. Imaging can take place using an IR- or UV-laser. IR-sensitive layers contain sublimation dyes which turn increasingly transparent proportional to the IR-radiation received. UV-sensitive layers change their density under UV-radiation and therefore allow different amounts of UV-light to advance through the mask layer to the photopolymer. There is a second mask technology which is non-integrated and involves ink-jet printing of the image negative onto the photopolymer sheet (Dykes, 1999). No further processing of the imaged mask layer is required beyond the step of ink-jet printing.

Several types of laser imaging technology are available on the market. The most common one is the conventional Gaussian laser characterised by the high intensity at the centre of the beam which falls off towards the edges in a bell-shape power profile creating soft dots (Figure 1.4). The proprietary SQUAREspot technology by Eastman Kodak (Rochester, New York, USA) utilises a beam of uniform lower power which is thought to result in hard dots with sharp edges. (Anderson, 2009)

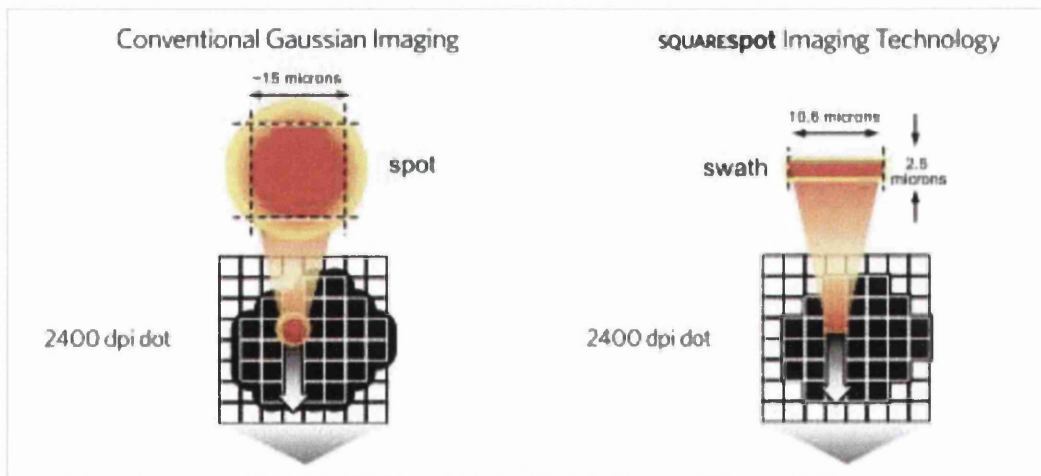


Figure 1.4: Comparison of conventional Gaussian and SQUAREspot laser imaging technology by the laser beam's power profile and resultant pixel shape (Kodak, 2012)

Before the printing features can be imaged on the plate, a base for them has to be created by exposing the photopolymer sheet to UV-A radiation through the backing sheet (Figure 1.3b). Once

the floor of the printing plate is established, the front exposure of the polymer takes place through the mask layer (Figure 1.3c). Where the UV-A light penetrates through the mask, the curing of the polymer takes place. Areas which are covered by the mask, and therefore not exposed, remain uncured and soluble. The incident angle of the light and its diffraction within the material determine the shape of the halftone dot on the printing plate. Light entering other than perpendicular results in asymmetrical dots leaning towards the light source. Extended diffraction creates a wider base of the dot and shallower shoulder angles. (Fioravanti, 2003) The duration of the exposure has to be matched to the requirements of plate material and image. If the exposure takes place for too long, small printing features in particular might get enlarged and the plate surface starts to crack (Liu, Guthrie and Bryant, 2002). If the exposure is not long enough, the printing features do not connect sufficiently to the plate floor and are removed during washout along with the mask layer and non-cured polymer material (Figure 1.3d). Depending on the plate material a water- or solvent-based solution is used for the washout combined with brushing.

Once the washout is completed, the remaining solution is evaporated from the plate surface and the bulk of the material through drying in an oven (Figure 1.3e) which improves the feature quality. This step is of particular importance for solvent-washable plates, as they swell and deform as a result of solvent-polymer interaction. During a subsequent stabilisation phase the form stability of the plate material is re-established. This drying and stabilisation step takes about 24 hours for solvent-washable printing plates. Mechanical and thermal polymer removal methods aim to eliminate washout and drying. In mechanical removal, instead of washing out the non-cured photopolymer after the imaging step, uncured photopolymer is melted and absorbed with a cloth revealing the hardened elements on the plate. The thermal removal evaporates the uncured material. (Novaković, Dedijer and Mahović Poljaček, 2010)

After the drying of the plate, a residual tackiness of under-cured polymer might remain on the plate surface. This can be removed by immersing the plate into a chlorine bath or exposing it to UV-C light. This is called the chemical or light-finishing step. Finally, the plate is exposed to UV-A light again in order to cure any remaining parts of the plate that might have been left un- or undercured during the previous exposure steps (Figure 1.3f). After this the plate is ready to be cut to size and mounted onto the plate cylinder.

Although the majority of digital printing plates follow this imaging process, a small proportion is manufactured by other laser technologies. In direct laser imaging the energy of the laser beam is sufficiently powerful to initiate the polymerisation reactions without requiring the exposure to UV-light (Kipphan, 2001). For direct laser engraving, the entire polymer sheet, disregarding any printing

features, is cured during a front exposure step. In the next step the polymerised material is partially removed by a high-energy laser beam to expose printing features. This process is comparable to the mechanical engraving of rubber plates. (Dykes, 1999; Birkenshaw, 2004)

1.2.1.2 Oxygen Inhibition of Imaging Process

The key constituents of the digital photopolymer plate usually are

- a functionalised oligomer as the main structural component of the polymer network,
- a mono- or multifunctional monomer as reactive diluent, and
- polymerisation initiators. (Decker, 1993; Liu and Guthrie, 2003)

UV-light initiates the free radical photopolymerisation in the material regions exposed. The process takes place in four steps: radical generation, initiation, propagation and termination of the chain reaction. Details of the process can be found with, for example, Hageman (1989), Selli and Bellobono (1993), Zumbur, Wilkes and Ward (1993) and Thompson (1998).

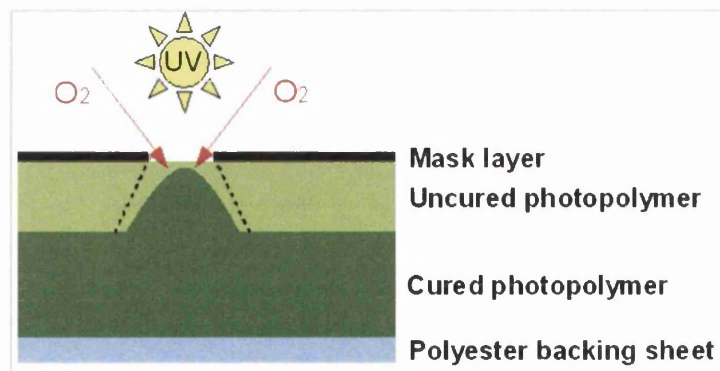


Figure 1.5: Effects of oxygen inhibition on feature geometry of curing halftone dots (dashed lines indicate nominal geometry)

Oxygen inhibition is the premature termination of the polymerisation reaction by the interference of molecular oxygen from the ambient air. The oxygen inactivates the initiator radicals as well as the intermediate products of the initiation and propagation reactions, before these have the opportunity to contribute to the growth of the polymer chain. The inhibition is characterised by a longer induction period before the start of the polymerisation, reduction of the rate of polymerisation, thereby necessitating longer exposure times, and incomplete polymerisation of the unsaturated educts. (Hageman, 1989; Selli and Bellobono, 1993) The significance of oxygen inhibition for the plate-making process is that the resultant geometry of the printing features is

misshapen and smaller in size compared to the nominal geometry (Figure 1.5). Due to the rounding of the feature top, standard digital imaging methods resulting in this kind of appearance are usually referred to as “round-top” technologies.

In the printing industry the problem of oxygen inhibition has been approached from two very different angles. Firstly, rather than resolving the underlying issue during the plate-making process, compensation is applied to the artwork by which the dots are imaged larger in the mask layer than nominally required. If feature loss occurs during polymerisation, the level would only fall back to about the nominally intended value instead of below (Mahović Poljaček et al., 2013; Tomašegović, Mahović Poljaček and Cigula, 2013b). However, this only addresses the symptoms of the problem and requires knowledge of the magnitude of feature losses during the inhibited polymerisation. (Kipphan, 2001; Charlesworth, 2008)

Solutions for the prevention of oxygen inhibition which are already in place for processes similar to plate-making include:

- high-intensity light sources to decrease the necessary exposure time for the polymer and providing a smaller timeframe for the oxygen to diffuse into the material;
- usage of oxygen barriers to prevent the diffusion of molecular oxygen into the material (barriers can be polymer films directly applied to the polymer layer, sheets of glass or coverage with liquids);
- removal of air from the exposure chamber through evacuation;
- displacement of air by inert gas or carbon dioxide in the exposure chamber;
- usage of oxygen scavengers;
- usage of surface-active initiators on the polymer;
- conversion of molecular oxygen into a state in which it readily forms complexes with acceptors and can support the chain reaction of the photoinitiated polymerisation. (Broer, 1993; Selli and Bellobono, 1993; Takimoto, 1993; Shibanov, 2012)

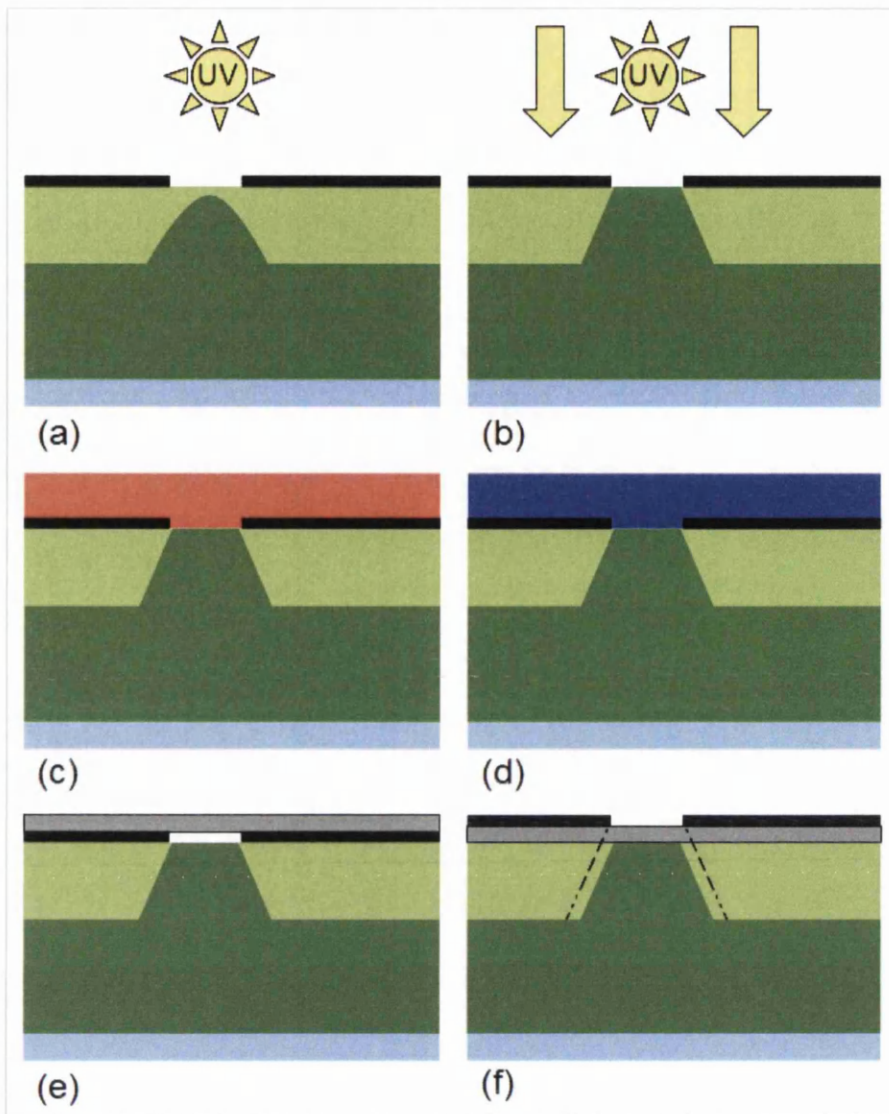


Figure 1.6: Schematic of industrial solutions against oxygen inhibition.

(a) Plate-imaging of standard digital plates affected by oxygen inhibition. Prevention of oxygen inhibition by (b) high-intensity light exposure, (c) air replacement through inert gas, carbon dioxide or air evacuation, (d) deaerated liquid as oxygen barrier, (e and f) different implementations of polymer film as barrier layer.

Several of these possible solutions have been adopted by different manufacturers of digital plate materials. The method of using high-intensity UV-light is employed by DuPont and the Flint Group (Figure 1.6b). PRPflexo replaces the molecular oxygen in the imaging chamber with carbon dioxide gas (Figure 1.6c), although gas conditioning in general is considered to be not efficient enough. Most other companies use some means of oxygen barrier. Exposing the plate under deaerated water is less common during the main exposure steps, but is currently used by some companies for the post-exposure of the printing plate (Figure 1.6d). The more widely used barriers are polymer films. While MacDermid laminates the barrier film on top of the ablated mask layer (MacDermid LUX technology; Figure 1.6e), Kodak provides an integrated solution in which the mask layer and barrier layer are

integrated into a sheet separate from the main plate material. The Kodak mask layer is imaged on the barrier film, before the film is laminated onto the polymer layer (Kodak Flexcel NX technology; Figure 1.6f). Toyobo also employs the method of having the mask above the barrier layer. This method might result in a slight enlargement of the printing feature, since the exposure light can diffuse within the barrier layer, thereby being projected into regions of the photopolymer it was not supposed to penetrate. Figure 1.6f shows the nominally polymerised dot with an indication of the possible enlargement by the dashed lines. (Shibanov, 2012) These approaches to prevent oxygen inhibition allegedly create plate features with a flat top and sharp corners, thus being described by the suppliers as “flat-top” technologies.

1.2.2 Plate Image and Optical Density

Functional device printing aims to transfer the same ink film thickness with all image elements independent of their size and geometry (Figure 1.7a). Graphical printing on the other hand has to be able to produce different gradients (Figure 1.7b) of each colour component, for example in a photographic image. To reproduce a range of colours from a standard process colour ink set of cyan, magenta, yellow and black (CMYK), the image is separated into its CMYK components and each separation divided into very small printing and non-printing areas. The human eye is unable to resolve the tiny elements and therefore averages the colour impression of the visible area covered with printed elements and the uncovered substrate in between (Figure 1.7c). An image region of 50% area coverage would be perceived as a 50% colour gradient (tonal value).

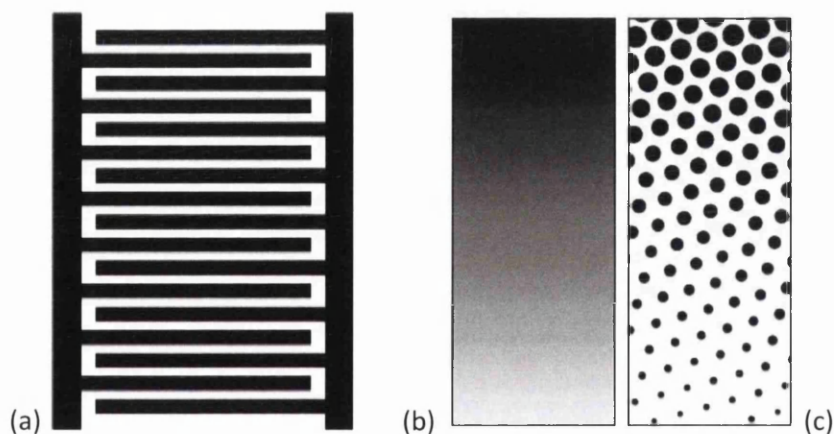


Figure 1.7: Typical image elements in functional printing (a) and graphical printing where a gradient (b) has to be replaced by halftone dots of different size (c) (Beynon, 2007)

The printing elements can be of different shape such as circular, elliptical, diamond or square, but are generally referred to as halftone dots. The desired area coverage can be achieved by several different combinations of halftone dot size, number and spacing, so-called screening methods. In

this study only the conventional screening employing amplitude modulation is used. By screening conventionally, the image area is divided into unit squares whose size is determined by the spatial wavelength, i.e. the line ruling. The amplitude modulation refers to the varying area coverage of the dot within the unit square dependent on the tonal value represented (Figure 1.8). In the case of round dots, the dot diameter reaches the edge of the unit square for theoretical halftone values of 78.5%. At higher values neighbouring dots join together creating a closed printing area that is characterised by holes. These halftones are generally referred to as shadows due to their dark resulting printed colour. The smallest, independent halftones are known as highlights which includes area coverages up to 20% for the purpose of this work. The halftones in the middle of the range are suitably called midtones and only join each other at their bases on the printing plate. “Solid” refers to an area coverage of 100%. Highlights, midtones and shadows exhibit differences in polymerisation during the plate-making process which will lead to variations in their physical behaviour during the printing process.

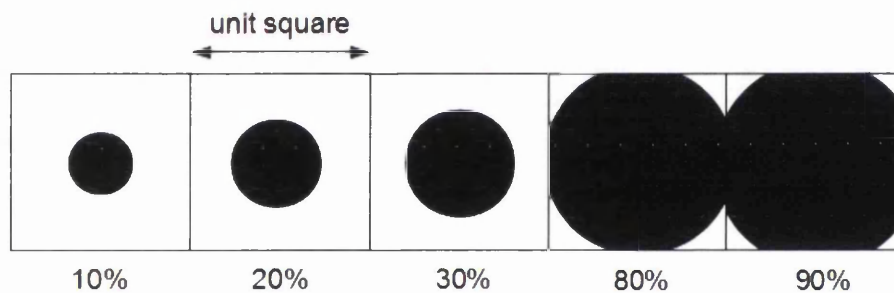


Figure 1.8: Representation of different tonal values by dots in the unit square

The designed nominal area coverage deviates from the “optically effective area coverage” of the prints for two reasons. Firstly, plate deformation and ink spreading cause actual dot enlargement which is known as physical dot gain (Figure 1.9). Secondly, light gathering underneath ink films creates the impression of dot enlargement which is referred to as optical dot gain. Together physical and optical dot gain account for the tonal value increase of printed halftones. (Kang, 1999; Kipphan, 2001) The total amount of light absorbed by the print is measured as optical density, D :

$$D = -\log \beta \quad \text{Equation 1.1}$$

where β is the reflectance factor of the sample. The optical density is dependent on ink film thickness and area coverage.

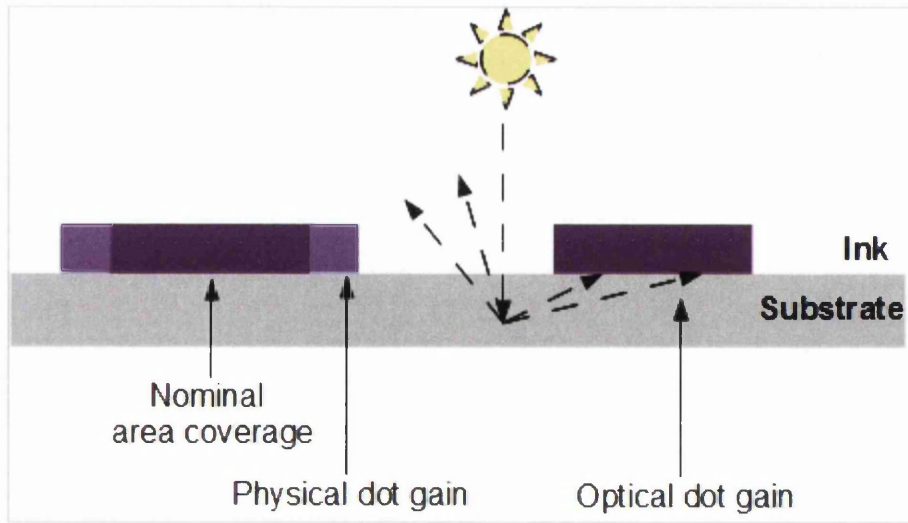


Figure 1.9: Schematic of physical and optical dot gain

1.2.: Printing Unit

The printing ink is fed into the anilox chamber which is in intimate contact with the anilox roll (Figure 1.10). The ink floods the finely engraved cells on the anilox surface. The metering blade (also called reverse angle doctor blade) removes excess ink from the surface of the anilox roll ensuring that ink only remains in the engraved anilox cells.

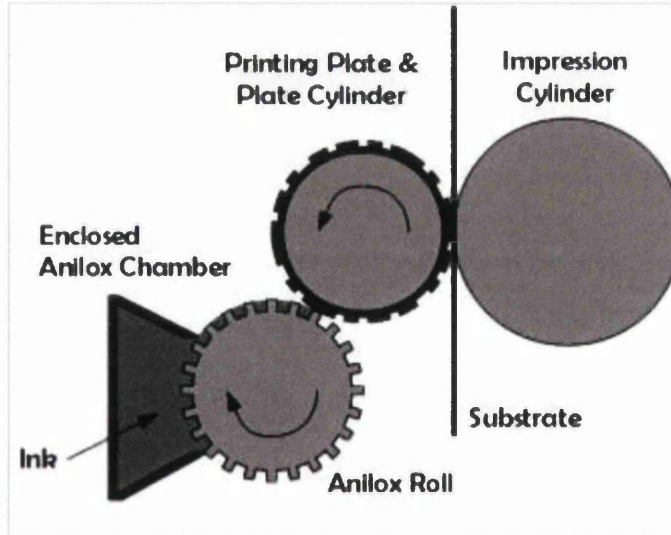


Figure 1.10: Schematic of flexographic printing unit containing ink chamber, anilox roll, plate cylinder with printing plate and impression cylinder

The printing plate is fixed onto the plate cylinder using double-sided mounting tape (also referred to as cushion or backing tape). The raised plate features make contact with the anilox surface and pick up ink from the anilox cells in the nip between plate and anilox cylinder.

In the printing nip (between plate and impression cylinder) the ink is transferred onto the substrate under light pressure. The three cylinders (anilox, plate and impression) can all be moved relative to each other to create different nip engagements. If plate and impression cylinder just about touch and the mean contact force between them is near enough zero, the position is referred to as “kiss engagement” or “kiss contact”. During printing this nip is formed by cylinder engagement, and a printing pressure is applied.

Several of these printing units can be installed in sequence on a printing press which allows several types or colours of ink to be transferred in different patterns next or on top of each other. (Birkenshaw, 2004; Wyatt, 2004)

1.2.4 Ink Delivery System and Anilox Roll

There are two main types of ink delivery systems – open ones with separate doctor blade and enclosed ones with integrated doctor blade. The closed ink delivery system can be found in most applications, because of its health, economic and quality advantages (Figure 1.11). (Birkenshaw, 2004)

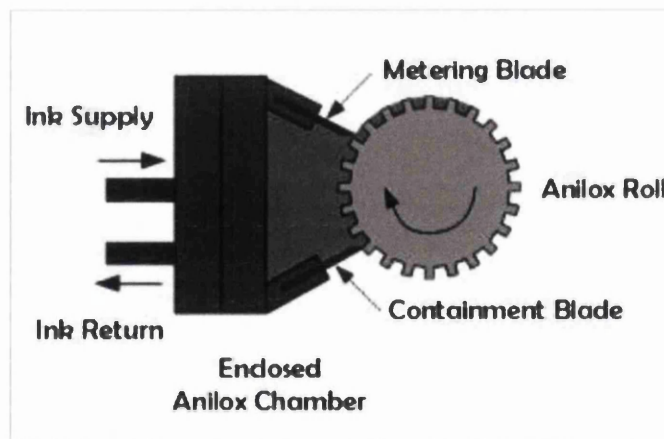


Figure 1.11: Enclosed ink delivery system with anilox chamber, doctor blades and anilox roll

The main component of the ink delivery system is the anilox roll. The anilox is a metal cylinder which is engraved using laser technology or mechanical means. Traditionally, hexagonal cells shaped like honeycombs orientated at 60° were used. However, there are now many different proprietary

engraving geometries (Figure 1.12). After engraving the anilox roll is coated with chrome or ceramic to make its surface more durable. (Birkenshaw, 2004)

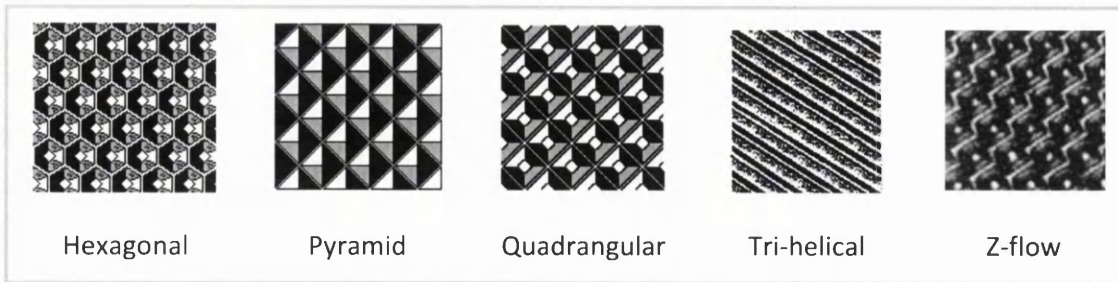


Figure 1.12: Selected anilox engraving geometries (Flexcor, 2012)



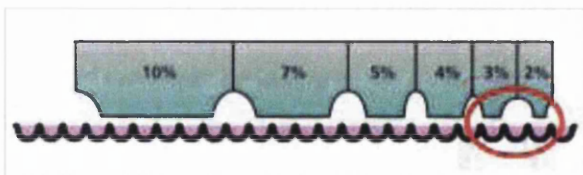
The printing feature is well supported by several cell walls.



The printing feature is insufficiently supported by the cell walls. Increased feature deformation causes plate wear. Early stages of dot dipping might occur.



Dot dipping occurs and too much ink is transferred to the printing feature and its sides. This results in deviations in the printed image.



The circled features are not supported and will experience dot dipping.

Figure 1.13: Schematic of interaction between plate feature and cell opening size (images by Niggemeier, 2002)

The anilox roll is characterised by the cell geometry, the number of cells and volume per unit area carried. For stable and uniform ink transfer, each feature on the printing plate has to be sufficiently supported by several anilox cell walls during contact (Figure 1.13). If the printing feature is insufficiently supported by the cell walls, it is deformed against the cylinder which increases the stress on the plate material and may lead to plate failure. If the size of the printing feature becomes smaller than the anilox cell opening, the entire feature can be immersed into the cell and the sides of the feature will be inked. This is known as “dot dipping”. The dipping increases the amount of ink

transferred from this feature and results in a larger printed area. This highlights the importance of matching the anilox screen ruling to the halftone line ruling on the plate typically at a minimum ratio of three-to-one (Cherry, 2007). It also indicates how different feature geometries and surface texturing might lead to altered ink transfer depending on parameter combinations.

1.2.5 Ink Composition and Drying Mechanisms

The term “ink” traditionally refers to a liquid that includes dispersed pigments and is used to make graphical information visible on a substrate. Although this terminology is still appropriate for graphical printing, its original definition does not apply anymore to the liquids used in the creation of functional applications. However, since the fundamentals of the flexographic printing process remain the same in both cases, no differentiation between the liquids is made, and for the purpose of consistency the term “ink” shall be used for any liquid transferred throughout this work.

There are three main groups of printing inks in flexography: solvent-based, water-based and radiation-curing inks. The radiation-curing inks can be divided into those curing under ultra-violet radiation (UV-curing) and by electron beam exposure (EB-curing). (Leach and Pierce, 2004)

Solvent- and water-based inks contain resin, colorant (dye or pigment) and additives dispersed in their respective ink vehicle (solvent or water) (Wyatt, 2004). Such inks are dried by force-evaporating the vehicle from the resin-pigment mix. This can be achieved by using hot-air or infrared dryers.

UV-based inks cure through photopolymerisation of the ink composites. The ink contains a mix of unsaturated oligomers and monomers to be cross-linked as well as a photoinitiator to start the polymerisation process. The cross-linking leads to a quick hardening of the ink film, thereby allowing high production speeds on a wide variety of substrates. The composition of the UV-curing ink is very similar to that of photopolymer printing plates and follows the same polymerisation principles. (Hargreaves, 2004)

EB-curing inks also harden through photopolymerisation, but they do not require photoinitiators, since the free radicals necessary to start the polymerisation process can be created directly by the high-energy photon impact. Although EB-curing inks do not contain any volatile organic compounds, they are still considered to be hazardous in the curing process as the electron gun does not only emit high-energy short-wavelength radiation, but also X-rays. The inks are very expensive, but even thick ink films can be cured in a very short time.

1.3 Objectives and Thesis Layout

Various new types of halftone geometry resulting from different imaging technologies and the surface texturing on printing areas allegedly improve the volume and consistency of ink released from a printing plate. While several such proprietary systems are experiencing increasing popularity in the market, the underlying mechanisms to validate the claims of improved performance have yet to be established. Since earlier studies of the flexographic printing plate have barely touched on these areas of interest, this research into new plate characteristics was instigated. It builds on previous works involving conventional and standard digital plate technologies (Bould, 2001; S. Hamblyn, 2004; Beynon, 2007). The research questions addressed are outlined below and compiled in more detail in section 2.4.

- Which dot top geometries exist? Is the applicability of halftone models independent from top geometry?
- Which effect do different dot top geometries and surface patterns have on ink transfer and laydown – in particular on optical density, print uniformity and printing defects?
- Which interactions with other material and process parameters can be observed?

An experimental investigation was undertaken using a printability tester as well as an industrial printing press to establish whether the industrial success claims of their recent panaceas, i.e. “flat-top” dots and microcell patterning, are holding true and what the ink transfer mechanisms behind the solutions are. This will place the technology on a firmer scientific footing which in return will underpin the implementation of improved parameters for the manufacture and use of printing plates. The ultimate goal is the contribution to a competitive advantage of flexography over other printing processes and the possibility to advance beyond limitations in graphic and functional device printing.

THESIS LAYOUT

Following this introductory background, Chapter 2 provides a review of the literature relevant to this work. The main part of the review is the printing plate as parameter for ink transfer in the flexographic printing process with special emphasis on different geometries of halftone dots and surface texturing. From this the guiding hypotheses for the research presented in this volume were derived. The experimental and analytical procedures employed to achieve the research goals are described in Chapter 3. This includes several newly developed methods for the characterisation of printing plates and ink depositions on prints.

The main chapters are thematically divided into the investigation of dot geometry and surface patterning. Chapter 4 is dedicated to the results of a print trial studying how dot geometries produced by different imaging technologies affect ink transfer on an industrial printing press. Chapter 5 details the findings of print trials on a printability tester and industrial press researching in-house surface patterning of solid printing areas and whether they have any effect on print quality. The two topics are synthesised and explored in more detail in Chapter 6 where a particular type of commercial microcell patterning is scrutinised in conjunction with standard digital and “flat-top” imaging technology. For this purpose halftone and solid prints were produced in print trials on a printability tester and industrial printing press. The work is concluded in Chapter 7 with an appraisal of the research findings with regard to the hypotheses laid out earlier. The chapter contains recommendations for better industrial practice in the application of the various imaging technologies and surface patterning. Lastly, suggestions are made for further research which emerged from this work.

Chapter 2 Literature Review

The purpose of this work was to study the effect of plate characteristics on ink transfer in flexographic printing. The emphasis was placed on novel plate-making technologies which alter the topography of the plate surface. As these cannot be scrutinised in isolation, other material and process parameters were also taken into account in the experimental investigations. The impact of these factors was determined by means of print quality measures.

The aim of this chapter is to review previous work that has been carried out on ink transfer in flexographic printing. For this purpose the chapter is divided into three parts. The first section examines wettability and ink transfer mechanisms in general, as well as the effect of material and process parameters relevant to this research. The second section focusses on dot top geometry and surface texturing of the printing plate, as these constitute the main focus of this work. The final section is dedicated to print characterisation, notably halftone models and typical flexographic printing defects. Historically, there are extensive literature reviews on several of these topics. However, only a reference to the most relevant reviews and articles together with a critical summary thereof will be provided in the respective sections.

2.1 Ink Transfer

Literature reviews on ink transfer mechanisms and process parameters affecting it have been conducted by S. Hamblyn (2004) and Beynon (2007). The studies featured findings obtained principally by experiments employing model setups or (for sources published until approximately 1992) the letterpress printing process, the predecessor of flexography that uses rigid printing plates. The validity of these review findings for the flexographic printing process with photopolymer printing plates was later confirmed in trials under laboratory as well as industrial conditions for many different combinations of printing inks and substrates.

2.1.1 Wettability and Ink Transfer Mechanisms

The fundamental principle of most printing processes is the transport of an ink through the roller train of the printing press onto the substrate. A successful process outcome requires that the ink wets the respective surfaces, while allowing the transfer of ink through the roller train. Traditionally, the wettability is quantified through the equilibrium contact angle, θ , at the triple contact line formed by a liquid, a solid and the surrounding equilibrium vapour phase (Figure 2.1) (de Gennes, 1985). The shape of the liquid drop, the triple contact line and thereby the contact angle are dependent on several factors. In the ideal case of a “small, axisymmetric sessile drop on a flat,

horizontal, smooth, homogeneous, isotropic, and rigid" (Shanahan, 1995) solid, the contact angle can be directly related to the surface energy of the solid, σ_s , the surface tension of the liquid, σ_l , and the interfacial tension between solid and liquid phase, σ_{sl} , through Young's equation (Equation 2.1). Wetting takes place if the surface energy of the solid is larger than or equal to the surface tension of the liquid. (Young, 1805; de Gennes, 1985)

$$\sigma_{sl} = \sigma_s - \sigma_l \cdot \cos\theta$$

Equation 2.1

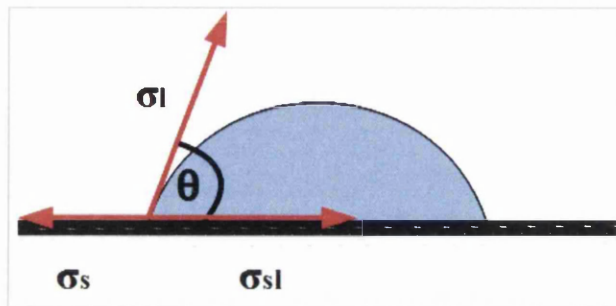


Figure 2.1: Contact angle θ at triple contact line of liquid, solid and vapour phase

Incomplete ink transfer between wetted surfaces relies on a film splitting process, when the physical bounding surfaces are drawn apart. Hübner (1991) defined two different classes of ink splitting based on the fluid volume involved. The 1st order process is a lamella separation and refers to the splitting in a divergent film section, as can be found in the exit region of a roller pair, and this is appropriate for solid printing patches. The 2nd order process is a point separation during which a localised ink volume is split, as is the case for halftone dots.

The fundamental ink splitting mechanisms are identical for both classes. At high printing speeds the ink splitting is preceded by the formation of cavitation bubbles in the liquid film (Figure 2.2), facilitated by the occurrence of negative pressures towards the exit of the roller nip which exert tension on the liquid. The critical speed for the onset of cavitation is dependent on the geometry of the roller system, the respective roller velocities and the ink viscosity. Examples for cavitation nuclei are contaminations, volatile compounds in the ink, air held in surface voids and entrained at the nip entrance. The cavitation bubbles grow and create liquid filaments when coalescing. The filaments are elongated by the diverging rollers and eventually rupture. (Banks and Mill, 1954; Miller and Myers, 1958; Taylor and Zettlemoyer, 1958; Myers, Miller and Zettlemoyer, 1959; De Grâce and Mangin, 1987; Voß, 2002; Barrow et al., 2003; Naito et al., 2004; Vlachopoulos, 2009; Deganello et al., 2011).

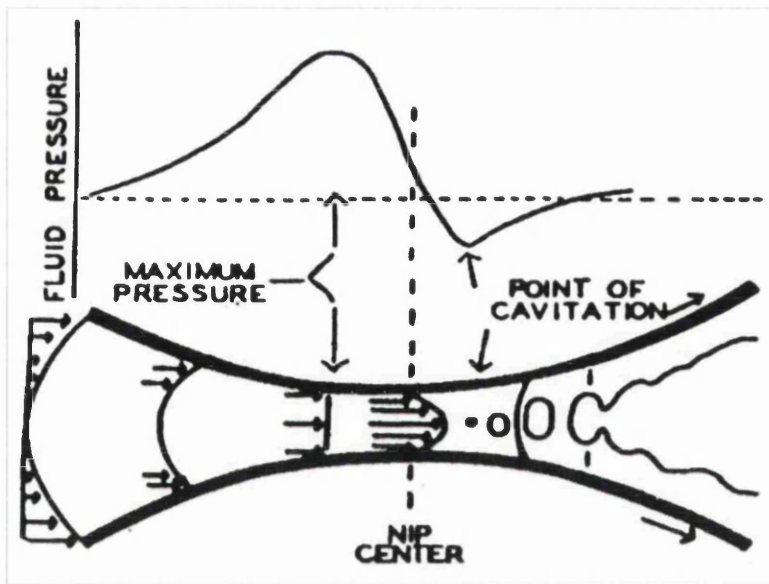


Figure 2.2: Schematic of the pressure distribution in the printing nip and film splitting by the mechanisms of cavitation and filamentation (Zettlemoyer and Myers, 1960)

Numerous attempts at modelling the location of the ink split relative to the two encompassing surfaces have been made. None of the models developed was universally valid for all printing processes, substrate and ink combinations (Walker and Fetsko, 1955; Zaleski, Schaeffer and Zettlemoyer, 1971; Zang, 1992), possibly because each model was only based on data from selected ink and substrate types investigated on test printing presses. However, good agreement was achieved on the effects of different process and material parameters on ink transfer, thus introducing high level process guidelines based on a scientific background. Following this early work, a number of studies have been undertaken to explore particular parameters in more detail.

2.1.2 Effect of Material Parameters on Ink Transfer

The three materials participating in the final ink transfer step on the printing press are the printing plate, ink and substrate. Key properties of these materials, notably plate geometry, elasticity, surface energy and roughness, ink viscosity, substrate roughness and porosity, will be discussed in this section.

2.1.2.1 Printing Plate

The printing plate is a core process component and, beside the image carried, defined by chemical, morphological, mechanical and topographical properties. Furthermore, beyond the conditions encountered during plate-making that have a large impact on the manifestation of these properties (Liu, Guthrie and Bryant, 2002; Galton, 2003; S. Hamblyn, 2004; Harri and Czichon, 2006; Harri, 2009;

Andersson, Johnson and Järnström, 2009; Johnson et al., 2009; Tomašegović, Mahović Poljaček and Cigula, 2013a), the dynamics in the printing nip can also alter the plate characteristics, temporarily or permanently (Mirle, 1989; S. Hamblyn, 2004; Olsson et al., 2006; Beynon, 2007). While the effects of some plate characteristics are well understood, others remain ambiguous or have not been investigated sufficiently as the following overview will show. A comprehensive literature review on the influence of plate-making parameters on plate properties has been conducted by S. Hamblyn (2004) and is omitted here.

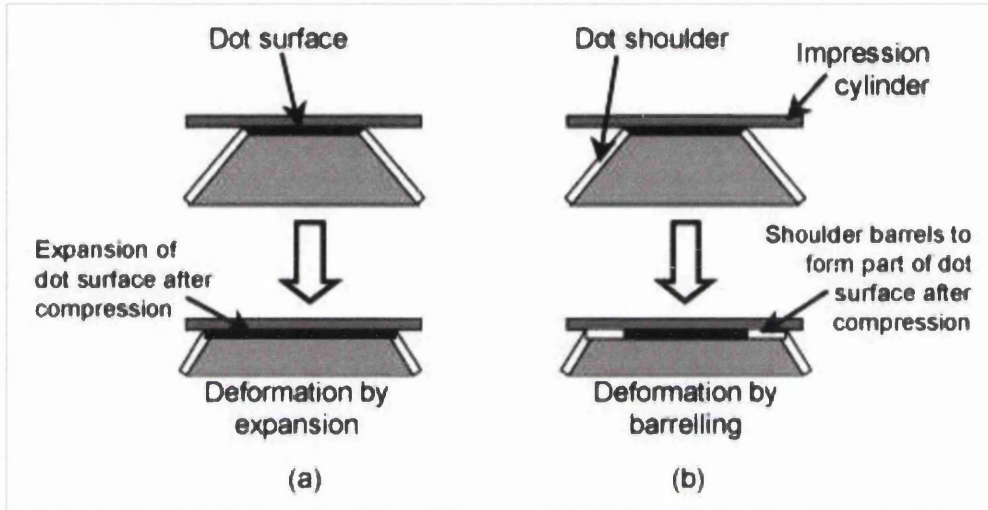


Figure 2.3: Mechanisms of plate deformation – (a) top expansion and (b) shoulder barrelling (Bould, Claypole and Bohan, 2004a)

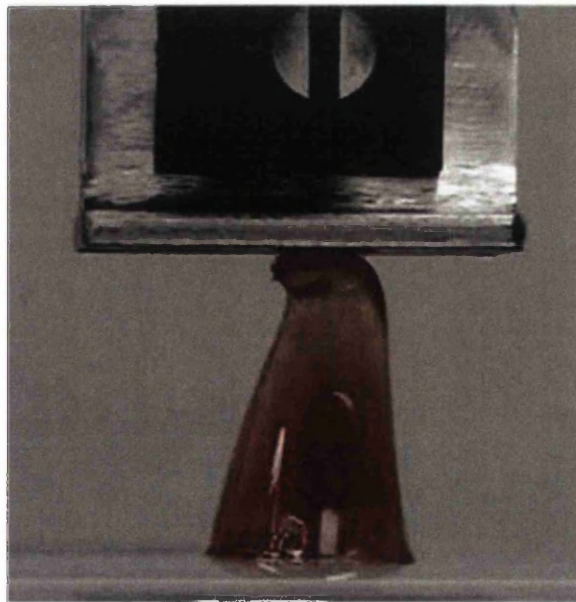


Figure 2.4: Folding-over of model halftone dot under axial load (Gotsick, 2014)

In tonal coverage, typical measurands of the dot geometry are height, shoulder angle and the size of the printing area. Bould (2001) used numerical modelling to identify two mechanisms by which the printing area and overall dot shape are altered in the printing nip: expansion of the dot top and barrelling of the dot shoulder (Figure 2.3). The increase of contact area between plate and substrate relates directly to the degree of dot deformation. The relative top expansion is almost constant for all dot sizes, but decreases once dot surfaces start to join together at higher area coverage. The smaller the dot size, the larger is the relative contribution of shoulder barrelling to the deformation. Deeper dots with steeper shoulders experience less barrelling. (Bould, Claypole and Bohan, 2004a) This leads to less increase in the contact area of the dot and thereby the dot gain. On the other hand these deeper, steeper dots tend to have a narrower base which renders them more susceptible to deformation potentially resulting in more dot gain (Liu, Guthrie and Bryant, 2002). Gotsick (2014) confirmed the dual mechanism of the shoulder angle on macro-models of dots and identified the critical angle for which the dot folds over under axial load (Figure 2.4). This dot failure changes the shape of printed dots from round to oblong and causes significant dot gain. It is therefore important to control the shoulder angle in the polymerisation process by adjusting the exposure parameters (Liu, Guthrie and Bryant, 2002). Conversely, Johnson et al. (2009) observed no influence of shoulder angle on ink transfer in their experiments, but suggested that the dual effects cancelled each other out. Gaining further understanding of the mechanisms causing dot gain is a major driver of the research presented in this work.

The structural response of the plate material to mechanical compression is often generically attributed to the property of plate "hardness" which on closer inspection comprises several individual material properties, notably indentation hardness (Shore A), Young's modulus and Poisson's ratio. The polymers used in flexographic plates are nearly incompressible, denoted by their Poisson's ratio being close to 0.5, and have a low Young's modulus. Bould, Claypole and Bohan (2004a) determined that the expansion of the dot top is governed by Poisson's ratio and the shoulder barrelling by Young's modulus. Because the plate is a polymer, Young's modulus is a dynamic property which was found to increase under high nip pressure or through multiple compressions of the printing plate, thus the material exhibits "stress-hardening" (Mirle, 1989; Bould, Claypole and Bohan, 2004a; S. Hamblyn, 2004). This mechanical property impedes deformation and thus reduces tone gain (Meyer, Dürholz und Bütterich, 1996; Liu, Guthrie and Bryant, 2004; S. Hamblyn, 2004; Johnson et al., 2009). At the same time, stiffer solid printing patches conform less well against substrate unevenness, thereby reducing ink transfer and consequently optical density (Johnson et al., 2003).

Some studies concluded that the deformation of more elastic printing plates, i.e. those having a lower Young's modulus, takes place primarily within the bulk of the material rather than in the individual printing feature, thereby lowering the contact force on ink and substrate. The thicker the printing plate, the more compression it can tolerate within the bulk. (Mirle 1989; Bould et al., 2004b; Holmvall and Uesaka, 2007) However, other studies saw no effect of plate hardness on ink transfer parameters investigated (Quinn et al., 1997; Johnson et al., 2009). Quinn and colleagues do not specify their hardness parameter, whereas Johnson and colleagues used the indentation hardness. Although the indentation hardness is related to Young's modulus, it might be insufficient to describe the dynamic structural response of printing plates. Furthermore, the plate hardness has to be viewed in conjunction with the mounting tape, as this alters the elasticity of the whole system and thus the apparent hardness of the printing plate (Meyer, Dürholz und Bütterich, 1996; Holmvall and Uesaka, 2007).

Overall, the plate deformation accounts for only a fraction of the print dot gain, whereas ink spreading constitutes the major cause (Bould, 2001). S. Hamblyn (2004) determined that shallower shoulder angles increase the ink-carrying capacity of the dot, and the larger ink volume held leads to increased tone gain by ink spreading. He also emphasised that if the dot top is smaller than the opening of the anilox cell, dot dipping occurs and increases dot gain by additional ink transfer from the dot shoulders.

The effect of the plate surface energy on ink transfer is still not fully established. This decreases the accuracy of models describing the ink distribution on and ink transfer from the plates. It also results in the pairing of non-compatible plate materials and inks leading to wettability problems, lack of ink transfer and print quality; a particular issue for uncommon non-standard inks such as used for functional printing or special graphical applications. Mirle (1989) and Hejduk (2010) transferred larger ink volumes by respectively increasing the hydrophilic component and overall surface energy of the plate. Pluhar (2004) found that the best ink transfer occurs from plate materials with a lower surface energy, although he did not specify which quality criteria of ink transfer this referred to. Other studies saw no effect of the printing plate surface energy on ink transfer (Quinn et al., 1997; Liu, Guthrie and Bryant, 2004; Johnson et al., 2009). On the one hand, the lack of any effects is attributed to incomplete ink transfer and ink remaining on the printing plate. Thus, during consecutive plate inking steps an ink-ink rather than a plate-ink contact takes place and the plate surface energy is rendered inconsequential (Liu and Guthrie, 2003). On the other hand the contact angle as a measure of the surface energy is a dynamic property and influenced by the process parameters, notably printing speed and pressure (Chadov and Yakhnin, 1988; Liu and Shen, 2008),

and other material properties, notably molecular orientation, chemical heterogeneity and surface roughness (Shanahan, 1995 and 1996). The surface roughness in particular is often not sufficiently taken into account.

Commonly, plates are imaged by digital means (refer to section 1.2.1.1) and the macro-roughness in the form of regular surface striae (as created by the tracing of the laser during plate-imaging) decreases surface energy and ink transfer (Johnson et al., 2009; Hejduk, 2010). Micro-roughness (anisotropic or isotropic) of the printing plate increases the contact area with the ink, thereby raising the adhesion force at their interface and the apparent surface energy (Mirle, 1989; Bassemir and Krishnan, 1990; Pluhar, 2004; Johnson et al., 2009; Hejduk, 2010). Although increased micro-roughness enhances the wettability of hydrophilic surfaces, it hampers the wettability of hydrophobic ones. Surfaces with nano-roughness are more likely to suspend liquids over air pockets trapped in surface cavities which increases the contact angle. (Jung and Bushan, 2006)

Jung and Bushan's findings are not unexpected, because it is known from research outside the field of printing that contact angles on rough surfaces tend to be larger than the Young angle (Kwok, Ng and Neumann, 2000). Wenzel (1936) described the wettability case of a liquid which completely displaces the air in the cavities of the rough surface on which it is placed. Cassie and Baxter (1944) expressed the case of the liquid not displacing the air, but sitting on top of the air pockets. Each of them developed an extension to Young's equation (Equation 2.1) to accommodate the respective contact angles measured (Whyman, Bormashenko and Stein, 2008). However, the Wenzel and Cassie-Baxter equations are rarely applied to printing plates. A few studies investigate the principles for offset printing plates (Rousset et al., 2001; Tian, Song and Jiang, 2013), but only a single study exists for flexographic printing plates (Dedijer et al., 2012).

Dot geometry, plate thickness, hardness and surface energy can be altered significantly by dissolution and swelling if the plate material is not chemically resistant to the solvents and ink components it is in contact with (Shanahan, 1996; Galton, 2003; Liu and Guthrie, 2003; Pluhar, 2004). Features altered in this way are temporally less stable under compression and can be permanently damaged. Such an incompatibility of materials becomes more likely with the introduction of new functional inks based on different chemistries in comparison to graphic inks. (Theopold et al., 2012)

Studies on the effect of printing plate properties on ink transfer remain inconclusive. Although good progress has been made in the numerical modelling of plate deformation, the models usually do not take into account interactions with the ink. The generic use of the term "hardness" for the plate

properties of indentation hardness, Young's modulus and Poisson's ratio, as well as the disregard of the mounting tape as part of the entire plate system, might have led to the vastly different findings regarding the effect of plate hardness on print quality. The determination of surface energy remains problematic, because of a lack of fundamental understanding in general. In the field of printing, interaction effects of surface energy and roughness are not sufficiently taken into account despite the availability of advanced approaches such as the Wenzel and Cassie-Baxter equations. All of these areas provide scope for more research.

2.1.2.2 Ink and Substrate

The ink and substrate are the two other key process components besides the printing plate. The lower the ink viscosity, the more likely the ink is to spread on non-porous substrates and penetrate into substrate pores (Fetsko and Walker, 1955; Walker and Fetsko, 1955; Damroth et al., 1996). Generally a viscosity decrease in printing inks results from shear-thinning as a consequence of high printing speeds (Zang, 1992), but can also be the result of a rise in temperature. Olsson et al. (2007) observed that lower viscosity ink penetrates better into porous substrate where larger ink volumes are then immobilised. Since the ink split occurs in the mobile phase of the ink, the relative ink transfer is increased. The low-viscosity ink also spreads and levels better, thereby decreasing print unevenness on the smaller scale.

Different from most other authors, Beynon (2007) concluded from his experiments that the decrease in optical density with lower viscosity inks was due to a reduction in ink pigment concentration and ink transfer. However, the data he presents suggests an increase in ink transfer with decreasing viscosity. He also observed a strong interaction between ink viscosity and area coverage. Lower viscosity led to reduced ink spread on porous substrate for highlights and midtones which was attributed to better hydraulic impression into the bulk of the substrate instead of lateral flow. Shadow halftones saw increased ink spread which was thought to be caused by a rolling nip contact and ink buildup in the non-printing areas of the plate. However, the supporting graphs were presented in such a way that it was difficult for the reader to draw the same (or any) conclusion regarding the relationship between ink viscosity and area coverage.

The contact area between ink and substrate, and thereby ink transfer, is influenced by substrate roughness. Smooth materials facilitate an increased contact area and enhance ink transfer. (Fetsko and Walker, 1955; Walker and Fetsko, 1955; De Grâce and Mangin, 1983; Laksin and Parris, 1997; Holmvall et al., 2011) Surface voids created by the roughness of non-porous substrates can potentially hold more ink, but the ink transfer to these substrates is hampered by air held in the

voids which is difficult to displace in the printing nip. Paper porosity and the pressure gradient between ink and the air in the capillaries govern the ink absorption into porous substrates. Pores of larger volume can take up more ink, but are prone to release it again once tension is exerted on it. (De Grâce and Mangin, 1983; Zang, 1992)

2.1.3 Effect of Process Parameters on Ink Transfer

There are many parameters that have the potential to affect print quality delivered by flexography (Figure 2.5). However within the scope of this research, the process parameters of printing pressure and speed, anilox volume and geometry as well as ambient temperature are discussed in this section.

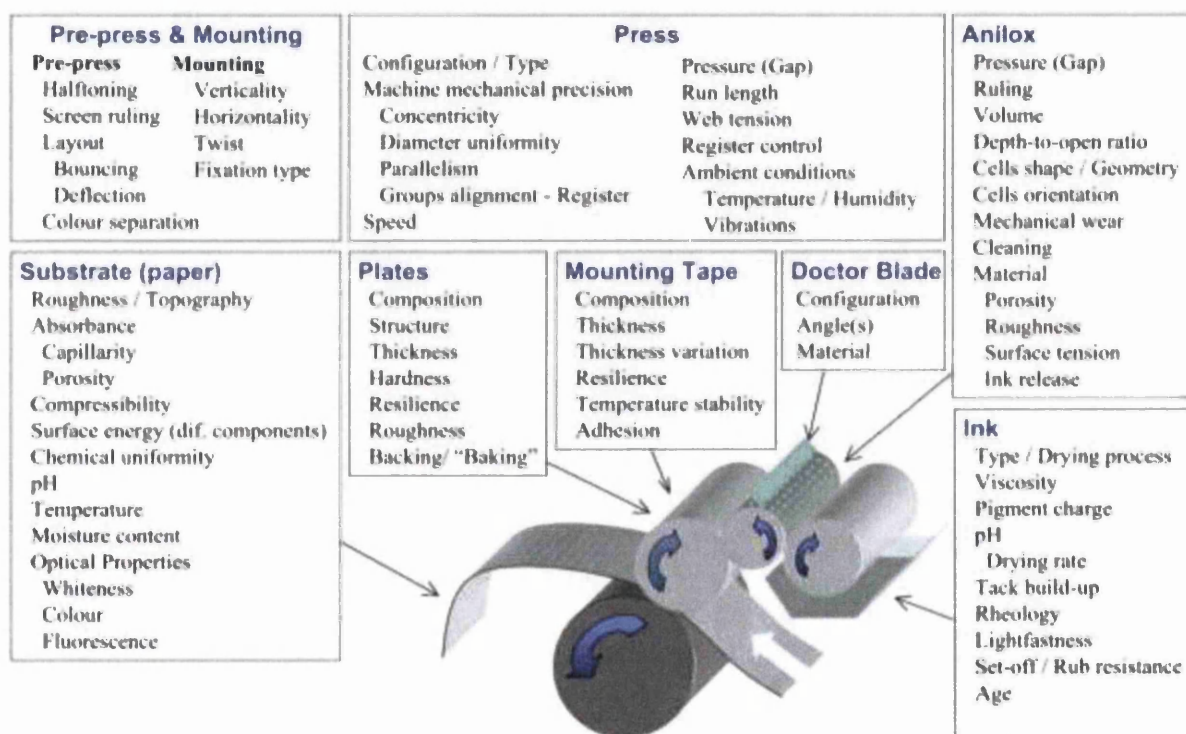


Figure 2.5: Flexographic process variables according to Barros (2004)

The printing pressure (between printing plate and substrate) affects the roughness of porous substrates, as larger forces are able to compress the fibre network and even fibre alignment which enlarges the contact area between the substrate and ink. Furthermore, increased pressure leads to lateral ink spreading on the surface and, in the case of porous substrates, into the bulk by capillary sorption. (Fetsko and Walker, 1955; Walker and Fetsko, 1955; De Grâce and Mangin, 1983; Laksin and Parris, 1997; Johnson et al., 2003; S. Hamblyn, 2004; Beynon, 2007; Bould et al., 2011)

Many studies observed an increase in print optical density with printing pressure in the lower pressure range. In the higher pressure range the effect is less pronounced and eventually levels off (Mirle, 1989; Johnson et al., 2003; S. Hamblyn, 2004; Holmvall and Uesaka, 2008a). There are a few exceptions to these findings. Bohan et al. (2003) deemed the effect of printing pressure insignificant in comparison to pressure effects at other locations in the printing press. Increased pressure between the ink chamber and anilox roll was found to improve ink transfer. This was attributed to the load on the doctor blade changing the doctoring angle and the deflection thereby reducing the wiping action of the doctor blade against the anilox cylinder. No explanation was provided for the reduction of ink transfer observed with increased pressure between anilox roll and printing plate. Olsson et al. (2006) report the highest optical densities at intermediate printing pressure. However, they state that the optical density measured does not correspond to the amount of ink transferred as determined by atomic absorption spectrophotometry. They provide no further clarification.

An increase in anilox volume leads to a rise in optical density attributed to an increased total ink supply for transfer (Damroth et al., 1996; Lindholm et al., 1996; Fouché and Blayo, 2001; S. Hamblyn, 2004, Beynon, 2007; Bould et al., 2011). The ink transfer between the anilox roll and printing plate is dependent on the geometry of the anilox cells (S. Hamblyn, 2004; Cherry, 2007; Bould et al., 2011). Smaller cells provide more resistance to the extraction of ink. In general, higher printing speeds reduce the filling of the anilox cells from the reservoir and their emptying to the plate. It was thought that speed also affects the amount of ink removed from the anilox cell by doctor blade action, the so-called "Kunz effect" (Kunz, 1975). Analogous observations were made by Davies and Claypole (2004) for the rotogravure process.

Furthermore, higher printing speeds decrease the nip dwelling time (typically milliseconds). As this is associated with the impression of ink into porous substrates, the ink transfer is also reduced. (Fetsko and Walker, 1955; Walker and Fetsko, 1955; De Grâce and Mangin, 1983; Zang, 1992; Damroth et al., 1996; Fouché and Blayo, 2001; Johnson et al., 2003; S. Hamblyn, 2004). In contrast Quinn et al. (1997) and Olsson et al. (2007) observed an increase in ink transfer with printing speed. The latter postulated that a shorter nip dwelling time caused less substrate compression which allows pores to remain open and take up more ink. However, the author of this work suggests instead an interaction with the construction of the laboratory testers used in these two studies.

The effect of printing pressure, speed and anilox volume on ink transfer from halftones on conventional and standard digital printing plates under industrial conditions followed the same trends as for solids, but showed interactions with area coverage of the halftones (Johnson et al.,

2003; Hamblyn, 2004; Beynon, 2007; Holmvall and Uesaka, 2008b; Borbély and Szentgyörgyvölgyi, 2011).

Temperature affects ink transfer in two ways which compete with each other. On the one hand, it lowers ink viscosity and thereby facilitates ink spread and absorption. On the other hand, higher temperatures promote faster ink-setting, so that the immobilised ink is anchored in place. This may impact print quality, e.g. by reducing print gloss through faster and less favourable setting of ink components. (Olsson et al., 2007)

Despite extensive research into flexographic process parameters, a number of factors remain unclear regarding their effects on ink transfer. The varying effects of, for example, printing pressure and speed suggest that there might be interactions with other process and material parameters which have not yet been considered or sufficiently explored. The constant introduction of new materials to the printing process does not simplify the matter. This provides numerous starting points for future research.

2.2 Flexographic Printing Plates

This section is dedicated to the plate parameters which constitute the main focus of this work, namely the geometry of the top of halftone dots and texturing of printing surfaces.

2.2.1 Geometry of Dot Tops

As overviewed in section 1.2.1.2, plate-making technology now has the capability to facilitate the production of different dot top shapes, notably round or flat. Conventional analogue plates have printing features with mostly level tops and a sharp edge to the dot shoulder. The introduction of standard digital printing plates brought dome-shaped dots without obvious distinction between dot top and shoulder (Figure 2.6). These are a product of oxygen inhibition during the polymerisation process. New digital imaging technology replicates conventional plate-making in that it prevents oxygen inhibition and therefore leads to the creation of level printing features. (Anderson and Schlotthauer, 2010) The method is referred to as “flat-top imaging technology” (Shibanov, 2012).

The differentiation of “flat” and “round” dot geometries is generally accepted, as this is perceived from microphotographs such as in Figure 2.6. However, microphotographs taken perpendicular to the dot top indicate the existence of concave geometries (Figure 2.7). Only three publications could be identified which refer to concave dot tops. Hornschuh (2005) attributes the “doughnut” printing defect (refer to 2.3.2.1) to erroneous plate-making which creates printing features with top edges higher than the centre. Claypole et al. (2008) observed ridges atop the edges of printing fields on

conventional and standard digital plates. Sievers (2011) described how all three types of top geometry (convex, flat and concave) can be achieved on the same standard digital plate material by varying the intensity of light exposure.

No publications were found which quantify the actual top geometry and investigate the resultant print quality. In general very little research into the printing behaviour of features with different dot tops is available. All scientific publications identified which directly compare the effects of top geometry are addressed below.



Figure 2.6: Comparison of microphotographs of standard digital (left) to “flat-topped” (right) plate features and their resultant print quality (inset pictures) (Charlesworth, 2008)

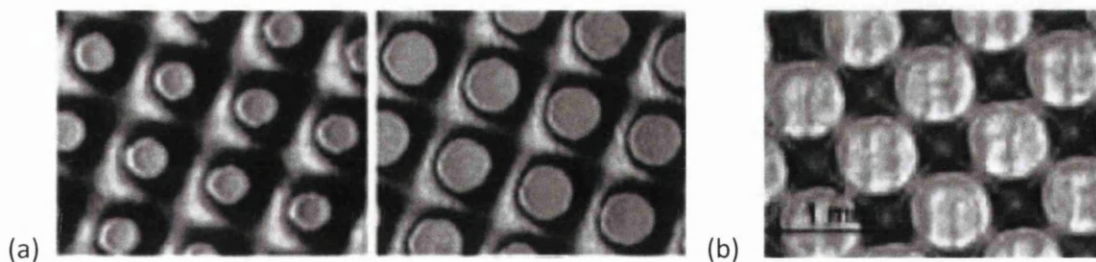


Figure 2.7: Microphotographs of halftone dots suggesting concave dot geometry on (a) conventional (Harri and Czichon, 2006) and (b) standard digital plate (Johnson et al., 2009)

2.2.1.1 Effect of Top Geometry on Ink Transfer

During the imaging of the design onto the printing plate, conventional plates experience an increase in feature size, i.e. dot diameter or line width, compared to the nominal values, whereas features on standard digital plates decrease. On “flat-topped” plates almost complete fidelity is achieved (DFTA, 2002; Beynon, 2007; Yusof et al., 2007; Claypole et al., 2008; Valdec, Zjakić and Milković, 2013). The negative plate gain on standard digital plates is usually addressed by increasing the feature size using correction curves (Mahović Poljaček et al., 2013; Tomašegović, Mahović Poljaček and Cigula, 2013b).

For the ink transfer from the plate to the substrate, little difference in relative dot gain was seen between conventional and standard digital plates (Claypole et al., 2008; Gilbert and Lee, 2008). In absolute terms conventional plates performed better at low printing engagement and line ruling where feature sizes were closer to target. Standard digital plates without correction excelled at high engagement and line ruling, because they compensated the effects of increased deformation and ink spread with negative plate gain. (Yusof et al., 2007) Corrected digital plates caused significant dot gain which was thought to result from identical printing engagement leading to more relative dot deformation and the lack of shoulder sharpness facilitating more ink spread (DFTA, 2002).

Studies attributing standard digital plates with higher dot circularity on the plate, improved print contrast and reproducible tonal range, but less print uniformity have to be treated with caution. Beynon (2007) concluded that halftone dots on conventional plates have a less circular dot shape due to a lack of intimate contact between the imaging film and plate allowing light leakage. This is disputable, because light leakage and scattering have the potential to improve non-circularity caused by irregularities in the film mask. Furthermore, the effect of oxygen inhibition on the circumference of standard digital halftones was completely ignored. Galton (2005a) investigated the effect of imaging technology on the uniformity of halftone prints using the approach of Design of Experiments. He attempted to calculate the effects of seven factors using only eight experiments which resulted in a position whereby the individual effects could not be resolved from their interactions. Therefore, the finding that conventional plates result in better halftone print uniformity remains unclear. Gilbert and Lee (2008) compared prints from conventional and standard digital plates. However, their prints were produced under different printing conditions and by several press operators casting doubt about the consistency of their experimental approach. Furthermore, the authors' results lack any critical explanation accounting for cause and effect.

Only one article compared the effect of standard versus "flat-topped" digital plates in a rigorous way (Valdec, Zjakić and Milković, 2013). The dots on the standard digital plate were very sensitive to changes in printing pressure and produced higher dot gain. Numerical modelling of the dots without ink showed that the flatter the dot, the more uniform was the pressure distribution across the printing surface and within the bulk of the material, and the less shoulder barrelling occurred. However, a significant stress concentration took place at the sharp transition of top to shoulder which indicated that "flat-topped" dots were unable to deform as continuously as round ones. (Holmvall and Uesaka, 2008b; Anderson and Schlotthauer, 2010) The exploration of ink transfer in flexography by numerical modelling remains incomplete to date and the approach to doing this can be better informed by experimental evidence typical of that which will be gathered in this work.

2.2.1.2 Related Publications

In the absence of research on the ink behaviour on varying dot top geometries, information can be obtained from related fields of investigation. Analogous to the behaviour of an ink drop on a halftone dot under compression, a simple model for the advancement of a liquid across a sharp edge of a conical frustum was developed by Gibbs (1873). The contact line of a growing liquid drop moves across a flat surface at an advancing contact angle, $\theta_{a,o}$ (Figure 2.8a). With further enlargement the contact line will be pinned to the sharp edge (of angle φ), while the contact angle relative to the frustum increases (Figure 2.8b). If the contact angle reaches a critical value θ_a (Figure 2.8c), the drop collapses down the side of the cone (Figure 2.8d). The critical contact angle was calculated by Gibbs as a purely geometrical extension to the contact angle in Young's equation (Equation 2.1):

$$\theta_a = \theta_{a,o} + (180^\circ - \varphi) \quad \text{Equation 2.2}$$

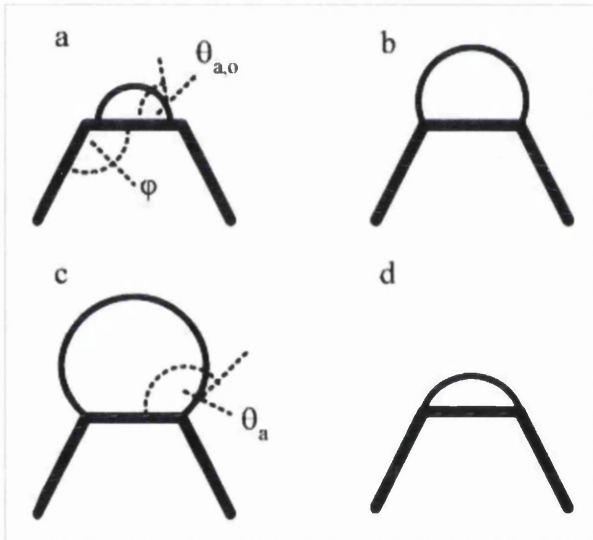


Figure 2.8: Mechanisms of liquid pinning to sharp edge of conical frustum – (a) drop inflation, (b) contact line advancement atop frustum, (c) liquid pinning to frustum edge and (d) drop collapse (Extrand and Moon, 2008)

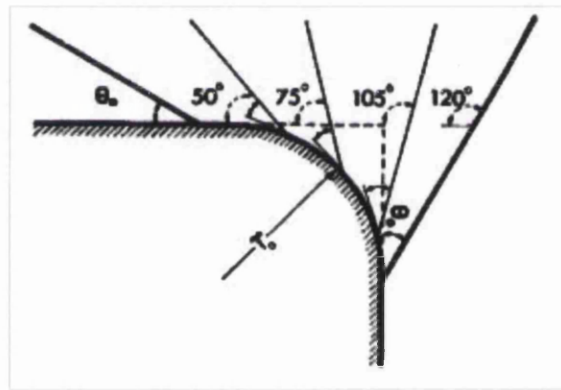


Figure 2.9: Apparent liquid pinning to imperfect sharp edge (Oliver, Huh and Mason, 1977)

The “Gibbs inequality” has been confirmed experimentally (Oliver, Huh and Mason, 1977; Extrand and Moon, 2008; Chang et al., 2010; Tóth et al., 2011). Oliver et al. specified that no edge could ever be perfectly sharp (Figure 2.9). Therefore, the contact line advances along the radius of the edge whenever the condition of the advancing contact angle $\theta_{a,o}$ is fulfilled. For any angle smaller than $\theta_{a,o}$ the contact line remains pinned in position. If the drop can maintain equilibrium, its advancement is continued on the new surface under the same conditions. In the dynamic case the critical angle θ_a will be exceeded and the liquid collapses down the sides. The contact line pinning

takes place in the case of invading as well as retreating liquids. The former is governed by the advancing, the latter by the receding contact angle. (Extrand and Moon, 2008; Chang et al., 2010) This is significant for the ink transfer process to and from halftones of any geometry as well as for the continuous buildup of ink on the dot shoulders. For example, more ink buildup would be expected for halftones with round top geometry and shallower shoulders, because the critical contact angle to overcome pinning can be achieved more easily under compression.

Gibbs' model was also found to be valid for pillars with triangular or square base, although the critical contact angle was formed at different times around the circumference of the non-circular edge. It was first achieved along the sides of the edge and last at its corners. The liquid could spread down the sides of the pillar at angles higher than the critical contact angle without collapsing the drop, because the entire volume was still suspended from the corners of the edge by pinning. However, circular pillars held more liquid (normalised to the surface area) than square and triangular ones at the instant of collapse. (Tóth et al., 2011) Furthermore, the suspended volume was not only dependent on the primary shape of the feature (side angles and edge geometry), but also on any secondary asperities present (Figure 2.10). Secondary texturing was found to be hierarchically dominant in the determination of wetting properties and improved the feature's ability to suspend a liquid drop. (Extrand, 2005) These two observations are of relevance for halftones dots with irregular circumference, such as those imaged with SQUAREspot laser technology which suffer from jagged edges, and dots with high surface roughness. It implies that the former have lower and the latter higher ink-carrying capacities.

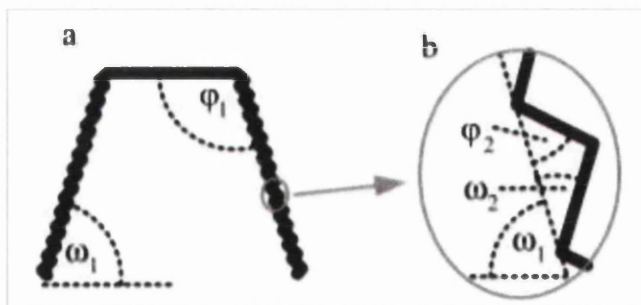


Figure 2.10: Secondary asperities on the sides of a conical frustum (Extrand, 2005)

2.2.2 Texturing of Printing Surfaces

Surface texturing on the printing plate falls into one of two categories: increased micro- or nano-roughness, and patterning. Roughness is a plate property and its effect on ink transfer has already been discussed above. Popular commercial implementations of patterning are MicroCells (EskoArtworks, Ghent, Belgium) and DigiCap (Eastman Kodak). They have in common that they are

made up of small recesses varying in size and pitch in the surface of the printing area. From here on they will be referred to as “microcell patterning”. The similarity in appearance to the engraving of anilox cylinders led to the assumption that the microcell functionality is analogous to the land areas and cells on the anilox. It is claimed that microcells carry increased amounts of ink which raise ink transfer and anchor the ink film more uniformly to the substrate (Samworth, 2001 and 2009; Kodak, 2010), but there is little scientific evidence to support this model. Patterning similar to microcells (Weichmann, 2002; Samworth and Cadogan, 2007; Stolt, Zwadlo and Rozzi, 2010) is used to control the ink film thickness by only transferring ink from the land areas of patterned surfaces. The pattern recesses are not considered to be ink-carrying, but are claimed not to be visible in the final print due to ink coalescence.

Only one publication on the investigation of microcells in an academic context was found (MacDermid Printing Solutions, 2011). In this work a print trial was conducted into the effects of microcells on print quality. Of 32 microcell patterns 15 achieved significantly higher optical densities than a plain reference solid when imaged on a standard digital plate. In combination with “flat-top” imaging technology, 22 microcell patterns outperformed the plain solid. (Cook, Recchia and Gotsick, 2014) No explanation was provided why some patterns performed better than others.

Very few other relevant publications on liquid transfer from patterned surfaces are available. Griesheimer (2013) investigated the ink transfer mechanism (filamentation in particular) from patterned surfaces using a model setup. His “patterning” consisted of halftone dots at a screen ruling of 48 and 60 lines/cm and varying area coverage. This choice of pattern is not representative of commercial surface patterning and holds more relevance for ink transfer from halftone patches. Other studies are limited to quasi-static liquid transfer between individual features rather than entire pattern assemblies (Gupta et al., 2007; Huang et al., 2008). Nevertheless, they emphasise the significance of different feature geometries and dimensions on liquid transfer, for instance pillar structures releasing liquid more easily than cavities, and shallower cavities improving relative liquid transfer.

Stolt and colleagues (2010) plainly admitted that knowledge about the underlying science of surface patterning is lacking, which has not changed to date. The only academic investigation of microcells might be biased, since the motivation for the investigation originated from the company which commercially distributes microcell patterning. In the light of increasing popularity of surface patterning in the printing industry, specific studies of the ink transfer from patterned surfaces are required to gain an understanding of any underlying mechanisms that are present and hence to optimise the printing process.

2.3 Print Characterisation

The first part of this section introduces halftone models which serve the purpose of relating print optical density to the area coverage of the printed ink film. This approach is imperative in industry where the determination of area coverage by other techniques is not viable. The second part of the section is concerned with typical flexographic printing defects, namely doughnuts and halos, uncovered areas and fingering instabilities.

2.3.1 Introduction to Halftone Models

The tool most widely used to monitor the consistency of industrial printing processes is the comparison of the area coverage of halftone control patches against target values. The area coverage is calculated from the reflectance factor measured for the respective patch using halftone models (mathematical equations expressing the relationship between parameters). This has the advantage of speed and simplicity over optical methods. A comprehensive review of halftone models was provided by Wyble and Berns (2000). Only mono-chrome approaches which are used as part of this research are introduced below.

The Murray-Davies model established itself as the standard method due to its straightforwardness and is implemented in the majority of spectrophotometers:

$$\beta_{\text{Halftone,Murray-Davies}} = (1 - A_{\%}) \cdot \beta_{\text{Substrate}} + A_{\%} \cdot \beta_{\text{Solid}} \quad \text{Equation 2.3}$$

where $A_{\%}$ is the area coverage, $\beta_{\text{Substrate}}$, β_{Solid} and β_{Halftone} are the reflectance factors of the substrate, reference solid and halftone area to be determined respectively. The disadvantage of the Murray-Davies equation are the model assumptions that all printed areas are characterised by sharp edges (i.e. hard dots) and uniform ink film thickness (Figure 2.11) as well as that no light scattering is taking place in the substrate (Murray, 1936). Changes in reflectance are purely a result of variation in area coverage. In practice neither assumption holds true and leads to the calculation of an area coverage different from the optically effective one.

The Yule-Neilson equation (Equation 2.4) accounts for light scattering and dot softness by introducing an additional parameter, n , which is dependent on substrate type (Yule, 1943; Yule and Neilsen, 1951). This additional parameter can only be established empirically for each individual substrate. However, Pearson (1980) determined that the n -value for most paper substrates lies between 1.4 and 1.8 (with a majority at 1.7).

$$\beta_{\text{Halftone,Yule-Nielsen}} = \left[(1 - A_{\%}) \cdot \beta_{\text{Substrate}}^{1/n} + A_{\%} \cdot \beta_{\text{Solid}}^{1/n} \right]^n \quad \text{Equation 2.4}$$

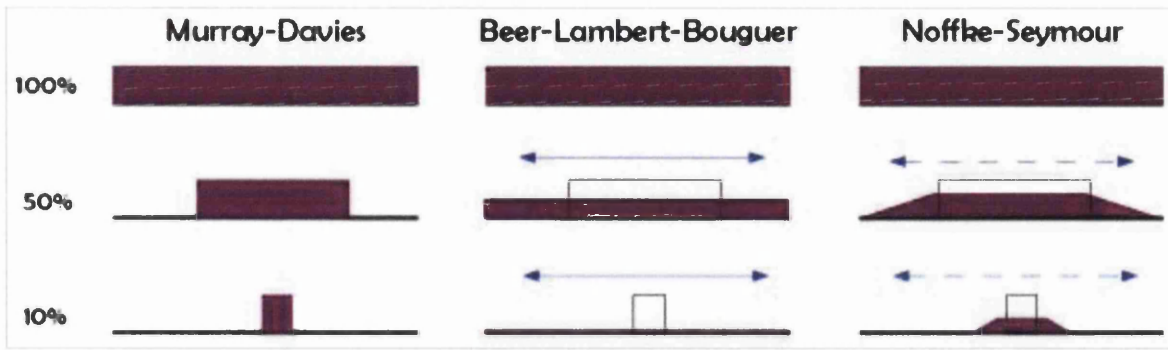


Figure 2.11: Schematic of underlying assumptions (dot sharpness and ink distribution) for different halftone models. Murray-Davies disregards ink spread and is based on uniform ink films of constant thickness and with sharp edges. Beer-Lambert-Bouguer assumes complete ink spread to 100% area coverage and accordingly changing ink film thickness. Noffke-Seymour considers partial ink spread to dots with varying ink film thickness and soft edges.

In the Expanded Murray-Davies model the effects of light scattering and dot softness are included by the separate parameters w and v (Arney, Engeldrum and Zeng, 1995), but the equations are arranged in a way that the parameters are interchangeable and no information on the underlying physics of the process can be deduced. The Expanded Murray-Davies equation (Equation 2.5) has the same form as the Murray-Davies equation (Equation 2.3) with the exception that the substrate reflectance, β_s , and the reflectance of the solid reference, β_i , become functions of area coverage and have to be determined by Equation 2.6 to Equation 2.8.

$$\beta_{Halftone, Expanded Murray-Davies} = (1 - A_{\%}) \cdot \beta_s\{A_{\%}\} + A_{\%} \cdot \beta_i\{A_{\%}\} \quad \text{Equation 2.5}$$

$$\beta_i\{A_{\%}\} = \beta_{Substrate} \cdot [1 - (1 - \tau_{Ink}) \cdot A_{\%}^w][1 - (1 - \tau_{Ink}) \cdot A_{\%}^v] \quad \text{Equation 2.6}$$

$$\beta_s\{A_{\%}\} = \beta_{Substrate} \cdot [1 - (1 - \tau_{Ink})(1 - (1 - A_{\%})^w)] \cdot [1 - (1 - \tau_{Ink})(1 - (1 - A_{\%})^v)] \quad \text{Equation 2.7}$$

$$\tau_{Ink} = \left(\frac{\beta_{Solid}}{\beta_{Substrate}} \right)^{1/2} \quad \text{Equation 2.8}$$

where τ_{Ink} is the ink transmittance of the reference solid (Equation 2.8).

A continuous tone model based on the Beer-Lambert-Bouguer law (Equation 2.10) was suggested by Seymour and Noffke (2012; Seymour, 2013a). It is based on the supposition that the printed ink volume is conserved, but spread out over the substrate until it forms a uniform solid ink film (Figure

2.11). The optical density then becomes solely dependent on ink film thickness. In its assumption of perfect ink spread the Beer model represents the other extreme to the Murray-Davies model which assumes no ink spread whatsoever.

$$\beta_{Halftone,Beer} = \left(\frac{\beta_{Solid}}{\beta_{Substrate}} \right)^{A\%} \cdot \beta_{Substrate} \quad \text{Equation 2.9}$$

For a more accurate representation of the actual limited ink spread in a soft dot (Figure 2.11), Seymour and Noffke (2012) combined the two models to form the Dot Spread equation (Equation 2.10), now known as the Noffke-Seymour equation (Seymour, 2013b).

$$\beta_{Halftone,Noffke-Seymour} = (1 - a_2) \cdot \beta_{Substrate} + a_2 \cdot \left(\frac{\beta_{Solid}}{\beta_{Substrate}} \right)^{a_1/a_2} \cdot \beta_{Substrate} \quad \text{Equation 2.10}$$

where a_1 and a_2 are the relative area of the halftone dot on the printing form and spread out in the print respectively. The equation cannot currently be solved in closed form. Neither the Beer nor the Noffke-Seymour equations take into account the optical dot gain.

There is currently no universal halftone model which predicts accurately the printed area coverage based on optical density. Only empirical studies reveal which model provides the best fit to data from different printing processes, substrates, halftone dot shapes, line rulings and so on. It is not known how innovations such as “flat-top” imaging technology and surface texturing of the printing plate in flexography change the suitability of the traditional halftone models. This is a topic of academic interest as well as industrial significance which merits exploration.

2.3.2 Printing Defects

Printers differentiate between many defects impacting print quality (Mathes, 2011 and 2012), but only a few of them are directly relevant to this research and addressed below.

2.3.2.1 Doughnuts and Halos

“Doughnuts” are printed halftone dots which assume a ring-shape due to lack of ink in their centre (Figure 2.12 left). It is generally assumed to be caused by the ink being displaced outward and away from the top of the printing feature during substrate contact, a hypothesis supported by the fact that doughnuts are more prominent at high impression pressure (Mathes, 2012). Hornschuh (2005)

suggested that the “Donald-Effekt” (sic! phonetic error) at the start of a print run is the result of only the edges of concave dot structures printing. With increasing run length the centre of the dot also transfers ink and the doughnut effect decreases. Industry does not necessarily differentiate doughnuts from halos (Mathes, 2012).

S. Hamblyn (2004) used concave dot tops to explain a printing defect of alternative form. “Halos¹” are ink-free annuli found in printed dots (Figure 2.12 right). Although he observed only convex dot tops on his printing plates, S. Hamblyn hypothesised that during contact between the printing plate and substrate a concave dot shape is created. The hydrodynamic squeeze film effect in the ink between printing plate and substrate raises the pressure at the dot centre above the ambient pressure at the dot edge and causes the dot centre to cave in on itself (Figure 2.13). The concave dot centre seals off ink within the cup, and the ink underneath the cup brim is squeezed out leaving an ink-free area under the edge (halo). The effect was thought to be supported by the polymer in the centre of the dot being softer than the surrounding material. This could either be an inherent property based on the imaging process, or be caused by stress-hardening of the outer polymer layer under loading. An indication of the latter was provided by halos only occurring at the higher printing pressures investigated, but not the lower ones.

The literature research has revealed that no work has been published on the origin of halos or potential interaction effects with dot geometry.



Figure 2.12: Printing defect of doughnut with approximately circular lighter area in the centre (left) and halo with crescent-shaped lighter area in the dot centre (right) (Hornschuh, 2005)

¹ The definition of “halo” provided is adopted from S. Hamblyn (2004) and employed in that sense throughout this research. The industrial definition of “halo” as an outline of ink buildup along the edges of printed areas (Mathes, 2012) is not the interpretation used here.

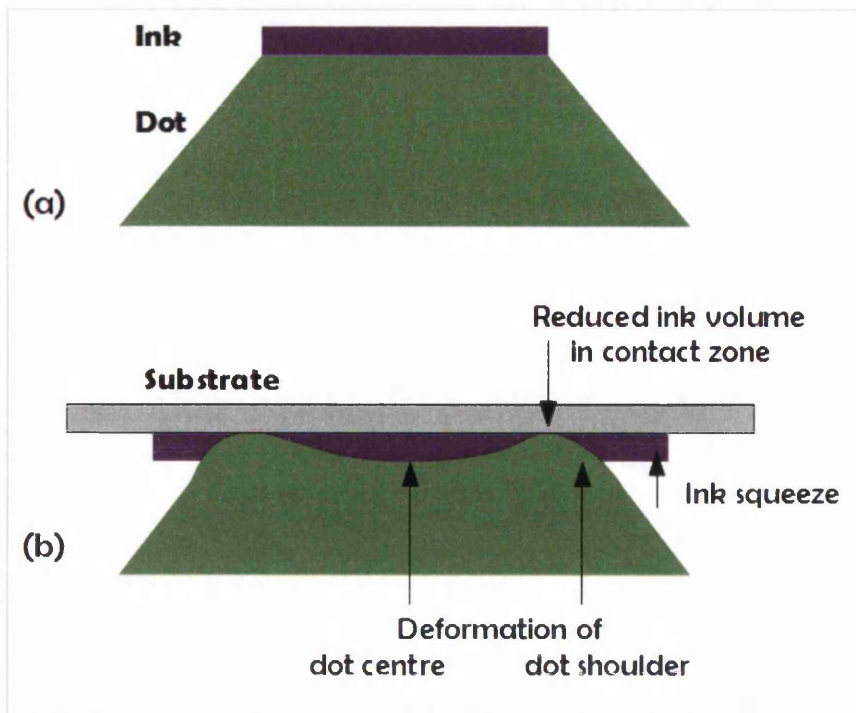


Figure 2.13: Schematic of potential cause for halo; (a) inked dot before impact, and (b) dot deformation during impact with substrate (adapted from S. Hamblyn (2004))

2.3.2.2 Uncovered Areas

Randomly occurring small holes in printed ink films are referred to as “pinholes” (Mathes, 2011) or more recently in academic circles as “UnCovered Areas” (UCAs). UCAs can be immensely important in printed functional devices where their presence can lead to complete device failure.

Barros, Fahlcrantz and Johansson (2006) saw very good correlation between flexo-printed UCAs and the location of topographical depressions in paper and paperboard surfaces. On printing, it was found that small substrate cavities could be bridged by ink, but above a critical lateral dimension or for low ink volume supplied, ink transfer failed (Naito et al., 2004; Barros and Johansson, 2006; Holmvall et al., 2011). Mettänen (2010) attributed only 20% of UCAs to the topography of super calendered and newsprint paper in offset and gravure printing. The remaining 80% were thought to be caused by other substrate properties and process parameters. Mesic and colleagues (2006a,b) compared the number of UCAs occurring in flexo-printed ink films on plastic-coated paperboard of different age and degradation after corona treatment. Since more UCAs were found on older degraded substrates, an uneven change of substrate surface chemistry and energy was assumed to affect UCAs, but conclusive proof could not be provided. Overall UCAs were attributed to wettability issues and surface topography in equal parts. Naito et al. (2006) observed the ink laydown process through the reverse of a clear plastic substrate. They reported the creation of UCAs in those

locations where air bubbles entrapped between substrate and ink film on the printing plate prevented ink transfer.

No publications were identified which investigate the role of the printing plate as a cause for UCAs, and whether UCAs are limited to solid printing patches or could also occur in printed halftones.

2.3.2.3 *Fingering Instabilities*

At very low printing speeds, ink splitting occurs as a stable smooth layer separation governed by hydrodynamic principles. Above a critical velocity, the ink-air interface at the exit of the printing nip destabilises, and printing defects occur. (MacPhee, 1997) These fingering instabilities demonstrate either transient or steady-state behaviour leading to different classes of printed patterns (McCloud and Maher, 1995). One such steady-state pattern is “ribbing” which has long been studied for different coating processes (Pearson, 1960). Ribbing is characterised by a regularly undulating ink film thickness transverse to the print direction (Figure 2.14a). A literature review can be found in Vlachopoulos (2009). It took until the late 1980s for Rabaud and colleagues (1991) to relate this so-called “printer’s instability” to a larger group of hydrodynamic defects first described by and named after P. G. Saffman and G. I. Taylor (1958). In general Saffman-Taylor instabilities are created when a less-viscous fluid (air) penetrates the interface to a more-viscous fluid (ink) forming channels in the ink known as “fingers”. The onset of fingering instabilities is governed by a critical capillary number, Ca_{crit} , which is dependent on the fluid properties and speed, or the system geometry:

$$Ca_{crit} = \frac{\eta \cdot u}{\sigma} \propto z_1 \left(\frac{h_0}{r} \right)^{z_2} \quad \text{Equation 2.11}$$

where η and σ are the dynamic viscosity and surface tension of the ink, u is the tangential velocity of the rollers, h_0 is the nip height, r is the radius of the interface curvature at the nip, and z_1 and z_2 are adjustment parameters for the respective parameter conditions (Pearson, 1960; Savage, 1984; Rabaud et al., 1991; Sauer, Bornemann and Dörsam, 2011). If the printing conditions divert from the steady state at which ribbing occurs, the fingers become transient and branched (Figure 2.14 b,c). Comprehensive literature reviews on Saffman-Taylor instabilities have been conducted by Saffman (1986), McCloud and Maher (1995). The term “viscous fingering” is currently establishing itself in the printing sector to exclusively describe branched printed patterns. “Ribbing” continues to be used for patterns of discrete, straight fingering. This convention will be followed in this work.

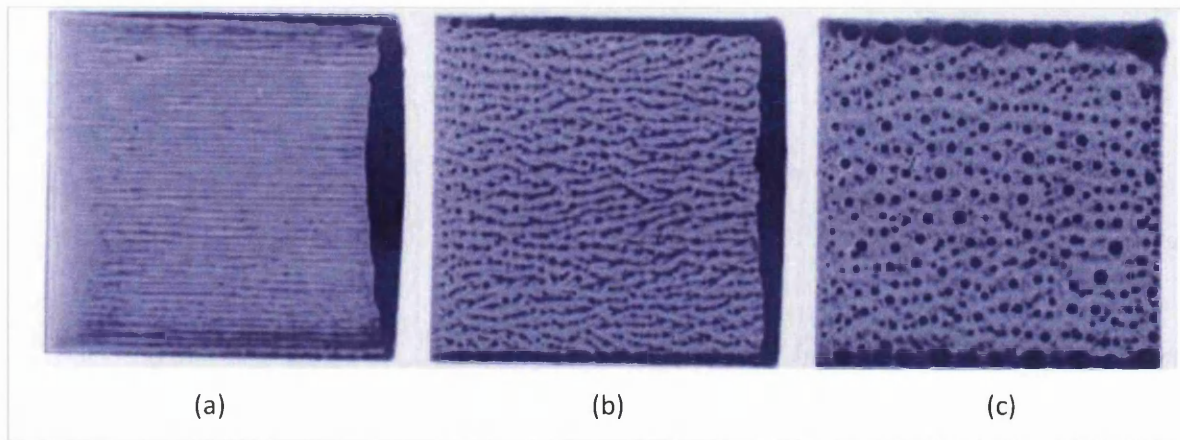


Figure 2.14: Different manifestations of fingering instabilities in prints – (a) ribbing, viscous fingering with (b) small and (c) large beads

Saffman-Taylor instabilities have been known to occur in other printing processes, although possibly categorised as one manifestation of the print defect “mottling” (Mathes, 2011). Behler (1993) attempted to demonstrate on the model of a lifting Hele-Shaw cell² how viscous fingering affected the edge structure of printed halftone dots. Voß (2002) used analytical and experimental methods to investigate Saffman-Taylor instabilities in halftone and solid flexographic prints. The experimental emphasis lay on the correlation of anilox topography with the frequency of ribbing observed in the solid prints. No correlation was found, because Voß failed to recognise that the final ink transfer step between printing plate and substrate will determine the appearance of the instabilities.

More recently the necessity to understand the mechanics behind Saffman-Taylor instabilities has gained more significance in flexographic, gravure and lithographic printing of electronic devices (Bornemann, Sauer and Dörsam, 2010). Since the instabilities cannot be avoided under sensible production conditions, the parameters affecting fingering have to be optimised to achieve the best production outcome possible (Reuter et al., 2007; Bornemann, Sauer and Dörsam, 2011; Sauer, Bornemann and Dörsam, 2011; Hernandez-Sosa et al., 2013). The graphics printing industry addressed the problem by introducing surface texturing on printing plates. That anisotropic, patterned surfaces are able to change the appearance of fingering has been demonstrated by several authors using Hele-Shaw cells³ with textured plates (literature review provided by McCloud and Maher, 1995). However, fundamental studies of the interactions between textured surfaces and hydrodynamic instabilities in a system setup that is appropriate for printing processes are missing to date.

² In general the Hele-Shaw cell consists of two parallel plates containing two immiscible fluids of different viscosity (Saffman, 1986). Behler (1991) used a lifting Hele-Shaw cell with parallel plate separation which allowed the air to penetrate the forming ink filament from the sides.

³ The Hele-Shaw cells in question had stationary plates and the less-viscous fluid was injected into the cell with more-viscous fluid through a small hole in of the plates (McCloud and Maher, 1995).

2.4 Conclusions

This literature review has shown that extensive research into flexographic printing has been conducted previously. However, due to the complexity of the process, each study can only investigate a small piece out of the big jigsaw puzzle that is flexography with findings having limited validity within the boundary conditions set. From the literature the following challenges have been identified:

- More detailed understanding of the plate deformation mechanisms causing dot gain is required as a precursor for accurate numerical modelling.
- Past numerical modelling of plate deformation did not take into account interaction effects with the ink and, in some models, disregarded the mounting tape as part of the entire plate system.
- The generic use of the term “hardness” for the plate properties of indentation hardness, Young’s modulus and Poisson’s ratio might have led to the vastly different findings regarding the effect of plate hardness on print quality.
- The determination of surface properties, including surface energy and roughness, remains problematic, because of a lack of fundamental understanding in general. In the field of printing, the interaction effects of surface energy and roughness are not sufficiently taken into account despite the availability of advanced approaches, such as the Wenzel and Cassie-Baxter equations.
- Despite extensive research into flexographic process parameters, no ultimate consensus has been reached regarding the effects on ink transfer, which suggests currently unknown interactions with other process and material parameters.
- There is no method for the quantification of halftone top geometries. Furthermore, very little research into the printing behaviour of features with different dot tops and the resultant print quality is available.
- There is currently no universal halftone model which predicts accurately the printed area coverage based on optical density. It is not known how different halftone dot geometries affect the applicability of the traditional halftone models.
- No research into the underlying science of the effect of surface patterning on print quality has been conducted to date.
- The origin of the halo printing defect is still uncertain. The influence of the dot top geometry on the defect is unknown.
- The role of the printing plate in the creating of the UCAs in prints is unknown.

- The effect of textured surfaces on the onset of hydrodynamic destabilisation of a liquid meniscus between rollers has not yet been explored in a printing context.

This review has identified a number of challenges. However, the work in this thesis will be confined to a subset of these and include a detailed exploration of two factors, namely dot geometry and surface patterning:

DOT GEOMETRY

- Are dot tops produced by standard digital technology convex; those produced by “flat-top” imaging technology level? Do concave dot tops exist? (Figure 2.15)
- Do “flat-topped” halftones achieve higher print quality by transferring larger ink volumes, causing less physical dot gain and more uniform ink laydown?
- Do dots imaged with SQUAREspot laser technology have a less circular dot top? If so, how does this affect the ink transfer from these dots?
- Do concave dot tops cause the printing defect of halos?
- Is the effect of process parameters, such as printing pressure and speed, on ink transfer independent from the geometry of the dot top?
- Is the applicability of halftone models independent from the geometry of the dot top?

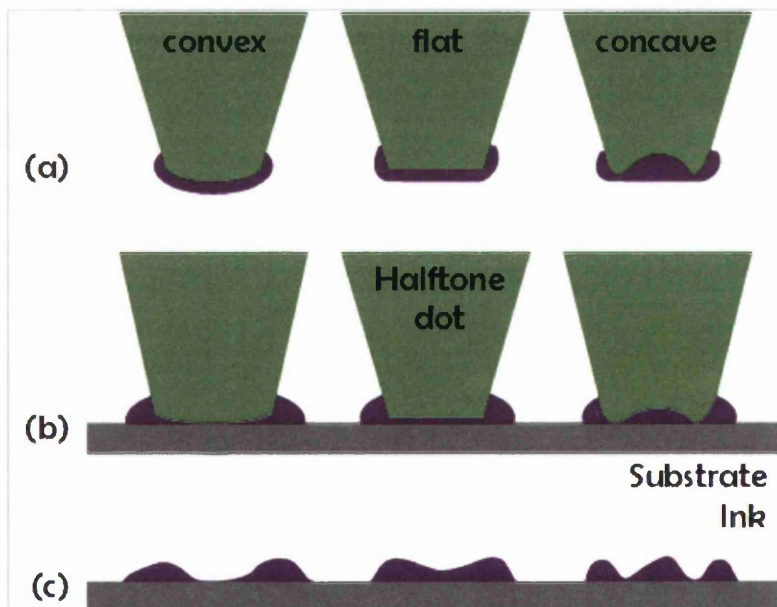


Figure 2.15: Schematic of potential ink transfer mechanisms depending on dot geometry – (a) inked halftone dots with convex, flat or concave dot top, (b) deformation of halftones against substrate, and (c) resultant ink distribution on substrate

SURFACE PATTERNING

- Does surface patterning of the printing plate increase the ink transfer to the substrate as quantified by the optical density of the prints? Does it reduce printing defects, notably UCAs and fingering instabilities? (Figure 2.16)
- Do microcell patterns act analogous to anilox cells and increase the ink-carrying capacity of the printing plate?
- Are the print results dependent on pattern design?
- Is the effect of process parameters, such as printing pressure and speed, on ink transfer independent from the geometry of the dot top?
- Is the efficiency of surface patterning increased when combined with flat-top imaging technology?

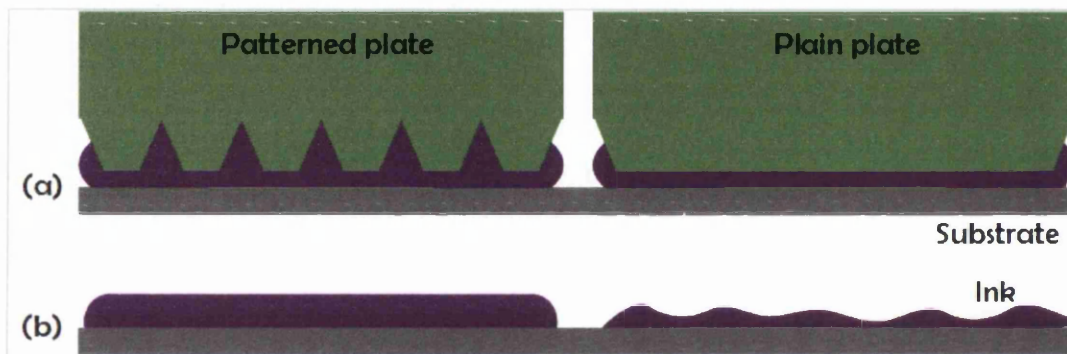


Figure 2.16: Schematic of potential ink transfer mechanisms depending on surface patterning – (a) inked plate patches with and without surface patterning, and (b) resultant ink distribution on substrate

Chapter 3 Methodology

This chapter is divided into sections reflecting the process steps employed in the investigations performed for this work: material characterisation, printing and print analysis. It was necessary to develop innovative applications of measurement techniques, in order to gain an in-depth understanding of the image transfer process.

MATERIAL CHARACTERISATION

The most important materials used in the print trials, namely printing plate, substrate and ink, were characterised with regard to their respective properties of interest for the print trials and analysis. As the main focus of this work, the printing plates received the most extensive characterisation using white light interferometry (WLI). Furthermore, it is common practice within the field of printing research to establish basic material properties such as surface roughness (plate, substrate), rheology (ink) and surface energy/tension (for all materials), because they can have significant influence on printability and print quality.

PRINTING

The print trials were performed on an IGT-F1 printability tester and under near-industrial conditions on a Timsons T-Flex 508 printing press. In order to improve the efficiency of data capturing and analysis, the technique of Design of Experiments (DoE) was employed. This method allowed the identification of the most important printing parameters (including materials) with regard to the target parameters of print quality.

PRINT ANALYSIS

The print analysis followed two different lines of inquiry. The first one saw the digitisation of the prints by scanning. Through the use of image analysis software the acquired digital images were investigated for print uniformity and density. The scanning methodology was refined in an extensive test series. The second line of inquiry involved digital microscopy, spectrophotometry and surface profilometry. Data on optical density, amount and structure of ink transferred was obtained.

3.1 Surface Profilometry

The surface profile is the key parameter explored in this work using WLI which performs contactless optical surface profilometry. The interferometer employed was a Wyko NT2000 (Veeco Instruments, Tuscon, USA) with the supporting software WYKO Vision32 (Version 2.303), and the working

principles may be found in Olszak, Schmit and Heaton (2001). It was used to determine the surface roughness of printing plates and substrates, the dimensions and geometries of printing elements on the plates, as well as the planar surface area and volume of printed features. The WLI data sets shown in this work are all false colour images obtained in the Vision 32 software (Figure 3.1). The colour coding is such that red shades in the image depict raised areas, whereas recesses are shaded blue. Surface points for which no data could be captured remained white. No data might result from surface points which are too steep or very rough, and thus reflect the incident light beam in such a manner that it cannot be detected by the microscope objective.

The descriptions of the measurement techniques are provided in the following sections. The determination of feature geometries and planar surface area were the most significant for this work.

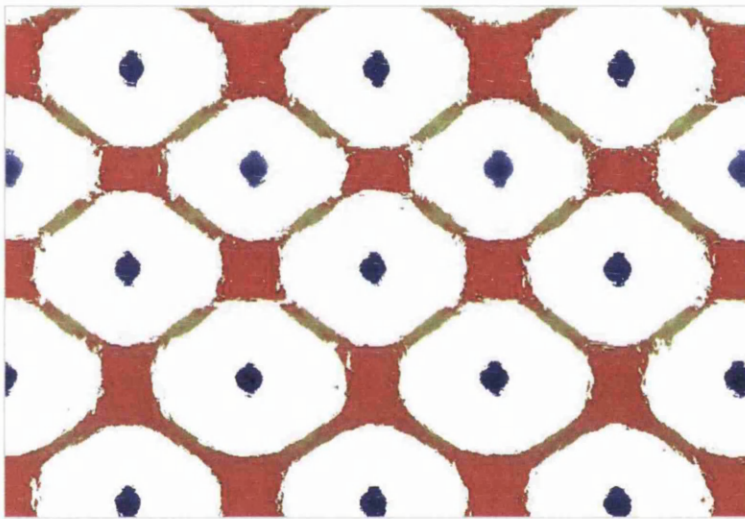


Figure 3.1: False colour image of a chequer pattern on a printing plate (blue pixels represent troughs, red pixels represent ridges)

3.1.1 Determination of Feature Dimensions and Surface Roughness

The Vision32 software has integrated display and analysis functions with which feature dimensions and geometry can be determined. For this work the “2D analysis” option was used to select a cross section through the 3-D data set and to display it as a height-width-diagram (Figure 3.2). Within the diagram, cursors may be positioned on opposite sides of the feature under investigation and the distance between the two cursors noted as feature width. Furthermore, the cursors were placed at the bottom and top of the feature to establish its height. Either measurement was dependent on the available content of the data set, e.g. the height of a printing feature could only be assessed if the data set included the relative floor height of the printing plate.

The surface roughness of a material is of interest, because it provides information on the potential contact area between two surfaces during the printing process, the surface volume in which ink can be carried, and tolerances for the determination of feature dimensions. The WYKO Vision32 software is able to calculate different predefined roughness parameters from the surface data of which two have been used in this work, notably R_a and R_z (Lippold and Podlesny, 1998).

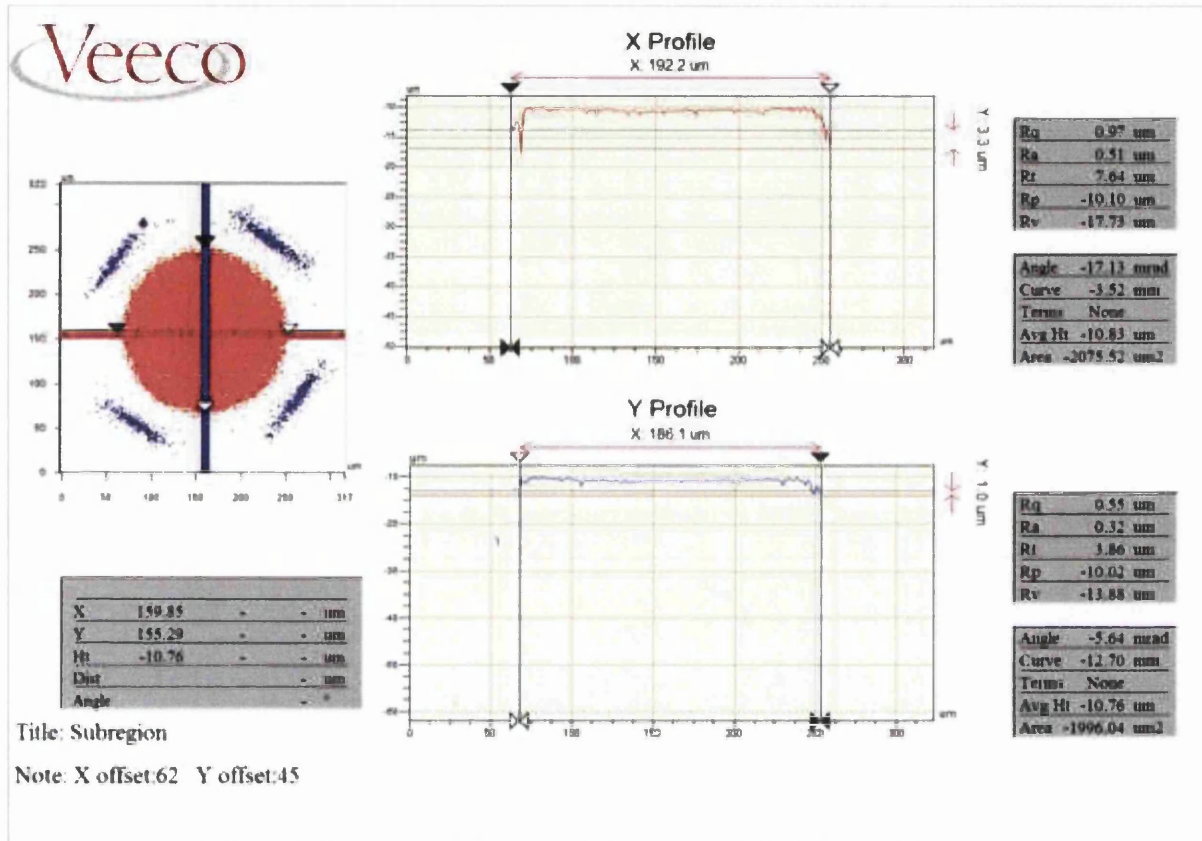


Figure 3.2: Display option “2D analysis” in WYKO Vision32 software showing 3-D representation of a halftone dot, 2-D cross sections along two different axes, surface roughness and various other parameters

3.1.2 Determination of Planar Surface Area of Printing Features

For numerous printing features it was not sufficient to determine their dimensions in order to gain information on the surface area involved in the printing process. This held particularly true for features with rounded edges. For example, the surface area of a flat top (Figure 3.3a) could be assumed to be the primary area from which ink was transferred. On the other hand, a multitude of different surface areas could be determined for convex dots depending on the extent of top curvature and sharpness of shoulder edges (Figure 3.3b). There is currently no standard in the printing sector which provides a single or separate methods covering both cases. The challenge lay in developing a robust approach using the Vision32 software which was applicable to any type of geometry.

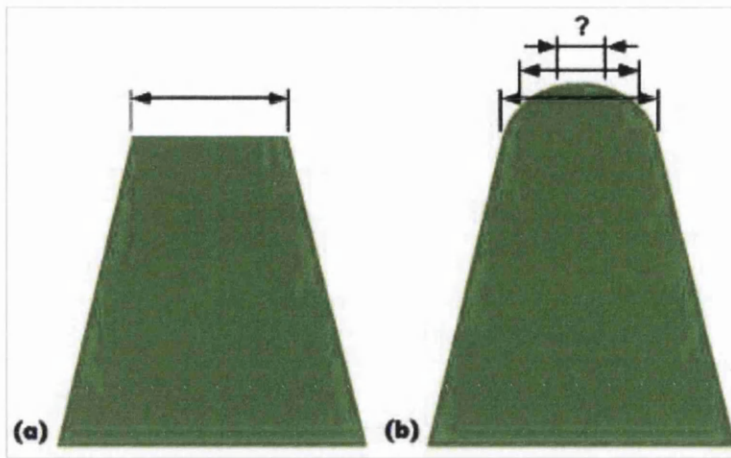


Figure 3.3: Challenge of determining the surface area for different feature geometries. The flat top of halftone dot (a) can be assumed to be the primary printing area, whereas the roundness of the halftone top (b) allows multiple possibilities for the definition of the printing area.

The next two sections contain an outline of the procedures for determination of planar surface area of halftone dots on the printing plate. Interconnected shadow halftones receive a very similar treatment to isolated dots, thus only a short explanation of necessary adjustments to the method is provided at the end of the second section.

3.1.2.1 Planar Surface Area in Wyko Vision32

Previously the planar surface area was determined based on the assumption of standard geometric shapes (Bould, 2001). For this a 3-D profile of the convex halftone dot on the plate was obtained by WLI and a 2-D cross section of this data set exported into a Microsoft Office Excel spreadsheet. There all data points that fell below a certain surface height (i.e. the dot shoulders) were removed in order to define the dot top. The expanse of the remaining data points was defined as the diameter of the dot top and the planar surface area calculated as a circle with such a diameter.

However, S. Hamblyn (2004) acknowledged that printing features rarely correspond to standard geometric shapes, and developed a method employing built-in functions of the WYKO Vision32 software. The principles of his technique were adopted for this work, and a new customised display and analysis function designed for the Vision32 software. The display comprised a 3-D view of the region of interest (ROI), the height histogram of the data points within the ROI and an analysis box providing information on planar surface area⁴ and volume⁵ (Figure 3.4).

⁴ The planar surface area function is called "lateral surface area" in Vision32.

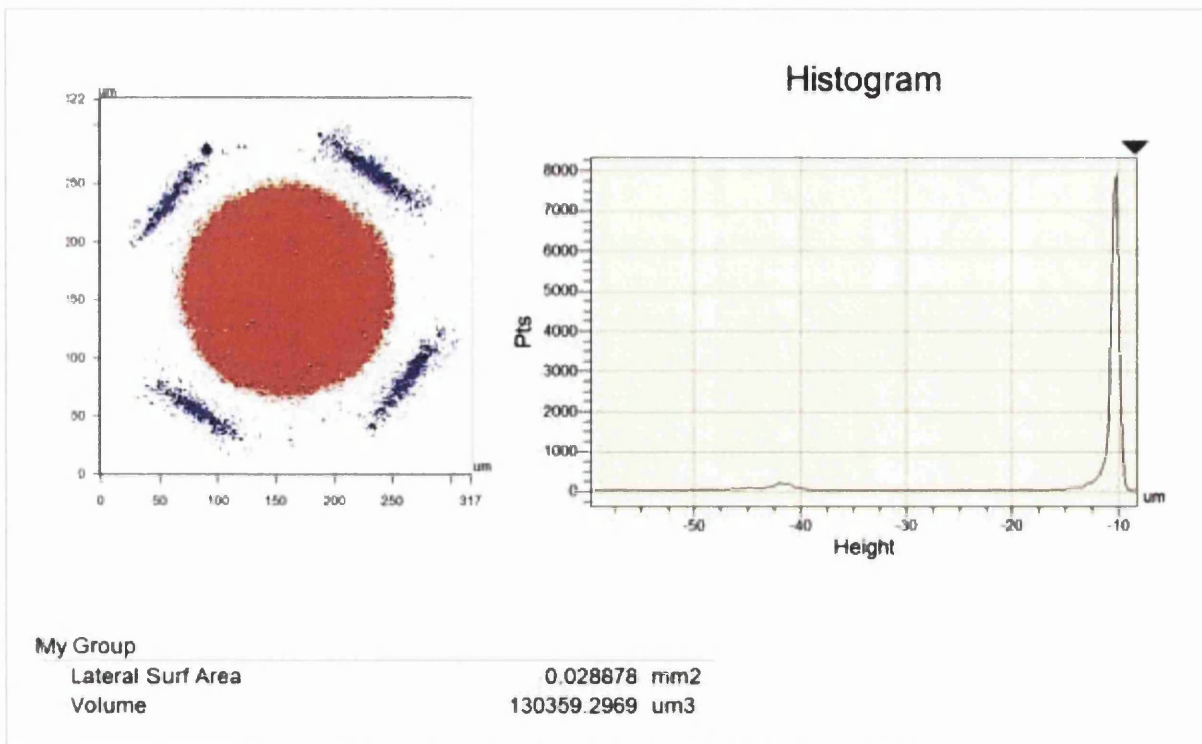


Figure 3.4: Customised display option in WYKO Vision32 software for determination of planar surface area and volume showing a 3-D representation of a halftone dot, a height histogram of the surface pixels and the measurand parameters

Firstly, if several printing features were contained within the original data set, a single dot was isolated using the subregion option in the 3-D viewing box. The utmost care was taken to avoid tilting the sample during the measurement stage. The option of tilt removal in the Vision32 software was not used, thus preventing height skew in the data set. The heights were then displayed in a histogram which characteristically shows one to three peaks in the height distribution. The peak at the largest height corresponded to the dot top. The peak at medium height denotes the valley between two adjacent dots on the plate. The third and lowest peak represents the plate floor. The latter was not usually captured, as measurements were normally performed within large fields of adjacent dots.

To isolate the planar surface area from the rest of the dot, the histogram peak for the dot top and the surface roughness R_z were used. This is based on the assumption that the planar surface consists of data points with heights centred around the dot top peak (DTP) and ranging from $(DTP - \frac{1}{2}R_z)$ to $(DTP + \frac{1}{2}R_z)$. All histogram data below $(DTP - \frac{1}{2}R_z)$ was masked (i.e. temporarily removed from the ROI shown), leaving only the data points constituting the dot top for analysis. The quality of the data displayed could be improved further by manually masking stray data

⁵ The volume function referred to is the “natural volume” and explained in section “3.5.2”.

points outside the main surface area, e.g. specks of dust or other contaminations, however manual intervention should be avoided to ensure a consistent approach and this was adopted in this work. The planar surface area was then determined by the software based on the number of pixels constituting the remaining image.

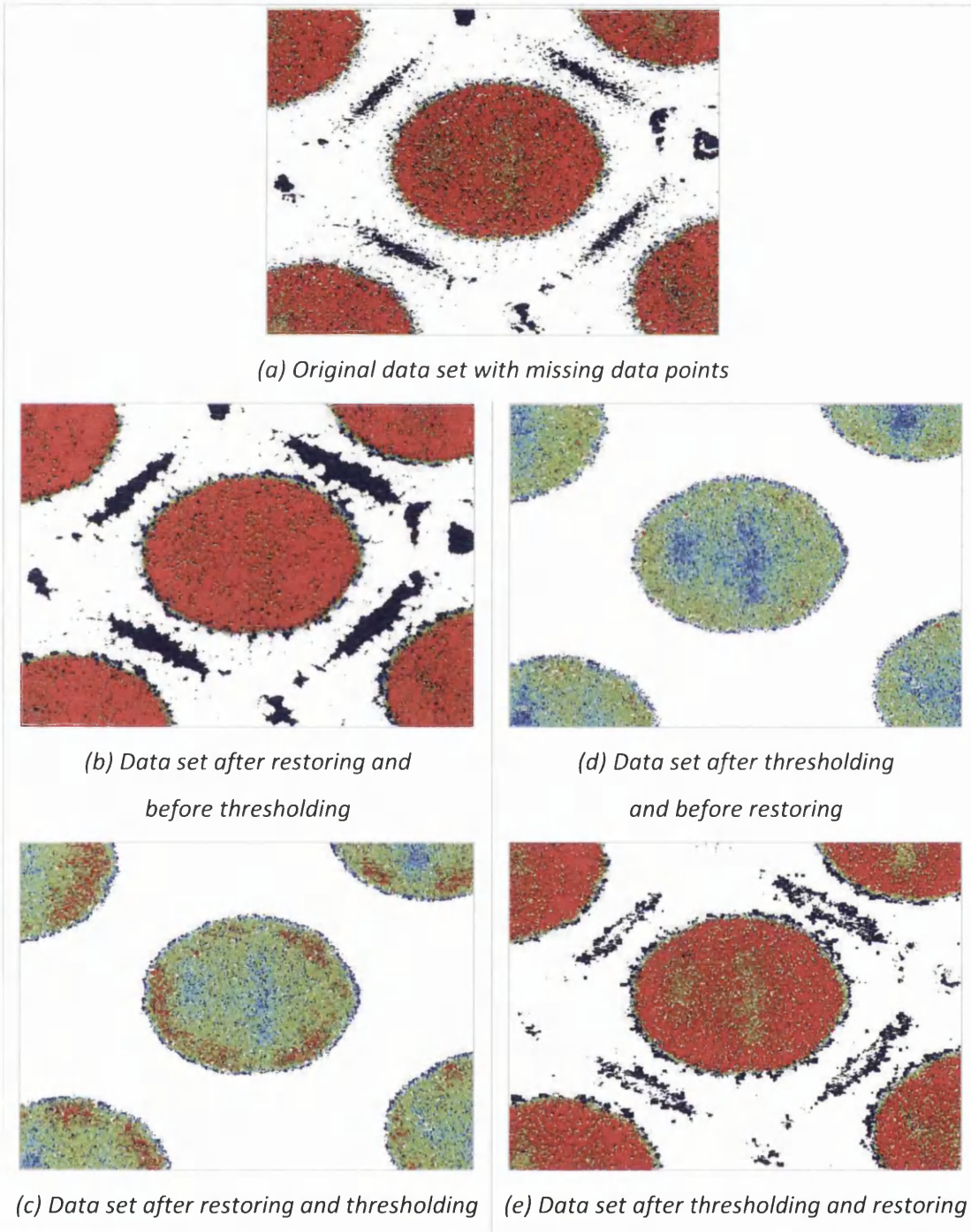


Figure 3.5: Comparison of 3-D appearance of halftone dot for different restoration and threshold sequences in Vision32

Since this method is dependent on the pixel count, it is important that minimum data points are missing from the original data set. This was the case for materials having low surface roughness, and the method worked well for these. The rougher the material under investigation, the higher was the likelihood that the data set contained gaps within the dot top where light scattering prevented data capture. The lack of data points inevitably resulted in an underestimation of the planar surface area. It was therefore necessary to introduce additional processing steps, before the planar surface area could be determined.

The Vision32 software contains an algorithm to infill missing data points by interpolation of surrounding data. The quality of the restored results is dependent on the amount of data missing. Figure 3.5 illustrates the effect that the order of restoring and thresholding had on the original data set (Figure 3.5 a). Only interior points were restored across a field of no more than five missing data pixels. The limitation of pixel number improved the data quality, but failed to infill all missing points within the dot area. Restoring the data first, had the disadvantage that the application of the height threshold created new missing data points within the area of interest, thereby leading to the original problem (Figure 3.5 b,c). A subsequent second data restoration was not possible. Applying the height threshold before restoration, in many cases resulted in fields of missing data larger than the restore option was able to fill, thereby yet again failing to resolve the original problem (Figure 3.5 d,e). This exhausted the capabilities of Vision32 without leading to the desired result of creating a data set of the dot top without missing pixels. Therefore, the final approach was to export the data set and to develop a new technique to infill the missing data.

3.1.2.2 Planar Surface Area in ImageJ

Strategically, image analysis may lend itself to improving the data set for the determination of the planar surface area, and ImageJ (version 1.44o) (Abràmoff, Magalhães and Ram, 2004) was adopted to explore this as well as being used for other parts of this work. Within the calculation sequence, once the data for the dot top was isolated in the Vision32 software through height thresholding (no data restore function applied), the data set was exported as a false colour image in TIFF. The created file was then processed in ImageJ. For ease and speed of analysis, an ImageJ macro containing the necessary processing steps was written (Appendix A.1). User interaction with the macro was possible only to permit the selection of the correct ROIs within the images.

The main function of the macro was to separate pixels belonging to the image background from those of the same colour representing the missing data within the planar surface area (both were white on export from Vision32) (Figure 3.6a). Pixels within the background area were flood-filled in

the colour black, thereby distinguishing them from points representing the dot top and the missing data points contained within the top area (Figure 3.6b). The colour-separated pixels could then be counted and stored to form a histogram. Other processing steps in the macro solely served the purpose of presenting the image and pixel count in such a way that the user could access the ROI and count efficiently. For this step the image was converted to binary black-white (originally black pixels remaining black and any other colour pixels rendered white) (Figure 3.6c). The user was then prompted to select the ROI, and only the number of white pixels was displayed in the histogram (corresponding to the planar surface area in “pixels” unit). Finally, the pixel count was converted into area (expressed in “ μm^2 ”) using calibration information recorded on image generation by the Vision32 software.

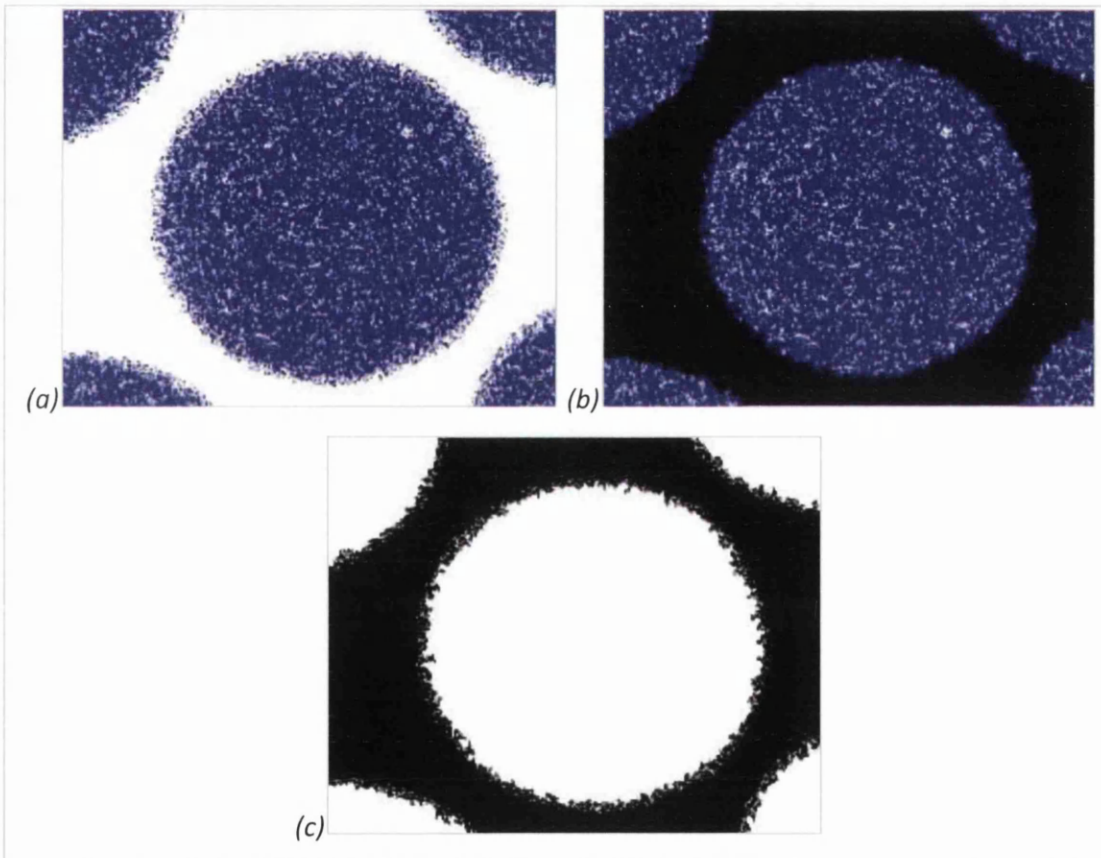


Figure 3.6: Image processing steps in ImageJ for determination of planar surface area of an isolated printing feature:
(a) original image with data points of the dot top (blue) and missing data points (white), (b) colour separation of background pixels (black) and missing data points within dot top (white) by flood-filling the background in colour black, and (c) rendering all surface pixels (previously blue and white) in colour white thereby including the missing data points of the dot top in the surface area

The macro was tested on data sets obtained from a very smooth plate material which did not result in missing data points. The relative difference in planar surface area calculated by the Vision32 software and the ImageJ macro was less than 0.1% for all samples and is attributed to the rounding

of the conversion factor between units. For consistency purposes this method was adopted for all plate materials regardless of their surface roughness. The number of individual halftone dots investigated for each line ruling and area coverage was dependent on the relative standard error of the planar surface area calculated. The number was steadily increased (up to a maximum of 30), until the standard error fell below 5.0%.

The planar surface area of shadow halftones, which were joined together, could not be determined by this version of the macro, since it was not possible to isolate the individual features from each other. Instead the planar surface area of the recess between halftones was computed with a second ImageJ macro built on the principles set out above (Appendix A.1) and then the halftone area calculated by subtracting from the square based on line ruling (refer to section 1.2.2). The two macros are distinct in that one counts the white foreground pixels for halftones and the other the black background pixels for the recesses. Both account for missing data points in the printing areas.

3.2 Surface Energy

Numerous methods exist for the determination of a surface energy (Adamson and Gast, 1967). For this work a DAT 1100 Dynamic Absorption and Contact Angle Tester (FIBRO system ab, Stockholm, Sweden) was available. This limited the options for the investigation of steady-state surface tension of liquids to the pendant drop method and of steady-state surface energy of solids to the sessile drop method.

3.2.1 Steady-state Surface Tension

For a detailed description of the pendant drop method and calculations involved therein refer to Andreas, Hauser and Tucker (1938). In this work the method was employed to determine the steady-state surface tension of the inks for the print trials, as well as to characterise the test liquids for the sessile drop method (see below). The surface tension was calculated automatically by the algorithms implemented in the DAT 1000. The method was found to be very consistent. The relative standard error of the surface tension obtained by this method on 16 drops of each ink sample was 0.1% maximum.

3.2.2 Steady-state Surface Energy

While the surface tension of a liquid can be found relatively easily using the pendant drop method, problems arise for the establishment of a solid's steady-state surface energy by the sessile drop method. The latter relies on a conversion of the Young contact angle which in itself is reliant on the

employment of the correct interfacial tension between solid and liquid. However, the nature of the interfacial interactions and thereby the mathematical expressions describing these relationships are still not fully known (Della Volpe et al., 2004; Żenkiewicz, 2007b). Two different schools of thought on the treatment of the interfacial tension dominate the field of surface science. The Equation of State approach takes the view that the interfacial tension and thereby the contact angle are only dependent on the total liquid surface tension and the solid surface energy (Spelt and Neumann, 1987; Spelt et al., 1996; Kwok and Neumann, 1999). The Surface Tension Component (STC) approach tries to reflect the origin of the total interfacial tension by dividing it into its contributing forces (Fowkes, 1962; Owens and Wendt, 1969; Kaelble, 1970; Rabel, 1971; van Oss, Chaudhury and Good, 1988; Good, 1992; Della Volpe et al., 2004). Both methods are limited by the assumptions they are based on, and practical results obtained are dependent on the test materials used (Kwok, Li and Neumann, 1994; Żenkiewicz, 2007a; Hejda, Solař and Kousal, 2010). Nevertheless, their results are considered to be very similar if the uncertainty of the methods is taken into account (Della Volpe et al., 2004).

In the field of printing research, the STC method named after van Oss, Chaudhury and Good is gaining importance (Mirle, 1989; Järnström et al., 2007; Debeljak et al., 2013), but the slightly less complex approach of Owens, Wendt, Rabel and Kaelble (OWRK) remains more popular (Quinn et al., 1997; Pluhar, 2004; Kaplanová and Hejduk, 2006; Griesheimer, 2013; Stahl, 2013). Since the surface energy components were not the focus of this work, where required, it was decided to use OWRK which limits the surface energy components to a dispersive part, σ^d , (based on molecular van der Waals interactions) and polar part, σ^p , (based on dipole-dipole interactions and hydrogen bonds):

$$\sigma_{total} = \sigma^d + \sigma^p \quad \text{Equation 3.1}$$

The solid surface energy is determined graphically employing Equation 3.2 which in essence is a linear equation. The dispersive part of the surface energy is deduced from the graph intersection with the ordinate, and the polar part from the graph slope. For a good explanation of the derivation, refer to Griesheimer (2013).

$$\frac{\sigma_l \cdot (\cos \theta + 1)}{2 \cdot \sqrt{\sigma_l^d}} = \sqrt{\sigma_s^p} \cdot \sqrt{\frac{\sigma_l^p}{\sigma_l^d}} + \sqrt{\sigma_s^d} \quad \text{Equation 3.2}$$

The contact angle determined by contour analysis of the sessile drops as well as the known dispersive and polar properties of the test liquids are inputs to the work model. To improve the data quality, it is necessary to choose a well-balanced set of at least two test liquids, one of which should be predominantly polar and the other one dispersive (Della Volpe et al., 2004; Hejda, Solař and Kousal, 2010). In this work water, ethylene glycol and diiodomethane were used to characterise the surface energy of printing plates and substrates. The consistency of the sessile drop method was verified on three different substrates (two polypropylene films, one standardised coated paper) using water as the test liquid. The relative standard error of the contact angle measured did not exceed 2.8% for any sample (based on 22 or 24 drops deposited). The approach was used to determine the surface energy of printing plates and substrates used in this work.

3.3 Rheology

A comprehensive introduction to the different rheological properties, equations and rheometers as measurement apparatus is provided by Barnes (2000). Of relevance to this work was foremost the property of shear viscosity which describes the ink's resistance to flow under a prescribed strain rate. In flexography, shear viscosities typically range between 0.05 and 0.5 Pa·s (Hübler et al., 2002) which renders it a low-viscosity process. In Newtonian liquids the shear viscosity is independent from the strain rate (Figure 3.7). Many flexographic printing inks display non-Newtonian, shear-thinning behaviour characterised by a decrease in shear viscosity with increasing strain rate, i.e. higher processing speed causes the ink to flow more easily. Furthermore, viscosity is temperature-dependent. A rise in temperature due to friction effects in the running printing press decreases the viscosity (Olsson et al., 2007).

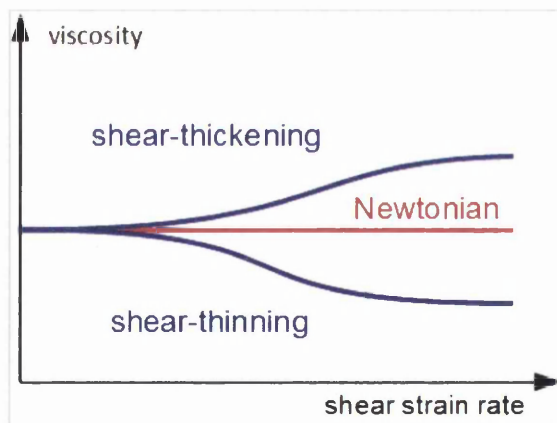


Figure 3.7: Schematic viscosity-shear rate diagram illustrating Newtonian, shear-thinning and shear-thickening properties of fluids

For this research the viscosity was determined using the shear rheometer Bohlin Gemini HR Nano (Malvern Instruments, Malvern, UK). The lower part of the test system is formed by a stationary Peltier plate, a thermal element which maintains the test liquid at a constant temperature. The upper part of the system comprised a metal cone, the size and angle of which are selected in accordance with the test fluid. The measurement space was enclosed by a solvent trap cover to prevent the evaporation of ink components and any interaction with the environment.

Before testing, the inks were homogenised in their containers by stirring. As this might affect the rheological properties, it was of essence to pre-condition the inks at very low strain rate on the rheometer prior to the actual viscosity measurement. This was followed by a time at rest to regain equilibrium. In order to capture any non-Newtonian behaviour during the test, the shear rate was step by step increased from a minimum to a maximum value, and the corresponding viscosity recorded. Tests were performed on three samples of each ink type and the relative standard error (averaged for all strain rates) did not exceed 2.8% for any of them. The actual instrument settings for the tests are provided in the materials part of each main chapter of this work.

3.4 Printing

The printing experiments for this work were conducted on a narrow-web industrial-scale printing press under conditions as close to industrial ones as possible in order to ensure industrial relevance of the research findings. Where applicable, the studies on the industrial-scale printing press were preceded by experiments on a laboratory printability tester for the screening of material and process parameters. The two different size machines employed and their related particulars are explained in the following sections.

3.4.1 Printing on Laboratory Printability Tester

The IGT-F1 printability tester (IGT Testing Systems, Amsterdam, Netherlands) is a laboratory-scale printer that simulates flexographic printing. The tester features the same main components (Figure 3.8) as an industrial printing press. However, its ink delivery system is reduced to a doctored anilox roll, and the ink is applied to the anilox using a pipette. The printability tester is pressure-driven, meaning the substrate carrier was advanced solely by the pressure exerted on it, when the anilox and plate cylinders were engaged and rotating against each other. The ink was pressed onto (and in the case of porous materials into) the substrate through the pressure in the printing nip. Adjustable settings on the IGT-F1 were: number of anilox roll revolutions before engagement with plate cylinder, printing speed, force between anilox roll and plate cylinder as well as between plate and impression cylinder. Samples produced with UV-ink were cured in a Jenton JA150SF UV-curing

conveyor unit (Jenton International, Whitchurch, UK). Where other ink types were used, the samples were air-dried.

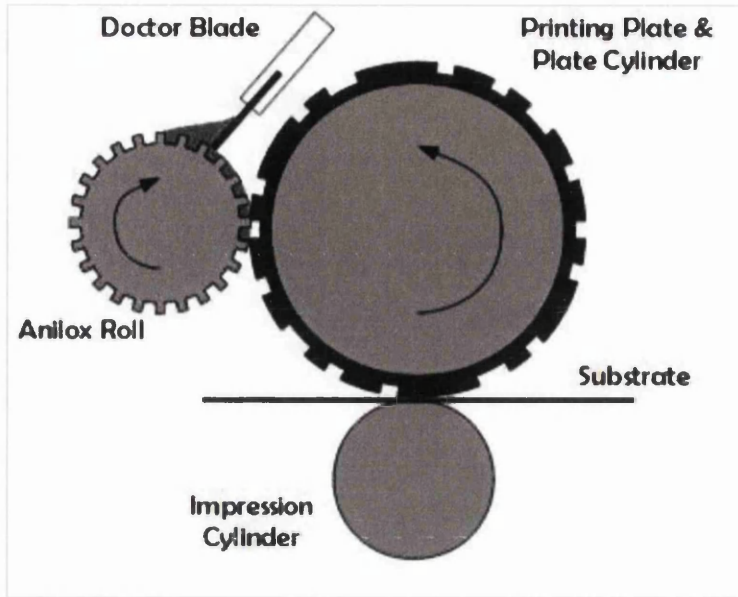


Figure 3.8: Schematic of IGT-F1 printability tester containing anilox roll, doctor blade, plate cylinder with printing plate and impression cylinder

3.4.2 Industrial-scale Printing

For the industrial-scale printing experiments the T-Flex 508 (Timsons, Kettering, UK) flexographic printing press was used. The T-Flex 508 was designed to run substrates from reel to reel. The substrate firstly travels through an alignment unit to ensure lateral registration. Consistent web positioning was essential for the fine alignment of the image produced in consecutive printing units. A corona treatment unit follows the web alignment unit, but its use was optional. The substrate then proceeded through all four printing units (Figure 3.9), before being rewound.

The web path, curing/drying station and air extraction were set up for the printing with UV-curing inks. Within each printing unit in operation, ink was circulated continuously from an ink bucket underneath the unit into the enclosed anilox chamber. The ink was transferred from the chamber to the anilox roll, printing plate and finally to the substrate. On exit from the printing unit, the ink was cured immediately under UV radiation. This avoids the potential occurrence of ink levelling and thereby loss of detail in ink laydown which is the essence of this work.

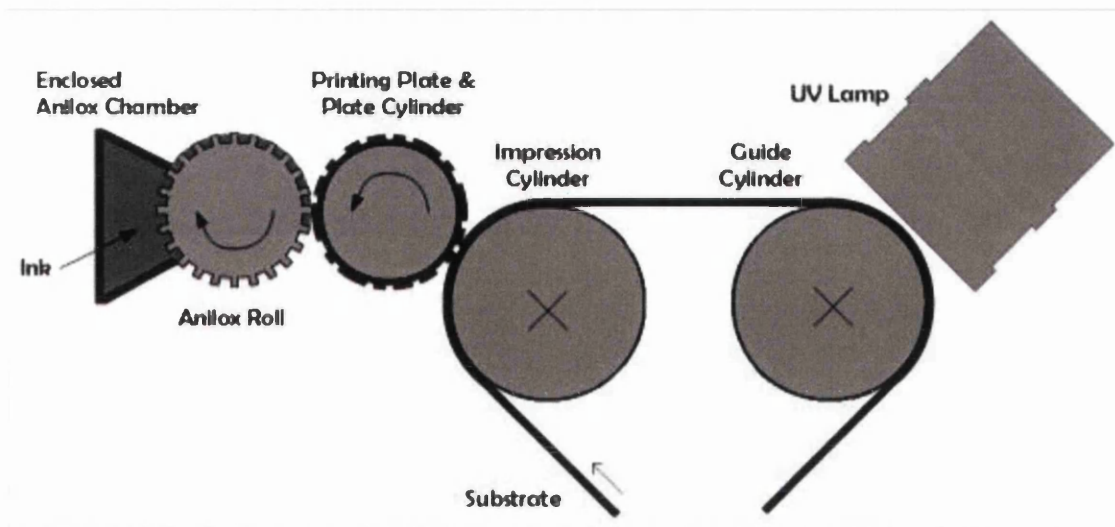


Figure 3.9: Schematic of T-Flex 508 printing unit with UV lamp containing anilox chamber, anilox roll, plate cylinder with printing plate, impression and guide cylinder

There are three main differences between the laboratory printer and industrial-scale printing press. Firstly, the ink supply by the anilox on an industrial-scale press is very consistent and is characteristically part of a closed chamber ink supply system. On the printability tester ink is supplied manually using a pipette and this leads to a source of variability, although the utmost care was taken to supply ink in a consistent manner. For the print trials on either machine, it is assumed that the entire land area of the anilox roll is wiped clean and that no ink is scooped out of the anilox cell under the doctor blade. Furthermore, the industrial press roller contact is set by engagement and not load, thus making the engagement independent of the image.

The following three sections contain details on the general setup of the T-Flex, the use of pressure sensors to establish the cylinder setup and the method to check for any cyclic variation in the print.

3.4.2.1 Setup of the T-Flex 508

The accurate fixing of the printing plate to the plate cylinder was achieved using a double-sided adhesive tape and a plate mounting station (Heaford, Altrincham, UK) equipped with high-magnification cameras to achieve precise alignment.

On the printing press itself, the most important parameters that had to be established during setup were: the engagement between the anilox roll and plate cylinder as well as the engagement between plate and impression cylinder. Firstly, the gap between plate and impression cylinder was set using a feeler gauge while bringing them together. The gauge was only slightly thicker than the combination

of adhesive tape and printing plate, thereby bringing the mounted plate within micrometer range from the substrate supported by the impression cylinder. Then the distance between anilox roll and plate cylinder was set in the same fashion.

In the next step the rotating anilox roll and ink chamber were engaged for filling, and the anilox was brought into contact with the printing plate. Any skew in the anilox cylinder was adjusted until the full length of the revolving printing plate received ink evenly and sufficiently. Then the ink chamber, anilox roll and plate cylinder system was moved towards the rotating impression cylinder. After the first contact any skew was removed and the initial distance between printing plate and impression cylinder was adjusted so that they made “kiss contact”, and minimal ink transfer took place in this zero reference position. The final engagement was then set by moving the two cylinders together beyond the kiss contact. The engagement could only be adjusted manually on the T-Flex 508 in increments of one thousandths of an inch (abbreviated as “1 thou”) which corresponds to 25.4 μm .

3.4.2.2 Thin Film Pressure Sensors

The kiss engagement at the printing nip is dependent on the printer’s perception of minimal, even ink transfer across the cylinder. Although the operator subjectivity cannot be removed from the process, crosschecks of engagement with other methods allow verification of good press setup, e.g. with regard to skew of cylinders. Since it is difficult to measure the engagement in the form of absolute distance between cylinders, the pressure in the cylinder nip served as indicator for engagement and uniformity across the cylinder width.

Engagement pressure was measured by an ELF force and load measurement system (Tekscan, Boston, MA, USA) using a single element, thin-film FlexiForce sensor. The sensor was placed on a continuous raised part of the image on the printing plate. The press was then inched forward and the sensor carried into the nip between the cylinders. The pressure was recorded the entire time, thus providing data for the nip inlet, nip itself and nip outlet. The maximum pressure recorded was used as an engagement indicator. If too large a pressure difference was detected between the two ends of a cylinder, the skew could still be adjusted before the print run. The pressure data obtained was also important for the comparability of printing results obtained from different printing plates. The latter will be elaborated on in Chapter 4.

3.4.2.3 Test for Cyclic Variations

S. Hamblyn (2004) revealed cyclic variations in the print quality produced on the T-Flex 508. The optical density of the prints varied at a frequency of four copies and a range of 0.15 between maximum and minimum density values. As this occurrence might be setup-dependent, prints from the main trials for this work were scrutinised for any periodic deviations in optical density obtained by spectrophotometry.

The range of solid densities measured on eight consecutive sheets of the dot geometry study (refer to Chapter 4) was below 0.03 (4.0%) for all plate materials investigated. This was not significant enough to require further analysis of cyclic variation, since this was within the noise range of the printing press. The range of solid optical densities observed for 16 consecutive prints of the meso-pattern study (refer to Chapter 5) was larger with 0.10 (11.0%). However, the extreme values of the range occurred on different sheets for neighbouring printing patches which rules out cyclic variation of the printing press (Figure 3.10). The cause of the temporal deviations observed could not be identified. To account for any variation, spectrophotometric data was obtained on eight consecutive sheets and averaged.

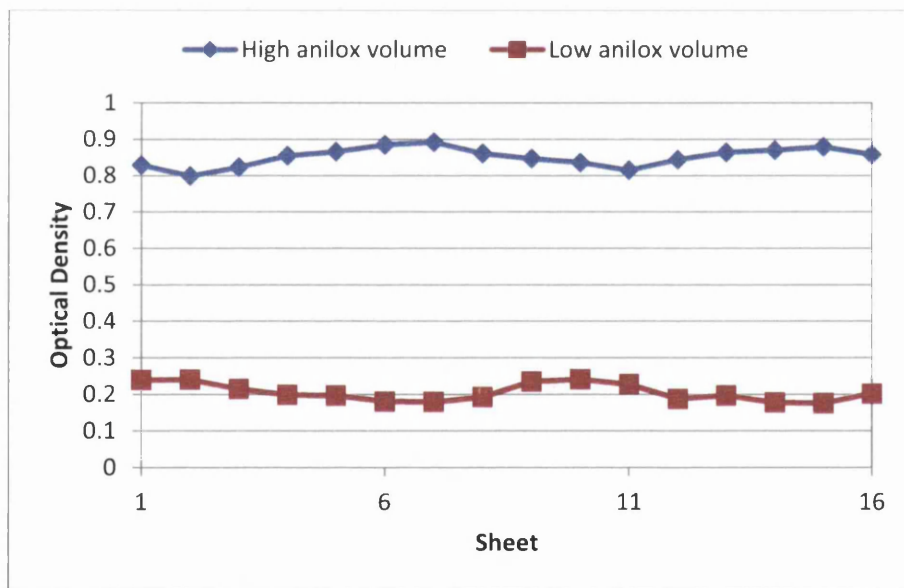


Figure 3.10: Temporal variation in solid optical density measured on consecutive sheets to test for cyclic variations

3.5 Print Characterisation

In order to evaluate the effect of plate characteristics on ink transfer, both qualitative and quantitative measures need to be considered. Print characterisation starts with the visual inspection of samples by microscopy which yields qualitative information. This can help to interpret the data

obtained by the following quantitative methods. The quantitative data comprises printed planar surface area, ink volume transferred, optical density and print uniformity. The respective approaches and apparatus are explained.

3.5.1 Visual Inspection of Samples by Microscopy

The VHX-1000 digital microscope (Keyence, Osaka, Japan) was used for the inspection of the prints. The high-resolution Keyence possesses a coaxial light source, i.e. the light path was in line with the optical path, which improved the contrast of the printed ink layer and substrate in the images captured. Furthermore, the Keyence was designed for capturing colour information at up to 1,000 times magnification which rendered it ideal for small printed features.

3.5.2 Determination of Planar Surface Area and Volume of Printed Dots

One way to determine the planar area of a printed dot would be to measure its diameter under a microscope and to calculate the surface area by assuming the dot to be a perfect circle. As can be seen from Figure 3.11, real dots are irregular around their circumference and might contain UCAs within the dot. Accounting for these voids by geometric techniques will give only a crude approximation of the surface area of such a dot. Another possibility would be the processing of the microscopic image in ImageJ where the exact number of pixels making up the printed dot could be established and then converted to planar area. However, this option is only viable for images with sufficient contrast between dot and substrate. In the case of the dot in Figure 3.11 any isolation attempt failed due to the varied coloration and brightness of the dot pixels. A required additional manual selection of pixels was not available in ImageJ.

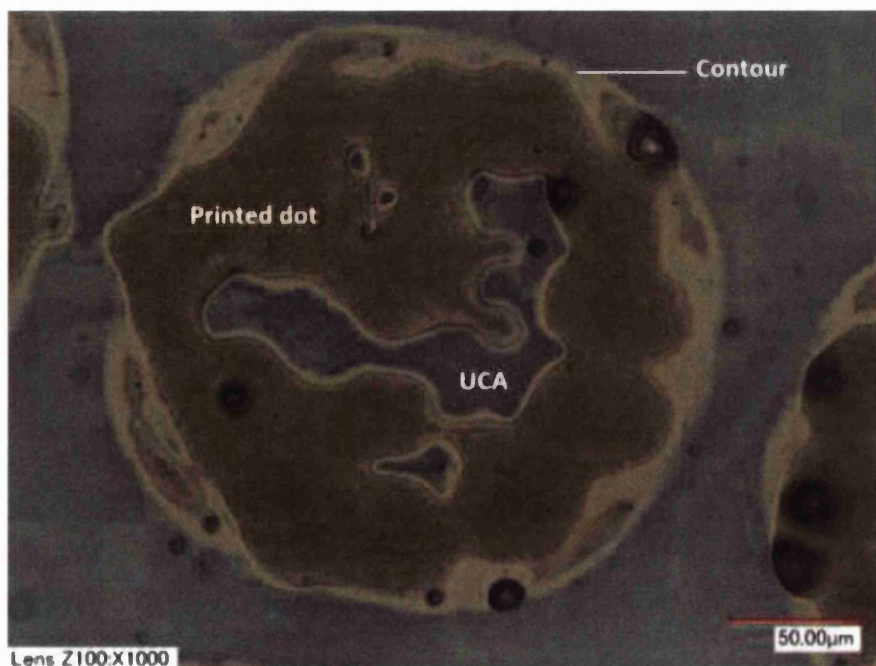


Figure 3.11: Microscopic image of printed dot showing irregular contour of the main ink volume and UCAs

It was therefore decided to adapt S. Hamblyn's (2004) methodology of using WLI and the built-in functions of the Vision32 software to determine the planar surface area and ink volume of a printed dot. The process steps were analogous to the measurement of the planar surface area of a halftone dot on the plate (above), but – instead of isolating the dot top from the shoulders of the plate feature – the ink volume transferred was isolated from the substrate by height thresholding. Although the method was suited for the thicker, defect-free, uniform ink films investigated by S. Hamblyn, it had to be refined for the dot structures deposited in this work.

The step of isolating data points representing the ink from those representing the substrate by height thresholding was replaced by the manual exclusion of substrate pixels from the data set. For this the outline of the printed dot (Figure 3.12a) was traced with a polygon tool to form a closed contour. The substrate pixels outside the contour were masked to not appear in the image analysis. Any unprinted areas within the dot were separately traced and excluded. All remaining data points denoted ink deposition and were used for the calculation of planar area and ink volume by Vision32 functions (Figure 3.12b). Before the volume function could be applied, an inversion of the height information in the data set had to be performed. This additional step was necessary, because by definition the (natural) volume calculated by the software is the “volume that the surface would hold if it were covered just to the surface of the highest peak” (Lippold and Podlesny, 1998), i.e., the volume above the printed dot instead of the ink volume itself (Figure 3.13a). The data inversion rectified this problem by matching both volumes (Figure 3.13b). The built-in function of planar surface area remained unaffected by the data inversion.

The method of manual ROI selection achieved very consistent results. Ten repetitions of masking the same data set of a printed dot resulted in a relative standard error of 0.1% for the planar surface area and of 0.6% for the ink volume.

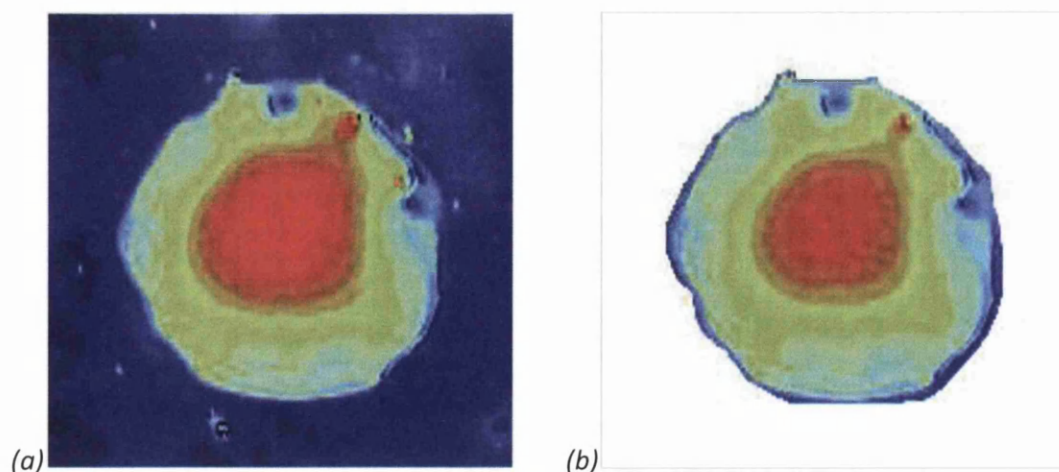


Figure 3.12: Manual selection of ROI for determination of planar surface area and ink volume
(a) printed dot before and (b) after the manual masking selection of data points

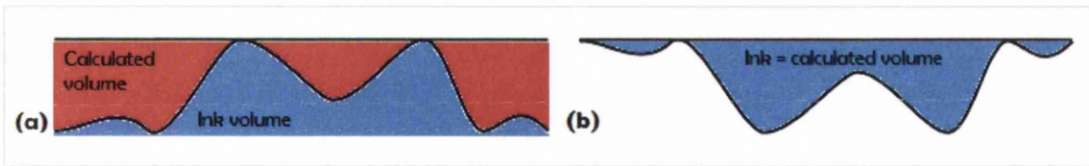


Figure 3.13: Schematic of (natural) volume algorithm in Vision32 software (a) showing difference between actual and calculated ink volume. Matching up of actual ink volume with algorithm by data inversion (b).

3.5.3 Determination of Optical Density by Spectrophotometry

For the colour measurements a Spectrolino measurement head by Gretag Macbeth (Regensdorf, Switzerland) was used. For measurements of smaller samples printed on the IGT-F1 the Spectrolino was utilised in hand-held mode, while for repetitive measurements of large T-Flex prints the instrument was attached to a ColorScout A+ measurement table (ColorPartner, Kiel, Germany). The ColorScout A+ software contained a template option which allowed for exact positioning of the instrument head in the XY-plane for every sample. This was achieved by matching three registration marks on the printed sheet with the alignment marks in the template (Figure 3.14). This enabled the repeatability of measurements at the same point of an image, as well as the direct comparison of colour information on several consecutive sheets or those produced under different printing conditions.

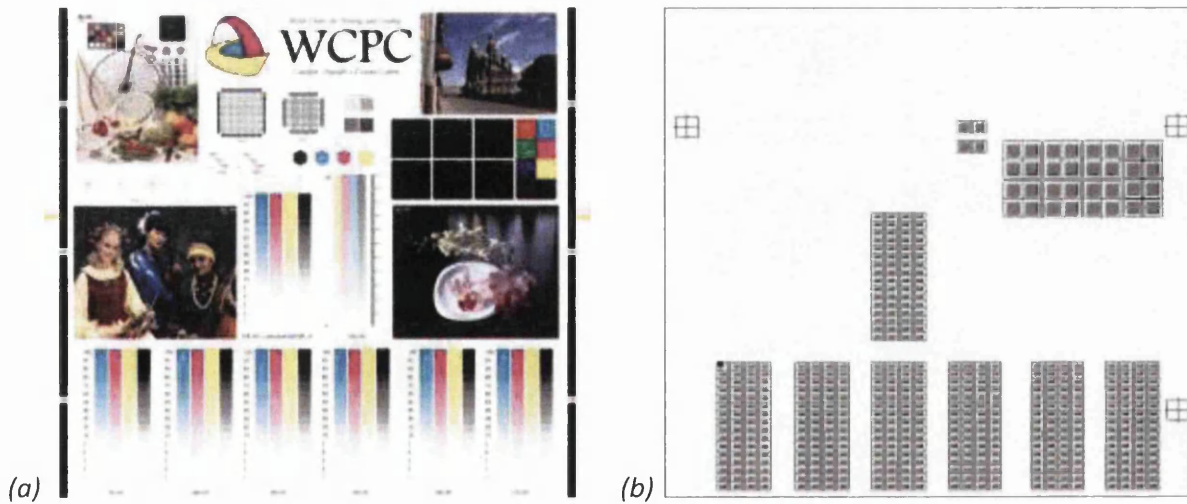


Figure 3.14: Original image of prints (a) versus positioning template for ColorScout A+ (b) including the three cross-hair marks for alignment and positioning

All measurements were taken in accordance with BS ISO 12647-1:2004 (Table 3.1). The Spectrolino measured the spectral response of the sample in the wavelength range of 360 to 730 nm at intervals of 10 nm (36 values in total). From the spectral response the software calculated the optical density separated by the channels CMYK. The selection of sample backing was dependent on the

experiment. At the time that the studies on the IGT-F1 were conducted, no standardised backing was available. Instead a sheet of non-standard, white card was used. This did not pose a problem, as all sample substrates were opaque and the colour influence of the background was therefore negligible. The T-Flex 508 print samples measured on the ColorScout A+ all profited from the matte, opaque white backing ($L^* < 92$, $C^* < 3$ according to BS ISO 12647-1:2004) which was part of the measurement table. The dimensions of the printed patches were optimised to the smallest size feasible (6 mm) in order to fit more elements onto the same printing plate, while at the same time not to compromise the necessary sampling aperture of the Spectrolino (4 mm in reflection mode).

Table 3.1: Measurement parameters for Spectrolino with ColorScout A+ measurement table

Measurement parameter	Value
Mode	Reflection
White base	Absolute
Backing	[dependent on experiment]
Geometry	45°/0°
Observer angle	2°
Illumination (calculated)	D50
Filter	D65
Polarisation	No
Instrument spectral response	ANSI Status T

3.5.4 Digitisation of Prints by Scanning

The prints had to be digitised in order to be able to perform the print uniformity analysis on the digital images (outlined in the next section). For the digitisation the Epson Perfection V700 Photo (Epson, Suwo, Japan), a flatbed scanner with dual lens system for colour images, was used. According to the manufacturer the maximum optical resolution achievable with the scanner is 4,800 by 9,400 dpi for reflective and contact sheet scanning at a maximum colour depth of 48 bit (just under 281.5 trillion) colours. With regard to archiving of the digitised data and potential future analysis, it might appear desirable to retain as much printed image information as possible, i.e. to scan as large an area in original colours at as high a resolution as possible. However, this approach will result in particularly long scanning times and large digital files which could not be handled easily by different types of software. A compromise between scan colour, resolution, sample and analysis area became inevitable, while at the same time a significant loss of image information expressed in deviant measurands had to be avoided. Besides the optimum scan parameters it had to be

established how stable and consistent the scanning was performed over time. Therefore, the print digitisation was preceded by an extensive screening of scanning specifications as outlined in Appendix A.2. The final parameters employed for this work are given in Table 3.2.

Only after completion of the scanning task had it been discovered that – unbeknown to the user – the scanner software applies a non-linear algorithm for image manipulation which has a significant effect on the scan results and image analysis measurands. Details on the linearity problem and its resolution are provided in Appendix A.2.4. A non-linearity inversion was applied manually to all relevant scan data series and new measurands calculated. All the data presented in this work is based on the corrected linearised scans.

In performing the scans it should be noted that great care was taken to remove any contaminations from the prints and scanner glass before scanning. At the beginning of each scan session the glass was cleaned with lint-free wipes and isopropyl alcohol. Before each scan the glass and print were dusted with a soft cloth.

Table 3.2: Scan parameters for digitisation of prints

Scan parameter	Value
Scan mode	reflective on document table
Scan type	photo
Scan quality	“best”
Scan colour	8-bit greyscale
Scan resolution	2,000 dpi
Sample area scanned	20 by 15 mm
Sample area analysed	10 by 10 mm
Compression	none
File format saved	multi-page TIFF
Gamma correction	1.66 (applied post-scanning)

3.5.5 Digital Image Analysis in ImageJ

The density of prints can also be estimated using ImageJ. This approach has the added advantage that the print uniformity of the image can be quantified at the same time.

3.5.5.1 Determination of Print Density

The prints were digitised according to the parameters outlined in the previous section. A macro (Appendix A.3) was employed to generate a histogram of greyscale levels (GSL) for the ROI selected

in each image level of the multi-TIFF file. Based on the 8-bit greyscale image, 256 different bins were included in the histogram comprising the range of colours from black (0) across the shades of grey to white (255) (Figure 3.15).

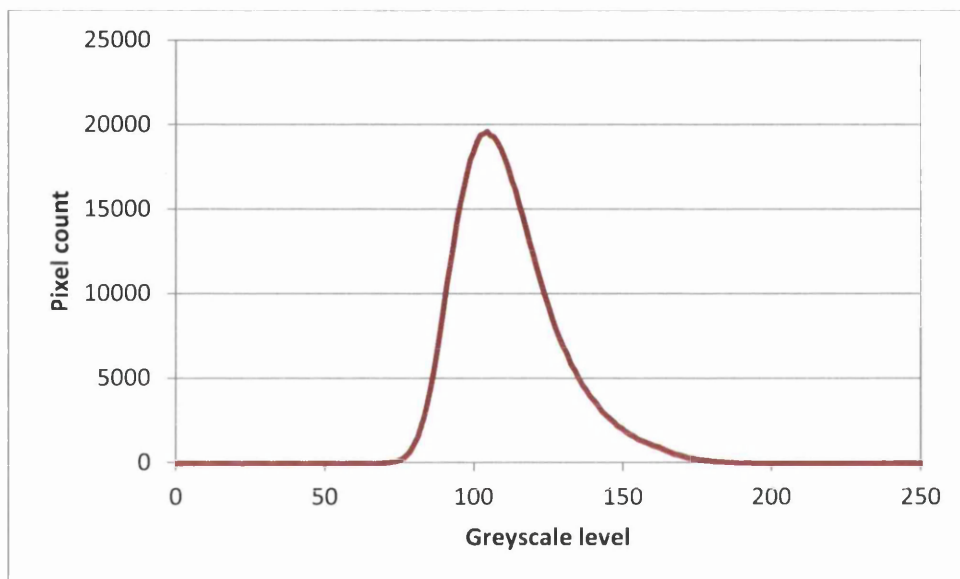


Figure 3.15: Example of GSL distribution in histogram for a printed and subsequently digitised sample (D = 0.46, MGSL = 154.04)

The spectrophotometer as well as the scanner capture reflectance values ($\beta=0\dots1$) of the printed samples which correspond linearly to luminance values ($Y=0\dots100$). The reflectance coefficient obtained by the spectrophotometer is an average value of the whole sample area covered by the measurement aperture and converted into optical density, D , using Equation 1.1. The scanner's reflectance coefficients are transformed into GSLs (GSL = 0...255) on the basis of a linear relationship and captured in the histogram. The mean greyscale level (MGSL) is the average value of the histogram and thereby the average reflectance coefficient obtained by the scanner. The MGSL corresponds to the optical density which is the average reflectance coefficient of the sampled area obtained by the spectrophotometer. Therefore, the MGSL is related to optical density in an exponential manner. (Hall, 1979) This was confirmed experimentally using data from the first meso-pattern trial on the printability tester (refer to chapter 5.1). Twelve patterned patches were printed using the IGT-F1 printability tester in 64 experiments featuring different combinations of six process parameters. Figure 3.16 compares the 768 experimental data pairs with the theoretical values computed using Equation 3.3 below. Clearly the correlation is very good. Optical densities obtained through spectrophotometry will be denoted as such, whereas optical densities calculated from GSLs will be denoted as "print density".

$$MGSL = 255 \cdot 10^{-D}$$

Equation 3.3

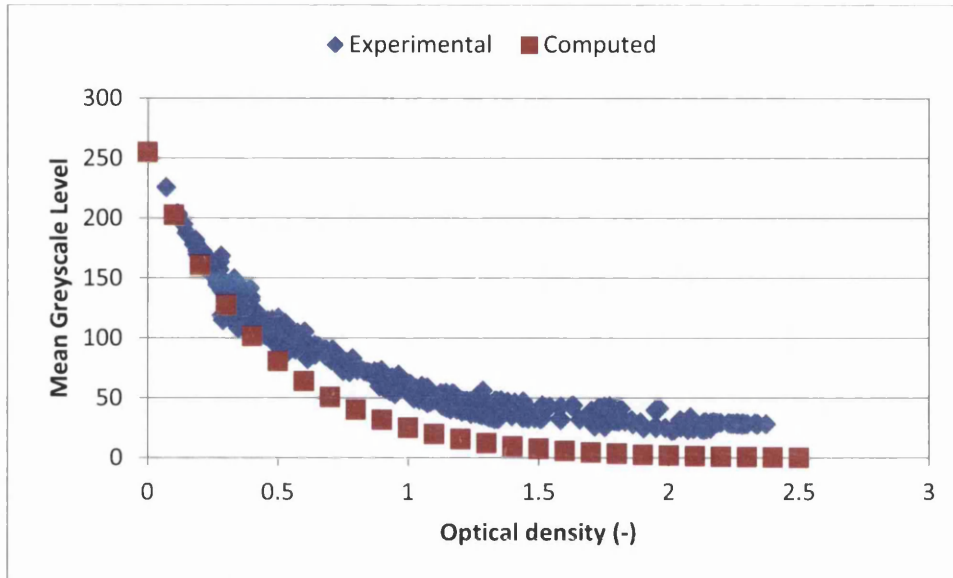


Figure 3.16: Correlation of optical density (spectrophotometry) and MGSL (ImageJ) for experimental and computed data pairs (computation using Equation 3.3)

3.5.5.2 Determination of Print Uniformity

Dependent on the type of print nonuniformity, many different approaches for its quantification can be found in the literature (Voß, 2002; Galton, 2004b; Dubé et al., 2005; Hallberg, Odeberg Glasenapp and Lestelius, 2005; Sadovnikov et al., 2005 a,b; Sadovnikov, Lensu and Kälviäinen, 2007; Barros and Johansson, 2007; Galton and Rosenberger, 2007; Rosenberger, 2010). An essential part of the majority of models is the mean optical density, \bar{D} , and its standard deviation, σ_D , across a sample area. Alternatively, the MGSL and its standard deviation, StDev (Equation 3.4), can be employed. Often they appear as the Coefficient of Variation, CV (Equation 3.5).

$$StDev = \sqrt{\frac{1}{n-1} \sum_{i=1}^n (GSL_i - MGSL)^2}$$

Equation 3.4

where n is the number of pixels in the image.

$$CV = \frac{\sigma_D}{\bar{D}} = \frac{StDev}{MGSL}$$

Equation 3.5

The CV has previously been used to characterise the uniformity of layers transferred in functional device printing (Stahl, Sauer and Dörsam, 2012). However, uniformity indicators obtained with this equation need caution in their interpretation. The mean optical density acts as a scaling factor and distorts the true uniformity value. Assuming two samples containing identical printing defects (i.e., = StDev), but different thicknesses of the underlying ink film (i.e., \neq MGSL), the sample having the higher MGSL will result in a lower CV and therefore could be interpreted as more uniform. Also, two apparently identical CV values might belong to samples of rather different print uniformity whose results were biased because of the MGSL magnitude (Figure 3.17).

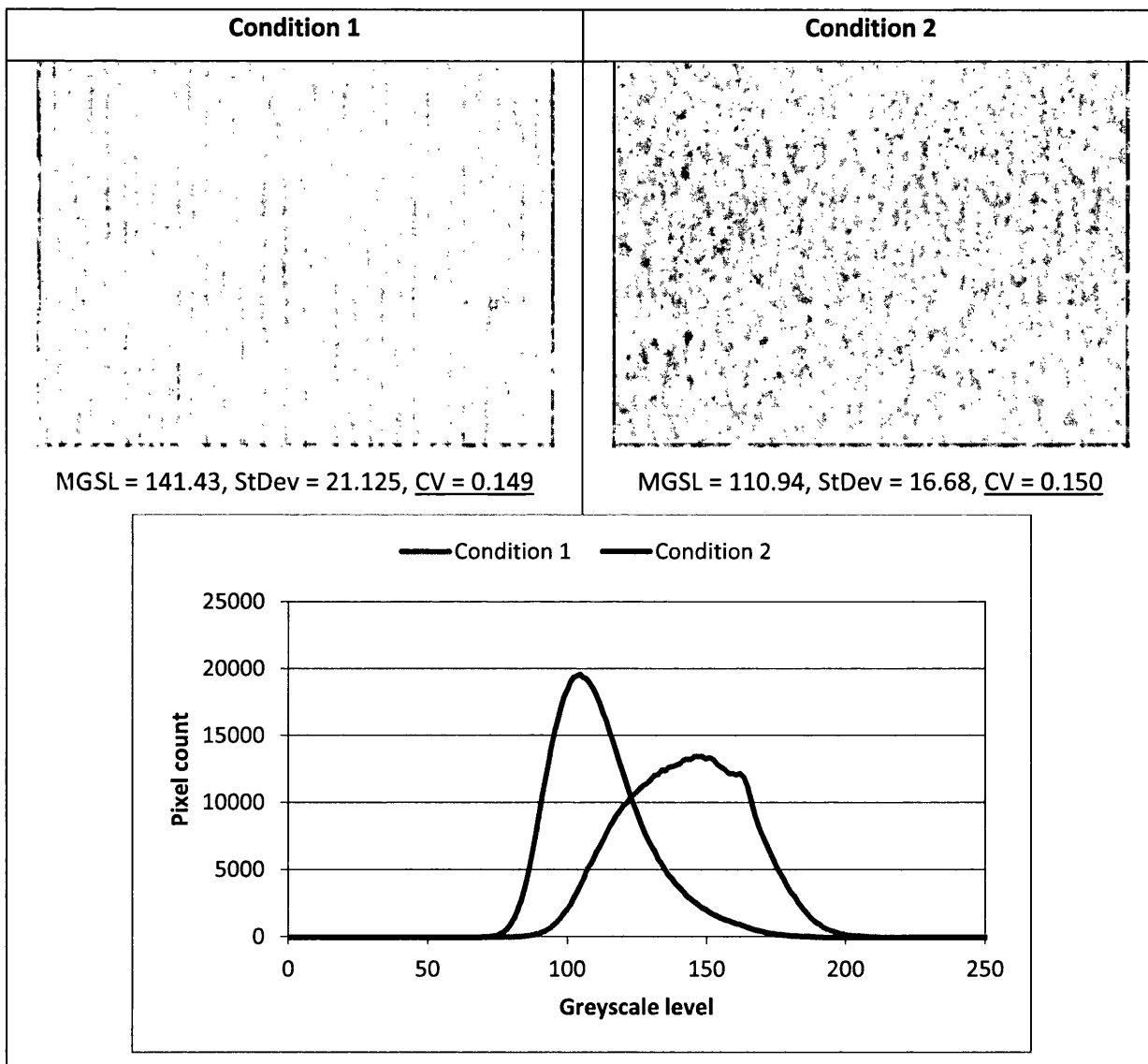


Figure 3.17: Illustration of deficiency of Coefficient of Variation approach for print uniformity on two examples produced under different printing conditions. Identical CV values represent strongly differing print uniformity better captured by the StDev parameter.

Hence it was decided to adapt the ISO Mottle approach according to ISO 13660:2001 which uses the standard deviation on its own. However, instead of dividing the sample image into smaller tiles, calculating the standard deviation for each tile, and then averaging them over the whole image as specified in the ISO standard, for this work only a single StDev was calculated for an image. The smaller the StDev, the more uniform was the print. Graphically high homogeneity of GSLs was represented by a narrow, unimodal distribution with very short tails in the histogram. Skewed, bi- or multimodal distributions with longer tails were the result of irregular GSLs in the ROI and implied nonuniformity of the print.

A small investigation was conducted to check the correlation between print uniformity and StDev. Ten people were asked to rank prints of nine different patterned patches produced on the IGT-F1 printability tester from “most uniform (1)” to “least uniform (9)”. All participants had normal or corrected-to-normal vision. The viewing conditions were the same for everyone (ambient lighting – indoors, daylight, overcast). The level of experience with this kind of task ranged from “expert” to “novice”. The decision on the worst and two best prints was unanimous. The ranking of the six samples in between was more varied and depended on the individual’s perception of random and periodic defects in the prints. The ranking results were averaged for all observers. The correlation of visual ranking and StDev for the samples produced a correlation of $R^2 = 0.79$ (Figure 3.18). Taking into account that the scale for visual ranking was a linear one and unable to capture the severe difference between some of the print defects as well as the participants’ variable sensitivity, then the correlation could be regarded as sufficiently good to allow the use of StDev as a measurand for print uniformity.

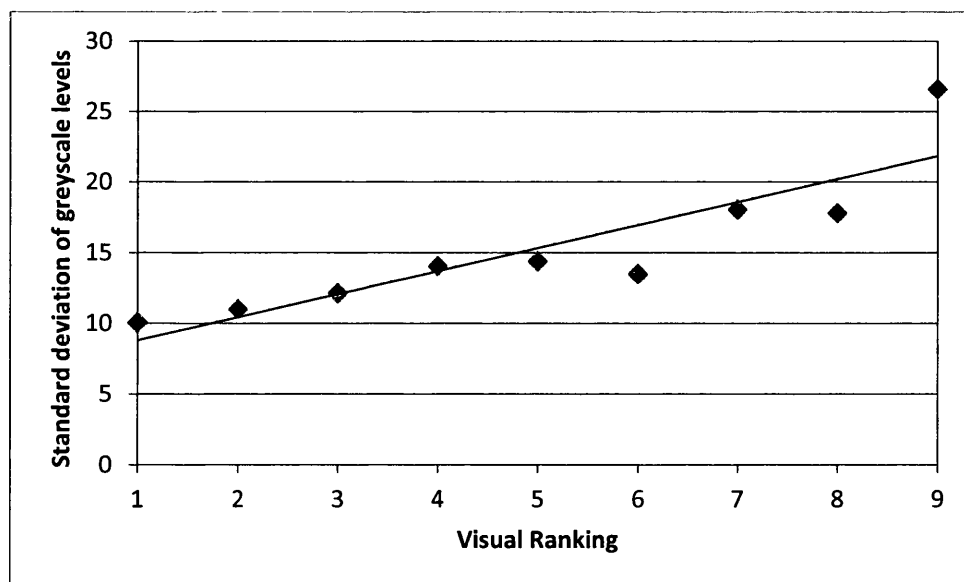


Figure 3.18: Correlation of uniformity ranking obtained by visual judgement (“most uniform (1)” to “least uniform (9)”) and uniformity parameter StDev obtained by image analysis software ImageJ (“most uniform (0)”, scale open-ended)

3.6 Design of Experiments

The majority of print trials conducted for this work were laid out as experimental plans according to DoE. This allowed quantifying the effects and interactions of printing parameters, such as plate material, printing speed and pressure, on quality criteria of prints, such as optical density and uniformity, in a simpler and more comprehensive manner. The first order, full-factorial plans were analysed according to Roch (2007) and Montgomery (2012). The latter provides an introduction to DoE and contains all related equations used in this work (calculation of main and interaction effects, variance and confidence intervals for judging the significance of effects).

Throughout this work all confidence intervals were determined by a two-sided significance test based on Student's t-distribution and a 5% error of probability. For sample sizes smaller than 13, the standard deviation was determined as the "alternative measure of spread" (Oakland, 1987).

3.7 Closure

This chapter has detailed the experimental methodologies employed in this research. WLI made it possible to characterise the printing plates non-destructively prior to printing. The plate surface roughness and selected feature dimensions were determined by standard procedures. A new method has been developed for the calculation of the planar surface area of rough materials in the image analysis software ImageJ after data preparation in the WLI software Vision32. Descriptions of the printing on the laboratory printability tester IGT-F1 and the industrial-scale printing press T-Flex 508 have been presented. A refined method for the determination of planar surface area and volume of printed dots using WLI was introduced. Furthermore, the standard method of measuring optical density of prints by spectrophotometry was supplemented by a newly developed method for digitised prints in ImageJ which allowed analysing print uniformity at the same time. The robust design of the developed methods has been established.

The procedures for plate analysis and printing formed the basis of the research conducted on dot geometry and surface patterning of printing plates presented in the next three chapters. The analysis of the planar surface area and volume of printed dots features in the investigation of dot geometry. Optical density and print uniformity are the key aspects to the investigation of surface texturing on printing plates.

Chapter 4 Dot Top Geometry of Halftones

One of the recent key areas of improvement in flexography has been the imaging technology as a means to control the dot geometry. “Flat-topped” halftones are claimed to be capable of superior print image quality because of higher ink-carrying capabilities and lower susceptibility to the plate deformation mechanisms causing physical dot gain in the prints. However, there is no satisfactory scientific explanation or justification to support these claims, and research on the detailed effect of dot geometry on the ink transfer mechanisms is lacking.

The work reported in this chapter seeks to fill in part of the research gap by comparing the influence of dot geometries resulting from different imaging technologies on halftone ink transfer. Four sets of printing plates (two imaged by standard digital technologies, two by “flat-top” technologies) were characterised through WLI and then used in a print trial on an industrial printing press. The ink transfer was evaluated using dot gain and film thickness parameters (calculated from the area and volume of ink transferred, determined by WLI on the prints), as well as the resultant optical density of the prints. Special attention was directed to the types of printing defects created and how they affect the applicability of selected halftone models.

4.1 Materials – Plates, Substrate and Inks

PLATE PROPERTIES

In order to generate different feature geometries on the printing plate, four separate combinations of plate material, imaging technology and resolution were employed (Table 4.1). The plate materials were by Asahi Photoproducts Europe (Shenfield, UK), Eastman Kodak and MacDermid (Waterbury, Connecticut, USA). An overview of the plate-making technologies was given in section 1.2.1.1. The standard digital, water-washable Asahi AWP-DEF and the solvent-washable MacDermid Digital Rave were chosen for the comparison of the ink transfer from standard digital printing features on plates of different chemistry (as indicated by their washability). The same MacDermid material was also imaged under identical conditions with LUX technology (proprietary to MacDermid), i.e. the plate was covered with an oxygen barrier layer during imaging, thereby preventing oxygen inhibition and supposedly resulting in “flat-topped” printing features. Using the same MacDermid plates imaged under different conditions served to directly compare the effect of imaging technology on dot geometry and ink transfer. Finally, a Kodak Flexcel NX material was imaged with Flexcel NX technology (oxygen barrier layer located underneath imaging layer) to facilitate a second group of “flat-topped” printing features. It was not possible to achieve the same imaging resolution for the

Kodak plates, because Flexcel NX is a proprietary technology which is supposed to be processed by Eastman Kodak's own platesetters exclusively. These only operate a SQUAREspot laser (Kodak, 2012) at the lower resolution of 2,400 dpi. The Asahi plates were imaged by Creation Reprographics (Daventry, UK) and all the other plates by SGS Packaging Europe (Hull, UK). For each parameter combination a set of four printing plates was produced (one for each process colour CMYK) and the sets were referred to as Asahi, Kodak, MacDermid and MacDermid Lux.

Table 4.1: Parameter combinations for the generation of different feature geometries on printing plate

Property	Asahi	Kodak	MacDermid	MacDermid Lux
Material name	AWP-DEF	Flexcel NX	Digital Rave	
Washability	water	solvent		
Surface roughness, R_a	171 nm	83 nm	89 nm	53 nm
Surface roughness, R_z	6.2 μm	1.0 μm	1.8 μm	1.7 μm
Steady-state surface energy	38.1 mN/m	36.2 mN/m	44.6 mN/m	
Thickness	1.7 mm			
Imaging technology	Standard digital	Kodak Flexcel NX	Standard digital	MacDermid LUX
Imaging resolution	4,000 dpi	2,400 dpi	4,000 dpi	
Laser geometry	Gaussian	SQUAREspot	Gaussian	

All printing plates were based on the same digital image (Figure 4.1). The following elements were relevant for the investigation of dot geometry:

- Halftone scales in the colours CMYK
 - 16 area coverages (1, 2, 3, 4, 5, 10, 20, 30, 40, 50, 60, 70, 80, 90, 95, 100%) each at
 - 6 line rulings (85, 100, 120, 150, 175, 200 lpi ; 33, 39, 47, 59, 69, 79 lines/cm respectively).

The range of line rulings chosen is representative of that found in industrial flexography. 85 lpi is used for coarser packaging printing; the intermediate line rulings of 100 to 150 lpi are standard practice in graphic printing; the higher resolutions of 175 and 200 lpi are the industrial goal, but cannot currently be achieved consistently by all plate-making processes. The choice of area coverages comprises highlights, midtones and shadows to allow observation of any influence of halftone structure on dot geometry and print quality. The lowest coverages of 1 to 5% were used to determine the smallest dot size that can be imaged on the plate.

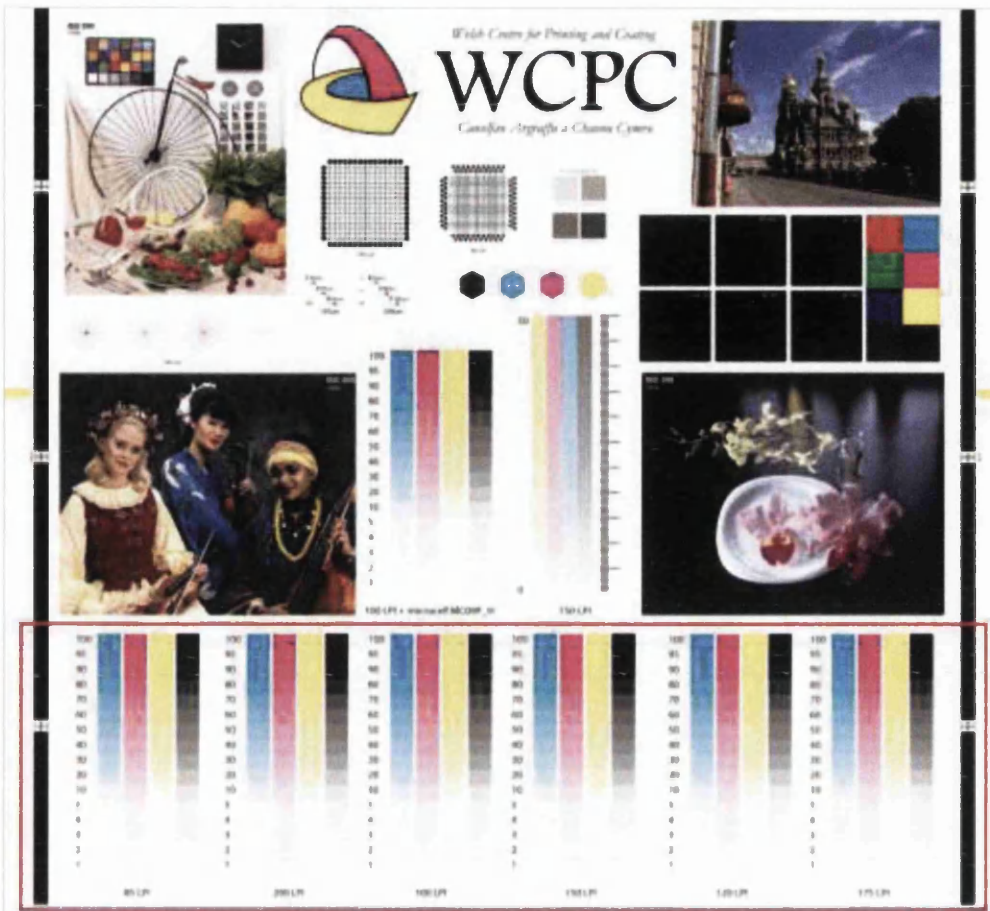


Figure 4.1: Image for print trial on dot geometry showing halftone scales in CMYK, full tone patches, photographs and various other test elements (image parts contained in red box taken into account for image analysis; red box not included in actual image) (0.3x magnification)

For the plate characterisation, WLI measurements were performed on the following plate patches:

- colour black – all halftone patches at all line rulings, and
- colours cyan, magenta and yellow – halftones of 50% area coverage for all line rulings.

For each patch, up to 30 printing features were investigated depending on the standard error of results. The planar surface area of each feature was determined according to the method stated in section 3.1.2.2, and the isolated dot tops were analysed for their geometry. The investigation found that the top geometries on the four plate types were not limited to simple round or flat shapes. The full range from convex to concave dot tops was encountered. A new term, “cupping” was introduced for non-planar dot geometries, which has not previously been described in literature. Cupping holds great industrial significance as it potentially increases the ink-carrying capabilities of the printing plate (explained in section 4.4.1.2) and affects the print uniformity of halftone dots (sections 4.4.2.1.1 f.). The measurand of top geometry was height (here referred to as “cup depth”). The

height of concave dot tops was measured between the apex of the cup brim and the bottom of the cup. For the purpose of comparison, the cup depth of convex dot tops was calculated as the height difference of the top edge to the apex (Figure 4.2). For every dot four values were obtained, two along each of the profiles A and B (Figure 4.3).

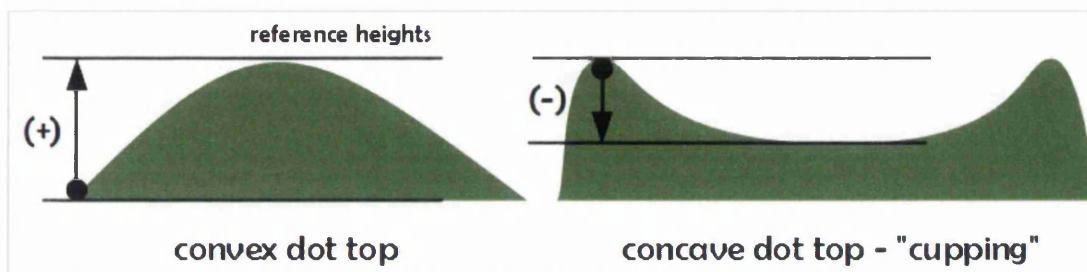


Figure 4.2: Methodology for quantification of dot geometry using dot apex and threshold height for convex dot top (positive sign) as well as cupping brim and bottom for concave dot top (negative sign)

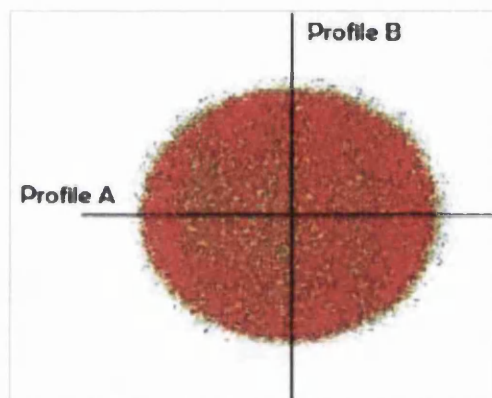


Figure 4.3: Location of WLI profiles along which the cup depth of the dot top was measured

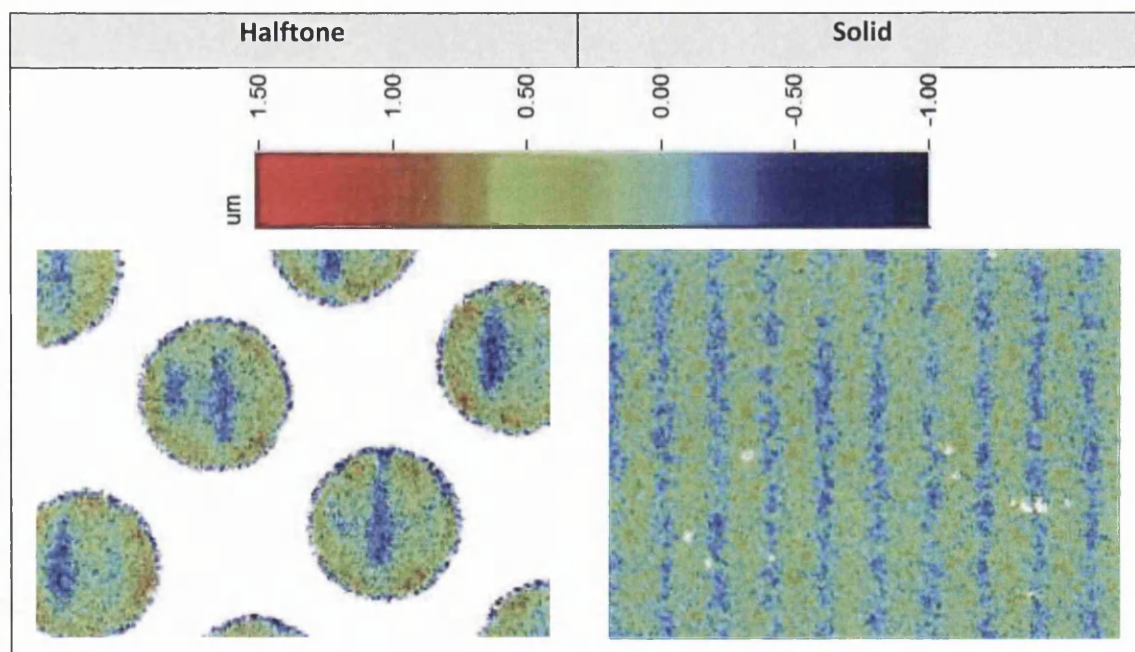


Figure 4.4: Comparison of surface striation in halftone dots (50% dot at 100 lpi) and solid for Asahi plate (110x magnification)

The determination of top geometry was impeded by surface striation that was encountered on the Asahi and both MacDermid plates. Figure 4.4 shows an example of striae in halftone and solid areas on the Asahi plates (complete tables of images and striation parameters for all plate types can be found in Appendix A.4). The striae are created by the laser beam during the ablation of the plate mask layer (Johnson et al., 2009; Hejduk, 2010). The Kodak plate was free of striae, because its mask is ablated separately on the barrier layer and only then laminated onto the printing plate. It was not possible to consistently select dot profiles that did not contain striae. Therefore, the striation was treated like any other surface point and included in the determination of top geometry. If the minimal surface point was required for the measurement, it was taken in the striation valley. The maximal point was found on the striation apex.

SUBSTRATE PROPERTIES

The film substrate Rayoface WPA59 by Innovia Films (Wigton, UK) was used for the print trial, because ink cannot penetrate into this non-porous substrate. This permitted easier quantification of the ink volume transferred and ink laydown by optical methods. The Rayoface substrate was a high gloss, white, biaxially oriented polypropylene film with proprietary top coating. The roughness of the print side was $R_a = 149$ nm and $R_z = 1.46$ μ m, and its surface energy was 43.2 mN/m.

INK PROPERTIES

For the investigation of the interaction between inks and plate features, it would have been desirable to employ several ink systems based on fundamentally different chemistries, such as UV-curing, solvent- and water-based ink. However, since the printing press was primarily designed for UV-curing inks, each of the four printing plates within a set was printed with one of the UV-curing process colours of the series Solarflex Nova SL Pro DK03 by SunChemical (Slough, UK). UV-inks have the advantage that they only experience minimal volume shrinkage during curing, because no solvent loss is taking place. This provides clearer information on the amount of ink transferred during the printing process. The inks were characterised in terms of their surface tensions (Table 4.2) and viscosity (instrument settings in Table 4.3 and Table 4.4). All four inks displayed a similar magnitude of shear viscosity between 0.7 and 1.7 Pa·s (Figure 4.5). The black and cyan inks were approximately Newtonian. The yellow and magenta inks had slight shear-thinning properties which distinguished them from the black and cyan inks.

Table 4.2: Ink surface tension of SunChemical Solarflex Nova SL Pro DK03 series process colours

Ink	Cyan	Magenta	Yellow	Black
Steady-state surface tension (mN/m)	32.5	35.3	31.9	32.4

Table 4.3: Rheometer settings for ink pre-conditioning and measurement geometry (inks of industrial printing press studies)

Pre-conditioning		Measurement geometry	
Type	controlled rate	Geometry	cone/plate
Shear rate	0.01 s ⁻¹	Cone	4° / 40 mm
Time	60 s	Gap size	150 µm
Equilibrium time	10		
Temperature	25°C (isothermal)		

Table 4.4: Rheometer settings for ink viscosity determination (inks of industrial printing press studies)

Type	shear-controlled rate
Minimum shear	0.1 s ⁻¹
Maximum shear	100 s ⁻¹
Delay time	10 s (decreasing time)
Integration time	10 s
Mode	up
Samples	21
Repeats	2
Temperature	25°C (isothermal)

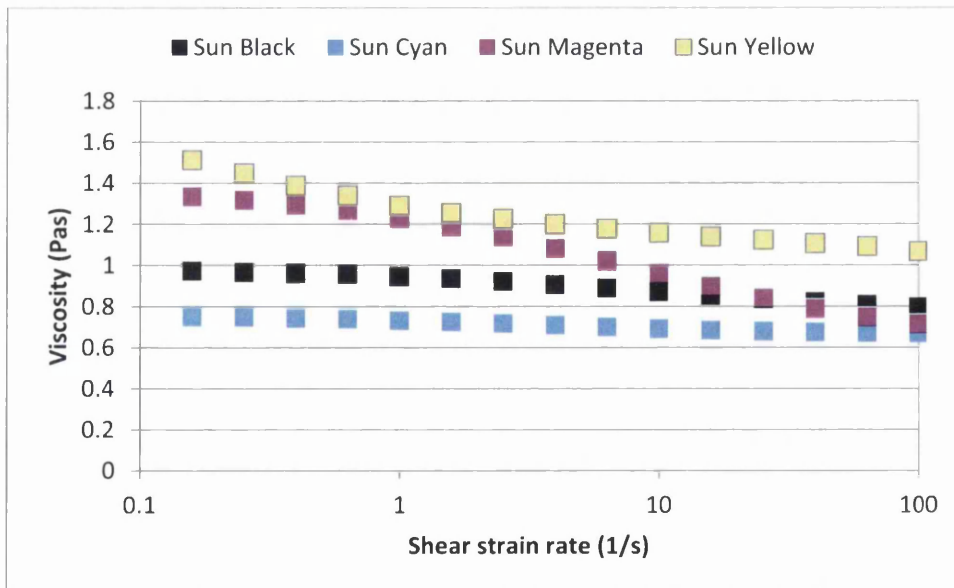


Figure 4.5: Ink viscosity of SunChemical Solarflex Nova SL Pro DK03 series process colours

4.2 Printing

4.2.1 Printing Conditions

The print trial was performed on the T-Flex 508 industrial-scale printing press. The trial was designed to test each set of plates under a broad range of printing conditions, notably printing speed and plate-to-substrate engagement (Table 4.5). The engagement between anilox roll and plate was not included as a printing parameter, because its setup could not easily be recreated for different plates. For each plate set, all parameter combinations of speed and engagement were executed in the order of increasing engagement, firstly at lower and then at higher speed. After printing at the highest engagement of 4 thou, the engagement was reduced and an additional experiment run at 2 thou. This served to check whether the system recovered fully once the load was removed from the printing plate.

Table 4.5: Combination of print parameters for dot geometry trial

Experiment number	Printing speed		Engagement plate-substrate	
	(ft/min)	(m/min)	(thou)	(μm)
1	150	45.7	1	25.4
2			2	50.8
3			3	76.2
4			4	101.6
5			2 (Hysteresis)	50.8
6	300	91.4	1	25.4
7			2	50.8
8			3	76.2
9			4	101.6
10			2 (Hysteresis)	50.8

The four process colours were all applied in the same print run using laser-engraved anilox rolls (Table 4.6) and cured at 70% power (standard settings) of the UV-lamps. This arrangement led to ten experiments per plate set and a total of 40 individual experiments for the investigation of dot geometry. The printing order of plate sets was Kodak, MacDermid, Asahi and MacDermid Lux. All plates were mounted onto the printing cylinders with the combination tape 1015 (3M, Bracknell, UK) which was suitable for the halftones as well as for the solid printing elements on the image.

Table 4.6: Anilox specifications for dot geometry trial

Colour	Anilox volume (cm ³ /m ²)	Screen ruling (pi)	Print order
Yellow	3.10	1,200	Unit 1
Cyan	2.39		Unit 2
Magenta	3.70		Unit 3
Black	3.32		Unit 4

4.2.2 Printing Force by Thin Film Sensor

To facilitate a direct comparison of the printing features on different plates, all were printed at identical speeds and engagements. To ensure that the engagement setting resulted in identical printing forces for all plates, these were checked using thin film sensors to measure the “anilox force” in the anilox-plate nip and the “printing force” in the plate-substrate nip (determined at 1 thou engagement). The former force promotes the inking of the printing plate, whereas the latter initiates the ink transfer to the substrate. The thin film sensor was placed on the plates’ bearer bars (Figure 4.6), as this provided a sufficiently large continuous area for testing.

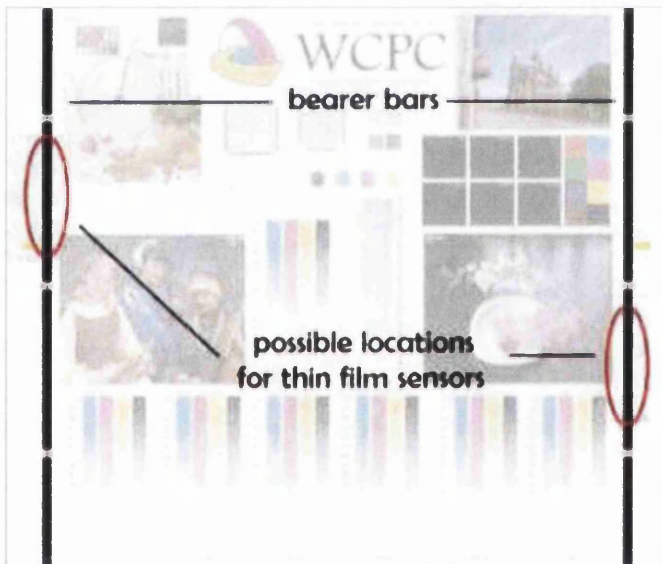


Figure 4.6: Possible locations along plate’s bearer bars for force measurement using thin film sensor

When the press was set up, the anilox pressures fell within a similar range for all four plate sets which implied a consistent setup of the engagement between anilox and plate (Figure 4.7). The mean printing force between the plate and substrate is shown in Figure 4.8 where the mean force is about 30 N and very consistent for the Asahi and Kodak plates. The MacDermid plates showed some inconsistency. This was due to low spots on the printing plates which did not make sufficient contact with the anilox or substrate at lower engagement. In order for the low spot to print, it was necessary

to increase the printing pressure to achieve kiss contact across the entire image, thereby potentially over-impressing other parts of the printing plate such as the bearer bars. This is a common issue in flexography and results in increased mean printing force for plates containing low spots.

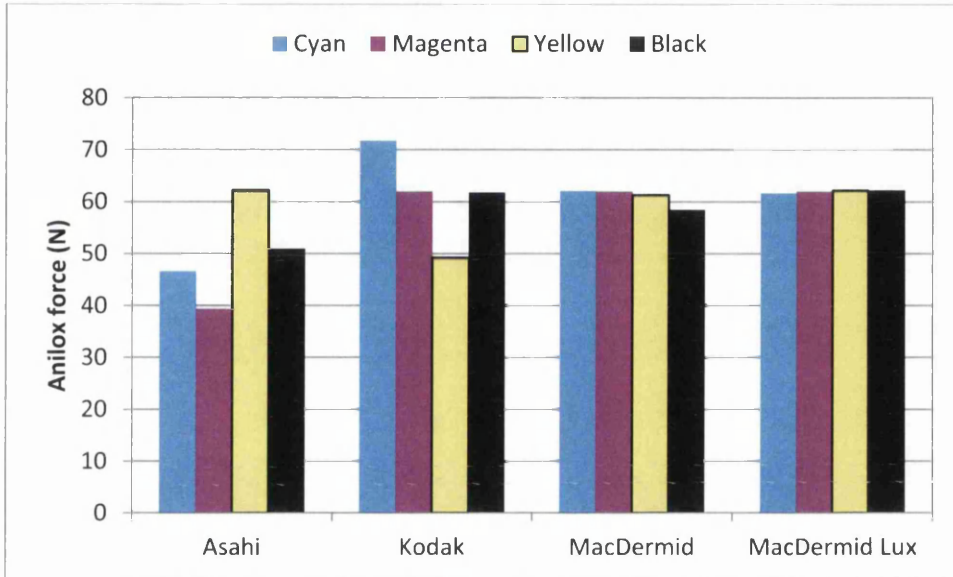


Figure 4.7: Comparison of consistent setup of anilox-plate cylinder nip using anilox force for all plate and colour types

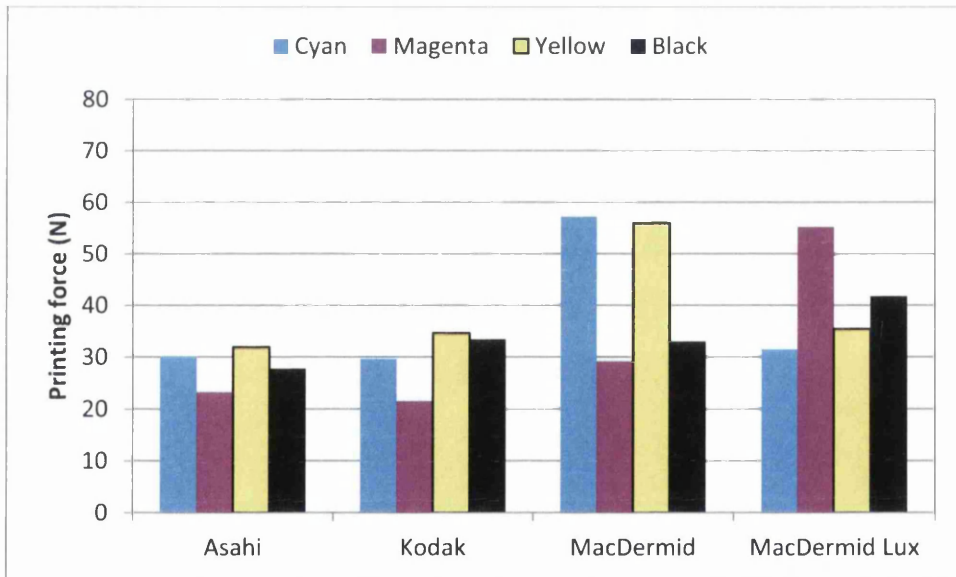


Figure 4.8: Comparison of consistent setup of printing nip using mean printing force for all plate and colour types

4.3 Print Characterisation

4.3.1 Planar Surface Area and Volume of Printed Dots

An inspection of the prints with regards to the quality of ink laydown was first performed with the Keyence digital microscope (1,000x magnification). The use of optical microscopy allowed the comparison of 2-D real colour images with 3-D false colour, topographic images obtained by WLI. The planar surface area and volume of printed dots were determined from WLI data for the different parameter combinations of printing speed and engagement for a representative selection of halftone line rulings and area coverages (Table 4.7). The 100 lpi and 150 lpi were chosen as these are two of the most frequently used line rulings in industry. The 10, 30, 50 and 70% halftone patches are characteristic of highlight, midtone and shadow regions on the print. The 90% patch was eliminated from the analysis, because the printed ink film could not be separated into individual features of which to calculate the ink volume transferred.

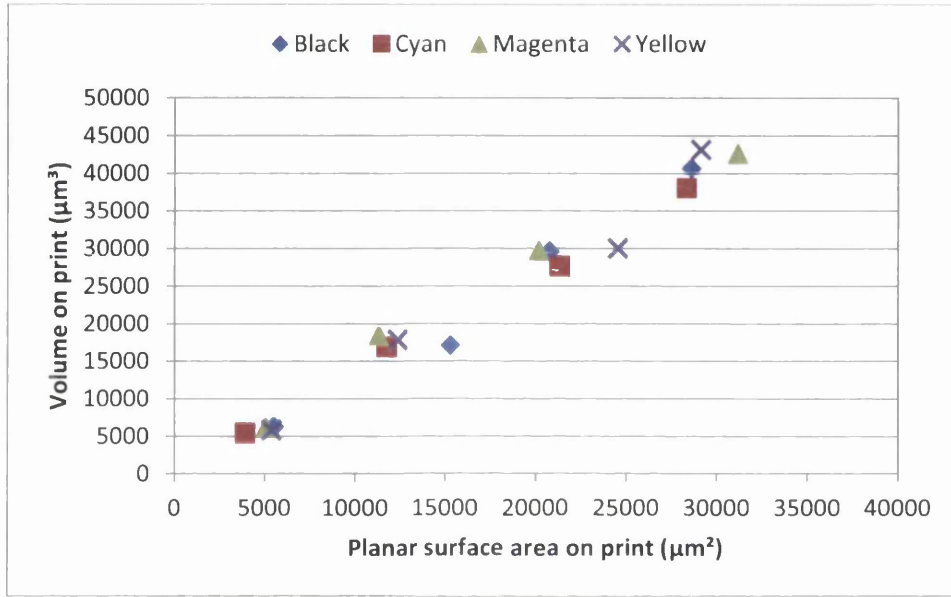
Table 4.7: Combinations of parameters for which planar surface area and volume of printed dots was determined

Colour	Line ruling	Speed			
		150 ft/min		300 ft/min	
		Engagement		Engagement	
		1 thou	4 thou	1 thou	4 thou
Black	100 lpi, 150 lpi	√	√	√	√
Cyan, magenta, yellow	100 lpi	√			√

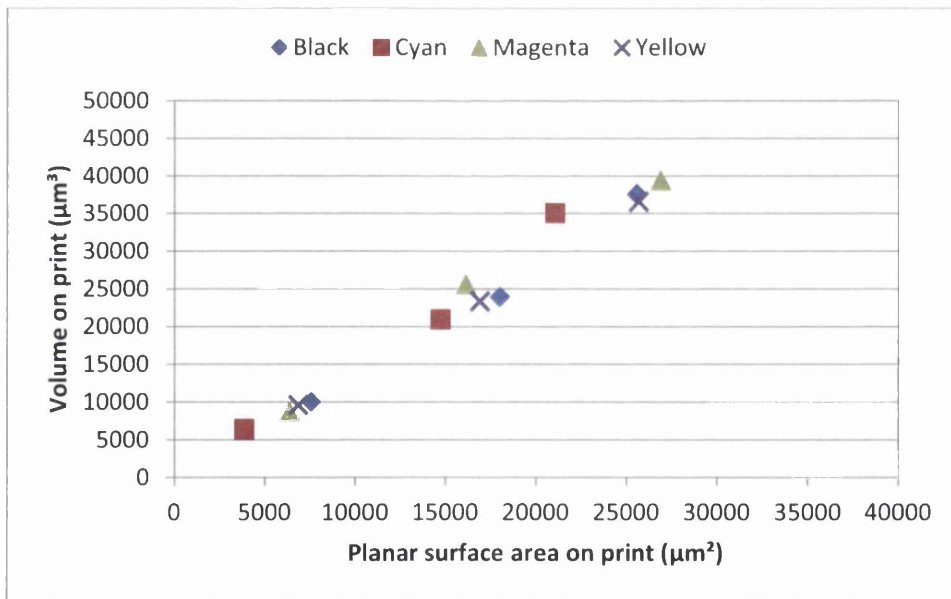
In order to determine whether significant ink transfer deviations exist for the inks of different colour, CMYK prints were compared for selected parameter combinations (Table 4.7). Figure 4.9 illustrates the results for the Asahi prints representative for all plate materials (the results for the other plate materials were as or even more consistent than the Asahi ones). The inks followed the same trends in printed planar surface area and volume for the two combinations of printing parameters. The slopes of the graphs are representative of the printed ink film thickness and were very consistent for the respective parameter combination. Any deviations between the inks were within the range expected under the given measurement uncertainty (see below) and through error propagation resulting from the setup of the inks' separate printing units on the printing press. Therefore, it was decided to concentrate the analysis of printed features on those produced with black ink.

The method of determining planar surface area and volume of printed dots based on WLI data was in itself very consistent (standard errors below 1%). However, the measurement uncertainty

increased with dot size, printing speed and engagement. The small dots printed at low speed and engagement had an approximate dome-shape which could easily be isolated from the substrate background (Figure 4.10). With increasing dot size, printing speed and engagement, the dot shapes became more irregular resulting in isolated islands of ink within the dot area surrounded by very thin residual ink films. Here, it was extremely difficult to separate inked from unprinted areas. This discrimination had a large effect on surface area and volume measured, but was minimised by a consistent approach to the manual separation of these features (refer to section 3.5.2).



(a)



(b)

Figure 4.9: Comparison of ink transfer (planar surface area and volume of printed halftones) for different inks; printing conditions:(a) 150 ft/min speed at 1 thou engagement and (b) 300 ft/min speed at 4 thou engagement

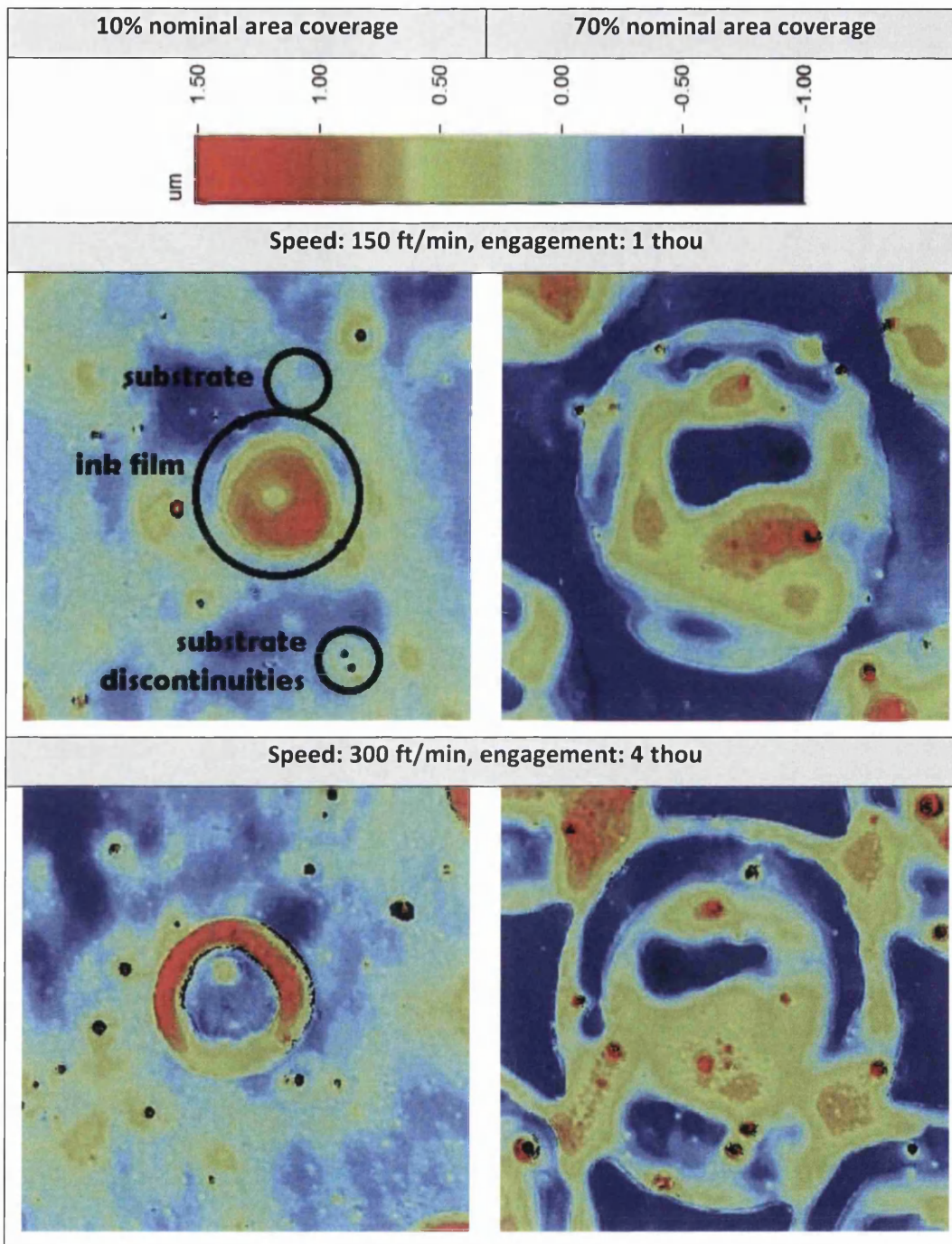


Figure 4.10: WLI images showing printed dot shapes dependent on dot size and printing conditions (Asahi material, 100 lpi line ruling; 210x magnification)

4.3.2 Optical Density

The optical densities (separated into their CMYK components) were obtained for the halftone patches for all the line rulings and printing parameter combinations. Eight consecutive sheets of each experimental number were measured and the mean optical density value for each halftone patch calculated in order to minimise effects of copy-to-copy variation. For this very large number of measurements the Gretag Macbeth Spectrolino spectrophotometer mounted onto the

ColorScout XY measurement table was used, which allowed for consistent positioning of the measurement head on each halftone patch. The analysis was not performed on the entire data set acquired, but matched to the selection of halftones taken into account for the investigation of planar surface area and volume of printed dots (Table 4.7).

4.4 Results and Discussions

4.4.1 Characteristics of Plate Features

The plate features were characterised for planar surface area, to provide information on the transfer of the design to the plate during the imaging process and the geometry of the feature top.

4.4.1.1 Planar Surface Area of Plate Features

The plate gain for all plate types is presented in Figure 4.11 to Figure 4.14. The two “round-topped” plates, Asahi (Figure 4.11) and MacDermid (Figure 4.12), experienced similarly large coverage losses, i.e. the dot sizes on the plates were smaller than specified in the digital artwork. The magnitude of the loss was dependent on the dot size. Smaller dots, i.e. highlights and dots at higher line ruling, had the most extensive losses relative to the nominal area coverage. This was due to the large ratio of dot circumference to dot area, at which oxygen inhibition of the polymerisation process occurred. At 200 lpi the Asahi plate could establish dots down to 5% coverage. With decreasing line ruling the lowest area coverage that could be held on the plate improved and reached 2% at 85 lpi. In absolute terms the smallest dot size corresponded to approximately $25 \mu\text{m}^2$ on the Asahi plate. The MacDermid plate fared slightly better with all area coverages imaged at 85 and 100 lpi. The lowest area coverage at 200 lpi was 3%, and the smallest absolute dot size was approximately $20 \mu\text{m}^2$. The shape of the dot circumference was nearly circular for these two materials (Figure 4.15).

In stark contrast, the MacDermid Lux plate (Figure 4.13) achieved almost complete design fidelity. The area coverages of the lower line rulings were within 1% of the nominal value. At higher line rulings, plate gain of up to 4% occurred due to the addressability of the laser. As the dots reduce in size, they approach the dimensions of the imaging laser beam, and it becomes increasingly difficult to address the laser in such a precise fashion, that it only ablates the mask area required. Thus, a slightly larger area than desired is ablated and imaged. The laser traces can be seen as steps around the dot circumference which is roughly circular (Figure 4.15).

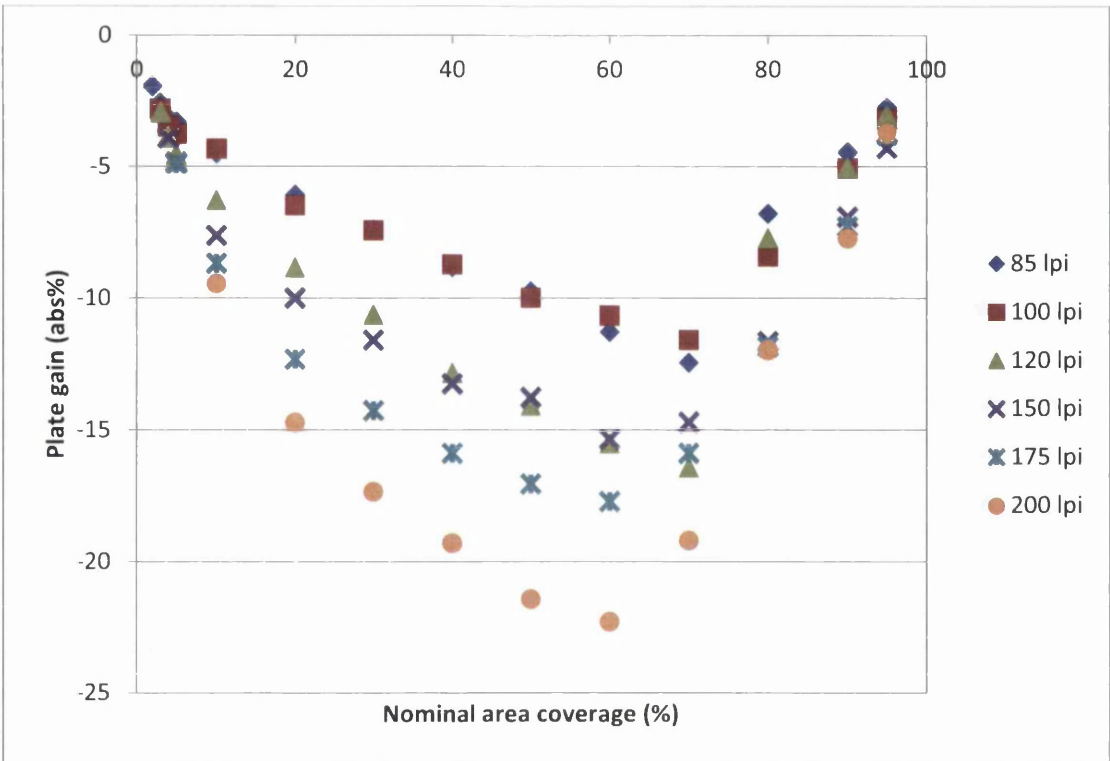


Figure 4.11: Plate gain for Asahi plate (standard digital imaging technology)

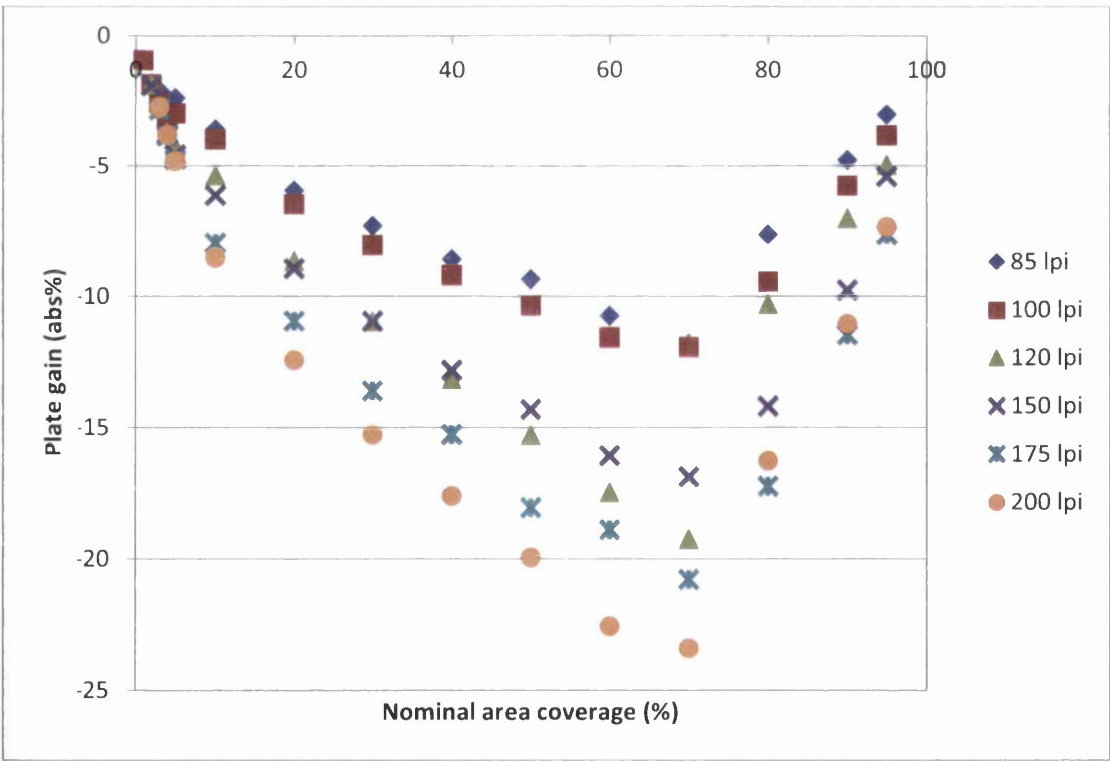


Figure 4.12: Plate gain for MacDermid plate (standard digital imaging technology)

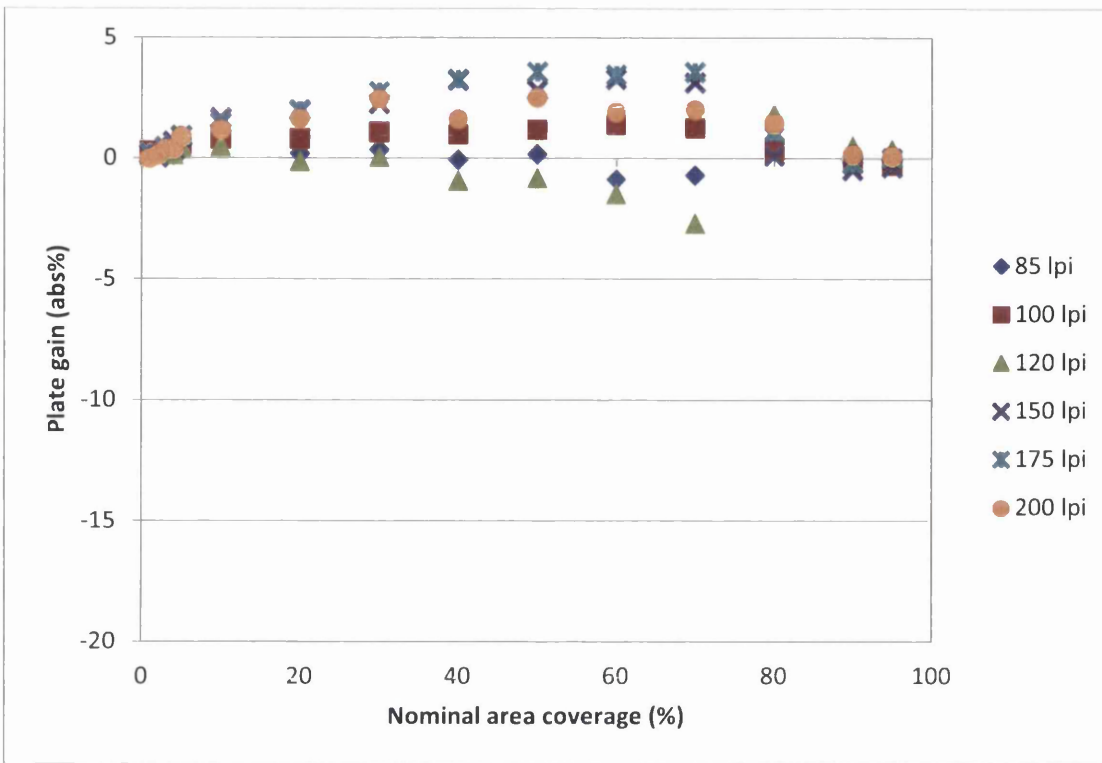


Figure 4.13: Plate for MacDermid Lux plate (LUX "flat-top" imaging technology)

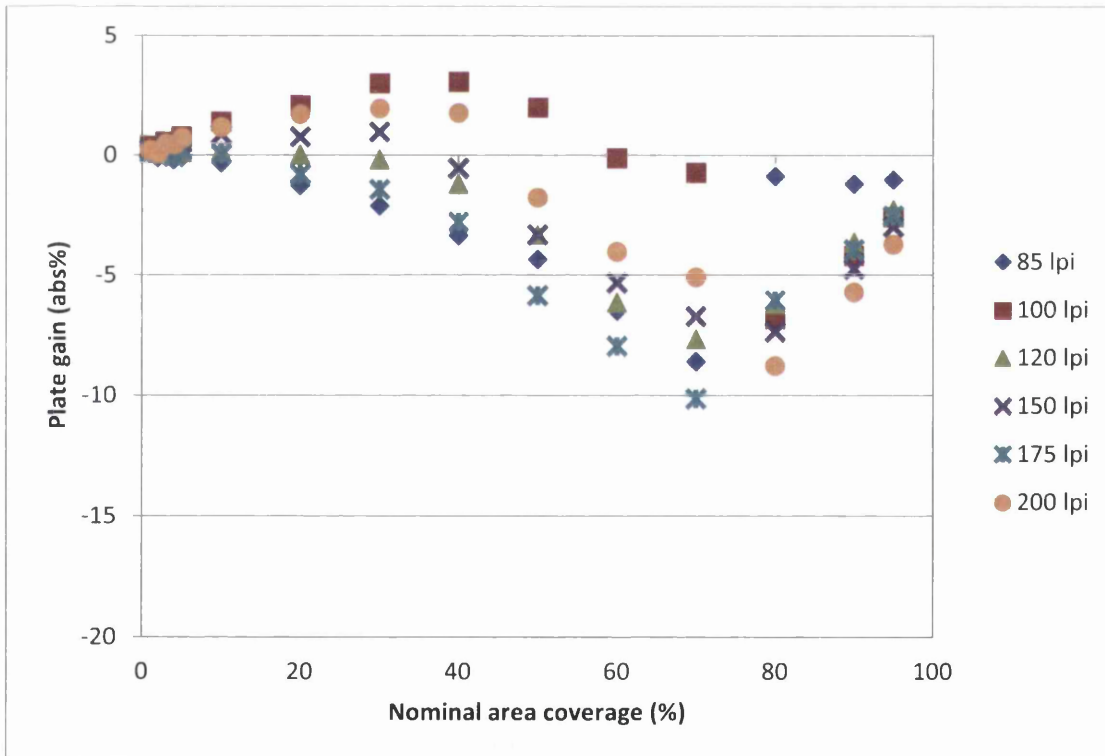


Figure 4.14: Plate gain for Kodak plate (Flexcel NX "flat-top" imaging technology)

The trend in plate gain for the MacDermid Lux plate was not observed for the Kodak plate (Figure 4.14). The highlights for some line rulings exhibited coverage loss, while they exhibited gain for others. In the midtones and shadows almost all features suffered losses with a sharp reversal in trend occurring between 70% to 80% nominal area coverage. This was attributed to the SQUAREspot technology which ablates distinctive square pixel areas of significant size (due to lower laser resolution) from the mask layer. Once the halftone dots start joining on the printing plate, the discrete laser pixels cannot resolve the contour of the holes between the dots anymore. Thus, smaller holes than expected are produced and the coverage losses in the shadow halftones improve.

The SQUAREspot technology creates very different dot shapes. Smaller dots and non-printing areas in the shadows approximate rectangular contours. The basic shape of the midtones is round, but the square laser pixel combined with the lower resolution create a stepped pattern around the circumference of the dot (Figure 4.15). All area coverages were established for the line rulings on the Kodak and MacDermid Lux plates. The smallest absolute dot size was $195 \mu\text{m}^2$ and $155 \mu\text{m}^2$ respectively.

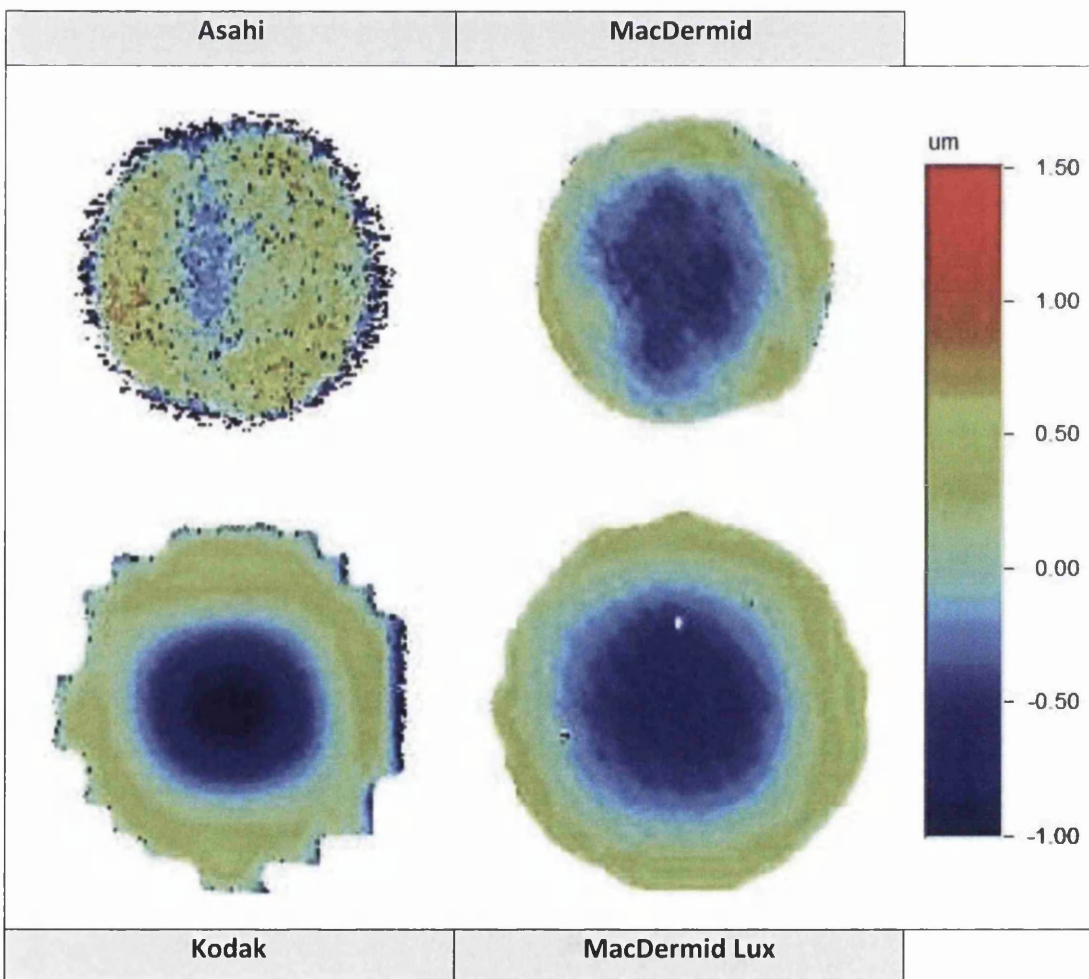


Figure 4.15: Comparison of dot shape for different plate materials and imaging technologies (50% dot at 150 lpi; 350x magnification)

4.4.1.2 Geometry of Plate Features

The cupping depths for all plate types are presented in Figure 4.17 to Figure 4.20. The water-washable Asahi plate, which theoretically falls into the category of “round-topped” plates, was the only material on which the full range of dot geometries could be observed (Figure 4.16). Dots below 10% nominal area coverage could not be investigated, because they were either not established on the printing plate or too small to distinguish the top geometry against the surface roughness. Halftone dots smaller than approximately $8,000 \mu\text{m}^2$ had pronounced convex top shapes (Figure 4.17), and the large positive values resulted from the increased surface roughness of this plate material. The roughness necessitated the isolation of the dot top data at a lower height in the histogram and this revealed more points on the dot shoulders. Consequently, the height difference between the dot shoulder and its apex increased. With increasing surface area, the convex shape transitioned to concave.

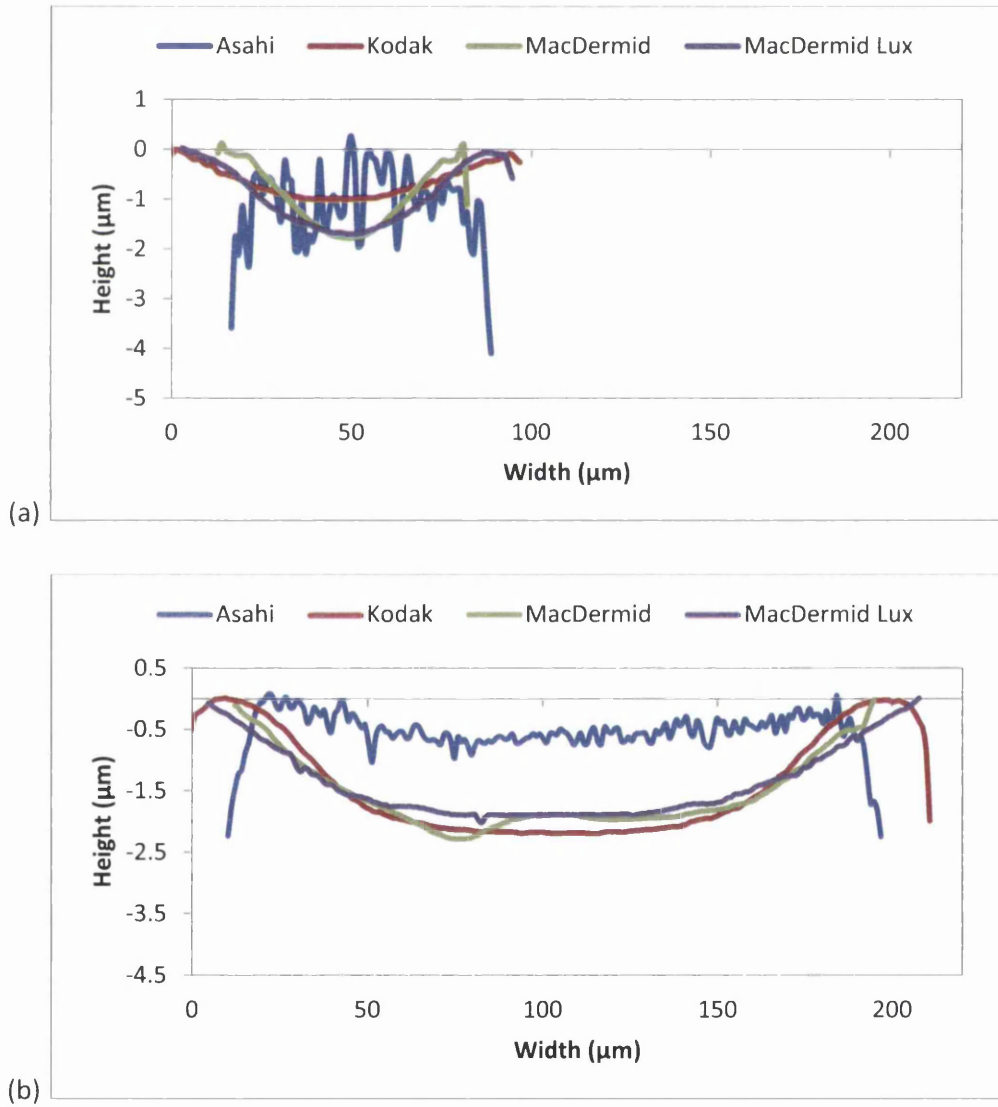


Figure 4.16: Profiles of (a) 10% and (b) 50% nominal area coverage dots at 100 lpi line ruling

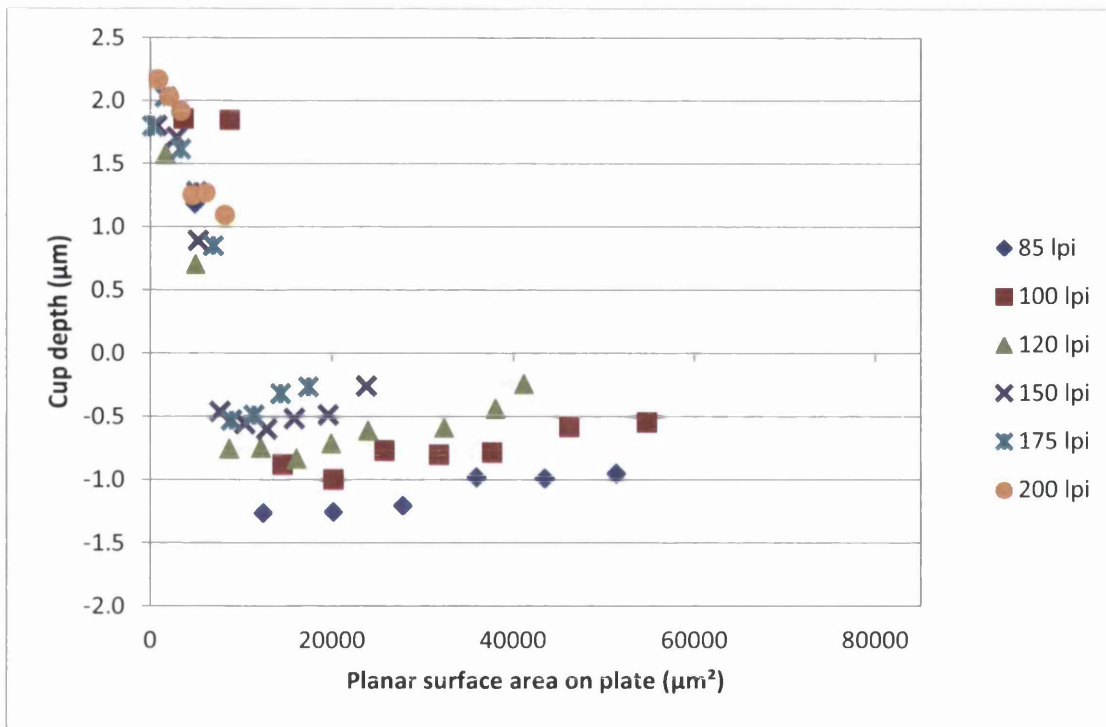


Figure 4.17: Cup depth for Asahi plate (standard digital imaging technology)

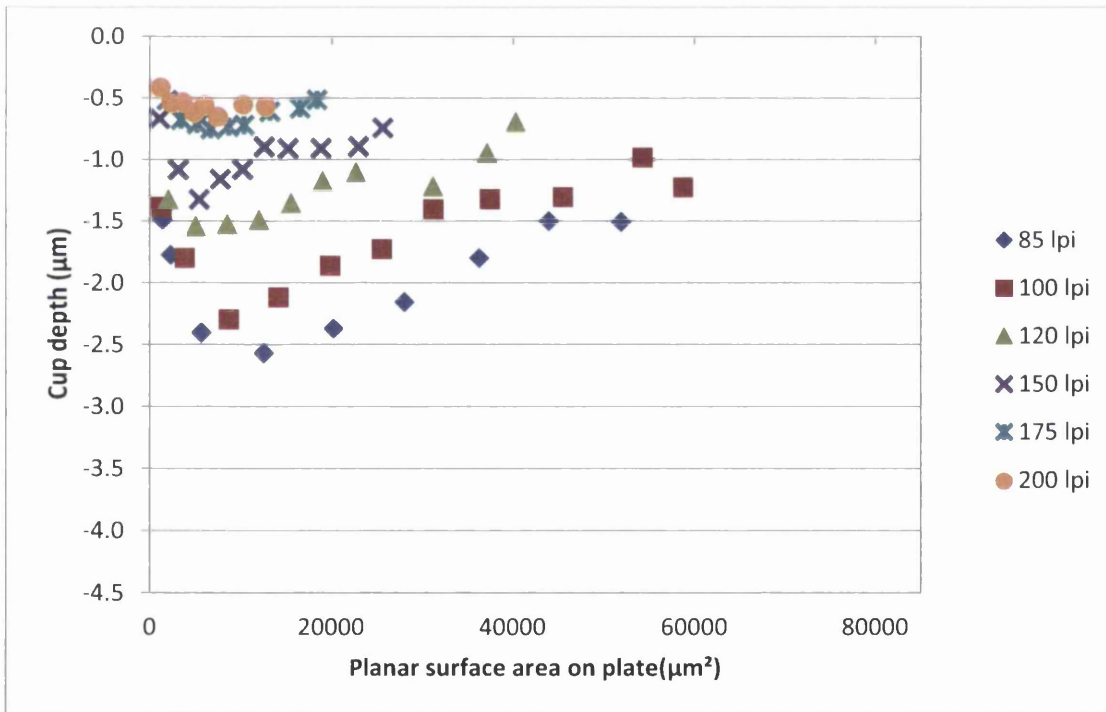


Figure 4.18: Cup depth for MacDermid plate (standard digital imaging technology)

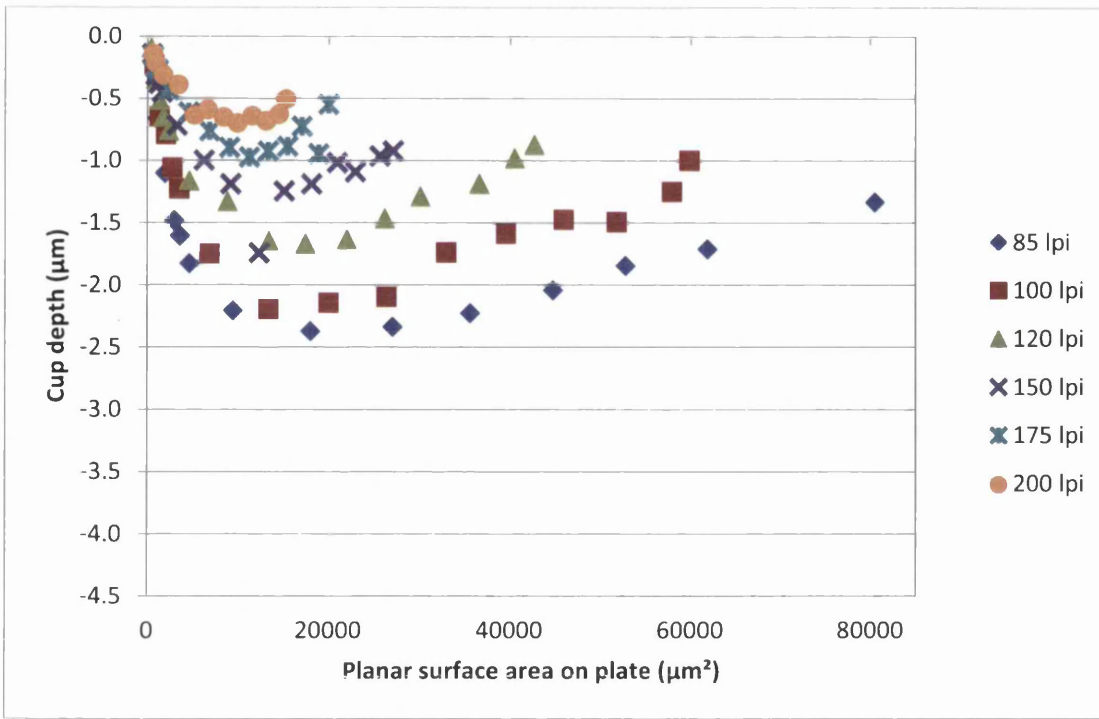


Figure 4.19: Cup depth for MacDermid Lux plate (LUX “flat-top” imaging technology)

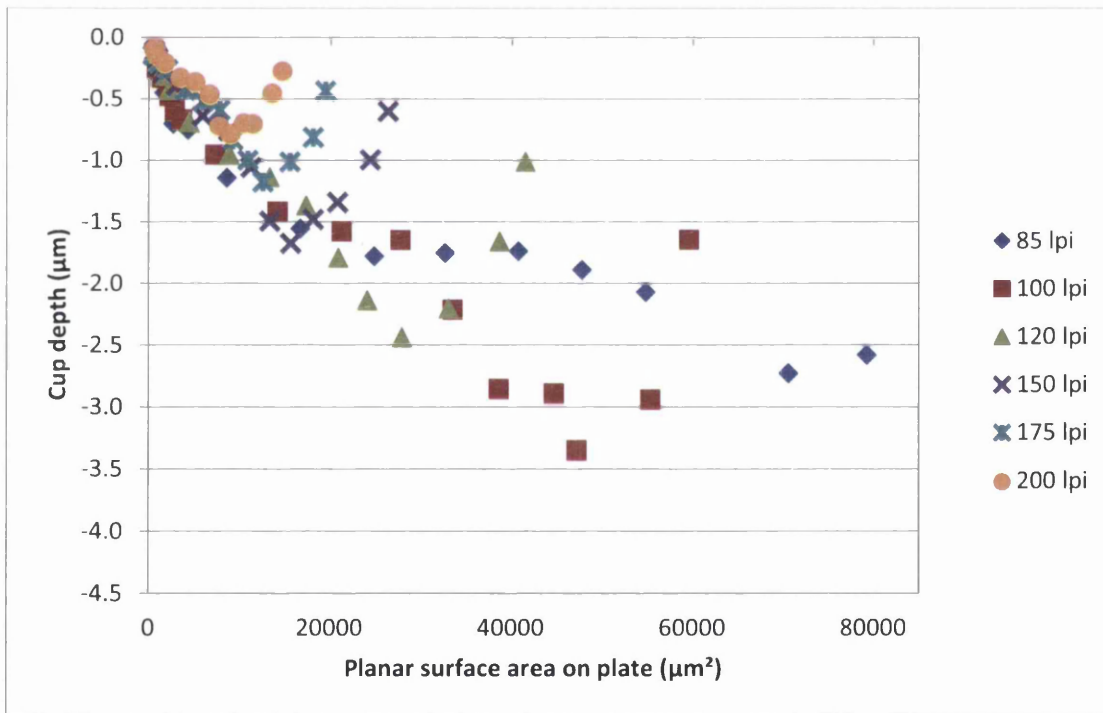


Figure 4.20: Cup depth for Kodak plate (Flexcel NX “flat-top” imaging technology)

The MacDermid (Figure 4.18), MacDermid Lux (Figure 4.19) and Kodak plates (Figure 4.20) resulted exclusively in concave dot tops with significant cupping. The dot shape and cup depth were dependent on dot size.

The change in dot geometry for the plates of different washability and the fact that the extent of the cupping was similar for the MacDermid plates indicates that the top geometry was independent of the type of imaging process used, but subject to the chemical composition of the plate material. Polymers in general are subject to shrinkage during curing. In an uncured polymer sheet only weak intermolecular attraction forces exist which pull the molecules together up to a distance of about 10^4 Å. During polymerisation the carbon-carbon covalent double bonds at the end of molecules are opened and two molecules joined to a chain through a new single covalent bond. This bond is much stronger than the attraction forces and closes the gap between molecules to a distance of about 1 Å. (Thompson, 1998) The effect is an increase of material density and volume shrinkage. Additional shrinkage results from better packing of the molecules during the polymerisation process which is dependent on temperature and steric interactions between molecules. (Broer, 1993; Hikmet, Zwerver and Broer, 1992) Any variance in curing degree and resultant polymer shrinkage creates material regions under tension or compression (Fuh, 1997).

The cupping of halftone dots is the result of this shrinkage during the plate-making process. The following shrinkage mechanism is suggested: After the main exposure of the plate material, a single printing dot consists mostly of cured polymer (Figure 4.21a). It is enclosed by uncured polymer with a buffer zone of partially cured material separating the two. The cured material tries to shrink in volume, but it is anchored in place by the uncured and partially cured polymer. This creates tension within the halftone dot. Once the uncured material is washed out, the anchor is released and the tension within the dot is reduced by a contraction of the cured polymer (Figure 4.21b). The shrinkage is most notable in the centre of the dot, because its sides are restricted in their mobility by partially cured molecules. The effect might not have been observable for the highlights on the Asahi plate, because the polymer at the dot top was removed during washing out. The morphology of printing dots could not be explored further within the scope of this work, thus a separate study is recommended.

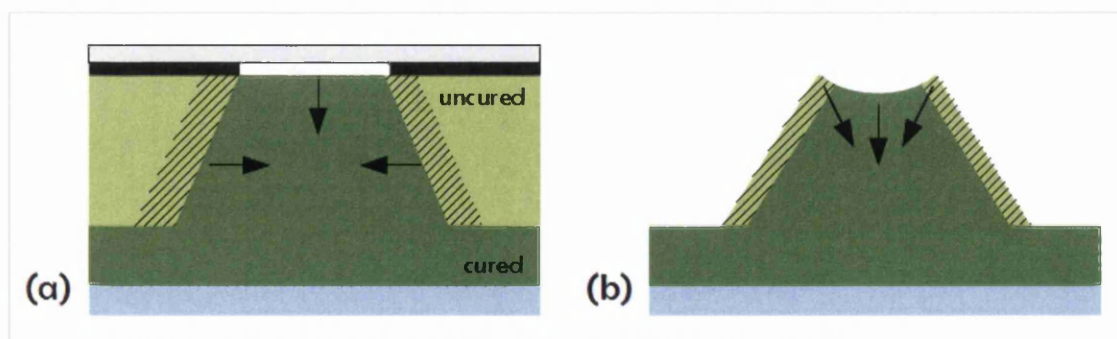


Figure 4.21: Schematic of potential cause for cupping. (a) cured polymer under tension after main exposure; (b) release of tension through contraction after washing out creates cupping

For all plate types, there is an almost linear relationship between cup depth and area coverage for highlights and midtones up to the point at which the maximum negative cup depth occurs (Asahi – Figure 4.17, MacDermid – Figure 4.18, MacDermid Lux – Figure 4.19, Kodak – Figure 4.20). The cupping effect became increasingly visible with area coverage, potentially because attraction forces in the dot sides had less effect at the dot centre. Beyond this point, i.e. for larger dots in the midtones and shadows, the cupping depth decreased. This was attributed to the reduction in intermediate dot height (refer to Figure 1.2 for definition). With increasing area coverage, these larger dots progressively join at their base, thereby reducing the intermediate relief depth (Beynon, 2007) and with it the volume of the dot column for which a density differential in the material could be created. The reduction in differential might result in less contraction of the dot.

Overall, the flattest dot tops were observed on the Asahi plate which is nominally a “round-topped” plate, whereas the other plates had concave top geometries. Therefore, the differentiation of “flat-” and “round-topped” plates by imaging technology and the terms themselves should be abandoned. Although cupping depths of up to 3.5 μm may appear insignificant compared to 500 μm nominal relief depth on the printing plate, the depression for the 50% Kodak dot in Figure 4.16 represents a volume of about 31,400 μm^3 if this cup could be filled with ink. If one square metre was imaged with this type of dot, their combined cup volume could take up 15% of the nominal ink volume supplied by the anilox.

Besides the very common measurands of dot height, shoulder angle and planar surface area, future investigations of halftone dots should also always take into account the cupping. The method introduced in this study has been aimed at the quantification of the cup depth. Cup width and volume as well as the radius of the cup rim could be included as additional measurands. Furthermore, the geometry of the cup shoulder (transitional region between dot top and shoulder) is expected to have a significant effect on ink transfer, but WLI could not capture data points on the shoulders of all plate types, as they were too steep (Figure 4.16).

4.4.2 Characteristics of Printed Features

4.4.2.1 Ink Distribution across Printed Features

The WLI and Keyence microscopic images were used to obtain information on the ink distribution across printed halftones and solids. The emphasis was placed on nonuniformities and printing defects, notably halos, uncovered areas and ink residue around the dot edges, and the following sections set out potential mechanisms to explain their occurrence. The effects of engagement and printing speed on the ink laydown were taken into account.

4.4.2.1.1 Halos

Halos, or the onset thereof, (Figure 4.22) were observed for all four plate sets, but the shape of the halo was strongly dependent on plate type and printing conditions. It became more pronounced with increasing speed and engagement. The defect created by the Asahi plate was approximately circular and enclosed very little ink, thus it is better classed as a doughnut defect which is characterised by a ring-shaped ink deposition. Since the Asahi plate was the only one of the four investigated which featured convex dot tops for 10% halftones, it may be assumed that the doughnut was created by complete displacement of ink underneath the top apex.

The Kodak, MacDermid and MacDermid Lux plates resulted in ring-shaped halos. Overlaying images of the halos with an outline of the concave dot top on the printing plate showed that their diameters were very similar (Figure 4.23). This implies an interaction between the halo defect and cupping by which the cup brim of the printing dots seals off some ink within the cup. The ink on top of the cup brim is displaced outward with the ink on the dot shoulders, thereby leaving a crescent-shaped ink-free impression on the substrate. That the halo diameter was slightly smaller than the cupped zone on the plate indicates that some additional deformation of the dot top has taken place. It is possible that, as described by S. Hamblyn (2004), a depression in the dot top could have occurred at its centre under hydrodynamic pressure causing the cup edges to fold in (Figure 4.24). In the actual printing process a rolling contact between the plate and substrate takes place which further complicates the deformation and deflection of the plate features, especially at higher engagements. Confirmation of this mechanism requires further investigation through the application of numerical simulation, and this needs to include the distribution of ink around the dot as substantial gain may be attributed to this mechanism. A suggested modelling sequence will be outlined for an analogous problem at the end of the next section.







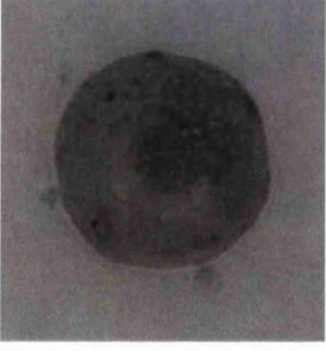


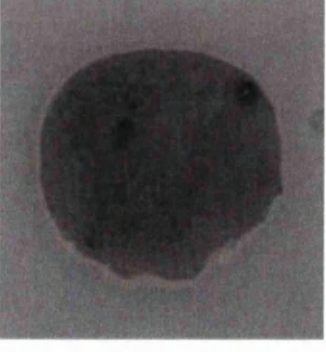


	Experiment 1	Experiment 4	Experiment 9
	150 ft/min, 1 thou	150 ft/min, 4 thou	300 ft/min, 4 thou
Asahi			
Kodak			
MacDermid			
MacDermid Lux			

Figure 4.22: Images of printed dots at 10% nominal area coverage and 100 lpi line ruling for different printing conditions showing the evolution of doughnut and halo defects (250x magnification)

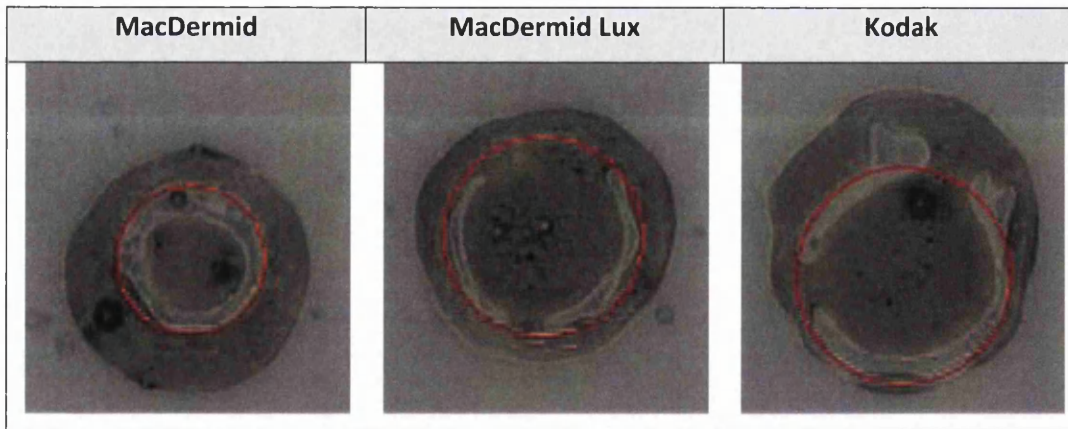


Figure 4.23: Comparison of printed halo with central diameter (red circle) of dot cupping on printing plate (10% nominal area coverage at 100 lpi line ruling; printed at 300 ft/min and 4 thou; 250x magnification)

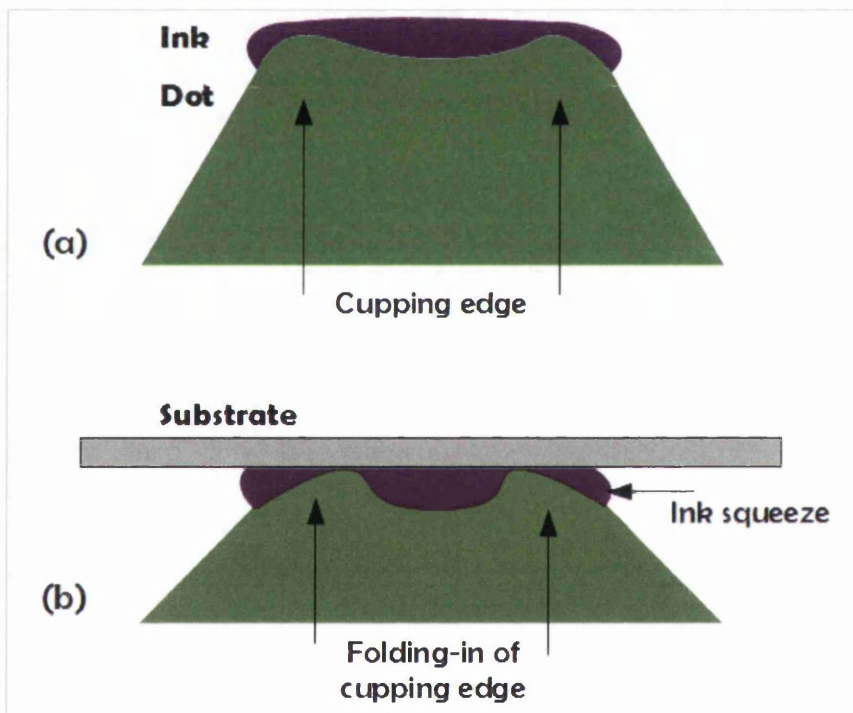


Figure 4.24: Schematic of potential interaction of cupping and halo. (a) concave dot top before impact, and (b) folding-in of cupping edge during impact with substrate

4.4.2.1.2 Uncovered Areas

A second defect, which predominantly occurred for larger features, was regions of missing ink within the dot. Examples of UCAs (at the centre of the dot and protruding from the halo) can be seen for 50% dots of all plate types in Figure 4.25. The minimum feature size at which the defect became apparent differed between line rulings. It ranged from 30% nominal area coverage ($23,500 \mu\text{m}^2$ printed dot area) at 85 lpi line ruling to 70% nominal area coverage ($10,500 \mu\text{m}^2$) at 200 lpi. The

UCAs became more pronounced with area coverage. Some of the UCAs appeared to contain ink residue, whereas others solely framed substrate which never seemed to have been in touch with ink. This prompted several potential causes for these UCAs. Since they manifested themselves only for dots having an area in excess of a certain size, surface depressions and nonuniform surface chemistry of the substrate (as suggested in the literature) were ruled to be unlikely reasons, as these would affect the appearance of the printed dot independent from its size.

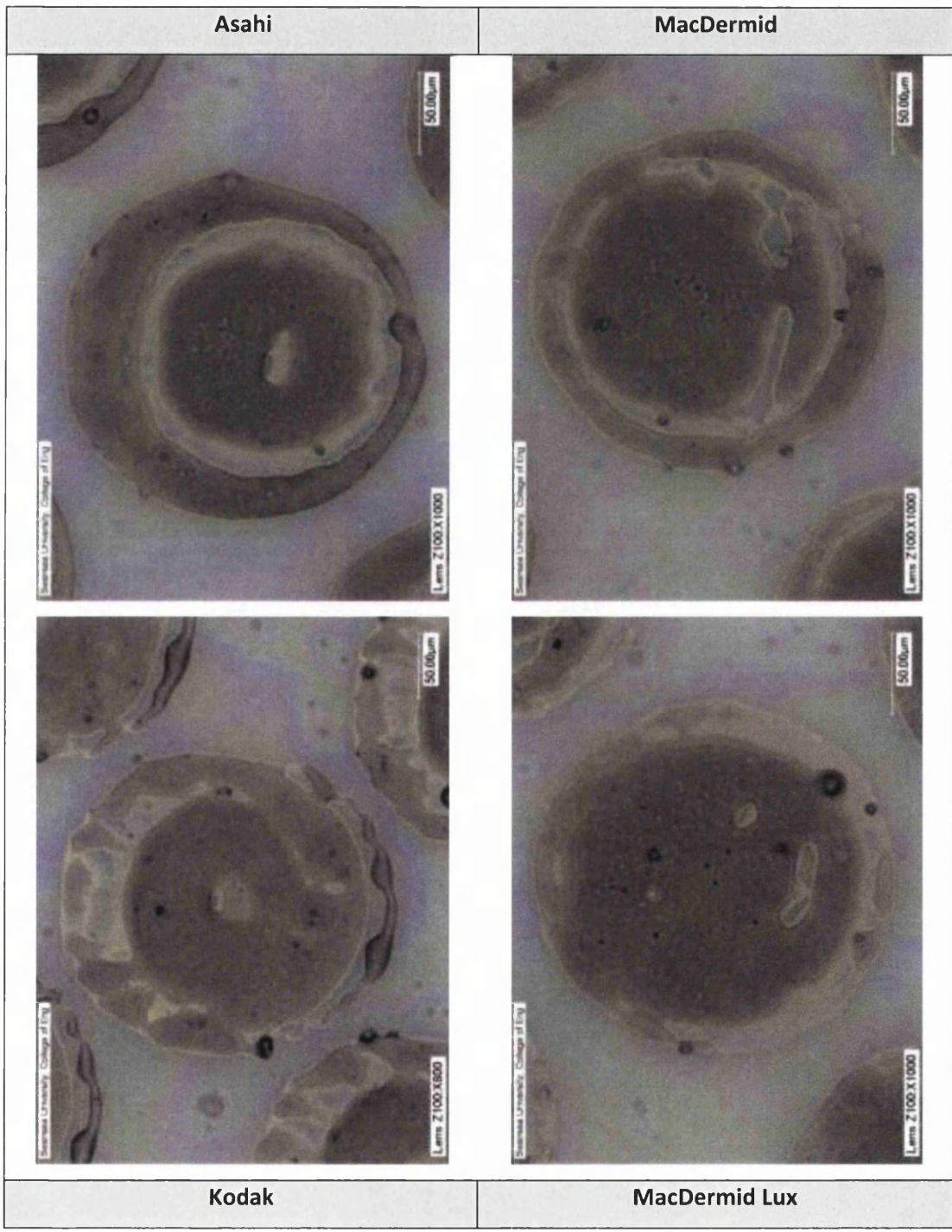


Figure 4.25: Images of printed dots compared for different dot top geometries at 50% nominal area coverage and 100 lpi line ruling showing UCAs and ink residue around the printed dot edges (printed at 300 ft/min and 4 thou)

Another possibility would be the formation of cavitation bubbles during the separation process of plate and substrate. At very high separation speeds as experienced during the printing process the stresses in the ink filament become very high. One mechanism to relieve the stresses is the appearance and growth of bubbles which provide extra volume in the bulk of the liquid (Gay, 2002). Nuclei of bubbles are already present in form of entrapped air, foaming of ink during transport to and within the anilox chamber, or small contaminants on printing plate and substrate (Poivet et al., 2003 and 2004). However, the size decrease of UCAs with increasing printing pressure, prompts a different mechanism relating to the cupping of the dot top.

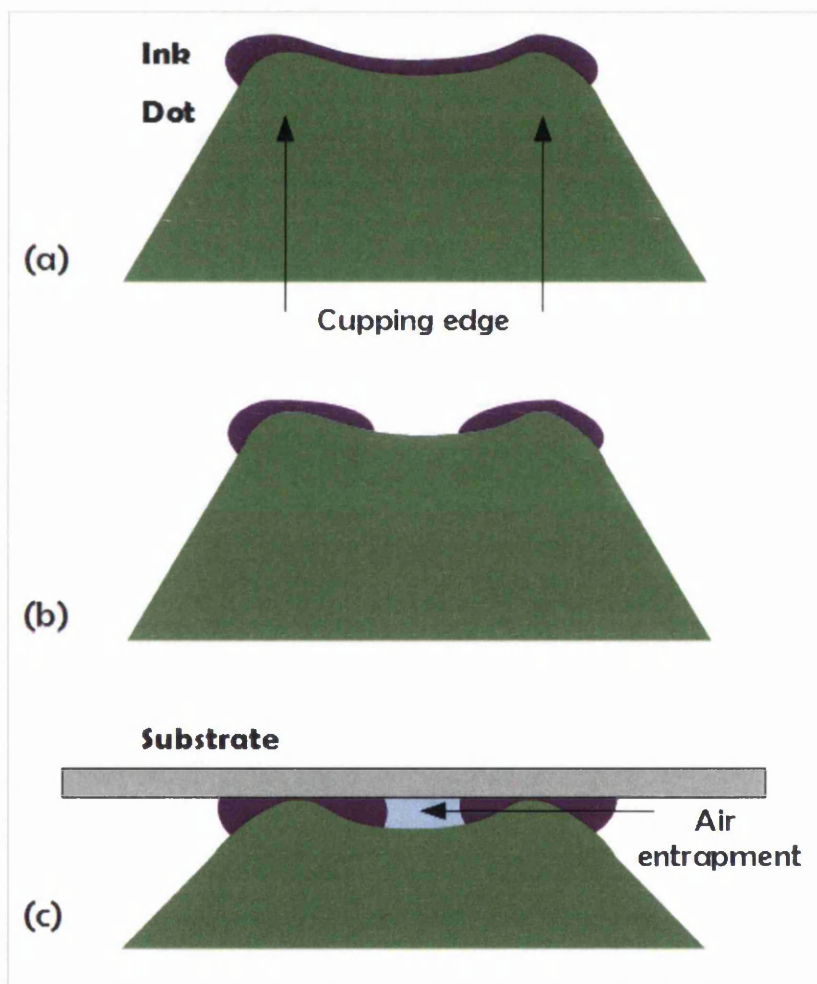


Figure 4.26: Schematic of the potential interaction of cupping and air entrapment. Before the impact with the substrate the ink does not fill the concave dot top entirely, but either (a) coats the contour of the dot top or (b) sits atop the cupping edges. During impact (c) air is entrapped within the dot cup by the cupping edge forming a seal with the substrate, thus preventing ink transfer.

The concept of the origin of halos in the printed dot shown in Figure 4.24 can be expanded by assuming that the concave dot top was not filled level with ink, but either coated with an ink layer following the contour of the cup (Figure 4.26a) or only inked atop the cupping edges (Figure 4.26b).

Due to the concave shape, on contact with the substrate a small volume of air is entrapped with the ink in the cup (Figure 4.26c). The air bubble prevents the ink transfer between plate and substrate, and an ink-free area remains in the print. This is supported by the observation that the size of the UCAs decreased with increasing printing pressure which would cause a compression of the entrapped air or its partial displacement outside the cup. Direct observations of air bubbles entrapped between the ink film on the printing plate and the substrate were made by Naito et al. (2006).

All plate materials exhibited deep cupping for nominal area coverages between 20% and 50% (except for the Kodak plate where it occurred at about 70%), whereas the UCAs were more pronounced for 50% dots and upwards. However, as the cup depth decreased for the midtones, the dot width increased more rapidly, thereby providing a rising cup volume and potentially more space for air to be entrapped in. This led to an increase in the size of UCAs in the higher midtones. For the shadows, the appearance of UCAs did not decline much further which suggests that the shallow cup depths became insignificant, and the creation of UCAs in the shadows was governed by the same mechanisms as for UCAs in solids. Since shadow halftones feature joined surfaces, the cupping might not have provided a seal for entrapping the air bubbles in the cup, and the bubbles could move between printing features or be released completely.

The detailed mechanisms remain a research challenge for the future and their study might employ numerical modelling. This will be a very complex task due to the multiple intricate steps involved in the printing process each of which might have to be covered by one or several individual simulations using varied numerical approaches, e.g. the finite element method for the deformation of the plate feature against the substrate in the printing nip and the Lattice-Boltzmann method for the ink behaviour during this deformation. A potential modelling sequence is depicted in Figure 4.27 and outlined below.

The first models of the sequence should be concerned with the filling of the anilox cells with ink, wiping action of the doctor blade and levelling of the ink in the cells thereafter, but these steps are omitted in Figure 4.27. There the starting point for the first simulation is the printing dot and inked anilox cells (a). The dot top is then brought into contact with the anilox which causes the polymer to deform against the cells as well as ink to squeeze out of the cells and across the deformed dot top (b). The output of this first model is the input to the second model in which the dot is disengaged from the anilox and the recovery of the dot shape studied (c). Additionally, the ink film splitting has to be taken into account. Ink is drawn out of the anilox cells forming filaments between the two surfaces. If the ink withdrawal from the anilox cells is incomplete, the filaments will elongate and

eventually rupture leaving depositions of ink in the cells and on the dot top (d). The potential levelling of these ink depositions on the dot have to be simulated before the inked dot can be input into the next series of models describing the ink transfer process to the substrate (e). Analogous to the inking process, the dot top engages with the substrate and is thereby deformed (f). The ink is squeezed across the substrate and dot top. When in the next model the dot is removed from the substrate (g), the deformation of the dot top is released, the ink extends into filaments between dot and substrate and either full or partial ink transfer takes place (h). The final model step is the ink levelling on the substrate (i). The size and geometry of the final printed dot in the model can be compared directly to the actual dot produced in the printing process in order to validate the modelling sequence.

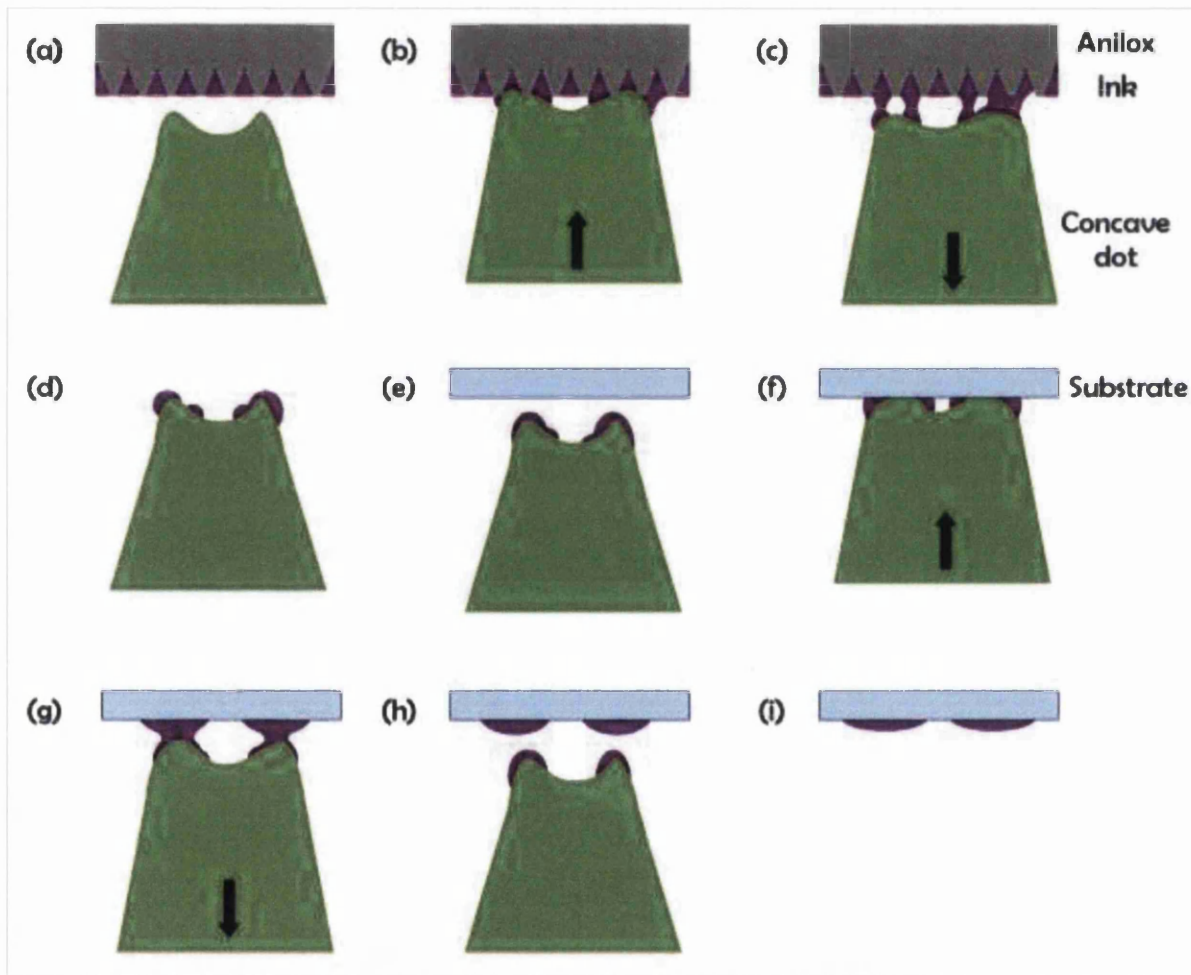


Figure 4.27: Potential modelling sequence for the future study of printing defects such as halos and UCAs. The starting point is the dot top and inked anilox cells (a). In the first model the dot is brought into contact with the anilox cells and deformed (b). Upon disengagement from the anilox, the dot recovers its shape and the ink is drawn into filaments (c). After the filament rupture (d), ink film levelling has to be taken into account in a separate model, before the inked dot can be input into the next simulation (e). The modelling sequence for the dot impacting with the substrate (f), dot recovery and ink filamentation upon withdrawal (g) as well as ink film splitting are analogous to the anilox sequence. Ink film levelling on the substrate is the final model step (i).

4.4.2.1.3 Ink Residue around Dot Edges

Ink residue (Figure 4.25) around the main body of the printed dot can be observed for all halftones independent of size and plate type for which there are a number of potential causes. Firstly, the substrate might have been dewetted when the ink was retracted during ink film splitting. Ink components, which adhered to the substrate surface or were trapped by it, resisted retraction and formed residual films. Secondly, monomers and oligomers which constitute the ink's vehicle could leach from the ink bulk and form a thin film around the main body of ink after curing. The film appears transparent if no pigments were removed from the ink bulk.

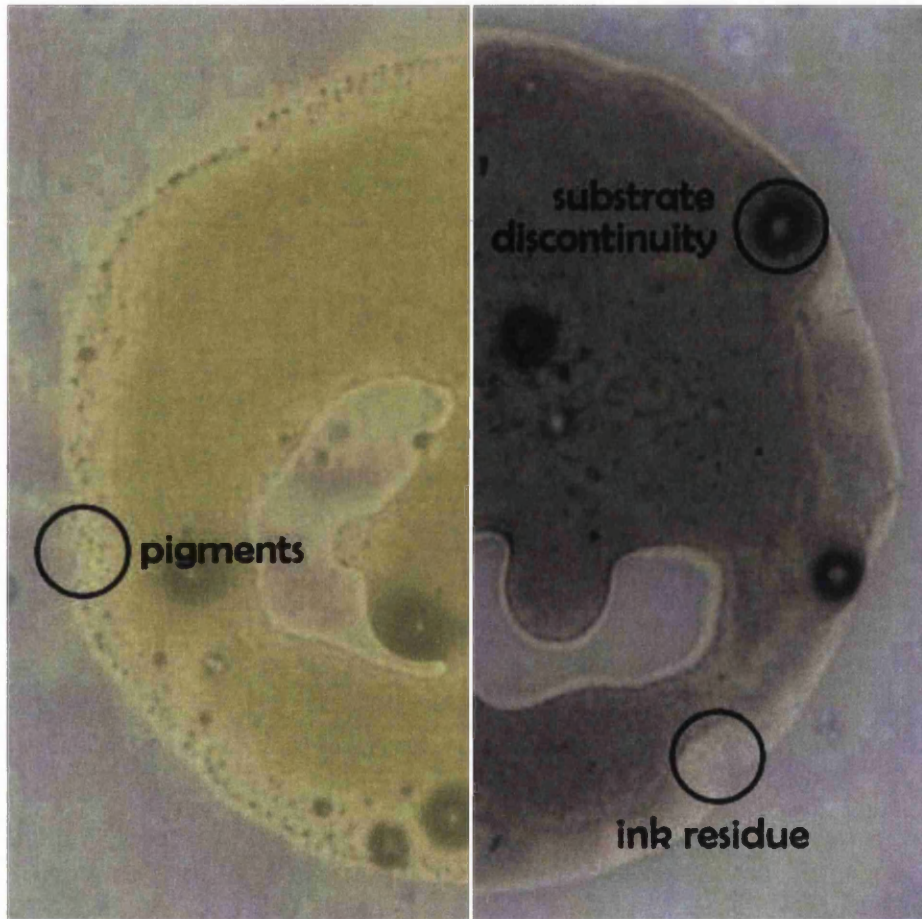


Figure 4.28: Comparison of ink residue around yellow and black dots showing varying amounts of pigments (MacDermid, 50% nominal area coverage at 100 lpi line ruling; printed at 150 ft/min and 1 thou; 450x magnification)

The two mechanisms suggested are not mutually exclusive, but the extent to which each occurs depends on the ink used (Figure 4.28). Yellow ink contains large pigments (visible in the microscopic image around the edge of the dot) which might offer more resistance to dewetting and would also hinder the ink vehicle in leaching. The result is a narrower region of ink residue. The nano-particles in black ink potentially lead to the opposite behaviour, in that they withdraw freely during dewetting as

well as slightly leach with the ink vehicle. Thus wider regions of ink residue are created. For each particular ink type, the width of the residue regions remains almost constant. Only a slight increase in width occurs with area coverage (compare Figure 4.22 with Figure 4.25). That it is not just an optical effect which makes the dots appear larger, can be confirmed with the WLI data. WLI is able to capture the ink residue around the dot (refer to Figure 4.10), but it is difficult to quantify its film thickness against the surface roughness, since it is in the region of 0.1 μm .

4.4.2.2 Planar Surface Area of Printed Features

The planar surface area of the printed features was determined from WLI data and compared to that on the plate. The effect of engagement and printing speed on the printed surface area were investigated for line rulings of 100 lpi and 150 lpi, chosen because these are two of the most frequently used line rulings in industry.

4.4.2.2.1 Line Ruling of 100 lpi

The planar surface area of printed dots tends to be larger than the surface area of the features on the plate. Bould (2001) and S. Hamblyn (2004) identified three mechanisms for this physical dot gain:

- ink spreading through squeezing action in the printing nip,
- top expansion and
- shoulder barrelling of the plate feature through deformation under pressure.

According to S. Hamblyn increasing the engagement enhances the effect of these mechanisms. Smaller plate features are subject to the largest increases relative to their original size, because their material volume is insufficient to stabilise them against deformation. They also have the larger relative ink-carrying capacity which adds to the ink squeezing effects.

This gain process has been identified for conventional flexographic plates and was found to be applicable to the digital plates used in this work. However, the magnitude of the effects differed significantly for the four plate sets investigated. Following S. Hamblyn (2004), the physical dot gain was captured in the Area Transfer Ratio (ATR) as expressed in Equation 4.1.

$$\text{Area Transfer Ratio (ATR)} = \frac{\text{Planar surface area on print } (\mu\text{m}^2)}{\text{Planar surface area on plate } (\mu\text{m}^2)} \quad \text{Equation 4.1}$$

At low printing speed and engagement the ATR was typically 1.15 for all plate materials (Figure 4.29). A clear difference occurs for the smallest dots (nominal area coverage of 10%, planar surface

areas below 10,000 μm^2). Also there is a clear distinction between the “round-topped” Asahi and MacDermid materials where the ATR = 1.7 and the “flat-topped” Kodak and MacDermid Lux materials for which the ATR = 1.2. This was attributed to the significant divergence in profile for the 10% dots (Figure 4.16a) compared to more similar larger dots (example of 50% dot in Figure 4.16b). The difference between the plates became even more apparent at the higher engagement of 4 thou (Figure 4.30). The larger dots approached ATRs of 1.45, except for the MacDermid Lux plate which remained lower at ATR = 1.2. The nominal 10% dots ranked Asahi (ATR = 2.5), MacDermid (2.1), Kodak (1.6) and MacDermid Lux (1.3). The MacDermid Lux plate was the most stable for all dot sizes under the different printing conditions, resulting in consistently low ATRs.

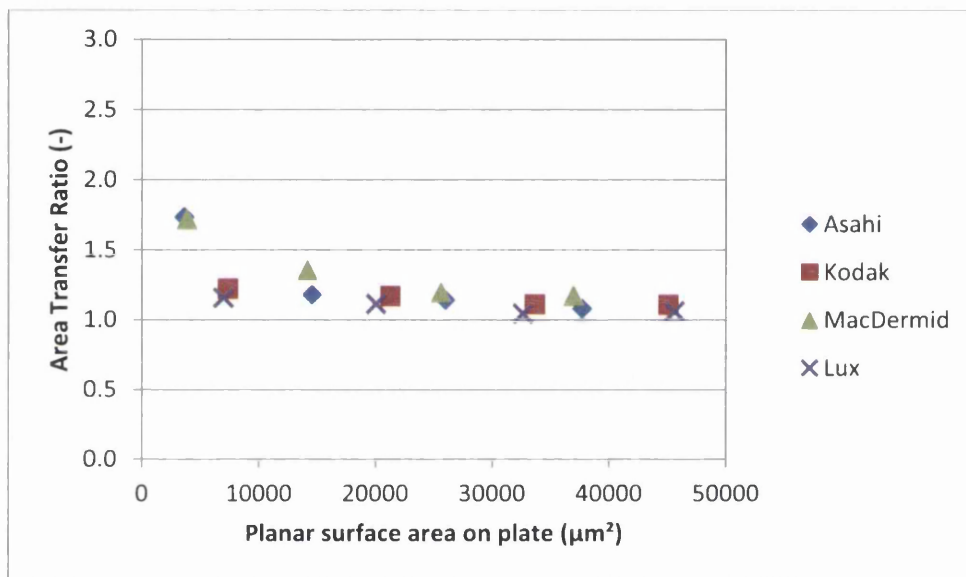


Figure 4.29: ATRs for dots of 100 lpi line ruling (printing conditions: 150 ft/min, 1 thou engagement)

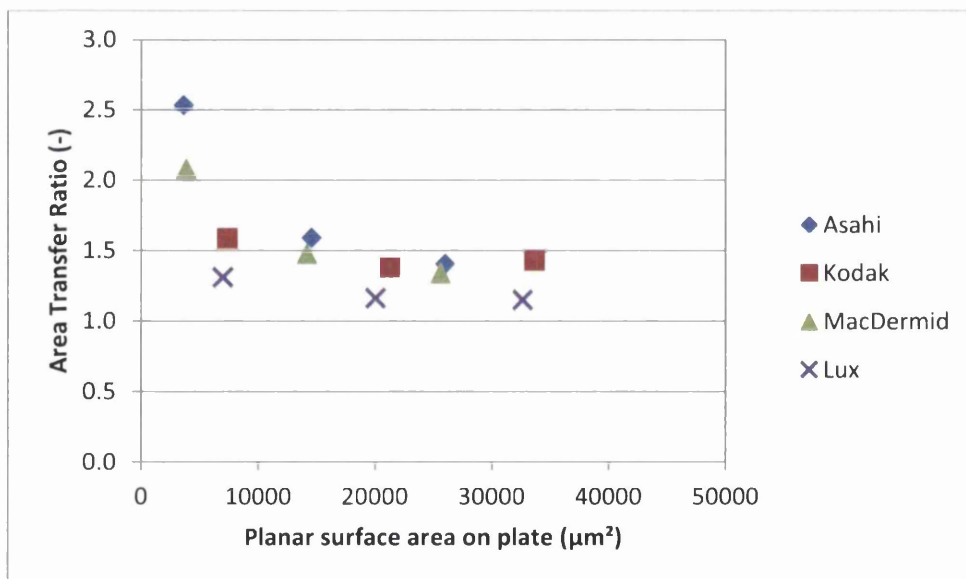


Figure 4.30: ATRs for dots of 100 lpi line ruling (printing conditions: 150 ft/min, 4 thou engagement)

S. Hamblyn (2004) showed that raising the printing speed decreases the ATR through the reduction of ink available for squeezing. However, in this study the higher speeds produced similar or larger surface areas indicating increased ink transfer (Figure 4.31). Rather than being a true effect of the change in printing speed, this has been attributed to the result of ink buildup along the edges of the printing features over the course of the printing trials. Image analysis of dots printed at 2 thou and 4 thou “Hysteresis” (experiment numbers 2 and 5 in Table 4.5) confirmed that the diameter of the printed dots had increased between the two nominally identical experiments, thereby indicating ink buildup.

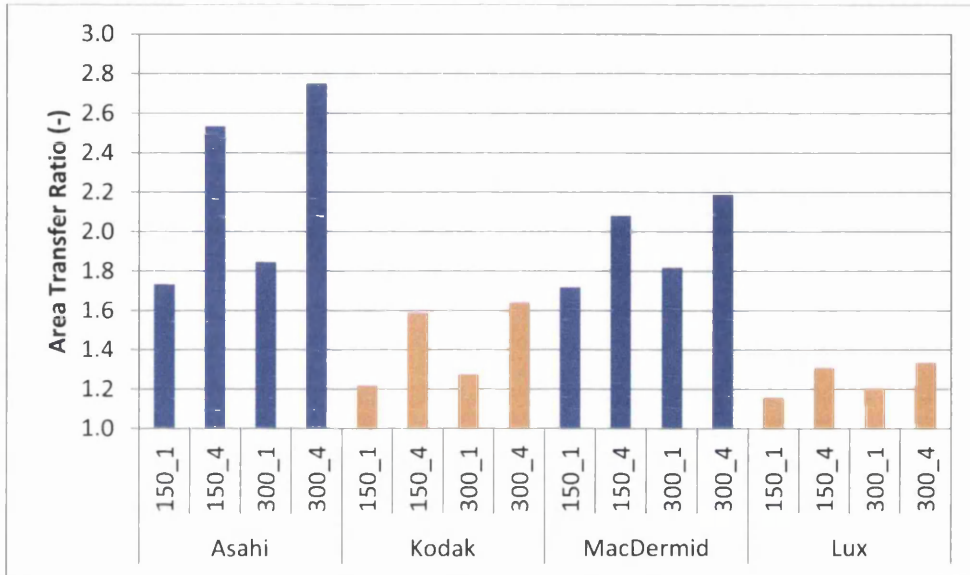


Figure 4.31: ATRs under different printing conditions for 10% dots of 100 lpi line ruling (printing conditions: “speed (ft/min)_engagement (thou)”)

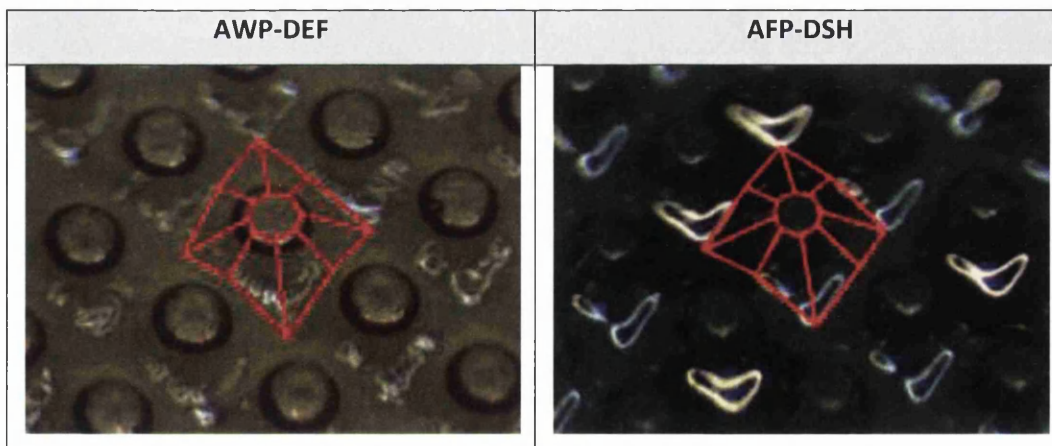


Figure 4.32: Comparison of magenta ink buildup on dots of 20% nominal area coverage at 100 lpi line ruling for two different plate materials (red outline of dot top in the centre and dot shoulders surrounding it)

Particularly when using high printing forces, the ink is not only spread across the substrate during impact, but also pushed from the dot top onto the dot shoulder, where it can build up with every consecutive impression. Figure 4.32 shows microscopic images of the ink buildup on two different printing plates (refer to section 5.1.1 for material specifications), both having completed print runs of a similar number of copies in excess of 12,000 impressions (the scoping print trial was specifically designed to investigate ink buildup, but is not included in this thesis). On the AWP-DEF material the magenta ink buildup is located on the dot shoulder near the top, whereas the ink spilled all the way down the dot shoulders on the AFP-DSH material and into the valleys between the dots. Ink remaining around the circumference of the dot potentially acts like an increase of plate surface area, thereby enlarging the printed dot.

The extent to which the ATRs increased with printing speed differed between the “round-“ and “flat-topped” plate materials. This indicates deviations in the progression of ink buildup and led to two hypotheses to describe the mechanism. Firstly, the cupping of the “flat-topped” dots served as restriction to the advancement of ink onto the dot shoulder, as the ink would have had to present higher advancing contact angles first, before it would have been possible for it to overcome the topographic obstacle (Oliver, Huh and Mason, 1977; Extrand and Moon, 2008). Secondly, the cupping edges in contact with the substrate sealed off the ink contained within the cup. Thus less ink was available to be squeezed out of the cup thereby reducing ink buildup and ATR. This second model is also consistent with the mechanism leading to the creation of the halo defect (refer to section 4.4.2.1.1).

The difference between the ATRs at different speeds, and thereby the ink buildup, was largest for the Asahi plate. This was possibly due to the convex shape of the dot top (Figure 4.16). As discussed in section 2.2.1.2, it is known that sharp surface features, e.g. as part of the feature geometry or surface roughness, are able to pin advancing liquid fronts in place. The Asahi plate was characterised by higher surface roughness than any of the other plates, with the potential associated impact on the contact angle formed with the ink. However, this might not have been sufficient to pin the contact line of the ink to the dot top. The accumulated effect was visible as increased ATR difference for the two speeds. In the image sequence of printed Asahi dots (Figure 4.22) the enlargement in dot diameter attributed to ink buildup is clearly visible.

The second largest difference in ATRs was observed for the MacDermid plate followed by the Kodak and MacDermid Lux plate, which meant the latter experienced the least ink buildup. This is in agreement with the manufacturers’ claims that these plate materials require less frequent cleaning during print runs (MacDermid Printing Solutions, 2012; Kodak, 2013) All three plates exhibited

prominent concave cup shapes on the dot top (Figure 4.16) potentially promoting the sealing-off and pinning of the ink. The slightly higher ATR values for Kodak over MacDermid Lux suggested that the ragged edges of the Kodak dot formed a less tight seal with the substrate, where the ink was able to squeeze out and onto the dot shoulder. The intermittent and undulating appearance of the Kodak dot's halo (Figure 4.22) supports this.

Despite its similarity to the Kodak and MacDermid Lux cup geometries, the MacDermid dot achieved results closer to the convex Asahi dot. There are a number of mechanisms that could lead to this, and they require further investigation using numerical modelling, geometrical and morphological analysis that will allow the material parameters to be explored systematically.

4.4.2.2.2 Line Ruling of 150 lpi

The ATR results for the line ruling of 150 lpi closely followed the findings of 100 lpi, but increased more significantly with engagement and speed. Figure 4.33 provides an ATR comparison for the two line rulings on the Asahi plate under different printing conditions which reflects the results for the other plate materials (refer to Appendix A.5).

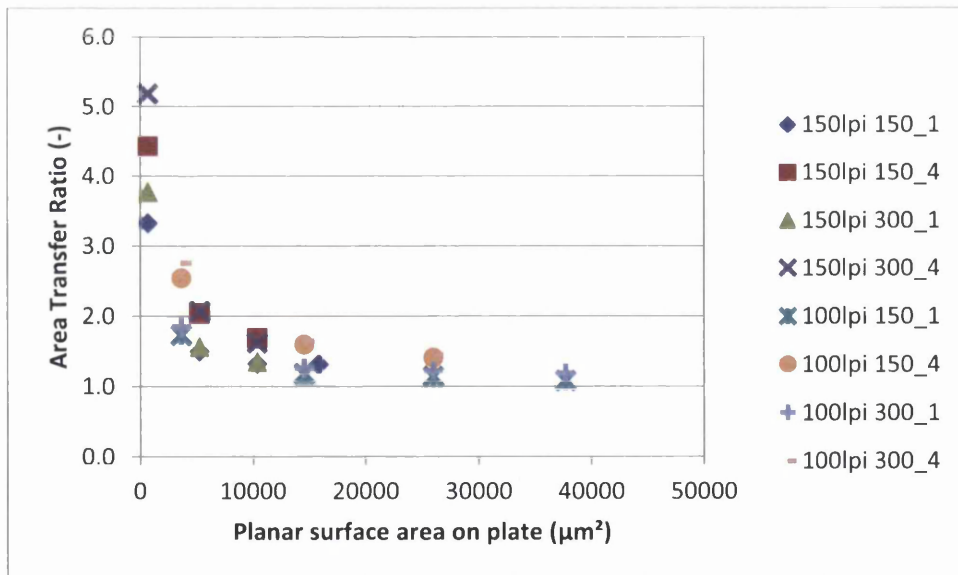


Figure 4.33: Comparison of ATRs for line rulings of 150 lpi and 100 lpi for Asahi plate (printing conditions: "speed (ft/min)_engagement (thou)")

The ATRs increased more significantly with engagement than speed. They also rose sharply for the smallest dots, observable in particular for dots of 10% nominal area coverage (approximately $880 \mu\text{m}^2$ planar surface area on the plate). Dot dipping and picking up of additional ink volume on

the dot shoulder was an unlikely cause, since all dots investigated had a larger diameter than the anilox cell opening. However, different to its counterpart at 100lpi, a 10% dot at 150 lpi will only make contact with three or four anilox cells at a time and could deform critically against the cell walls, thereby releasing ink from the anilox cells with its shoulders. This effect became negligible for dot sizes of 10,000 μm^2 upwards, and the ATR curves levelled off.

4.4.2.3 Volume of Printed Features

The volume of the printed features was determined from WLI data and compared to the planar surface area of the plate and printed features. The ink volume transferred from the printing plate is an indicator for the ink-carrying and ink-releasing capabilities of the plate material. The ink volume deposited for a given printed area represents the average ink film thickness. The effects of engagement and printing speed on volume were taken into account.

4.4.2.3.1 Line Ruling of 100 lpi

The trends observed in the ATRs were approximately reproduced by the Volume Transfer Ratios (VTR) from the printing plate (equation by S. Hamblyn, 2004):

$$\begin{aligned} \text{Volume Transfer Ratio (VTR)}(\mu\text{m}) & \qquad \qquad \qquad \text{Equation 4.2} \\ & = \frac{\text{Volume on print } (\mu\text{m}^3)}{\text{Planar surface area on plate } (\mu\text{m}^2)} \end{aligned}$$

At lower engagement the VTR for all plate materials lies between 0.8 and 1.1, and there was no particular order by plate material to the results. Only for the smallest dots of 10% nominal area coverage did the standard digital plates from Asahi and MacDermid produce larger VTRs of 1.3 to 1.5. At the higher engagement of 4 thou and 150 ft/min speed, all VTRs increased, especially for the 10% area coverage on the Asahi plate (Figure 4.34). The VTRs of the two “flat-topped” materials remained similarly lower. The most extreme printing conditions (300 ft/min and 4 thou) saw the largest differences between the plate materials (Figure 4.35). The VTRs ranked from Asahi over MacDermid and Kodak to MacDermid Lux. The latter was the only material which experienced a decrease in VTR with changing printing conditions.

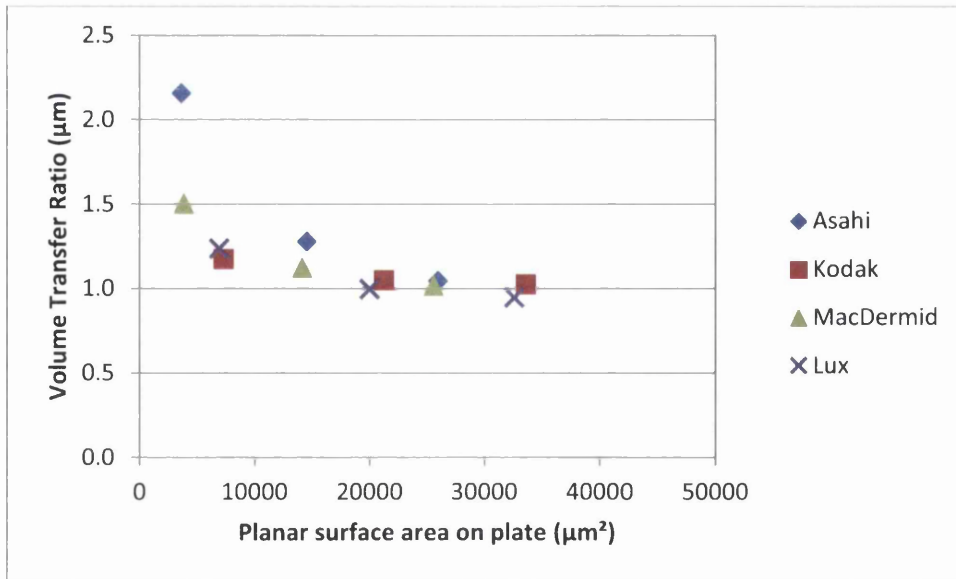


Figure 4.34: VTRs for dots of 100 lpi line ruling (printing conditions: 150 ft/min, 4 thou engagement)

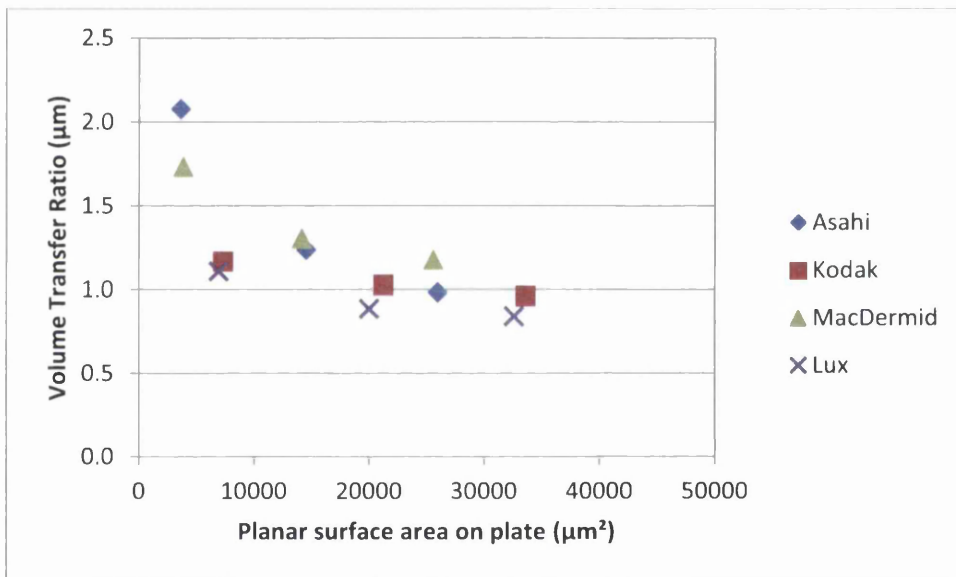


Figure 4.35: VTRs for dots of 100 lpi line ruling (printing conditions: 300 ft/min, 4 thou engagement)

The similarity of the VTR trends to the ATR ones suggested that the ink volume transferred was a function of the planar surface area printed. This was confirmed through a very high correlation coefficient ($R^2 = 0.97$) for the ink volume-area graph (Figure 4.36). The slope of the graph represents the mean film thickness (FT) (Equation 4.3) and was approximately constant. Most FT values were between $0.7 \mu\text{m}$ and $0.9 \mu\text{m}$ with a mean $\text{FT} = 0.79 \mu\text{m}$ (Figure 4.37).

$$\text{Mean film thickness (FT)} (\mu\text{m}) = \frac{\text{Volume on print} (\mu\text{m}^3)}{\text{Planar surface area on print} (\mu\text{m}^2)} \quad \text{Equation 4.3}$$

This implies that, although the printed surface area itself was dependent on plate material and printing conditions, the film thickness was not. Therefore, the ink transfer would primarily be governed by the ink and substrate properties. This is in agreement with previous assumptions that the surface characteristics of the printing plate play a minor role once the plate is inked, because some ink would always remain on the printing plate after the impression, and the plate-ink contact would turn into an ink-ink contact (Liu and Guthrie, 2003).

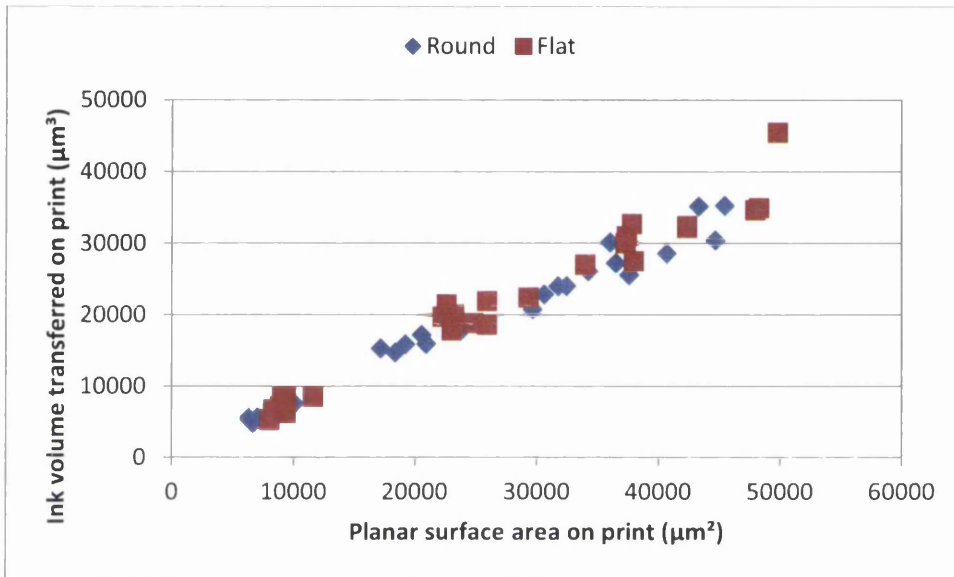


Figure 4.36: Relationship of ink volume transferred and planar surface area of printed dot at 100 lpi line ruling (all plate materials under all printing conditions included)

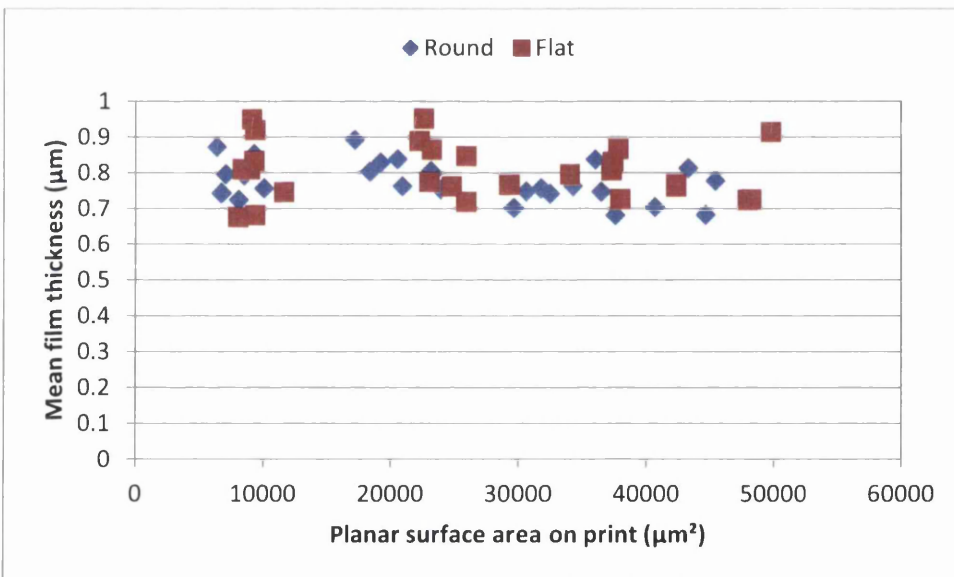


Figure 4.37: Mean film thickness for dots of 100 lpi line ruling (all plate materials under all printing conditions included)

4.4.2.3.2 Line Ruling of 150 lpi

Just like the ATR results, the VTR trends at 150 lpi followed their 100 lpi counterpart closely. Figure 4.38 provides a VTR comparison for the Asahi plate which was representative of all plate materials (refer to Appendix A.6). The smallest dots produced by the Asahi and MacDermid plates (10% nominal area coverage, approximately 880 μm^2 planar surface area on the plate) resulted in disproportionately large VTRs. Analogous to the ATRs, this was attributed to the increased susceptibility of smaller dots to deform against the anilox and pick up additional ink with the dot shoulders. The VTRs decreased significantly between 10% and 30% nominal area coverage due to dot stabilisation against deformation through their own material size and volume as well as increasing support by neighbouring dots. The larger dots produced similar VTRs to dots of the same size at 100 lpi.

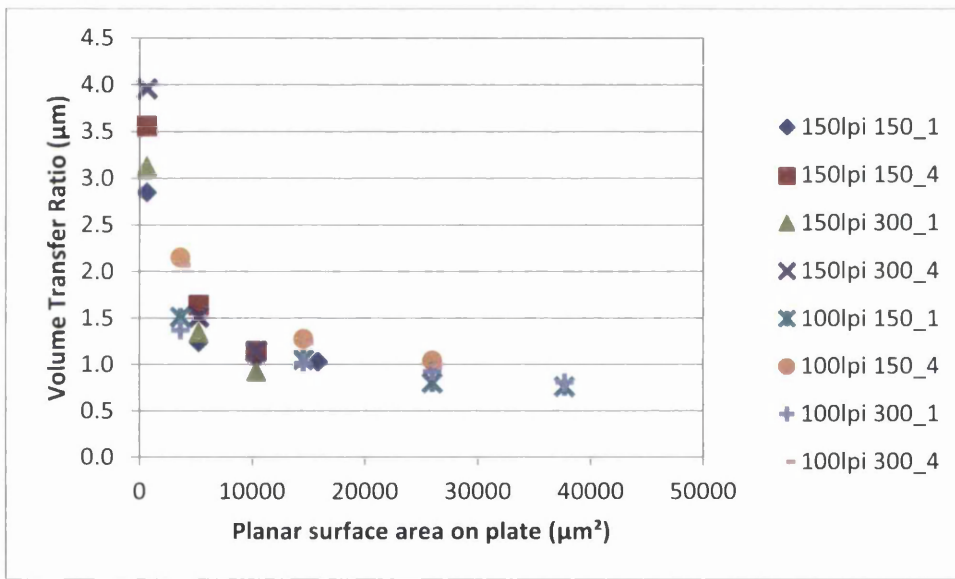


Figure 4.38: Comparison of VTRs for line rulings of 150 lpi and 100 lpi for Asahi plate (printing conditions: "speed (ft/min)_engagement (thou)")

The data comparison of the relationship of ink volume transferred to planar surface area printed showed the similarities between 150 lpi and 100 lpi line ruling (Figure 4.39). At 150 lpi, the correlation coefficient of the two measurands was a very high at $R^2 = 0.98$. The mean film thickness (FT=0.76 μm) was slightly lower than at 100 lpi (0.79 μm) (Figure 4.40) which might be due to a difference in the dot geometries. For dots of similar planar surface area, the shape of the cupping differed depending on their associated line ruling (Figure 4.41). At 100 lpi the 10% dots had a comparable planar surface area to the 30% dots at 150 lpi, but their cups were slightly deeper and could therefore potentially hold more ink.

Having explored the geometry of the printed dots, the next stage is to consider the impact on print density, and this will be dealt with in the next section of this chapter.

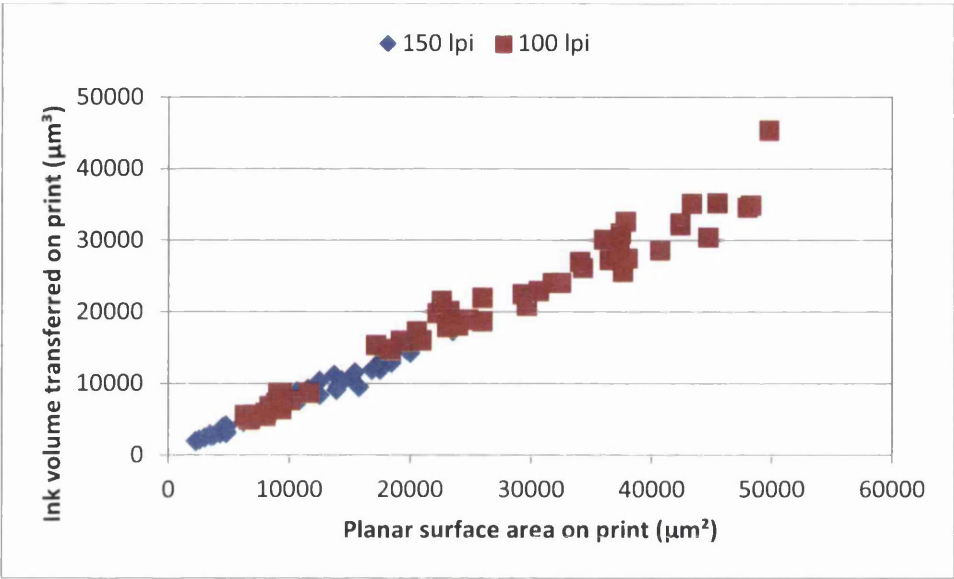


Figure 4.39: Relationship of ink volume transferred and planar surface area of printed dots compared for 150 lpi and 100 lpi line ruling (all plate materials under all printing conditions included)

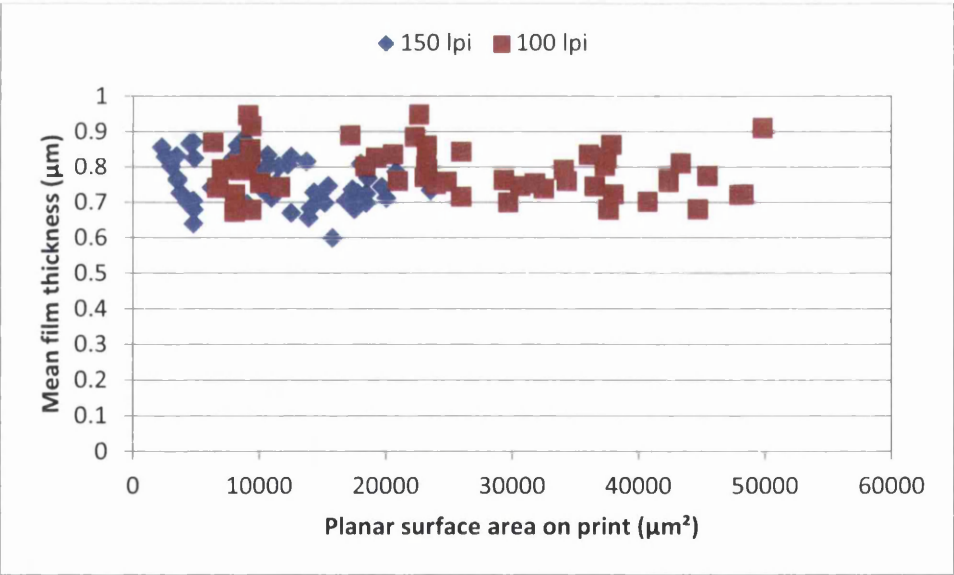


Figure 4.40: Mean film thickness compared for dots of 150 lpi and 100 lpi line ruling (all plate materials under all printing conditions included)

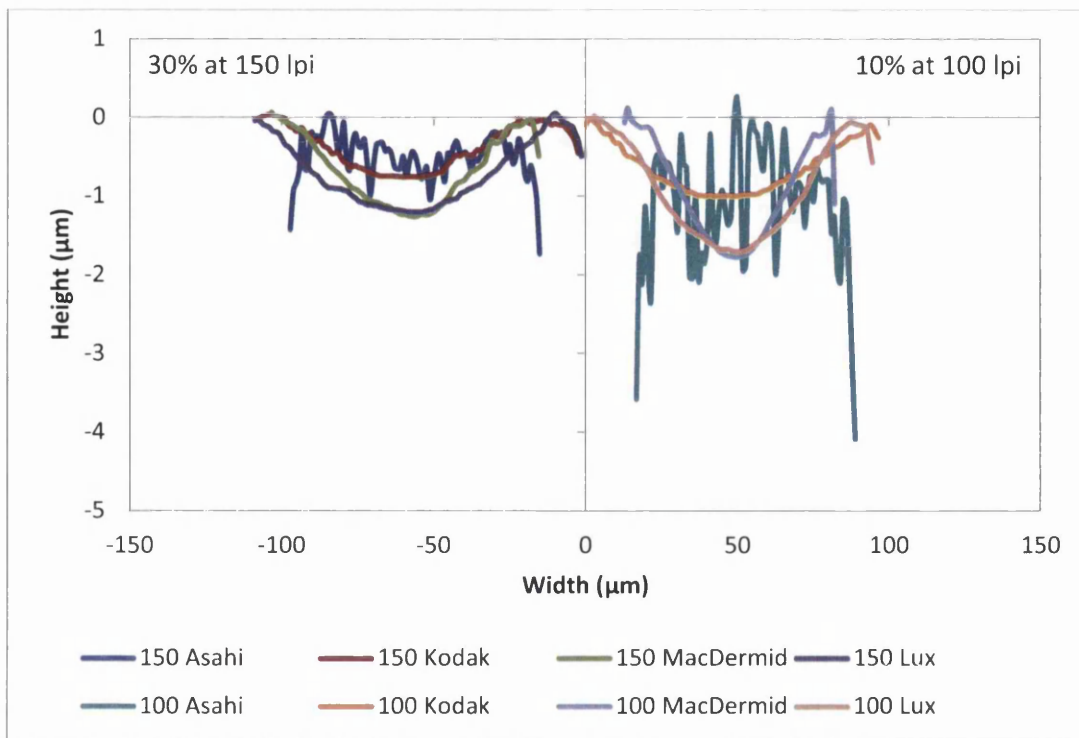


Figure 4.41: Comparison of cup geometry for similar dot sizes at different line rulings (left: 30% nominal area coverage at 150 lpi; right: 10% at 100 lpi)

4.4.2.4 Optical Density of Printed Features

The optical density of the printed features was determined by spectrophotometry. This was measured for the conditions that correspond to the physical measurements of dot features. Thus it was possible to explore the relationship between physical measurands and print density.

4.4.2.4.1 Line Ruling of 100 lpi

For all plate materials an increase in optical density with engagement and printing speed was observed (Figure 4.42). The trends were similar to those found for the printed area coverage (compare section 4.4.2.2.1). Figure 4.43 shows the relationship of optical density to area coverage of the printed features sorted by the different imaging technologies and taking into account all printing conditions. The very strong correlation indicates that optical density was directly dependent on printed area coverage, which thereby explains the analogous effects of engagement and speed on optical density. It also supports the Murray-Davies halftone model which states that different optical densities are generated by changing area coverage. The largest deviation between plate types occurred between 60% and 80% printed area coverage for all plate materials, and was attributed to the increasingly nonuniform ink distribution with dot size. The printing defects were slightly more pronounced for “flat-topped” Kodak and MacDermid Lux plates which expressed itself in slightly lower optical density.

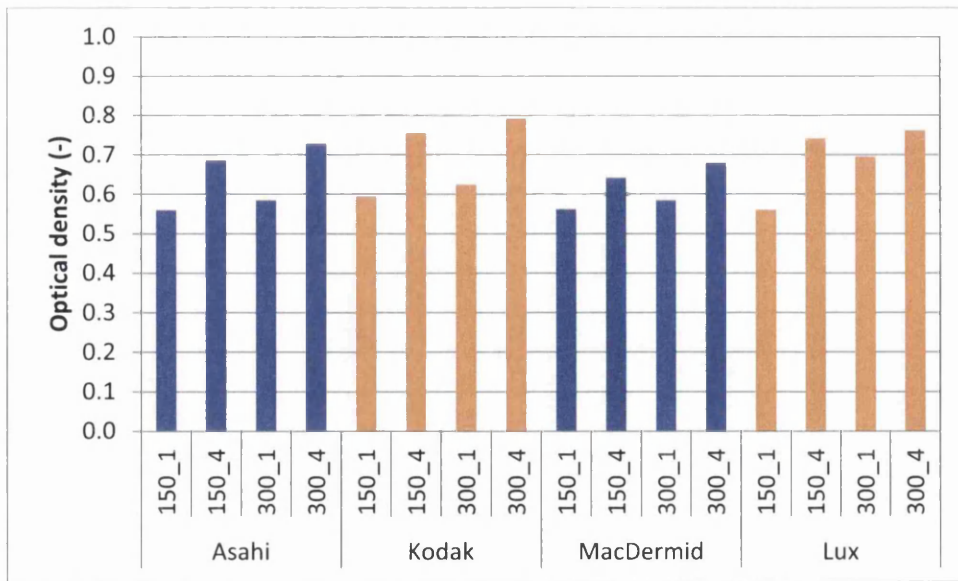


Figure 4.42: Optical density under different printing conditions for 70% dots of 100 lpi line ruling (printing conditions: "speed (ft/min)_engagement (thou)")

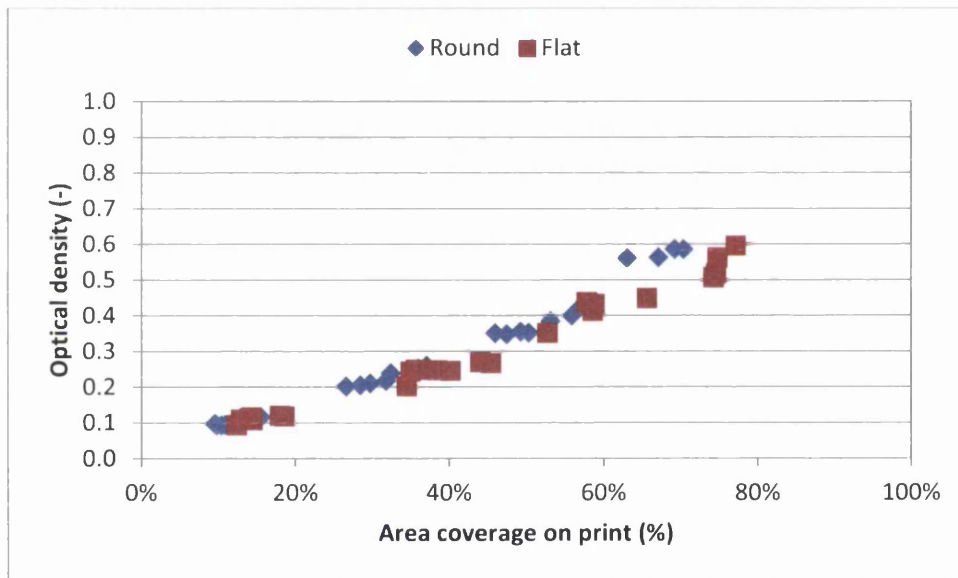


Figure 4.43: Relationship of optical density and area coverage on print for dots of 100 lpi line ruling sorted by imaging technology (all plate materials under all printing conditions included)

4.4.2.4.2 Line Ruling of 150 lpi

The findings regarding optical density of features printed at 150 lpi line ruling confirmed the results discussed for 100 lpi (Figure 4.44). However, no density difference could be distinguished between "flat-" and "round-topped" plate materials at 150 lpi. This was attributed to the more coherent ink distribution of these dots for all plate types as a result of their reduced size.

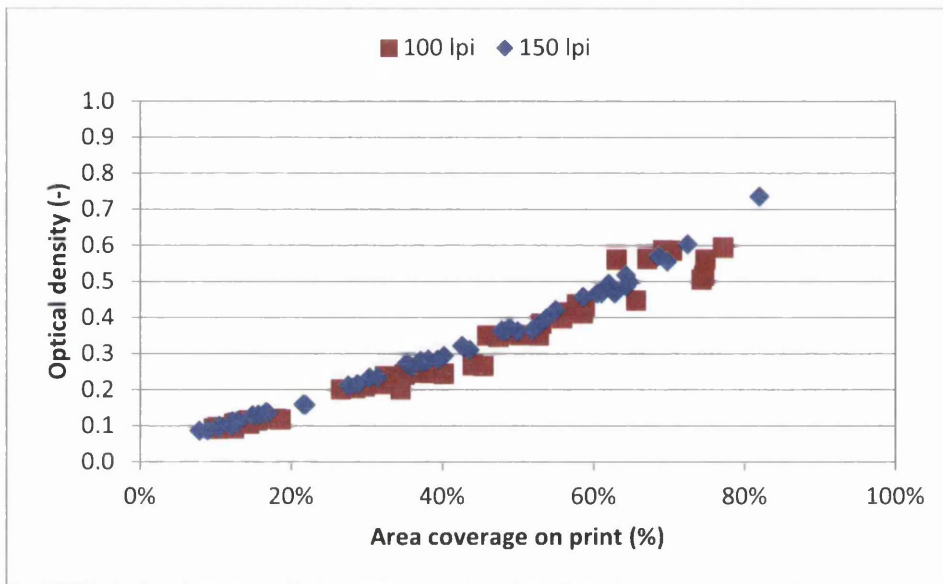


Figure 4.44: Relationship of optical density and area coverage on print compared for 150 lpi and 100 lpi line ruling (all plate materials under all printing conditions included)

4.4.2.5 Applicability and Comparison of Halftone Models

Halftone models are used to calculate the area coverage of a halftone patch from the optical density (i.e. reflectance) measured on it. They are the most widely used tool to determine area coverage as part of process control in industry. The previous section established that a very good correlation of optical density and area coverage (prerequisite for the Murray-Davies halftone model) was observed for the four plate materials. This section compares the prediction of this particular model with the experimental data. Other models were also evaluated to determine whether they are better able to cope with the particular challenges posed by the printed features of the different plate types. The models are Yule-Nielsen, Expanded Murray-Davies, Noffke-Seymour and Beer's Law, and their descriptions are provided in section 2.3.1.

The equations of the Expanded Murray-Davies and Noffke-Seymour models cannot be solved for the area coverage in closed form, as is possible for the Murray-Davies model. Thus, all model equations were rearranged to calculate the expected halftone reflectance produced by a given area coverage, which was then compared to the actual reflectance. The model error was determined using Equation 4.4.

$$Error = \sqrt{\frac{\sum_i^N (\beta_{actual,i} - \beta_{model,i})^2}{N}} \quad \text{Equation 4.4}$$

where β_{actual} is the actual reflectance measured by spectrophotometry, β_{model} is the reflectance calculated from the respective model, and N is the number of points in the data set. The Yule-

Nielsen n -value as well as the parameters ν and w in the Expanded Murray-Davies model were optimised for the best fit of model to actual data, i.e. the minimum model error. The respective values employed are provided with the error results below.

4.4.2.5.1 Line Ruling of 100 lpi

Figure 4.45 illustrates the wide range of modelled reflectance values at 100 lpi line ruling obtained from the different halftone equations. The corresponding model errors are listed in Table 4.8 and each model is discussed separately below.

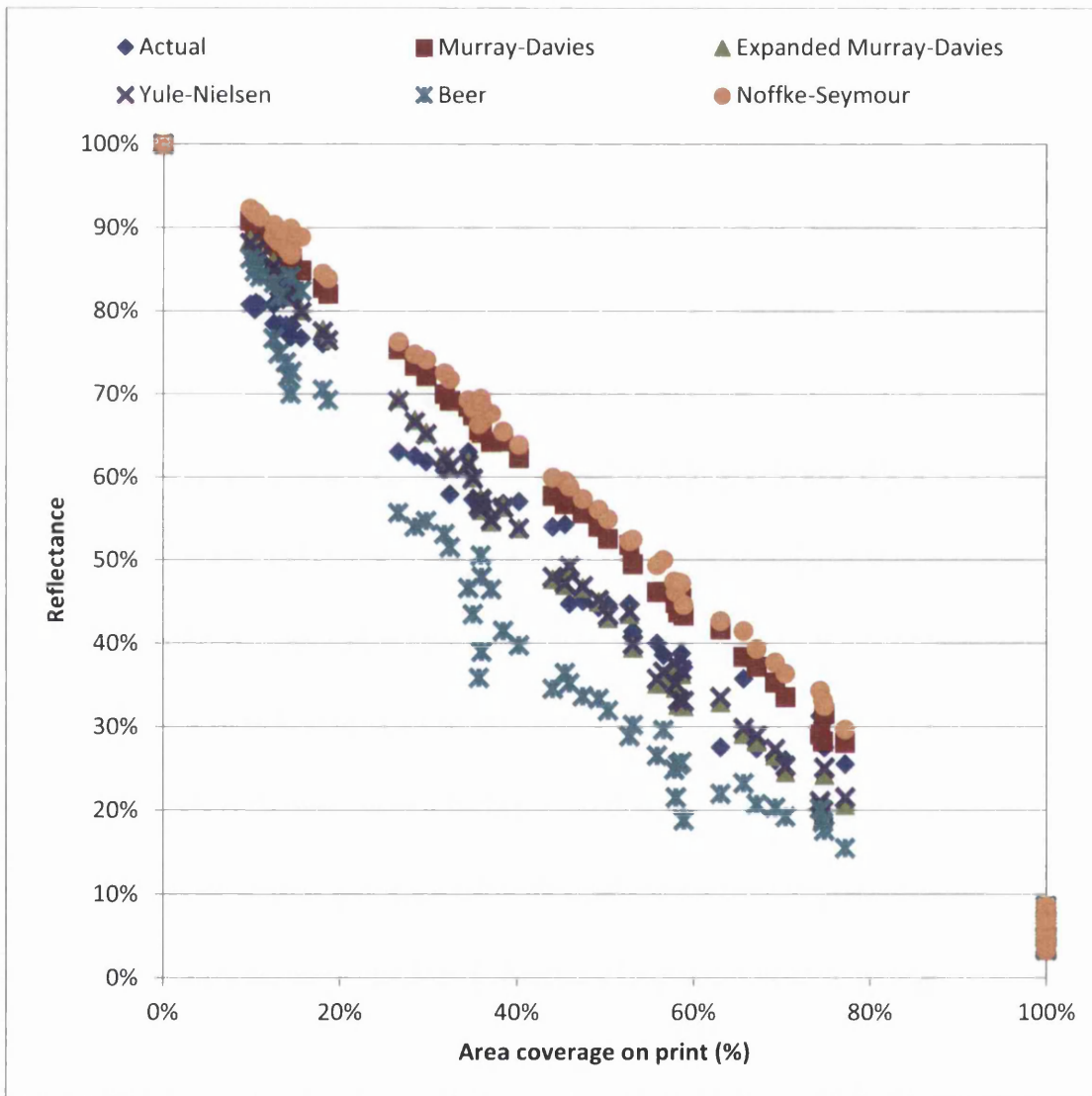


Figure 4.45: Comparison of actual and calculated reflectance at 100 lpi line ruling obtained from different halftone models (all plate materials under all printing conditions included)

Table 4.8: Comparison of model errors for different halftone models at 100 lpi line ruling

Model	Murray-Davies	Expanded Murray-Davies	Yule-Nielsen	Beer	Noffke-Seymour
Parameters	-	$v=0.5705; w=0$	$n=1.4877$	-	-
Error	0.0847	0.0462	0.0432	0.1077	0.1028

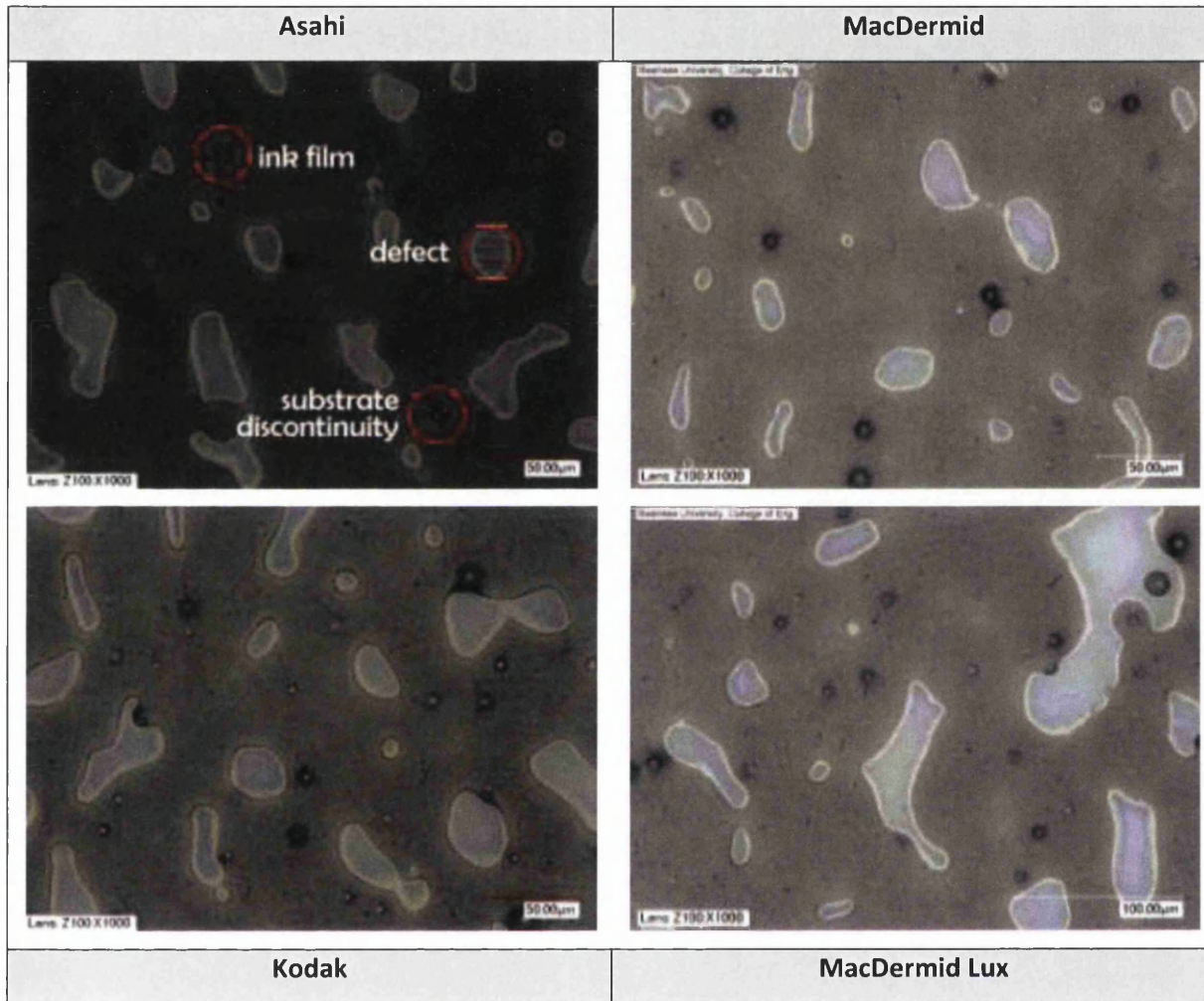


Figure 4.46: Comparison of print defects included in solids produced by different plate materials (100% nominal area coverage at 100 lpi line ruling; printed at 150 ft/min and 1 thou)

MURRAY-DAVIES MODEL

The standard Murray-Davies model overestimates the reflectance value for all halftone dots at 100 lpi line ruling. The primary cause is the result of the assumption that the solid reflectance, β_{Solid} , which is at the heart of the Murray-Davies equation, is obtained from a printed patch which features 100% nominal area coverage. However, independent of plate type all solid patches suffered from

considerable print defects in the form of UCAs (Figure 4.46). The defects reduced area coverage and increased reflectance of the reference solid which consequently increased all modelled halftone reflectance values. Basing the Murray-Davies equation on such a flawed measurand would inevitably lead to deviating results in halftone reflectance, unless all the corresponding area coverages in the calculation demonstrated similar flaws. However, this was not the case.

The defects in the 50% and 70% halftones of all plate materials, notably halos, residual ink films and UCAs, were comparable in appearance to the UCAs at 100% area coverage, and their respective reflectances increased in line with each other. Thus, actual and modelled reflectance show a lower deviation. The highlights were characterised by very uniform ink films with little or no defects which resulted in reduced actual reflectance out of line with the reference reflectance provided by the flawed 100% area coverage. Consequently, the actual and modelled reflectances deviate. Additionally, the midtones and shadows printed with “flat-topped” Kodak and MacDermid Lux plates suffered from more irregular ink films than those printed with standard digital plates. This rendered them more similar in appearance to the reference solid, their reflectances aligned better and reduced the model error (Figure 4.47).

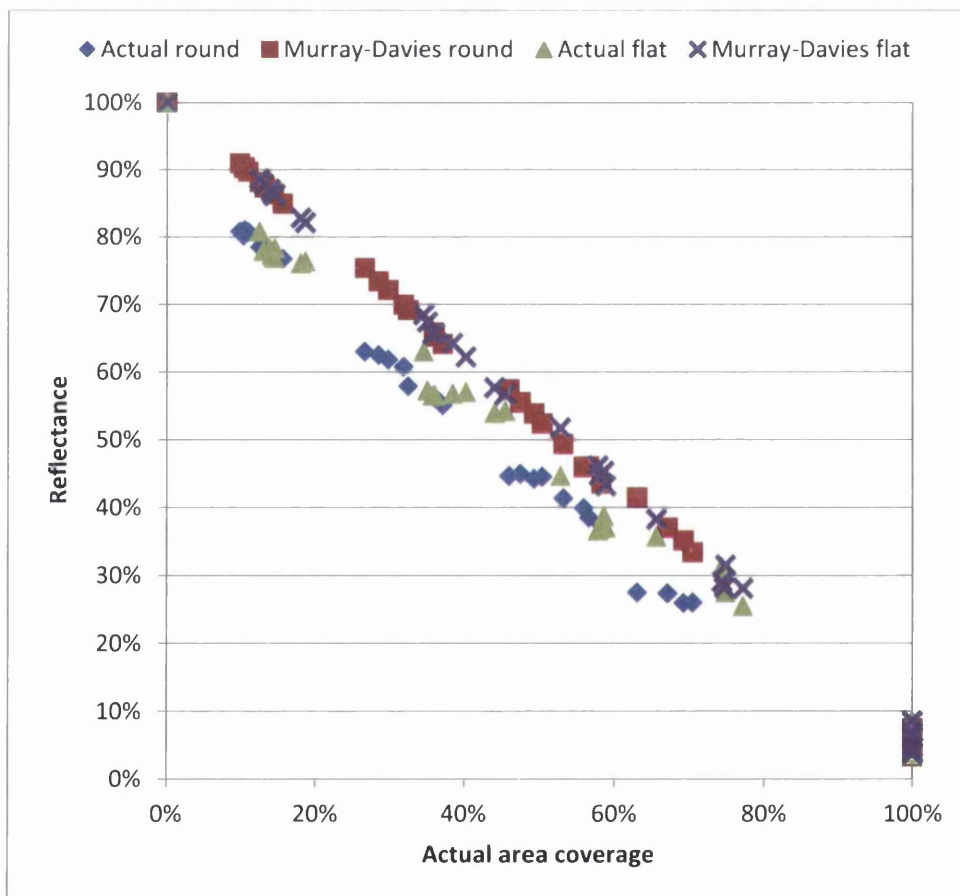


Figure 4.47: Comparison of actual and calculated reflectance obtained from Murray-Davies model for 100 lpi line ruling sorted by imaging technology

BEER'S LAW

Beer's Law represents the other extreme to the Murray-Davies Model by assuming that the printed ink film spreads out completely and covers the entire substrate. The majority of modelled reflectance values significantly underestimated the true values. The only exception was the values calculated for highlights on standard digital plates which were overestimated (Figure 4.48). The overall model error was the largest out of all models investigated (Table 4.8). The underestimate was a direct result of ignoring the substrate's reflectance in the equation, thereby producing overall reflectance values which were too low.

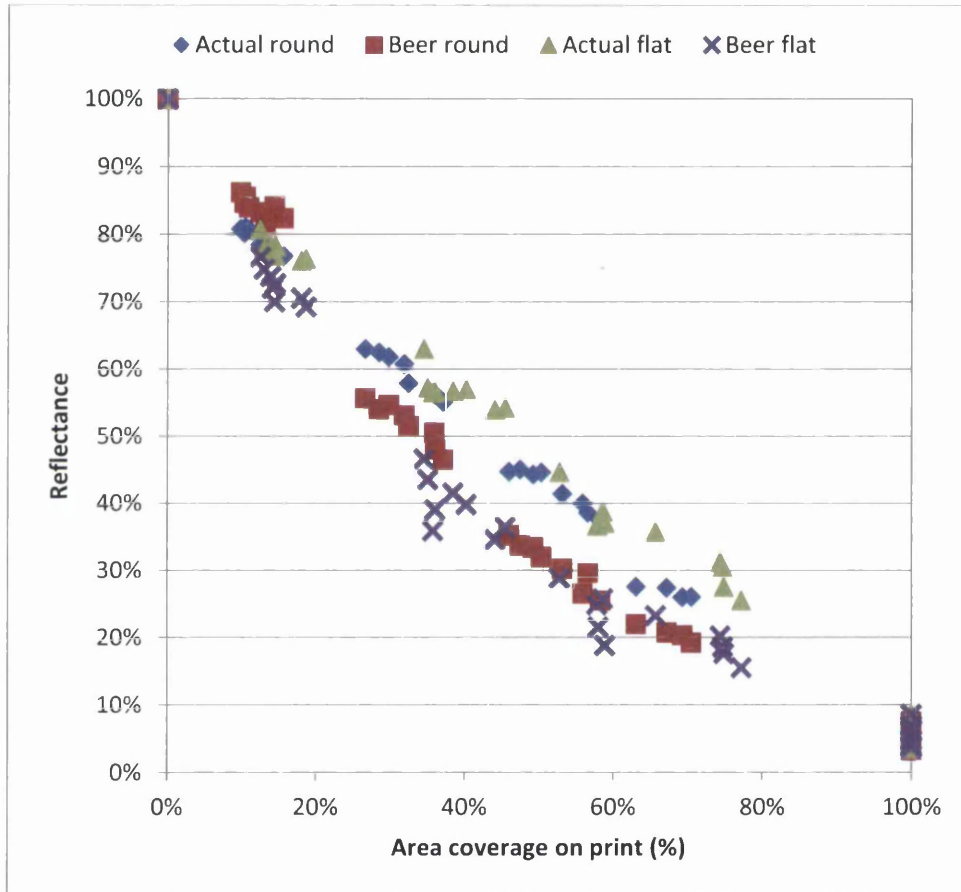


Figure 4.48: Comparison of actual and calculated reflectance obtained from Beer's Law for 100 lpi line ruling

The highlights achieved the best data fit, because their printed structure resembled most closely the theoretical dot on which Beer's Law was based. Unlike the other models, this theoretical dot is not characterised by the actual printed area coverage but the dot size on the printing plate. The model presumes that all plate dots (independent of size) carry an ink film of identical thickness, have very sharp edges, and there is no ink spread or printing defects. The actual printed dots that got closest

to this description were the highlights. The printed structure of the larger dots increasingly deviated from this ideal dot and the model error increased.

The modelled reflectance of the highlights on the standard digital plates (Asahi and MacDermid) was higher than for the “flat-topped” plates (Kodak and MacDermid Lux), because their size on the printing plate was significantly smaller. The real reflectance of these dots was reduced by additional ink transfer from the ink buildup around the dot tops which created a proportionally larger printed dot.

NOFFKE-SEYMOUR MODEL

The Noffke-Seymour equation was designed to estimate the reflectance value of the full range of halftone structures – from hard printed dots which did not spread out over the substrate to soft dots which completely spread out. The true spectral reflectance is expected to lie somewhere between these extremes, and the model has previously been used successfully to estimate it (Seymour and Noffke, 2012). However, this success could not be repeated in this work, and the modelled reflectances were an even larger overestimate (model error = 0.1028) than the Murray-Davies results (model error = 0.0848).

The Noffke-Seymour model is subject to the same problem discussed for the Murray-Davies equation above, that the reflectance of the reference solid is increased because of the UCAs it contains. Since the halftones do not exhibit any defects to the same extent as the solid, i.e. their reflectances have not increased in line with the solid reflectance, their modelled values are overestimated. The problem aggravates in the Noffke-Seymour equation, because the solid reflectance is increased further by the adjustment for ink spread. The model assumes that dot gain in the prints is the result of ink spread across the substrate which is accompanied by a thinning of the ink film. This in return increases the reflectance. However, it has been shown in section 4.4.2.3 that the mean ink film thickness is approximately constant for all halftones. Thus the real halftone reflectance is solely governed by the area coverage, and the ink spread adjustment based on ink film thickness in the Noffke-Seymour equation overestimates the modelled reflectances. The basic concept behind the Noffke-Seymour model has potential, but the equation itself requires revision, as in its current form it does not represent an improved alternative to the Murray-Davies equation.

YULE-NIELSEN MODEL AND EXPANDED MURRAY-DAVIES MODEL

The parameters of the Yule-Nielsen and Expanded Murray-Davies models were optimised to achieve the best fit of modelled to actual data. The two model errors were of similar magnitude (model error Yule-Nielsen = 0.0462; Expanded Murray-Davies = 0.0432) and only half as large as the Murray-Davies model error.

The improved fit was only achievable because of the retrospective parameter optimisation process step which at the same time constitutes one of the disadvantages of these two models. However, following Pearson's (1980) recommendation for the optimal Yule-Nielsen factor $n=1.7$, the resultant model error of 0.0478 would only be slightly larger than the error of the optimal fit and still represent an improvement over the Murray-Davies model.

The largest deviations in the fit occurred for the highlights (about 15% actual area coverage) where both models overestimated the reflectance. If these dots were excluded from the data set, the model errors could be further improved (Table 4.9). This was yet another indicator of the dissimilarity of highlights compared to midtones and shadows. As has already been explained for the Murray-Davies model, the solid reflectance entered into the models was increased due to the printing patch containing defects. Modelled and actual reflectance values of printing dots with similarly flawed structure were more likely to correspond to each other. This could be seen for midtones and shadows in Figure 4.45. The more coherent highlights had lower actual reflectance values which were not anticipated by the models.

Table 4.9: Comparison of model errors for Yule-Nielsen and Expanded Murray-Davies halftone models

Model	Expanded Murray-Davies		Yule-Nielsen	
	incl. 10% dots	excl. 10% dots	incl. 10% dots	excl. 10% dots
Data range				
Parameters	$v=0.5705; w=0$	$v=0.4711; w=0$	$n=1.4877$	$n=1.4101$
Error	0.0462	0.0405	0.0432	0.0381

4.4.2.5.2 Line Ruling of 150 lpi

At 150 lpi line ruling the modelled reflectance values showed similar trends to the ones at 100 lpi line ruling (Figure 4.49). The Murray-Davies and Noffke-Seymour models produced the largest error by significantly overestimating reflectance (Table 4.10). Beer's Law, the Expanded Murray-Davies and Yule-Nielsen models resulted in good fits of modelled and actual reflectance. Compared to the 100 lpi line ruling, Beer's Law was able to perform better with the 150 lpi data set, because all halftone dots retained a more consistent, less flawed structure approximating the sharp dot which

stands at the base of this model. Further, Beer's Law was the only model which resulted in significant variations of calculated reflectance values for "flat-" and "round-topped" plate materials (Figure 4.50). This was owed to the large deviation in the plate area coverage for different plate types which was entered into the equation, whereas the printed dots were more similar in area coverage and structure. The other four models employing actual printed area coverage showed little variance between plate types. It was particularly notable that the best fit of Beer's Law, the Expanded Murray-Davies and Yule-Nielsen models occurred for the midtones and shadows, while the reflectance of the highlights (about 15% actual area coverage) was almost always overestimated. An exclusion of these dots led to an improvement in model error (Table 4.10), as previously observed at 100 lpi line ruling.

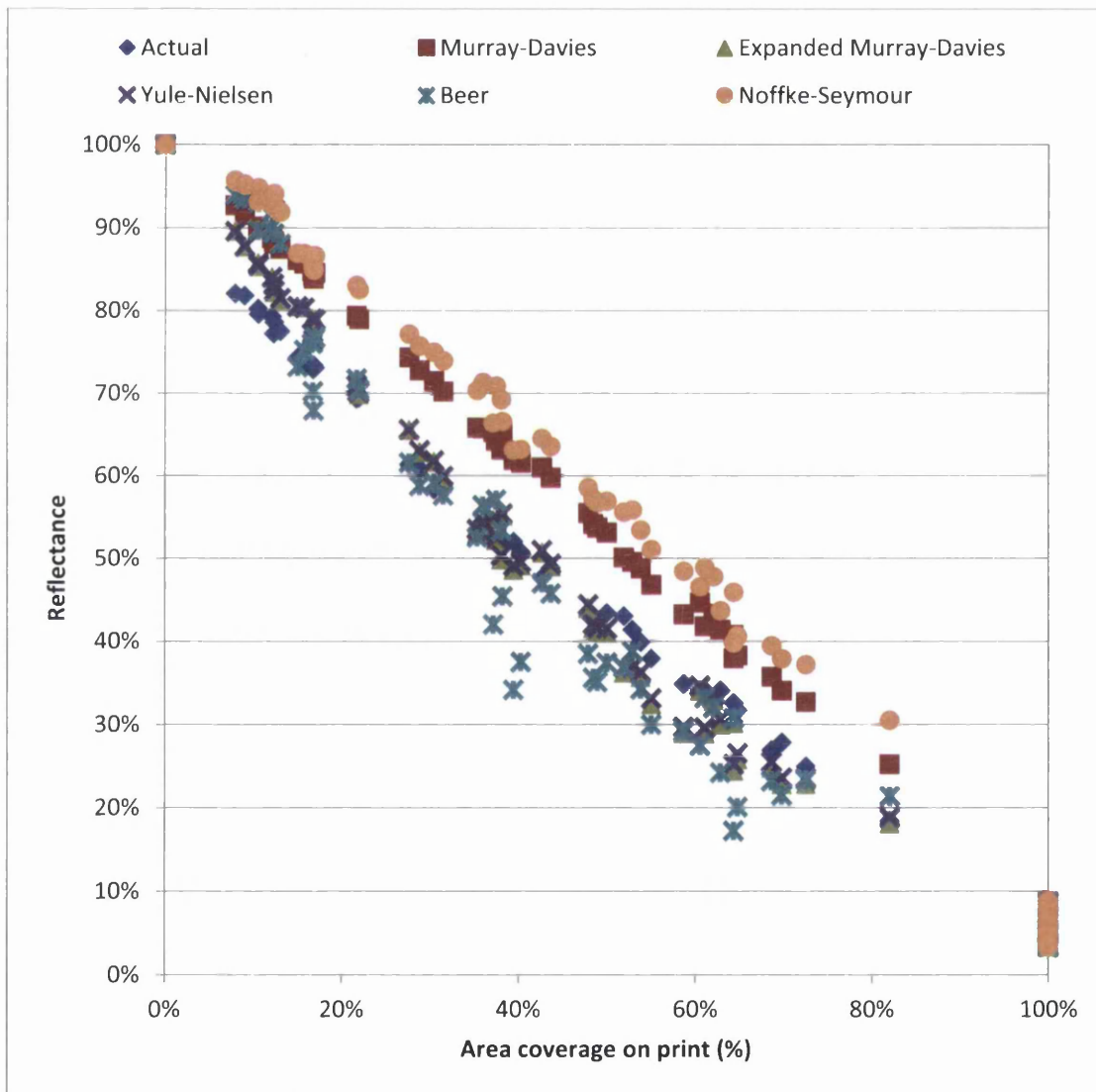


Figure 4.49: Comparison of actual and calculated reflectance at 150 lpi line ruling obtained from different halftone models (all plate materials under all printing conditions included)

Table 4.10: Comparison of model errors for different halftone models at 150 lpi line ruling

Model	Murray-Davies	Expanded Murray-Davies	Yule-Nielsen	Beer	Noffke-Seymour
incl. 10% dots					
Parameters	-	$v=0.8223; w=0$	$n=1.7314$	-	-
Error	0.1039	0.0411	0.0393	0.0746	0.1396
excl. 10% dots					
Parameters	-	$v=0.6761; w=0$	$n=1.6078$	-	-
Error	0.1034	0.0318	0.0296	0.0689	0.1412

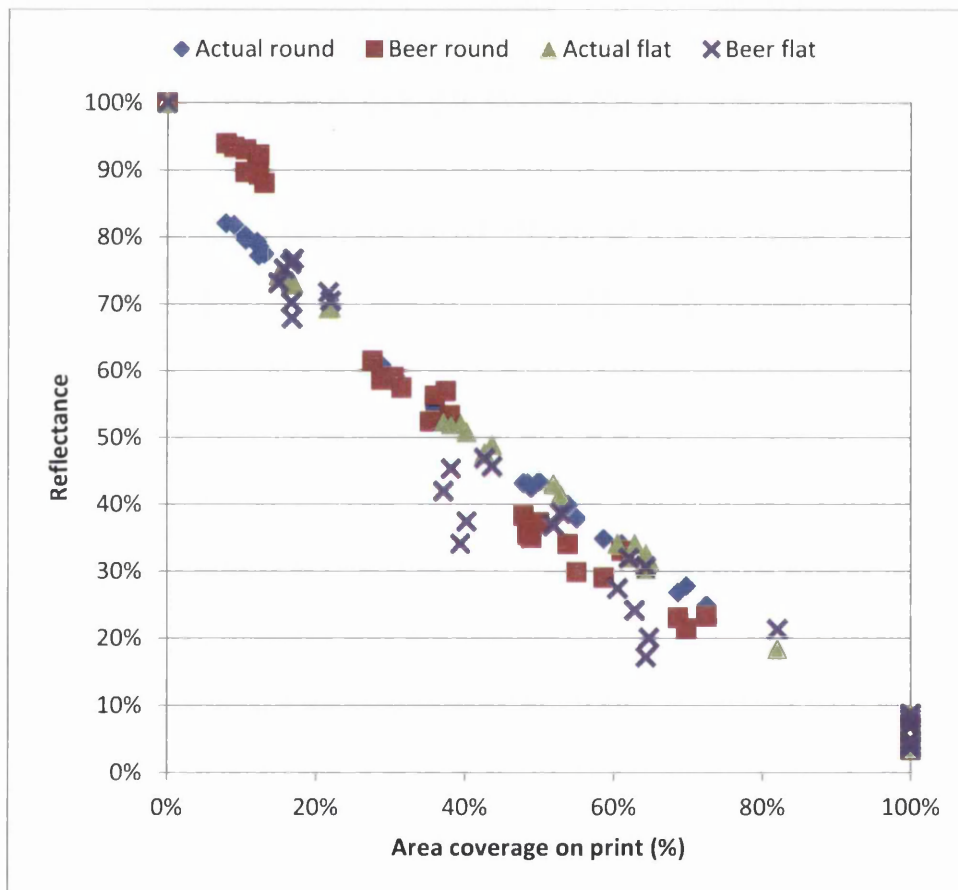


Figure 4.50: Comparison of actual and calculated reflectance obtained from Beer's Law for 150 lpi line ruling

The deviation in model fit for different halftone area coverages might have been based in the origin of the Murray-Davies model. The equation was developed to fit data obtained from the photoengraving process which features particular dot shapes across the halftone scale (Murray, 1936). There the highlight dots are mostly round, midtones are curvilinear quadrangles and shadows

framed round unprinted areas (Figure 4.51). Due to ink squeeze, the centre of the dots printed lighter than their perimeter, but for the calculations an average density was assumed for the entire dot. The dot structures observed in this trial were predominantly round in the highlights and midtones, and square in the shadows. Thus deviations caused by dot structure would have been expected to occur in the midtones and shadows, whereas they are most severe in the highlights.

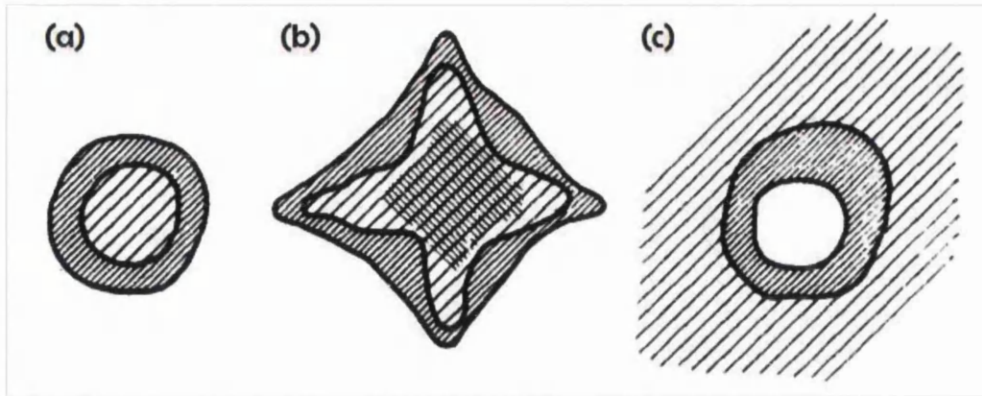


Figure 4.51: Printed dot structure of (a) highlights, (b) midtones and (c) shadows in photo-engraving where darker areas represent higher ink film thickness (Murray, 1936)

The halftone scale is divided into two or more different classes of dot structures – sharp highlights versus softer midtones and shadows (specifically: midtones with UCAs; midtones and shadows with UCAs and residual ink films; solids with UCAs). No differentiation of this or a similar kind is currently addressed in any halftone model. So far, alternative halftone models introduce expansions and additional parameters to the basic Murray-Davies equation which apply equally to the entire halftone scale. Neither had it been investigated whether it would be more appropriate to apply different halftones models or at least correction factors to selected ranges of the halftone scale.

The issue is hereby recommended for future research, as it holds particular industrial relevance in the form of improved models for more precise process control in graphic and functional device printing. The starting point of such research should be the validation of existing halftone models (selective popular models are reviewed for example by Kang (1999), Wyble and Berns (2000)) with empirical data obtained from samples printed under different conditions in the major printing processes. This will allow the identification of the halftone models which in general lack accuracy and those which perform well under particular conditions or for certain parts of the halftone scale. The reasons for the performance then have to be identified, e.g. whether the models simulate the underlying physical principles inappropriately or a difference in halftone dot structure exists across the halftone scale. In the former case the model equations would have to be adjusted or new

equations developed, whereas in the latter case different halftone models might have to be applied across the halftone scale. The new model solutions can then be validated against the empirical data and further changes made where necessary.

4.4.3 Conclusions

The plates produced by standard digital imaging technologies suffer severe coverage losses. The plates imaged with “flat-top” technologies almost achieved complete design fidelity, although the lower imaging resolution and SQUAREspot laser technology led to deviations in Kodak’s higher midtones and shadows. Furthermore, the ragged edges of the Kodak dots, which translated into severely destabilised edges of the printed dots, would leave this plate less suitable for the manufacturing of printed electronics (especially those orientated diagonally to the print direction) which requires stable, uniform ink films.

The “flat-top” imaging technologies resulted in concave dot tops. This was the predominant shape on all four plate types which renders top geometry independent of imaging technology. A new method for the quantification of the top geometry by cup depth was introduced and should be considered to be adopted within a standard for halftone characterisation. The Asahi and MacDermid plates led to higher dot gain attributed to increased ink buildup on the plate and ink squeeze on the prints, but achieved a more uniform ink distribution. The Kodak and MacDermid Lux plates resulted in less dot gain, yet suffered from more pronounced UCAs and unstable edges in the printed dots. This reduced the amount of ink transferred per unit area. The severity of printing defects increased with area coverage, printing speed and engagement for all plate types. The effect was reduced through the usage of finer line rulings on the printing plate.

For most of the criteria investigated a differentiation in results was possible between the two groups of printing plates, standard digital Asahi and MacDermid versus “flat-topped” MacDermid Lux and Kodak. This stood in contrast to the very similar cupping geometries of the latter three materials, a distinction which might have arisen from differences in the geometry of the cupping edge and dot shoulder. Due to the very high industrial relevance, this research question merits a further, more focussed investigation.

The ink distribution of the printed dots influenced the optical density of the prints. More stable and uniform printed dots increased the optical density. Therefore, the Asahi and MacDermid materials had a slight advantage over Kodak and MacDermid Lux. However, the latter two exhibited slightly improved agreement with the halftones models. The Murray-Davies model fitted the Kodak and

MacDermid Lux data better, because the defects found in their printed dots resembled the faults in the reference solids more closely. All five models investigated were found lacking in accuracy. The optimisation of equation parameters only achieved improved fit for subsets of data. One of the reasons identified is the existence of different classes of dots within the halftone scale – a problem which has not yet been addressed by any halftone model.

4.5 Closure

A study was conducted on the industrial-scale printing press T-Flex 508 to investigate the effect of different imaging technologies on the output quality of graphic halftone printing. Two plate sets imaged by standard digital technologies and two by “flat-top” technologies were included in the trial. Since the predominant top geometry identified on all plates was concave, the terms “flat-topped” and “round-topped” do not truly reflect the dot shape and are misleading. No imaging technology or plate material investigated exhibited ultimate superiority with regards to print quality. Each sample bore its particular advantages and disadvantages. The “flat-top” technologies produced dots closer to target size on plate and print. Yet, it was the standard digital plates which resulted in more stable, more uniform printed dots and higher optical density. Therefore, careful considerations are required to match a plate type to the desired quality output of each printing application.

Chapter 5 Meso-Patterns on Printing Plates

The previous chapter highlighted the recurring problem of defective UCAs in printed patches and its impact on process control through halftone models. Surface patterning of printing plates is claimed to prevent this type of defect (Miller and Zmetana, 2005) by pattern recesses functioning analogous to anilox cells (Samworth, 2001 and 2009; Kodak, 2010). Allegedly, the volume of ink transferred is raised and the ink film anchored more uniformly to the substrate. This work sought to gain a deeper insight into whether surface patterning affects ink transfer and, if so, which mechanism governs it, as well as how it depends on different material, printing and pattern parameters.

The investigation was divided into two parts: an initial study on a printability tester followed by a confirmation trial on an industrial printing press. Eleven different surface pattern designs, influenced by Stolt, Zwadlo and Rozzi's (2010) recommendation of regular geometries, were created in-house and explored in this chapter. The nominal width of the pattern features was $50\ \mu\text{m}$ and thereby slightly larger than the commercial microcell patterns ($\leq 25\ \mu\text{m}$) studied in the next chapter. For easier differentiation of the two different pattern scales, the former will be referred to as meso- and the latter as micro-patterns (Figure 5.1).

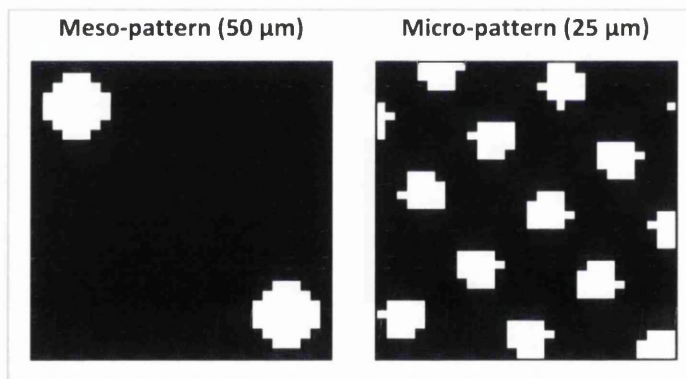


Figure 5.1: Schematic comparison of scale between meso- and micro-patterns (200x magnification)

MESO-PATTERN EFFECT USING A PRINTABILITY TESTER

The aim of this study was to establish whether surface patterning applied to solid printing areas of a flexographic printing plate has any effect on print quality. The print trial was carried out on the IGT-F1 printability tester using DoE and six different input variables, one of them being the pattern design.

MESO-PATTERN EFFECT USING AN INDUSTRIAL PRINTING PRESS

The study was repeated on the T-Flex 508 printing press. This served to confirm whether the findings obtained from prints made with the IGT-F1 were transferable to industrial-size setups.

5.1 Meso-Pattern Effect using a Printability Tester

This study was designed for the systematic investigation of surface patterning in conjunction with different printing parameters, substrate and plate materials. The main focus of this trial was to explore whether patterning had an effect on mean print density and uniformity. Closer inspection of the various types of printing defects produced provided the first information on the mechanisms of surface patterning in ink transfer.

5.1.1 Materials – Plates, Substrates and Inks

PLATES

The two plate materials employed were AFP-DSH and AWP-DEF (both by Asahi Photoproducts). These were chosen because the former has a solvent-washable composition, whereas the latter is water-washable. The two underlying polymer chemistries also had a direct effect on the plate surface energy and roughness (Table 5.1).

Table 5.1: Selected properties of plate materials used for meso-pattern study on the IGT-F1

Property	AFP-DSH	AWP-DEF
Washability	solvent	water
Surface roughness, R_a	154 nm	257 nm
Surface roughness, R_z	1.2 μm	3.0 μm
Steady-state surface energy	45.0 mN/m	38.1 mN/m
Hardness*	69 Shore A	70 Shore A
Thickness	1.7 mm	
* hardness according to publications by Asahi Photoproducts (2011 and 2011a)		

The plates were imaged with 12 printing patches in a standard digital process by V&W Graphics (Alford, UK). Every patch contained a different surface pattern each of which was designed to force changes in the ink splitting process and hence the ink transfer to the substrate. One of these patches remained without surface patterning and served as a solid area reference patch. The other eleven patches contained meso-patterns based on a nominal feature size of 50 μm (Figure 5.2 and Table 5.2). The hole and polka dot patterns were based on midtone and shadow halftone screens commonly found in flexography. The grid, hexagon and chequer patterns are stylised geometries based on these halftone screens. They served to observe the effect of edge geometry on ink transfer compared to the standard flexographic halftones. The intermittent tile and continuous line patterns at different orientations have been further stylised and simplified. Together with the two chequer

patterns they were introduced to investigate whether the directionality of patterns affects the ink transfer. The actual area of pattern features on the printing plates was captured with WLI to confirm compliance with the nominal design and will be discussed in section 5.1.4.1.

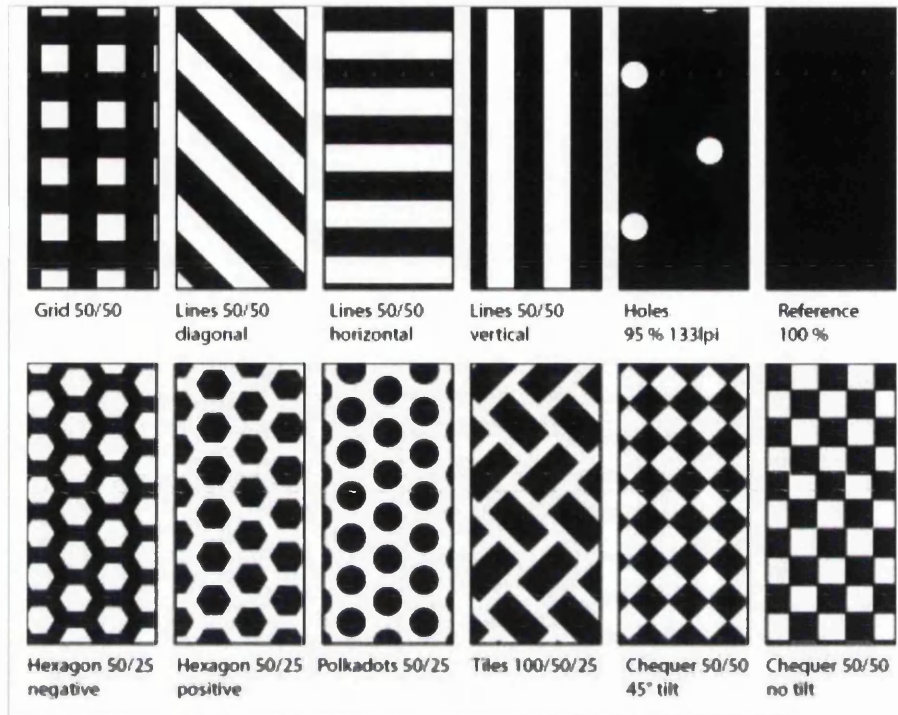


Figure 5.2: Illustrations of the 12 meso-patterns and reference solid (76x magnification)

Table 5.2: Specifications of meso-patterns

Surface pattern	Nominal pattern dimensions	Nominal area coverage (%)
Reference solid	-	100.0
95%	48 μm diameter/191 μm pitch	95.0
Vertical lines	50 μm track/50 μm gap	50.0
Horizontal lines		
Diagonal lines		
Grid	50 μm by 50 μm width/50 μm track	75.0
Chequer (no tilt)	50 μm by 50 μm width	50.0
Chequer (45° tilt)		
Tiles	100 μm by 50 μm width/25 μm gap	53.3
Polka dots	50 μm diameter/100 μm pitch	40.3
Positive hexagons	50 μm width/25 μm gap	44.5
Negative hexagons	50 μm width/25 μm track	55.5

SUBSTRATES

The substrates chosen were a coated paper APCO (Papierfabrik Scheufelen, Lenningen, Germany), denoted as APCO, and a highly absorbent paper Ford's Gold Medal (Arjo Wiggins Fine Papers, Manchester, UK), denoted as Ford. The two substrates were chosen, because they have significant differences in their material properties (Table 5.3).

Table 5.3: Material properties of substrates used for surface patterning studies on the IGT-F1

Property	APCO	Ford
Class	coated	uncoated, absorbent
Surface roughness, R_a	0.40 μm	4.16 μm
Surface roughness, R_z	4.89 μm	40.21 μm
Steady-state surface energy	35.6 mN/m	- *
<i>* not possible to determine surface energy of Ford due to very high absorbability</i>		

INK

Two fundamentally different ink systems with a distinct contrast in their rheological properties were chosen for the investigation of interaction effects with the surface patterns. The first ink was an in-house formulation on a water base. It contained 6% low-molecular polyvinyl alcohol, 0.5% surfactant "Tween 20" and 5 mg/l dye "Crystal violet" dissolved in phosphate-buffered saline solution. Its surface tension was 39.9 mN/m. Secondly, a commercial UV-curing ink FlexoCure Gemini (Flint Group UK, Wrexham, UK), colour cyan, with a surface tension of 37.0 mN/m was employed. The UV-curing ink is a typical flexographic ink, whereas the water-based formulation is representative of inks used for biomedical functional device printing. Since the print analysis is based on the optical properties of the inks, it would have been preferential to use two ink systems which achieve equal colour strength in print. However, in practice this is very difficult to match, and the investigative focus was placed on the rheological properties of the inks rather than their colour in order to cover the wide range of flexographic applications.

The ink viscosity characterisation was performed on the Bohlin rheometer (instrument settings according to Table 5.4 and Table 5.5). The water-based ink exhibited a nearly constant viscosity of about $6 \cdot 10^{-3}$ Pa·s at all strain rates and thereby can be considered to be Newtonian (Figure 5.3). The viscosity of the UV-curing ink was on average 120 times higher than for the water-based ink, but at around 0.8 Pa·s the ink could still be classed as a low-viscosity liquid. At higher shear rates it demonstrated slight shear-thinning properties, but was mostly Newtonian over the rates explored.

Table 5.4: Rheometer settings for ink pre-conditioning and measurement geometry (inks for IGT-F1 studies)

Pre-conditioning		Measurement geometry	
Type	controlled rate	Geometry	cone/plate
Shear strain rate	0.01 s ⁻¹	Cone (water-based ink) (UV-curing ink)	2° / 55 mm 4° / 40 mm
Time	60 s		
Equilibrium time	10		
Temperature	25°C (isothermal)	Gap size	150 μm

Table 5.5: Rheometer settings for ink viscosity determination (inks for IGT-F1 studies)

Viscosity measurement	
Temperature	25°C (isothermal)
Type	shear-controlled rate
Minimum shear strain rate	0.1 s ⁻¹
Maximum shear strain rate	100 s ⁻¹
Delay / integration time	5 s (decreasing time) / 5 s 10 s (decreasing time) / 10 s
(water-based ink) (UV-curing ink)	
Mode	up and down
Samples	21
Repeats	2

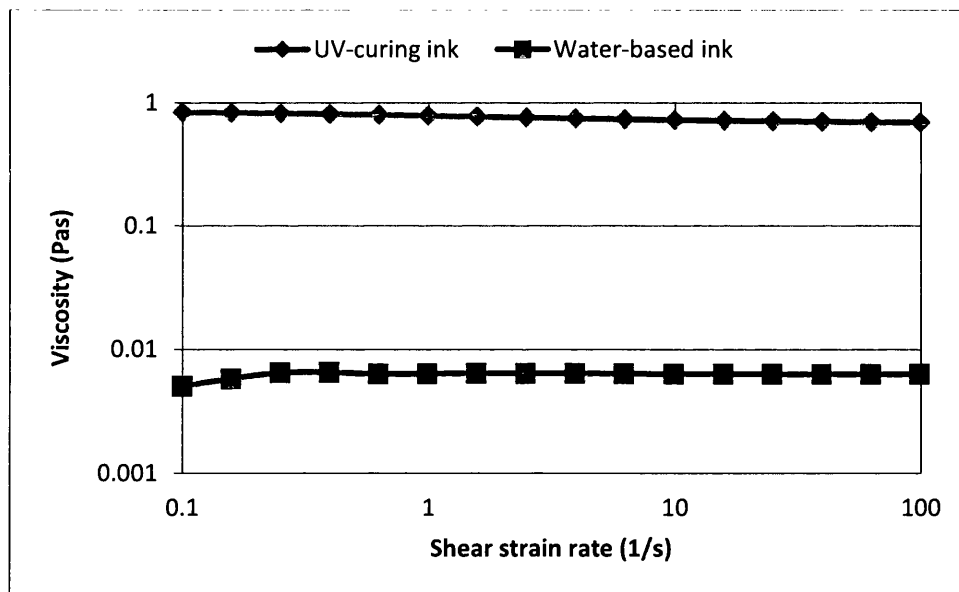


Figure 5.3: Viscosity of the UV-curing and water-based inks used for surface patterning studies on the IGT-F1

5.1.2 Printing

The parametric study was based on an exploration of six factors which were all adjustable at two levels (Figure 5.4). The resulting full-factorial plan consisted of 64 individual experimental points which took into account all possible parameter combinations. This allowed studying the effects of the main factors and their interactions on print density and uniformity obtained through image analysis. The three material parameters, namely printing plate, substrate and ink, have been described above. Printing was executed under varying conditions on the IGT-F1. The process parameters were anilox volume, printing force and speed. The two levels for all parameters are specified in Table 5.6. Based on a scoping study, the anilox force remained constant at 125 N, and one inking revolution of the anilox was used throughout. The water-based ink was air-dried after printing, whereas the UV-ink was cured on the Jenton conveyor unit.

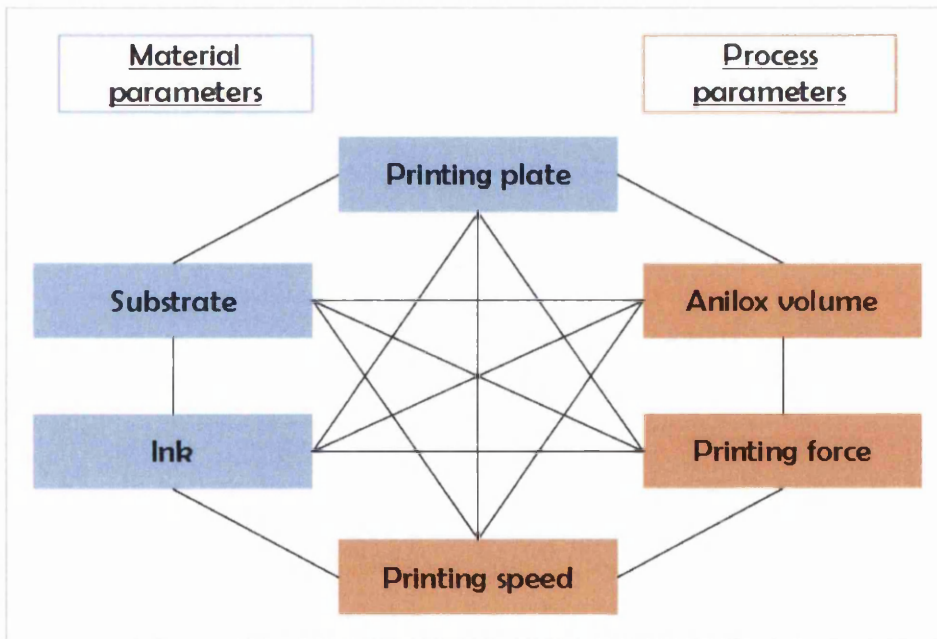


Figure 5.4: Parameters and their potential interactions in meso-pattern study on the IGT-F1

Table 5.6: Parameter levels for experimental plan of meso-pattern study on the IGT-F1

Factor	Lower level	Upper level
Plate material	AWP-DEF	AFP-DSH
Substrate	APCO – coated paper	Ford – uncoated, absorbent paper
Ink	UV-curing	water-based
Anilox volume	8 cm ³ /m ² (350 lpi)	12 cm ³ /m ² (300 lpi)
Printing force	50 N	150 N
Printing speed	0.2 m/s	0.8 m/s

Note: the analysis was conducted separately for each pattern geometry

5.1.3 Print Characterisation

5.1.3.1 Definition of Fingering Instabilities

This research has revealed fingering defects resulting from interfacial instabilities at the printing nip exit in all prints from the meso-pattern trials. Dependent on the scale of interest, fingering can lead to improved uniformity on a large scale while presenting transfer variation at the scale of the plate patterning that may be classed as a defect. In this section the terms for the different fingering instabilities are defined as they will be used in the further print analysis.

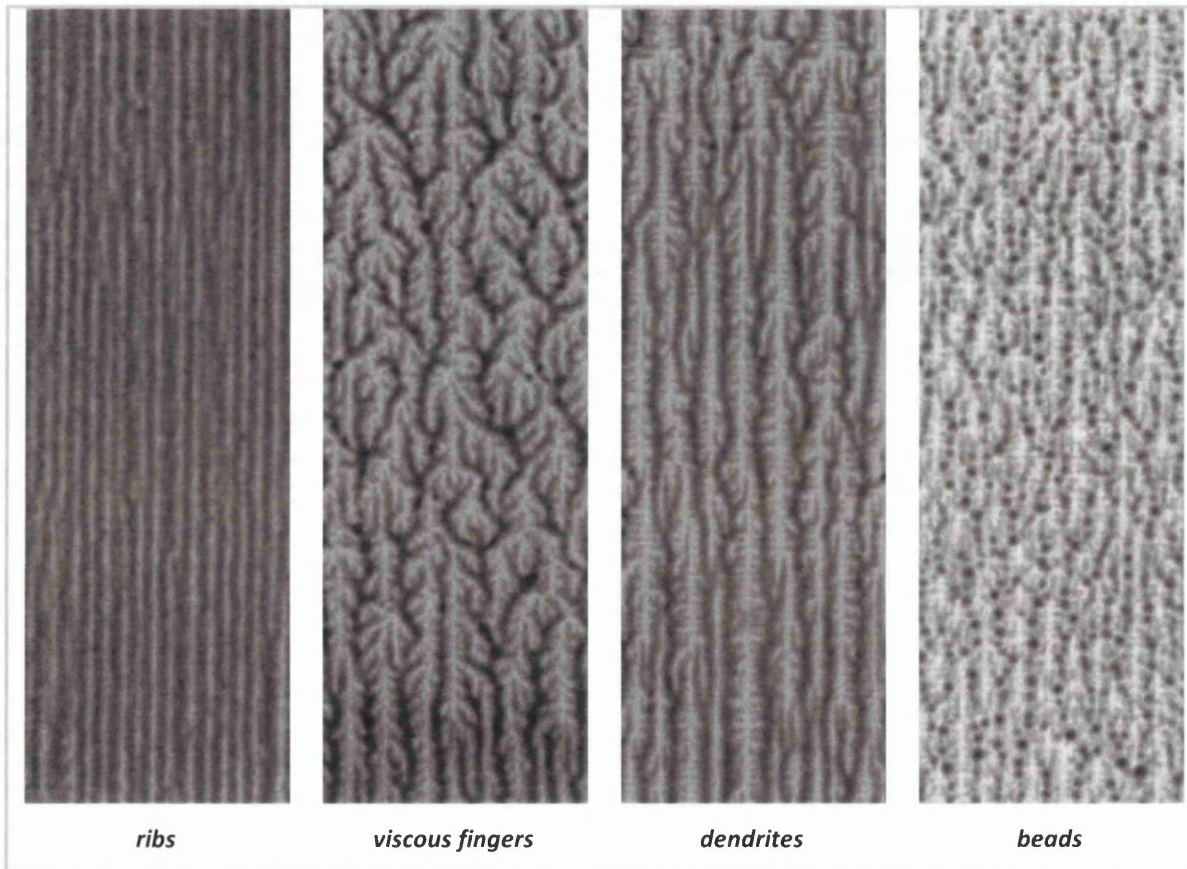


Figure 5.5: Classes of fingering instabilities as observed in the meso-pattern trials. Ribs separate steady-state discrete fingers. Finger tip bifurcation driven by external disturbance leads to viscous fingering. Stabilised bifurcation creates more ordered dendritic defects. Beads are potentially superimposed on fingering defects as result of dewetting. (7x magnification)

The fingering defects can be divided into four classes: beads, dendrites, viscous fingers and ribs (Figure 5.5). The latter three are classic examples of hydrodynamic instabilities of the Saffman-Taylor type (Ben-Jacob et al., 1985; McCloud and Maher, 1995). As has been explained in section 2.3.2.3, these instabilities can be created when a less viscous fluid invades a more viscous fluid along the paths of least resistance. A more viscous fluid would be able to shift the less viscous fluid while maintaining a uniform interface. (Fernando, 2012) In this work the printing ink was displaced by the

surrounding air at the nip exit between the printing plate and substrate. Depending on the conditions acting on the system, the ink meniscus in the nip might separate in a continuous stable fashion which does not lead to any defects. However, it is more likely that the meniscus is destabilised and air breaks through the interface nonuniformly.

The simplest pattern is the rib structure which can be interpreted as steady-state discrete fingers. The ribs are distributed evenly retaining a definite shape. However, if the initial finger tip is disturbed by external factors, it splits to form two fingers which propagate separately and in different directions. Over time the finger tips continue bifurcating. Some fingers will eventually die off, while others progress unhindered, creating the branched structure known as "viscous fingering". Ben-Jacob and colleagues (1985) suggest that viscous fingers transition to dendrites if the bifurcation stabilises under very large driving forces or in the presence of an anisotropic enclosing surface. Dendrites are characterised by a linear main stem from which smaller side branches protrude at a roughly normal angle.

The bead structure might not appear to fall into the category of Saffman-Taylor instabilities. But if a digital image of it is transformed from greyscale to black-and-white by thresholding, the underlying fingering instabilities (a mix of dendrites and viscous fingers) are revealed (Figure 5.6). The nature of the beads themselves is not entirely clear, but the following mechanism is proposed. It might be possible that the advancing air concentrates the ink at certain locations between adjacent fingers. The additional amounts of ink form liquid bridges between the printing plate and substrate at the nip exit where the liquid bridges are drawn out into filaments by the diverging cylinder surfaces. While the filaments are being stretched, further ink is pulled into the filament by dewetting the areas surrounding its contact zones at both cylinders. In this case, the dewetting might be aided by the difference between the ink surface tension (39.9 mN/m) and the substrate surface energy (35.6 mN/m) which indicates that the substrate is not easily wetted by the ink. Finally, the filament breaks, and the impression of a bead remains in its place. The other defects might not exhibit this feature, because the ink concentrations between fingers do not break up into filaments at the nip exit, but the ink film splits continuously with the advancing meniscus. Potential future studies of the issue could explore the effect of surface tension-surface energy combinations by using different test liquids, substrates and plate materials.

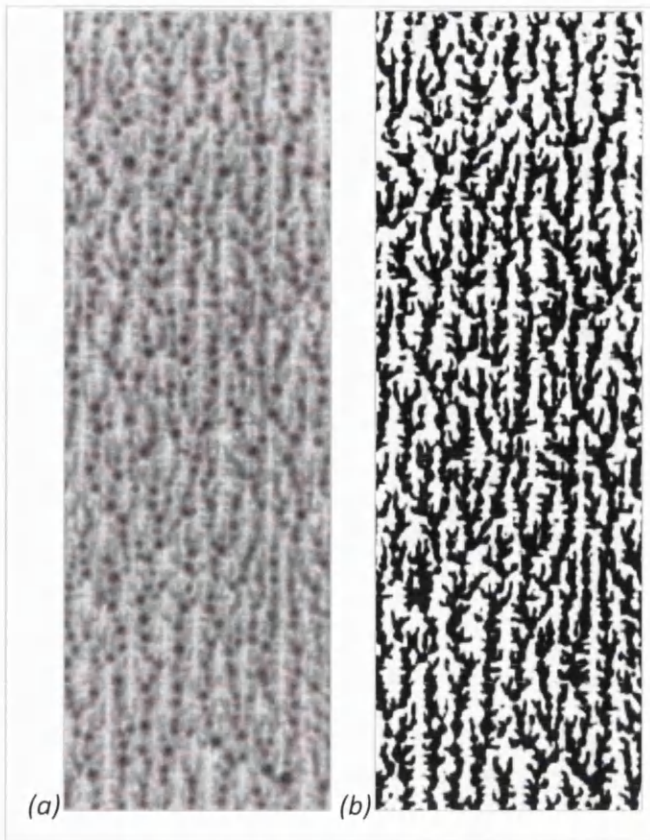


Figure 5.6: Revelation of fingering instabilities underneath bead pattern – (a) original image, (b) thresholded black-and-white image (7x magnification)

5.1.3.2 Introduction to DoE Analysis Approach

Quantitatively the fingering instabilities are defined through the uniformity parameter StDev (explained in section 3.5.5.2). The effects of material and process parameters on StDev are analysed using DoE. To gain a clear understanding of the challenges in the analysis approach employed in this and the following studies, the effect of a single process parameter change on print uniformity and density is demonstrated on two samples produced by the chequer pattern at 45° tilt using the water-based ink on the APCO substrate (Figure 5.7). Although the only process parameter altered was the printing force, significant difference in print density, uniformity and class of fingering instability can be observed in the image. This is reflected in the histogram of GSLs, resultant MGSL and StDev.

Discounting any other factors for this example, the effect (E) of printing force on MGSL is calculated as the difference in MGSLs observed at the two levels investigated. By increasing the force from 50N to 150N, the MGSL decreases by 14.3 GSLs ($E_{MGSL} = -14.3$) which is equivalent to a rise in print density and can be observed as a darker image. The effect of printing force on StDev is also a negative one ($E_{StDev} = -6.5$) describing that the StDev decreases due to improved print uniformity (also evident in the images).

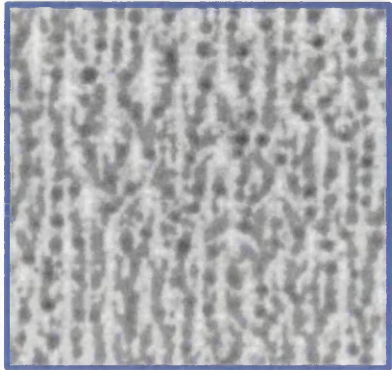
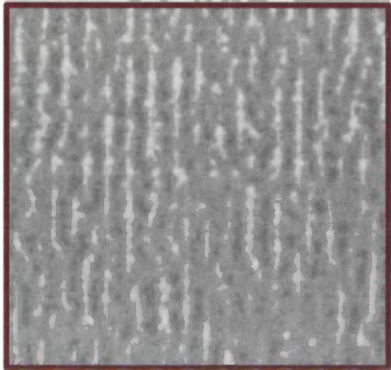
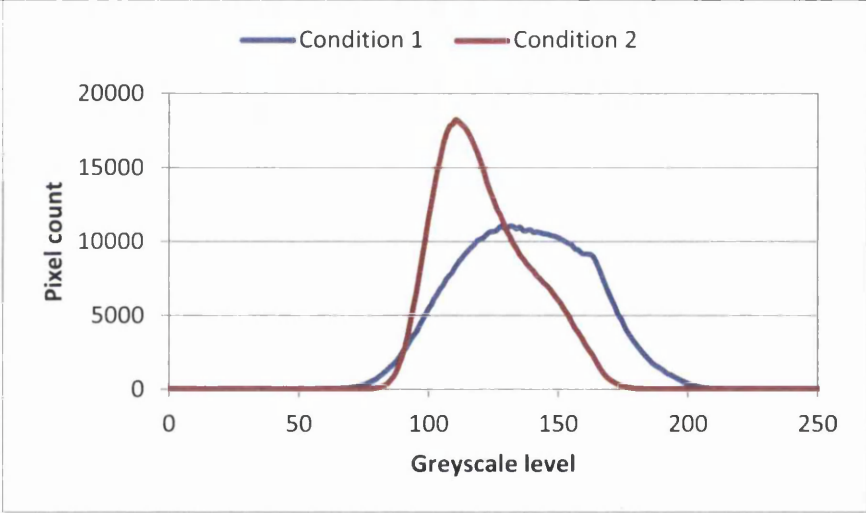
	Condition 1	Condition 2
Anilox volume	8 cm ³ /m ²	
Printing speed	0.8 m/s	
Printing force	50N	150N
Image (10x magnified)		
MGSL	134.9	120.6
StDev	24.1	17.6
Histogram		

Figure 5.7: Comparison of optical and histogram data for two print samples produced by checker pattern at 45° tilt

The full-factorial experimental plan this study was based on facilitated the exploration of 63 main factor and interaction effects for each of the surface patterns and the plain reference solid, revealing detailed information about the underlying processes of ink transfer. An exemplary data set of effects referring to the MGSL of the plain solid reference is provided in Appendix A.8.⁶ It illustrates that the significance of effects decreases with increasing number of factors participating in an interaction. Four-factor and higher interaction effects are usually negligible. Therefore, the discussion will be limited to significant main and lower order interaction effects which are the most relevant to this study.

⁶ The complete effect data for MGSL and StDev of all surface patterns, as well as the uncertainty of the effects stating their significance, is provided on the CD-ROM attached to this thesis.

5.1.4 Results and Discussions

5.1.4.1 Plate Characterisation

The image analysis of the plates' WLI data revealed significant losses in area coverage due to oxygen inhibition of the polymerisation process. The AFP-DSH material (Figure 5.8) was seemingly more affected with area coverage losses between 12% and 47% than the AWP-DEF plate (Figure 5.9) with coverage losses between 4% and 27%. The considerable difference between the plates is attributed to their surface shape and roughness (Figure 5.10). The rougher AWP-DEF material scattered the incident beam of light which allowed data capturing on the shoulders of the printing features that would otherwise be too steep to be measured. Furthermore, the feature tops were quite large and dome-shaped with gently declining slopes which provided a larger area suitable for data capture. On the smoother AFP-DSH material minimal light scattering took place and only areas perpendicular to and on the centreline of the incident beam were recognised. The sharply truncated feature tops were significantly smaller than on the AFP-DSH plate and provided less area for data capture. The steep feature shoulders became invisible to the microscope, thus data points missing from the shoulder region impede the quantification of the precise shape of the dot and how it may contribute to the surface from which ink is transferred.

Overall, all plate images differed strongly from the nominal artwork for both plate materials. For example, the corners of the shapes for the grid, tile and hexagon patterns were missing. The features became more rounded, and the gaps between them widened. A complete list of images (WLI data prepared for image analysis) can be found in Appendix A.7. These shapes, as measured, were used in the print analysis.

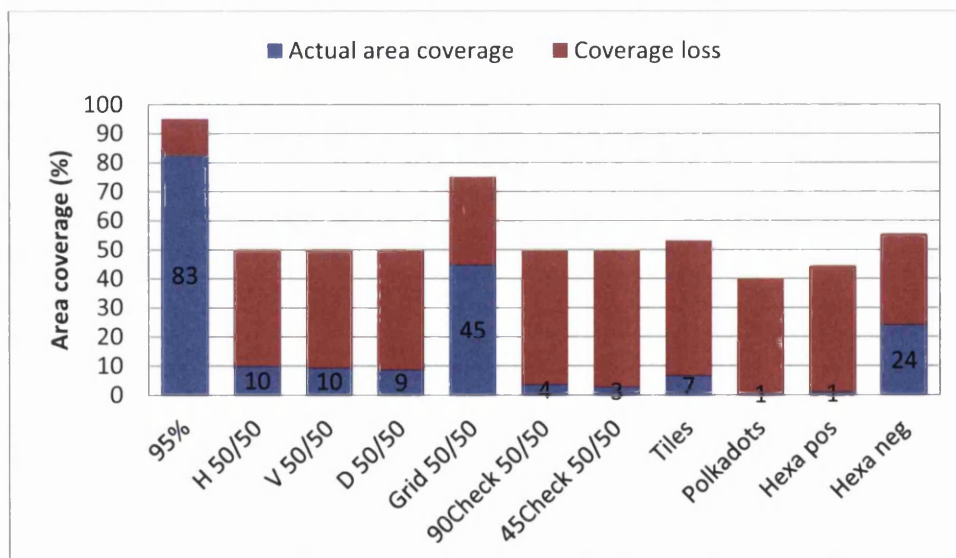


Figure 5.8: Actual area coverage of meso-patterns on printing plate and coverage loss compared to the artwork for the AFP-DSH plate

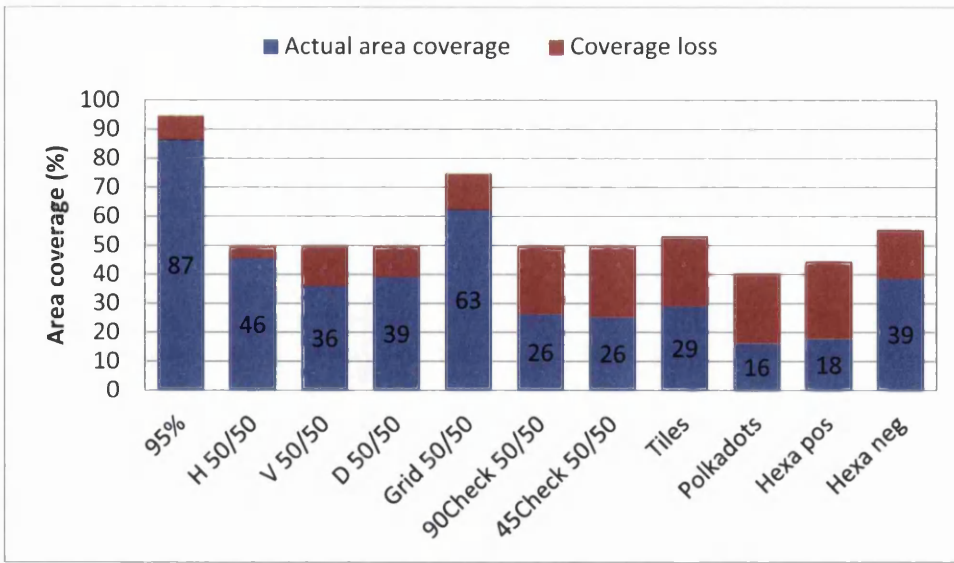


Figure 5.9: Actual area coverage of meso-patterns on printing plate and coverage loss compared to the artwork for the AWP-DEF plate

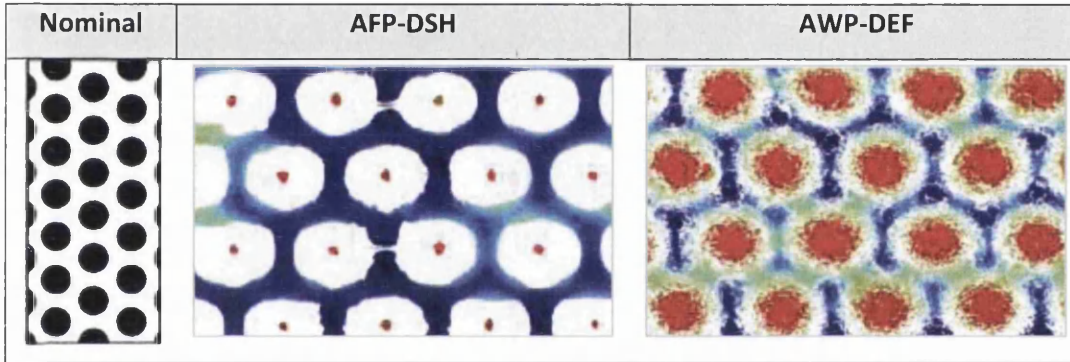


Figure 5.10: Comparison of nominal polka dot design and plate geometry captured by WLI (red data points correspond to raised areas from which will be printed; 76x pattern magnification; 180x sample magnification)

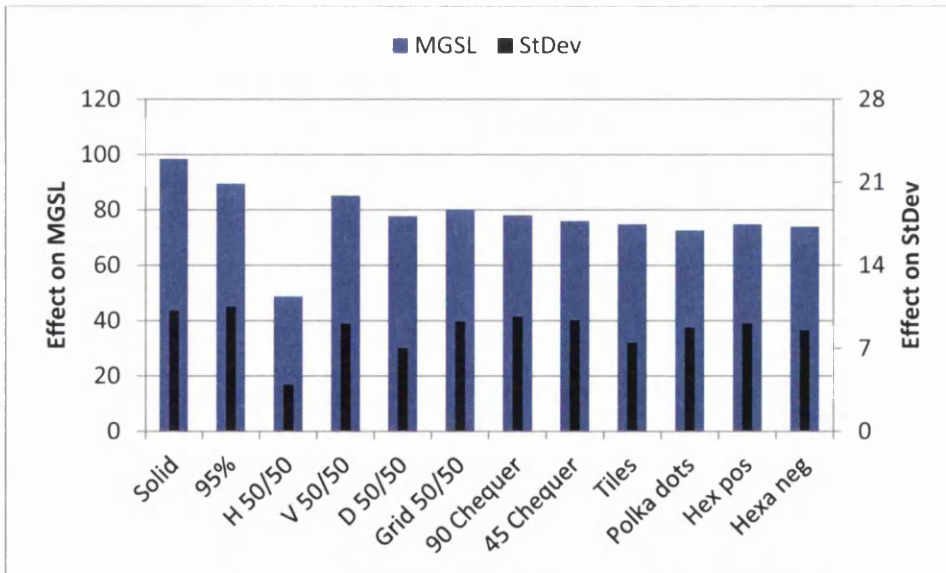


Figure 5.11: Main effect of ink type on MGSL and StDev compared for plain solid reference and all surface patterns



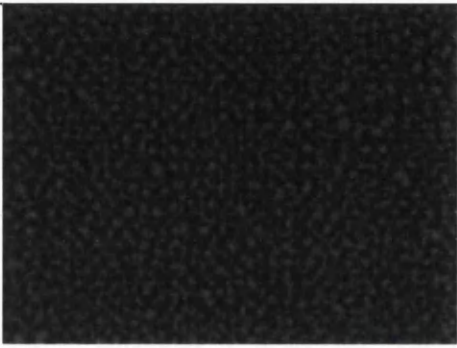

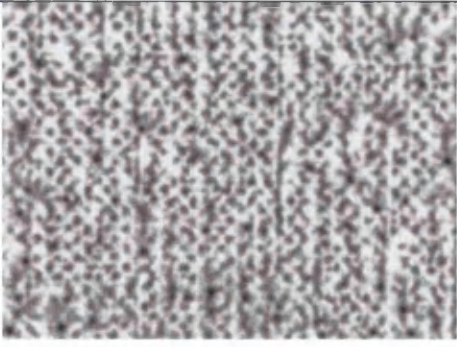
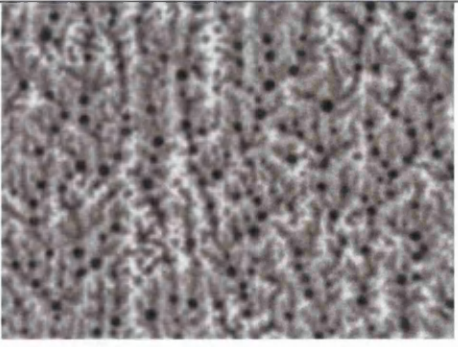


UV-curing ink		Anilox volume	
		8 cm ³ /m ²	12 cm ³ /m ²
Printing force	50 N		
	150 N		
Water-based ink		Anilox volume	
		8 cm ³ /m ²	12 cm ³ /m ²
Printing force	50 N		
	150 N		

Figure 5.12: Nonuniformity of ink films printed with polka dot pattern using different inks and printing conditions (AFP-DSH plate, APCO substrate, low printing speed). At low anilox volume and printing force, areas of missing ink can be observed for both ink types. For all the other printing conditions, the UV-curing ink achieves good area coverage which is reflected in improved optical density and print uniformity. On the other hand the uniformity of water-based prints decreases significantly due to the occurrence of fingering instabilities under high printing force and anilox volume. (6x magnification)

5.1.4.2 Effect of Ink Type

Figure 5.11 shows the main effect of the ink type on MGSL and StDev. When compared with all other effects that will be presented below, this showed the most significant influence on these output parameters for the plain solid reference and all surface patterns. As expected by their different colour strengths, changing from the UV-curing to the water-based ink increased the MGSL by over 70 levels for most printing patches, because the rich blue pigmentation of the UV-ink created a much higher opacity than the transparent dye in the water-based ink. At the same time, the higher StDev for the water-based ink indicated a drastic decrease in print uniformity resulting from printed patterns within the ink films on all substrates which are associated with fingering instabilities (Figure 5.12).

5.1.4.3 Effect of Substrate Type

Figure 5.13 shows the effect on MGSL and StDev when the substrate is changed from APCO to Ford. Out of all the effects presented in this subchapter, the substrate type had the smallest influence on MGSL, but was important for StDev. The very high surface roughness of the Ford paper provided less contact area for the ink and allowed only partial ink transfer to the raised parts of the substrate (Holmvall et al., 2011). The substrate recesses remained ink-free, thus increasing MGSL and StDev.

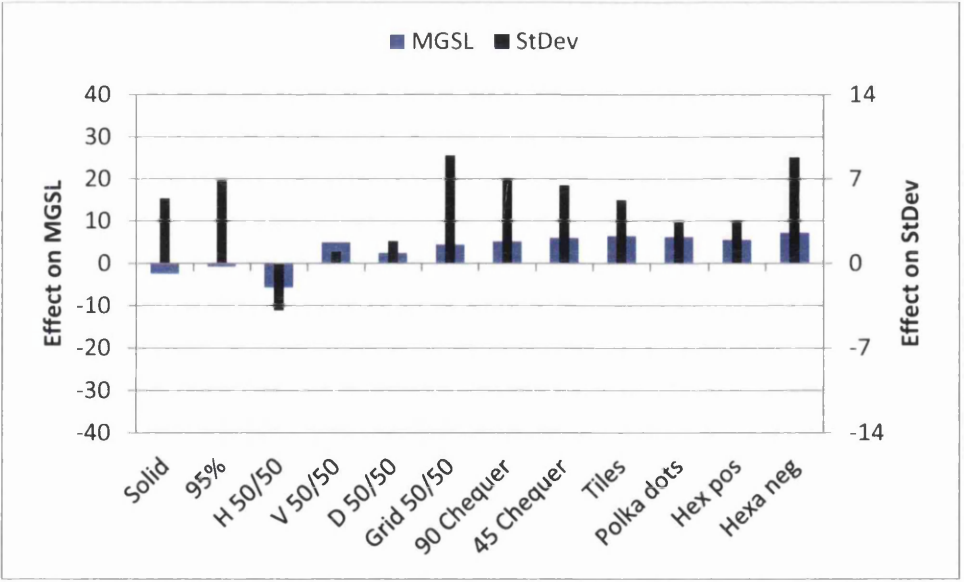


Figure 5.13: Main effect of substrate type on MGSL and StDev compared for plain solid reference and all surface patterns

In conjunction with the ink type, a strong negative interaction effect was observed ($E_{MGSL} = -9.7$ and $E_{StDev} = -5.1$ on average). This implies that even though individually Ford paper and water-based ink hampered print quality, together these trends were moderated. The reason for this was that the low-viscosity water-based ink was readily absorbed by the Ford paper, thereby spreading from the peaks of the surface into the valleys and covering more of the substrate. The more viscous UV-ink failed to cover all of substrate, as it remained on the top of the paper fibres.

The contribution to the calculation of the main substrate effect by those individual experiments which benefitted from the interaction between water-based ink and Ford substrate was very large for certain surface patterns. Thus, an overall negative MGSL main effect was achieved for the plain solid reference, 95% and horizontal line patterns. The uniformity of prints produced by the horizontal line pattern improved in particular with this ink-substrate combination, because the pronounced printing defects formed by the water-based ink on APCO could not evolve on Ford. This was attributed to the fast ink absorption into the substrate and its unavailability for the formation of fingering instabilities at the printing nip exit.

5.1.4.4 Effect of Plate Material

The change in plate material from AWP-DEF to AFP-DSH had a small positive effect on MGSL, but resulted in very large StDev effects for some surface patterns (Figure 5.14). As both plates had the same thickness and hardness, these material properties were ruled out as causes for the difference.

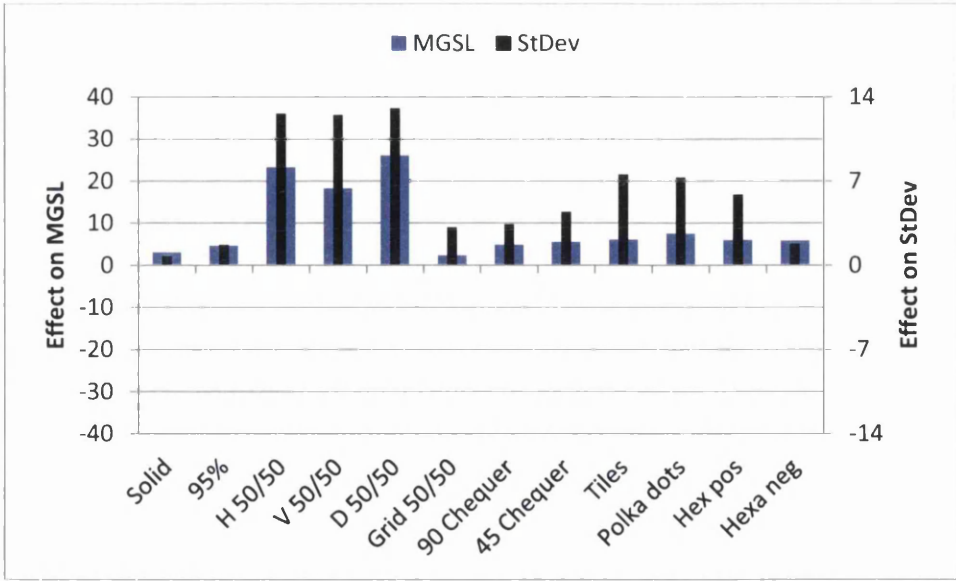


Figure 5.14: Main effect of plate type on MGSL and StDev compared for plain solid reference and all surface patterns

As identified in Table 5.1, Figure 5.8 and Figure 5.9, the other properties to consider were surface energy and roughness as well as area coverage. For successful ink transfer to take place in the printing press, the printing plate should have a higher surface energy than the ink, but a lower surface energy than the substrate (Thompson, 1998). Noting surface energy, the AFP-DSH was more likely to be wetted with ink from the anilox roll. However, the surface energy was determined using the static contact angle which does not reflect the highly dynamic conditions in the printing press. Studies suggests that printing speed and pressure affect the influence of surface energy on ink transfer (Chadov and Yakhnin, 1988; Liu and Shen, 2008), but this could not be explored further within the scope of this work.

With regard to image transfer, the lower surface energy of AWP-DEF might have been compensated for by its larger planar surface area and roughness. The plate characterisation (Figure 5.8 and Figure 5.9) showed higher area coverage for the AWP-DEF which would translate directly into a larger contact area between the ink and substrate. More extensive ink film transfer in general results in lower MGSL. The influence of the lack of area coverage on MGSL was observable for the line, tile, polka dot and positive hexagon patterns on AFP-DSH in particular (Figure 5.14). This was accompanied by a rise in StDev, because the smaller pattern features did not carry sufficient amounts of ink and were spaced too far apart in order to create closed ink films by coalescence resulting in print nonuniformity.

The increased surface roughness on AWP-DEF (Table 5.1) potentially served a dual purpose. Firstly, it increased the contact area on which ink could be received from the anilox, thereby raising the plate's ink-carrying capability and the amount of ink transferred in the printing process. Secondly, it might have acted as a surface patterning on the nano-scale improving print uniformity by raising the anisotropy of the printing surface. The anisotropy affected the transition between the regimes of different defect dynamics thereby producing fingering with the AWP-DEF plate which remained similar in scale and visually unobtrusive for the majority of printing conditions and surface patterns (Figure 5.15). (Ben-Jacob et al., 1985; McCloud and Maher, 1995)

The AFP-DSH plate on the other hand produced a wide range of striking printing defects which had a detrimental influence on StDev (refer to Figure 5.16 for an example of the chequer pattern at 45° tilt and to Appendix A.9 for the chequer pattern without tilt together with the polka dot pattern which are representative of the range of fingering patterns produced by all meso-patterns on the AFP-DSH plate).

		Speed = 0.2 m/s		Speed = 0.8 m/s	
		Force = 50 N	Force = 150 N	Force = 50 N	Force = 150 N
Anilox volume: 8 cm ³ /m ²					
Anilox volume: 12 cm ³ /m ²					

Figure 5.15: Chequer pattern at 45° tilt on AWP-DEF plate material. Little change between fingering defect regimes with printing conditions observed for water-based ink on APCO substrate (7x magnification)

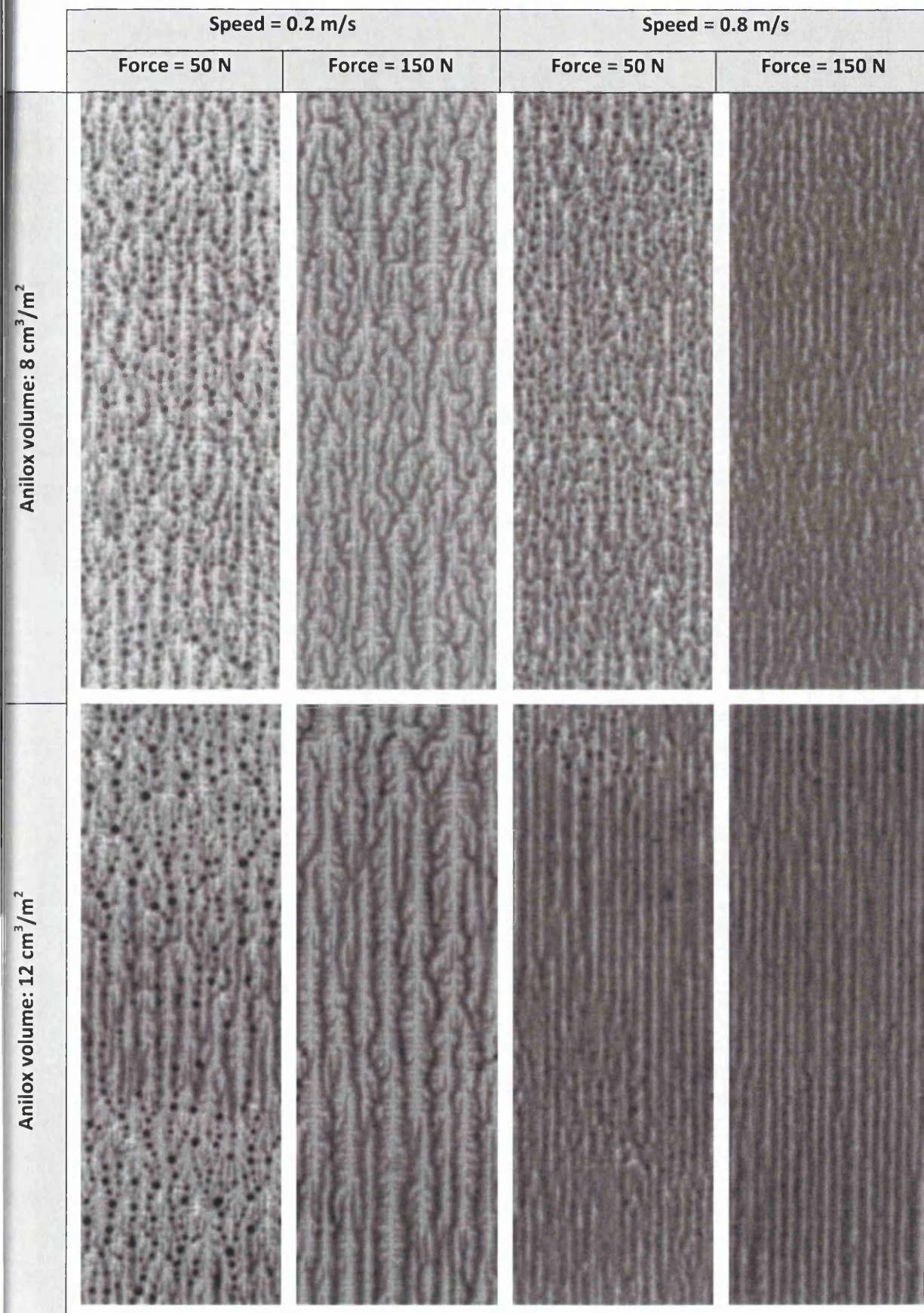


Figure 5.16: Chequer pattern at 45° tilt on AWP-DEF plate material. Strong change between fingering defect regimes with printing conditions observed for water-based ink on APCO substrate (7x magnification)

5.1.4.5 Effect of Anilox Volume

The second largest influence on MGSL was the anilox volume (Figure 5.17). More ink supplied by the anilox led consistently to an increase in the amount of ink transferred, and higher ink film thicknesses appeared darker (Damroth et al., 1996; Lindholm et al., 1996; Fouché and Blayo, 2001; S. Hamblyn, 2004; Beynon, 2007; Cherry, 2007). Furthermore, with rising ink film thickness the opacity of the ink layer increased and the contrast between unevenly printed areas diminished.

The performance of the AFP-DSH plate was improved by interaction with the higher anilox volume which was attributed to a proportionally larger increase in ink transfer compared with the AWP-DEF plate. This might have been caused by ink migration onto the feature shoulders which then acted similar to an increase in area coverage of the plate. This could be investigated in future trials by capturing images of the plate before and after printing, similar to the work done during earlier scoping trials (refer to Figure 4.32).

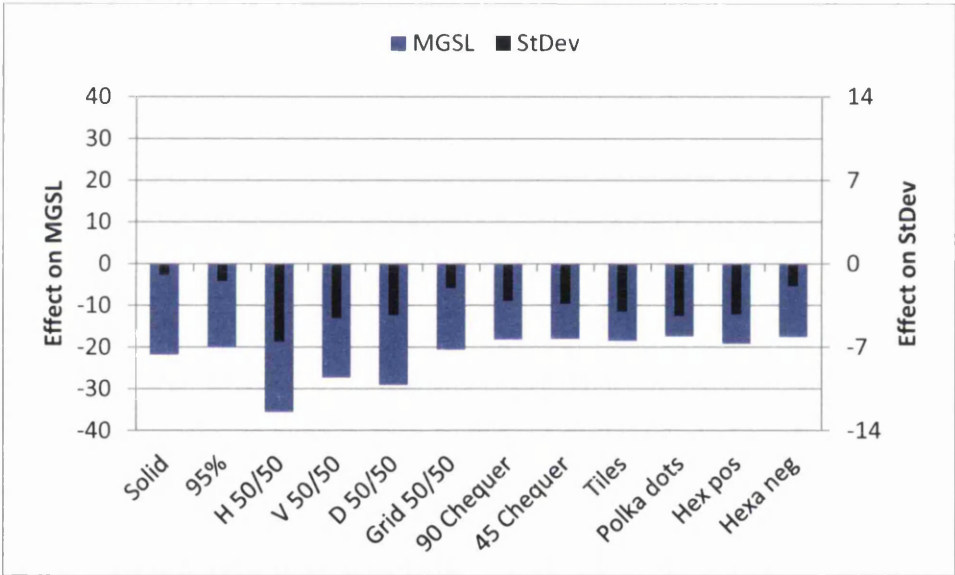


Figure 5.17: Main effect of anilox volume on MGSL and StDev compared for plain solid reference and all surface patterns

5.1.4.6 Effect of Printing Force

Increasing the print force improved the ink transfer as indicated by decreasing MGSL (Figure 5.18) (Bohan et al., 2003; Johnson et al., 2003; S. Hamblyn, 2004; Beynon, 2007; Cherry, 2007; Holmvall and Uesaka, 2008a) and a number of mechanisms can contribute to this. At higher force the printing plate may mould more closely to the substrate and increased the contact area. At the same time for a porous but incompressible substrate, potentially more ink is impressed into the substrate and immobilised, becoming independent from the ink split ratio between the substrate and printing

plate. Furthermore, on Ford paper a negative interaction effect may take place, attributed to the compression and smoothing of the substrate under higher force. This will not only increase the contact area, but also promote the capillary action to take up more ink into the bulk of the substrate.

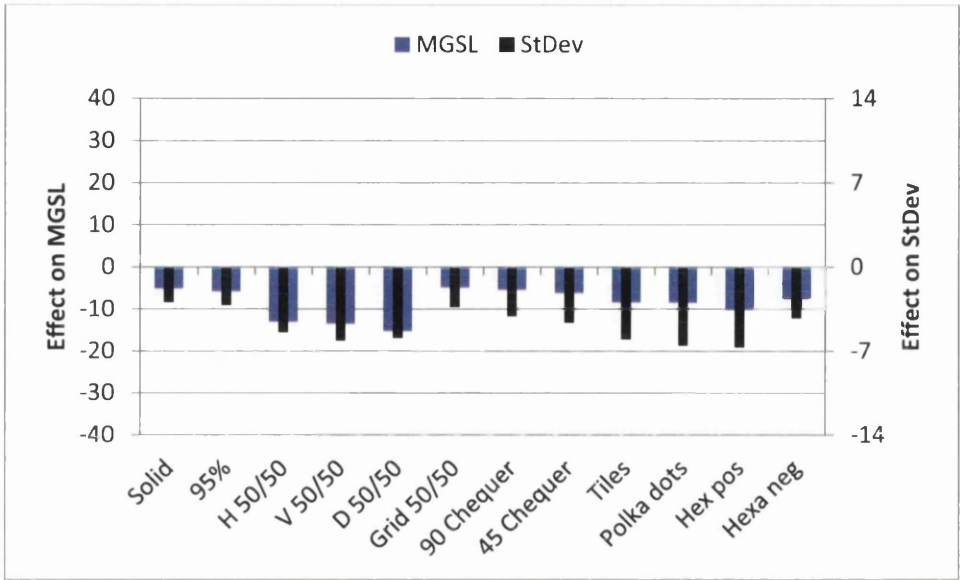


Figure 5.18: Main effect of printing force on MGSL and StDev compared for plain solid reference and all surface patterns

While noting the comments in the paragraph above, the force increase aided print uniformity in several ways. Firstly, the rise in contact area decreased the portion of non-printed substrate. Secondly, lateral ink flow and coalescence to closed ink films was encouraged. However, the printing force affects the final ink splitting process and manifests itself in various types of printed patterns, in particular for prints with water-based ink (Figure 5.12).

It is possible that the reduction in nip height under higher printing force affects the hydrodynamic stability of the ink meniscus at the nip exit. A thinner gap is thought to increase the frequency at which fingering patterns occur (Voß, 2002; Bornemann; 2013) which will result in a perceivable improvement in print uniformity. Although a reduction in StDev was observed for higher printing forces in this trial, a frequency analysis of the prints to confirm the correlation of printing force, finger frequency and print uniformity was not part of this work. However, the prints indicate that the uniformity improvement results from a change in printed pattern type with printing force rather than the increase in finger frequency (refer to Figure 5.16).

5.1.4.7 Effect of Printing Speed

Previous investigations found that the ink transfer decreased at higher speeds (Damroth et al., 1996; Fouché and Blayo, 2001; Johnson et al., 2003; S. Hamblyn, 2004; Cherry, 2007). This was attributed to a hampered filling of the anilox cells with ink and a less favourable ink splitting ratio between the plate and substrate. In this investigation the increase in printing speed had a negative effect in all but two cases (Figure 5.19), implying that more ink was transferred.

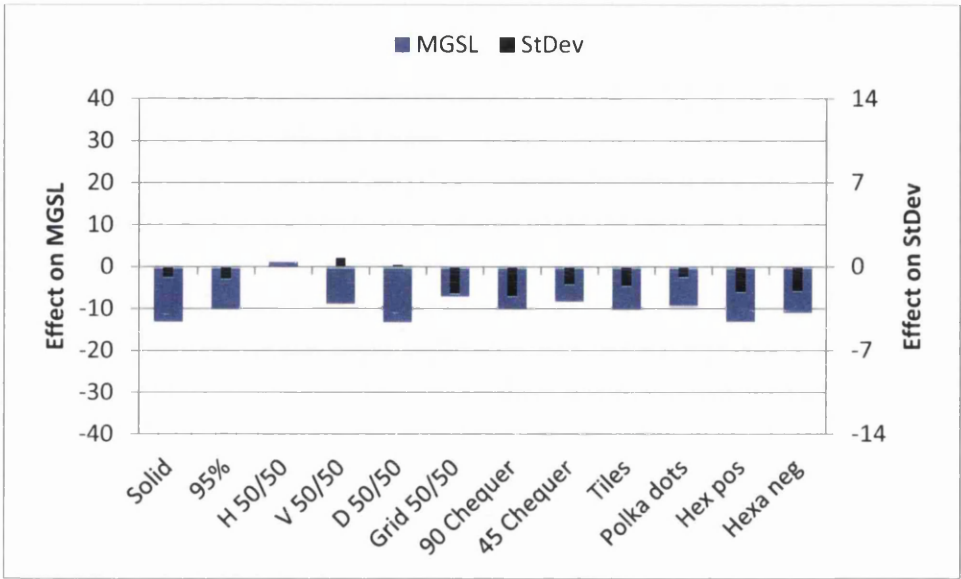


Figure 5.19: Main effect of printing speed on MGSL and StDev compared for plain solid reference and all surface patterns

The same effect was observed in the trial on the IGT-F1 discussed in section 6.1, as well as by Quinn (1997) and Olsson (2007). On all three occasions printability testers were used. This suggests that the particular construction of the testers (open doctoring systems) causes a noise factor which influences the calculated speed effect on MGSL and StDev. Through hydrodynamic action, it is possible that the doctor blade was deflected during rotation of the anilox cylinder, where increasing printing speed leads to higher force levels between the doctor blade and anilox. This will in return result in a gap change through blade deflection, thereby allowing more ink to pass under the doctor blade. The availability of different levels of ink at the printing nip exit will impact on the critical capillary number (Equation 2.11) and the ink splitting process which may create different fingering patterns as shown in Figure 5.16 and Appendix A.8. The change in printed pattern characteristics was in agreement with the literature that suggests an increasing dominant frequency of fingering instabilities at higher speed (Voß, 2002; Bornemann, 2013). In the prints from this trial, smaller pattern structures were also observed with increasing speed which led to a more homogeneous appearance recorded as a reduction in StDev.

An improvement in print density and uniformity with speed was more notable for the water-based ink. This was attributed to its low viscosity which may in turn allow better filling of the anilox cells even at higher speed. The more viscous UV-ink requires more time to invade and evacuate the anilox cells, thereby performing less well at increased speed. However, further work is required to gain a clear insight into the mechanisms that are present.

The combinations of printing conditions (anilox volume, printing force and speed) lead to distinctive regimes for the formation of different types of fingering instabilities. The sensitivity of fingering defects to printing conditions is discussed here using the example of the chequer pattern at 45° tilt printed with water-based ink on the APCO substrate using the AFP-DSH plate material (Figure 5.16). At low printing force and anilox volume, the printing speed had little effect on the type of fingering defect (beads in both cases), but increased the finger frequency. At higher printing force, two completely different classes of fingering instabilities evolved dependent on printing speed. Low speed led to dendrites, whereas high speed resulted in ribs (the same type of pattern was observed for low and high anilox volume). Again the finger frequency increased with speed. The anilox volume had no effect at higher printing force, but led to a gradual transition between defect regimes (Sinha and Tarafdar, 2009) for the prints produced at low printing force and high anilox volume. The tops and the bottoms of the printed patches still exhibit beads (or at least traces thereof), while the centre already shows the new patterns of dendrites or ribs which are characteristic of the regimes otherwise observed at higher printing force. This suggests that the regime transition is force-driven and the anilox volume affects the local pressure in the printing nip. Small variations in the printing conditions have a large impact on the fingering instability created.

5.1.4.8 Effect of Surface Patterning

Compared to the material and process parameters, the surface patterns had a more subtle effect on the values of MGSL and StDev (Figure 5.20). With the exception of the line patterns which hampered MGSL and StDev severely, all surface patterns increased print density, but aggravated uniformity. It has been suggested that surface patterns act similar to anilox rolls in carrying additional ink in the pattern recesses (Samworth, 2001). This would increase the ink volume supplied compared to the plain solid reference. Differences were observed for UV-curing and water-based ink.

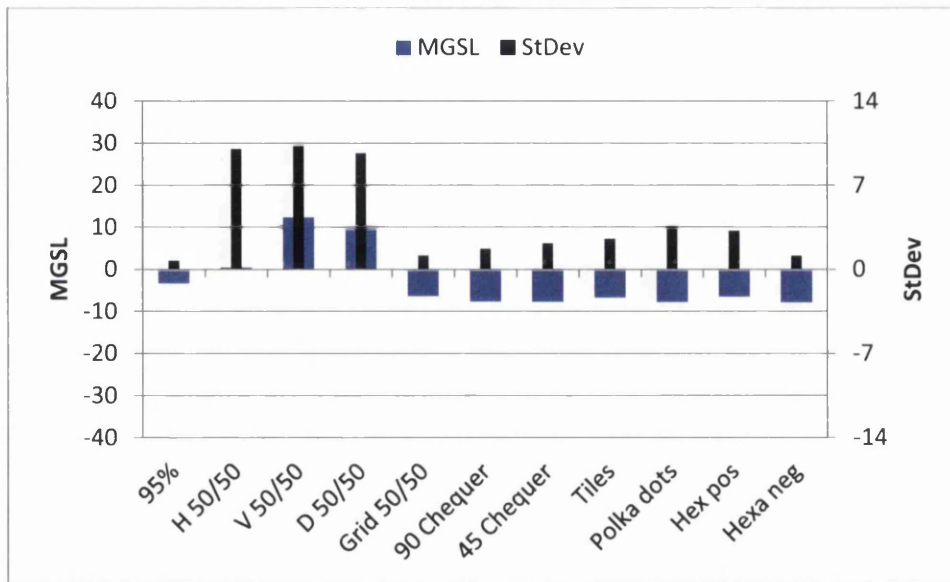


Figure 5.20: Main effect of surface patterning on MGSL and StDev for all surface patterns compared to the plain solid reference

Images of the prints produced with UV-curing ink at low printing pressure and low anilox volume show that partial ink films with individual pattern features have been reproduced (Figure 5.12). Increasing the anilox volume and printing pressure respectively leads to an increase in closed film area which suggests two different mechanisms. The first proposed mechanisms sees the larger anilox volume supply more ink causing flooding of the pattern recesses with ink and consequently additional ink transfer from non-printing areas on the plate. That would mean pattern recesses act like anilox cells under certain process conditions.

The second proposed mechanism is instigated by the printing force. If the UV-ink is only deposited on the printing features, but not in the recesses, it is necessary for the formation of closed, homogenous printed areas to squeeze the ink out from underneath the features and into the gap between where it coalesces with the adjacent ink films. If the gap between features is too wide or the ink volume available not large enough, the ink squeeze is insufficient. Consequently, the ink films do not connect and the substrate remains visible, disturbing print uniformity. If the printing force is too high, all the ink might be squeezed out from under the pattern feature, thereby creating a lighter impression in its place on the print. The hypothesis of the second mechanism is supported by the MGSL and StDev data from the individual printing experiments. It shows that the surface patterns produce lighter and less uniform prints compared to the solid reference under all printing conditions; at best the prints are similar.

The print uniformity of samples produced using water-based ink show distinct fingering patterns for all conditions. At low anilox volume and printing force individual features can be discerned in the prints (Figure 5.12). The finger pitch is approximately four times as large as the feature pitch on the printing plate, and a potential mechanism is ink film dewetting followed by coalescence rather than the actual ink transfer from the plate features. The ink surface tension and substrate surface energy also point to this. With increasing printing force and anilox volume, the ink film coalesces. Although this reduced the nonuniformity arising from visible substrate, it also facilitated the evolution of striking fingering instabilities.

Under all printing conditions, higher MGSLs were achieved using surface patterning compared to the plain reference solid which implies improved ink transfer by pattern recesses acting analogous to anilox cells. This could prospectively be corroborated by capturing WLI data of the printing plate between inking and printing, as well as after printing, since this would provide information on whether the pattern recesses are filled completely or only partially, and how much of the ink is released from the recesses during printing. Furthermore, this raises a number of questions concerning the detailed mechanisms of ink transfer to and from the pattern patches themselves which should be explored in the future in order to gain further detailed insight.

The line patterns achieved the worst effects on MGSL and StDev, because they failed to create closed ink films in the prints under most parameter combinations. This suggests that neither the UV-curing nor the water-based ink fully occupied the recesses in these patterns; even the highest volume of ink supplied by the anilox being insufficient to flood the gap between the elongated cell pattern entirely (Samworth, 2001).

In summary, patterning has a small positive effect on MGSL for prints produced with UV-ink, whereas the effect is much larger and negative for prints produced with water-based ink, because the surface patterns act analogous to anilox cells for this ink type. Thus, the net effect of the entire experimental plan is negative (Figure 5.20). The print nonuniformity arising from the partial ink laydown is improved in conjunction with higher anilox volume and printing force (both are negative 2-factor interaction effects), but worsened through the emergence of distinctive printing defects, when all three factors interact (positive 3-factor interaction effect). Imaging the patterns on the AWP-DEF plate material had a negative effect on MGSL and StDev which was attributed to an increase in ink supply by the material leading to better coalescence of individually printed areas. There was a positive interaction effect between the surface pattern and the substrate. As already explained for the main effect of the substrate, the rougher surface of the Ford paper leads to a

smaller contact area for ink transfer, increasing MGSL. This influence was amplified with decreasing area coverage by the surface patterns.

Although the main factor effect demonstrates that surface patterning has an adverse influence on print uniformity, by taking into account all interaction effects, homogeneity improvements can be achieved for almost any combination of material and process parameters through the use of surface patterning. However, without prior tests it is currently not possible to predict which surface pattern has the most beneficial impact at a given combination of parameters. For example, if APCO substrate is printed with an AWP-DEP plate and water-based ink at low anilox volume and printing pressure, then the grid pattern results in the best print uniformity at lower speed (StDev = 10.69 compared to reference StDev = 11.32), but the tile pattern is better at higher speed (StDev = 9.38 compared to reference StDev = 17.57). The latter is a significant improvement, while the former is a marginal change which might be accompanied by a disadvantageous shift in the type of fingering pattern produced. Furthermore, the surface pattern which improves print uniformity might not be the one to result in best optical density at the same time. Using the exemplary process parameters, the highest density would be produced by the polka dot pattern at the lower speed (MGSL = 144.78 compared to reference MGSL = 182.07) and at higher speed (MGSL = 100.69 compared to reference MGSL = 136.23).

The effect of surface patterning on printed patterns is illustrated on a single print of the water-based ink on APCO substrate in Figure 5.21. Excepting the vertical and diagonal line patterns which reflect the image of the printing plate, the reference solid and all the other surface patterning resulted in different classes of fingering patterns. The reference solid suffered from viscous fingering which was also the dominant defect class for the chequer pattern at 90°, patterns made up of holes, tiles, positive hexagons, negative hexagons and horizontal lines; the latter two adorned with beads. The images strongly suggest that the orientation of the surface patterning has a direct influence on the propagation of the instabilities. Although the viscous fingers roughly followed the direction of the recesses on the printing plate when bifurcating, the actual angle of propagation was usually smaller than the one on the printing plate (see the tile and chequer pattern without tilt in Figure 5.21).

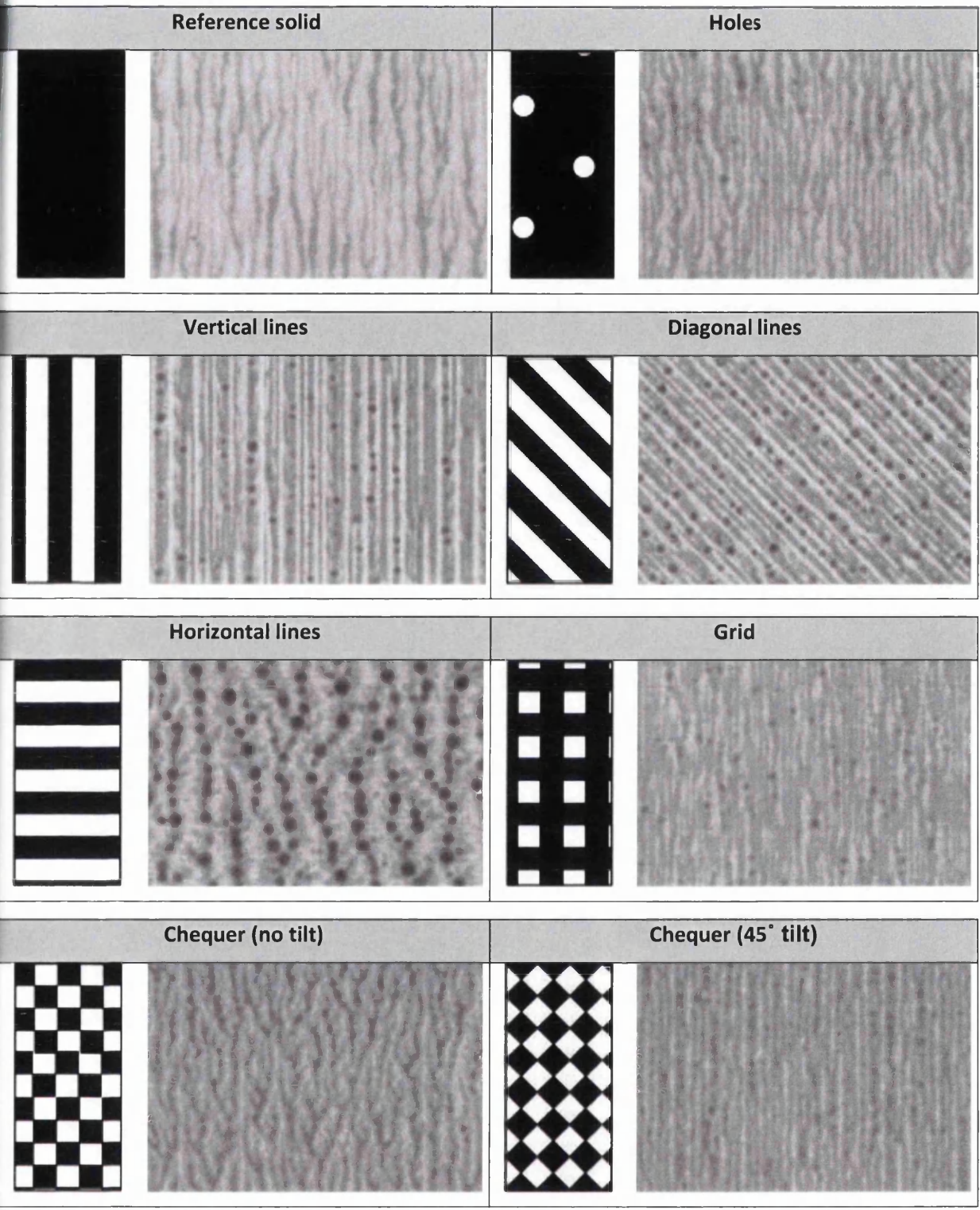


Figure 5.21: Effect of the meso-patterns on fingering demonstrated on the example of a single set of printing conditions (water-based ink on APCO substrate, AWP-DEF plate material, speed = 0.2 m/s, force = 50 N, anilox volume = 8 cm³/m²) (76.4x pattern magnification; 6.5x sample magnification) (continued on next page)

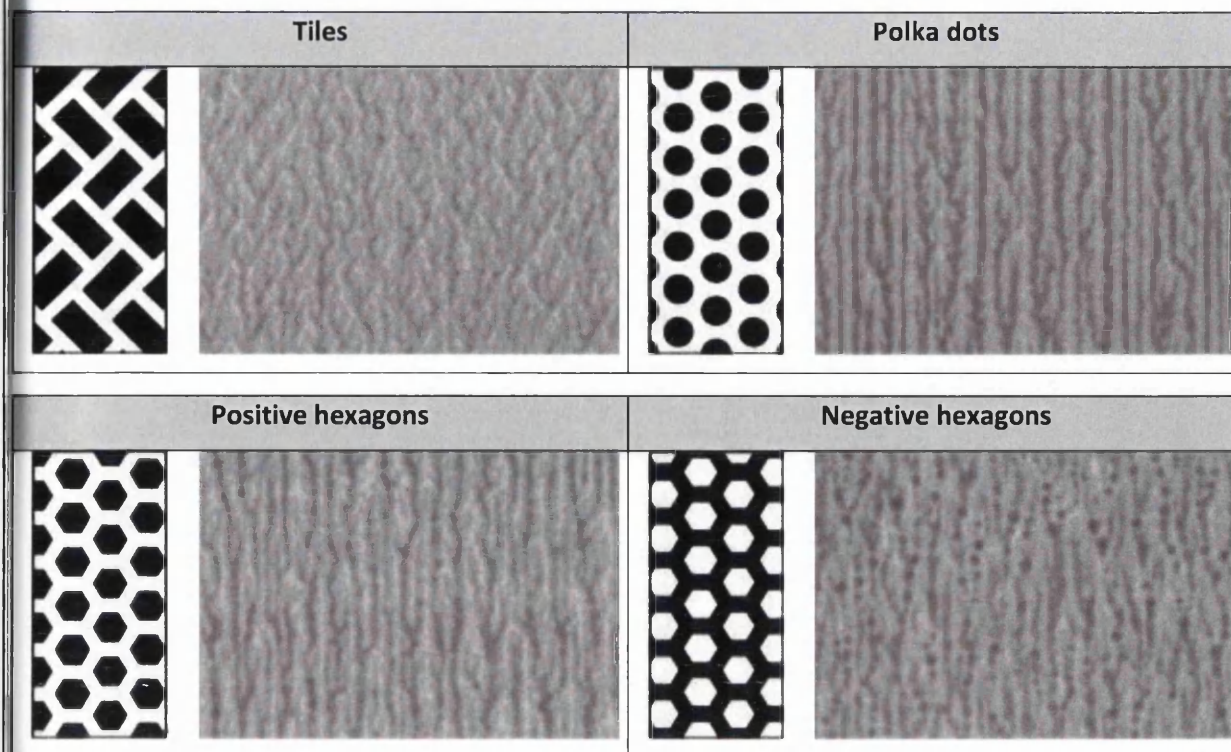


Figure 5.21: (continued from previous page)

When the pattern orientation was changed to align the non-image areas of the printing plate with the printing direction, the finger propagation seemed more contained and linear. The rib instabilities for the grid and chequer pattern at 45° tilt are an example for this. The orientation of the polka dot pattern also created less obstructed channels in the print direction which resulted in mostly linear main fingers. However, the gaps to the left and right of these channels seemed influential enough to slightly destabilise the main finger and give rise to short side branches and occasional bifurcation. That these systems are very sensitive to small changes in conditions can also be seen by comparing the polka dot and positive hexagon patterns. They are nominally very similar and strongly resemble each other on the printing plate (the sharp corners of the hexagons were not reproduced on the plate). Nevertheless, the positive hexagons were the slightly larger printing features and protruded minimally more into the plate channels orientated in the print direction. This small difference was sufficient to cause the transition from dendritic ribs to branched viscous fingers.

Overall the patterns seem to be able to affect the frequency of the fingering instabilities in the prints, although more detailed evaluation is required, for example using one- and two-dimensional frequency analysis. Sometimes the shift in frequency was accompanied by stabilisation towards ribs, sometimes by changes towards appearances that are even more branched. However, the latter was not necessarily a disadvantage and on occasion resulted in at least as uniform an impression as the reference solid (see the tile pattern). That this is also beneficial for functional device printing was

concluded by Reuter et al. (2007): if the instabilities cannot be avoided, then the parameters should be chosen towards increasing frequency and branching of viscous fingering, as this will improve the overall uniformity of the ink film transferred.

5.1.5 Conclusions

Eleven meso-patterns were investigated under a variety of printing conditions on the IGT-F1 to determine whether they are able to alter print density and uniformity compared to a plain reference solid. This was found to be the case and governed by two different ink transfer mechanisms dependent on the ink type used. The dual pattern functionality in flexographic printing has not been documented in literature previously:-

- Lower-viscosity water-based ink floods the recesses of the surface patterns analogous to anilox cells, thereby increasing the ink-carrying capacity of the printing plate and the amount of ink transferred to the substrate. Fingering instabilities in the ink transfer process create striking printed patterns. The types of fingering patterns produced and their frequency could be controlled by pattern geometry and orientation, as well as the process parameters. Improvements in print uniformity resulted from the increase in defect frequency.
- Higher-viscosity UV-curing ink is more likely to be held on the pattern features. The creation of closed ink films has to be achieved through the mechanism of ink squeeze under pressure in the printing nip causing the coalescence of neighbouring printed features.

The best pattern for print uniformity did not necessarily correlate with the one for highest print density, and the print quality was highly dependent on the combination of surface patterning, material parameters and printing conditions. Material and process parameters had a larger influence on the print quality than the surface patterns. All the parameters have to be well-matched, otherwise the process output deteriorates.

5.2 Meso-Pattern Effect using an Industrial Printing Press

The study using the IGT-F1 demonstrated the potential of surface patterning to improve print quality. Although the literature suggests that trials performed on certain printability testers are representative of industrial-scale printing (Aspler, 2004), there is also substantial experiential evidence that printing on full-scale equipment will lead to improved results. Thus the study in this subchapter investigated whether the same effects of surface patterning on ink transfer and distribution could be observed if the experiment was scaled up to near industrial conditions.

5.2.1 Materials – Plate, Substrates and Ink

The same plate materials (AFP-DSH and AWP-DEF; Table 5.1) and surface patterns (Figure 5.2) were used. The 12 patterns were organised in a band and seven such bands were repeated next to each other to make up the final design of the printing plate (Figure 5.22). Each band was later printed with a different anilox volume. The actual feature sizes were determined from WLI data and presented in section 5.1.4.1.

Details of the materials (substrate Rayoface WPA59 by Innovia Films and the magenta UV-curing ink of the series Solarflex Nova SL Pro DK03 by SunChemical) are provided in section 4.1.

5.2.2 Printing and Print Characterisation

The parametric study was based on six factors, namely surface pattern, plate material, mounting tape, anilox volume, plate-substrate engagement and printing speed (Figure 5.23), which were all investigated at two levels (Table 5.7). The first mounting tape, 1015 by 3M, is suitable for printing solids and halftones on the same printing plate. The second tape was the softer, more compressible 1115 by 3M which is recommended for halftone printing. The printing and curing took place on the T-Flex 508 industrial printing press by Timsons. The anilox employed contained seven bands of different cell volumes (Table 5.8). The other anilox specifications were identical for all bands: laser engraving, 60° screen angle and 500 lpi screen ruling. All bands were printed at the same time, but only the prints using anilox volumes of 3.04 and 8.31 cm³/m² were analysed. Although only the higher volume is comparable with the specifications used on the IGT-F1, the lower volume was representative of conditions generally found in industrial colour printing. The experimental order is outlined in Table 5.9.

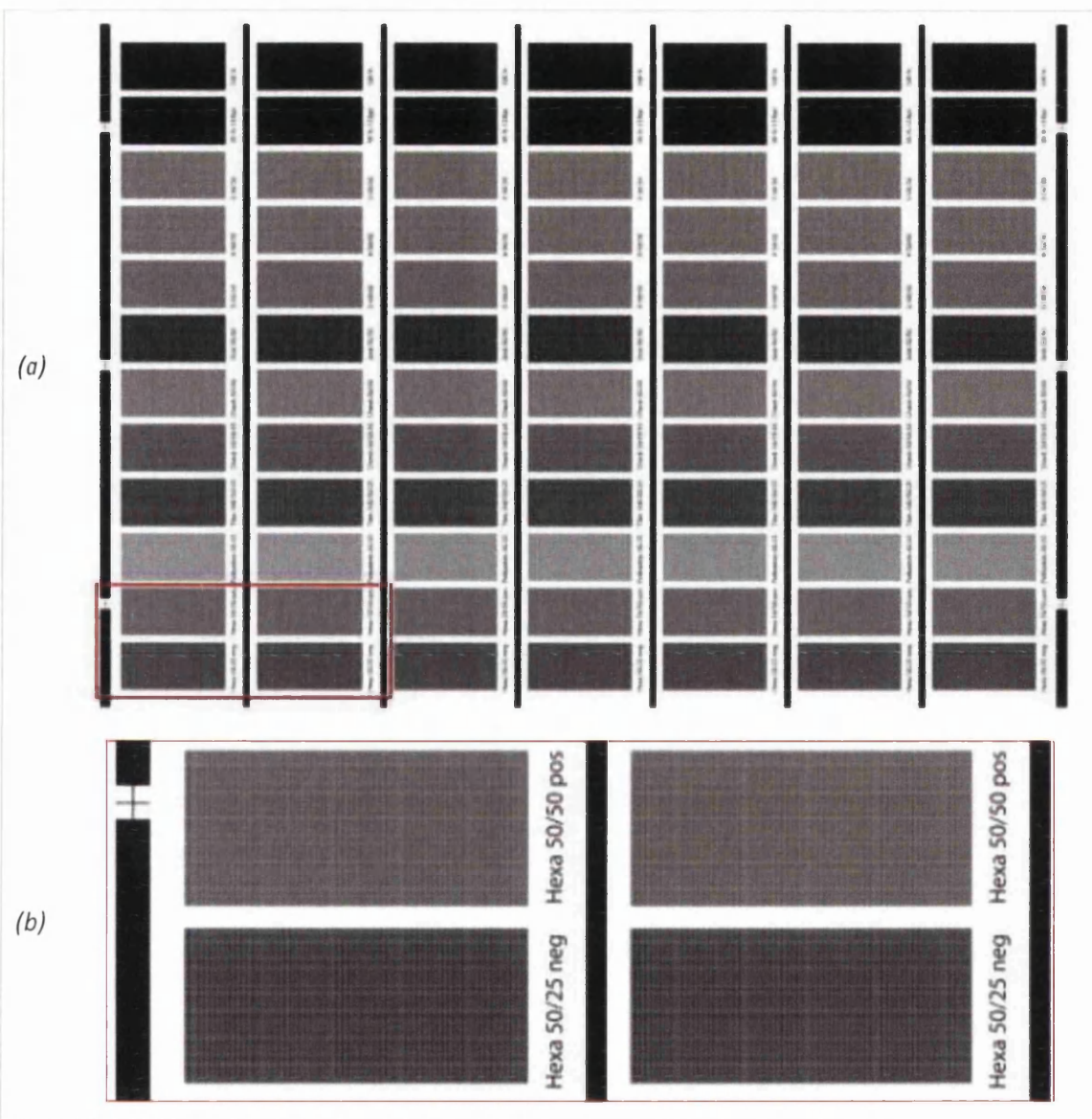


Figure 5.22: Image for meso-pattern trial on the T-Flex 508:

(a) seven identical bands containing the printing patches with 11 surface patterns and plain reference solid are arranged in columns (0.2x magnification); (b) image detail corresponding to the red box in (a) showing the positive and negative hexagon pattern patches on neighbouring bands (to scale)

Visual inspection of the patches directly after printing revealed that most surface patterns had failed to create a closed ink film on the substrate. Since the optical density of the prints was governed by area coverage rather than ink film thickness, it was deemed unnecessary to digitise the prints for analysis of print uniformity with image analysis software. Information on optical density and the effects of printing parameters on it could be obtained more efficiently by spectrophotometry. Therefore the optical density of printed patches was measured on eight consecutive sheets for each possible combination of parameters listed in Table 5.7.

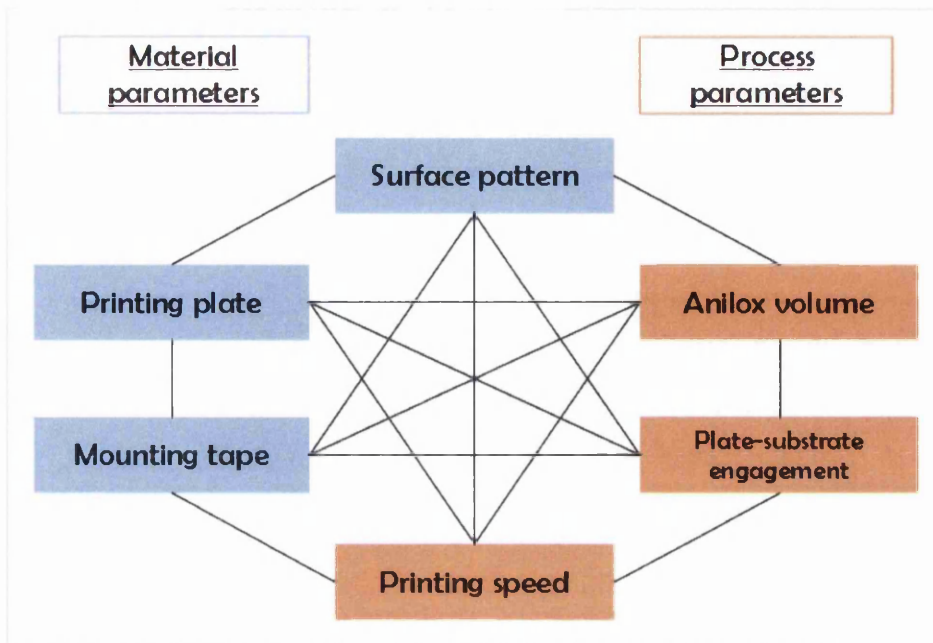


Figure 5.23: Parameters and their interactions of meso-pattern trial on the T-Flex 508

Table 5.7: Parameter levels for experimental plan of meso-pattern trial on the T-Flex 508

Factor	Lower level		Upper level	
Surface patterning	Reference solid (no pattern)		Pattern	
Plate material	AWP-DEF		AFP-DSH	
Mounting tape	Soft (1115)		Combination (1015)	
Anilox volume	3.04 cm ³ /m ²		8.31 cm ³ /m ²	
Printing engagement	3 thou	76.2 μm	5 thou	127 μm
Printing speed	100 ft/min	30.5 m/min	300 ft/min	91.4 m/min

Table 5.8: Volume specification of anilox bands

Band	1	2	3	4	5	6	7
Anilox volume (cm ³ /m ²)	1.63	3.04	4.20	5.49	6.59	8.31	1.63

Table 5.9: Combination of print parameters for meso-pattern trial on the T-Flex 508

Experiment number	Tape	Plate	Speed		Engagement	
			(ft/min)	(m/min)	(thou)	(μm)
1	Medium	AWP-DEF	100	30.5	3	76.2
2					5	127.0
3			300	91.4	3	76.2
4					5	127.0
5		AFP-DSH	100	30.5	3	76.2
6					5	127.0
7			300	91.4	3	76.2
8					5	127.0
9	Soft	AWP-DEF	100	30.5	3	76.2
10					5	127.0
11			300	91.4	3	76.2
12					5	127.0
13		AFP-DSH	100	30.5	3	76.2
14					5	127.0
15			300	91.4	3	76.2
16					5	127.0

5.2.3 Results and Discussions

The spectrophotometric analysis confirmed the visual observation that for no combination of printing parameters did any of the patterns achieve as high an optical density as the reference solid (Figure 5.24). Although the reference prints were not perfectly homogenous and included numerous defects, the UCAs in the printed pattern patches were more extensive and significantly decreased the optical density of their prints (Figure 5.25 shows the exemplary comparison of the reference solid and chequer pattern at 45° tilt). The UCAs are likely to be the combined result of entrapped air bubbles which prevented complete ink transfer and non-printed areas in the patterns which remain if not enough ink volume or pressure is applied to form closed ink films through the mechanism of ink squeeze (as discussed for the IGT-F1 in section 5.1.4.8).

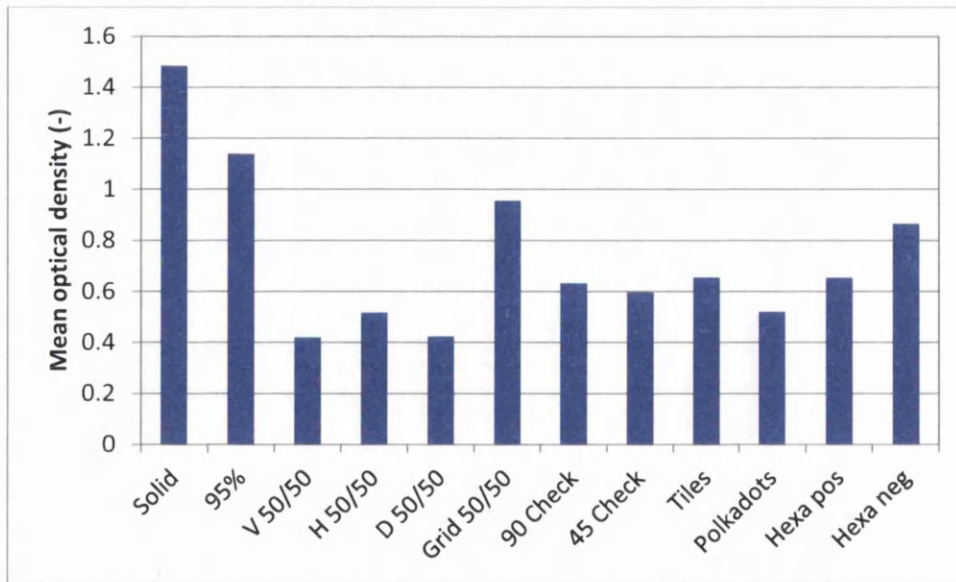


Figure 5.24: Mean optical densities (averaged over all printing conditions of the entire experimental plan) for plain solid reference and all surface patterns in meso-pattern trial on the T-Flex 508

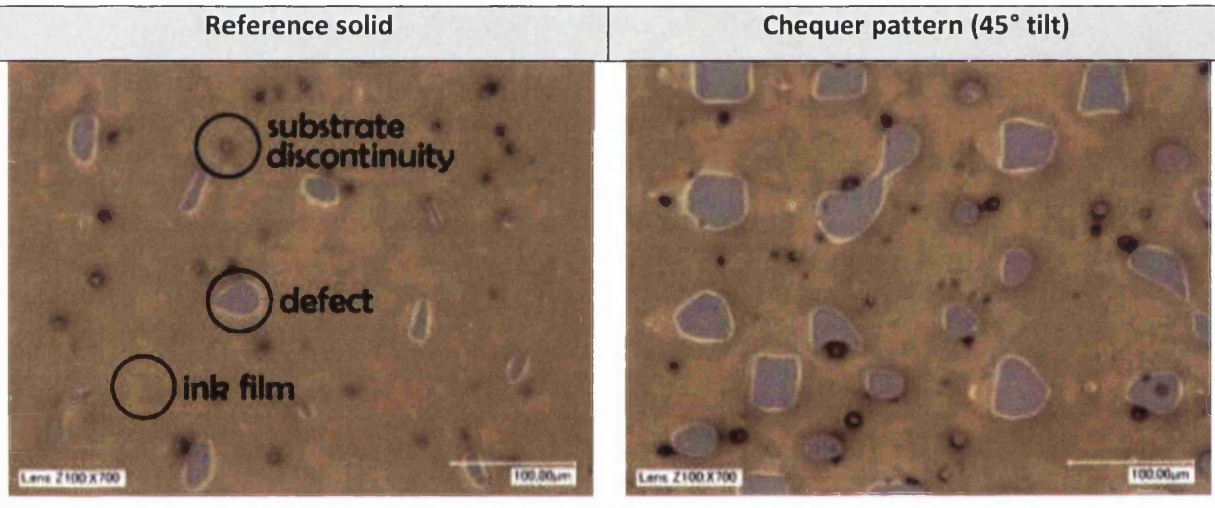


Figure 5.25: Comparison of printing defects (areas of missing ink) in meso-pattern trial on the T-Flex 508 (AWP-DEF plate material, soft tape, high anilox volume, 100 ft/min printing speed at 8 thou engagement)

To facilitate a comparison between the trials on the IGT-F1 and T-Flex 508, the DoE analysis of the data has been undertaken. The complete data set on optical density for all surface patterns, as well as the uncertainty of the effects stating their significance, is provided on the CD-ROM attached to this thesis. All surface patterns resulted in main factor effects having an identical impact and very similar magnitude. As an example, the 15 largest effects for the chequer pattern at 45° tilt are provided in Figure 5.26. They are all significant based on the effect uncertainty of $\Delta E = \pm 0.003$. For this pattern the mean optical density for the entire experimental plan was $D = 1.04$, and effects of $E_{D1} = 0.10$ and $E_{D2} = 0.90$ correspond to changes in MGSL by approximately $E_{MGSL1} = 10$ and $E_{MGSL1} = 65$ levels respectively. Only the most relevant main and interaction effects for all surface patterns are discussed below.

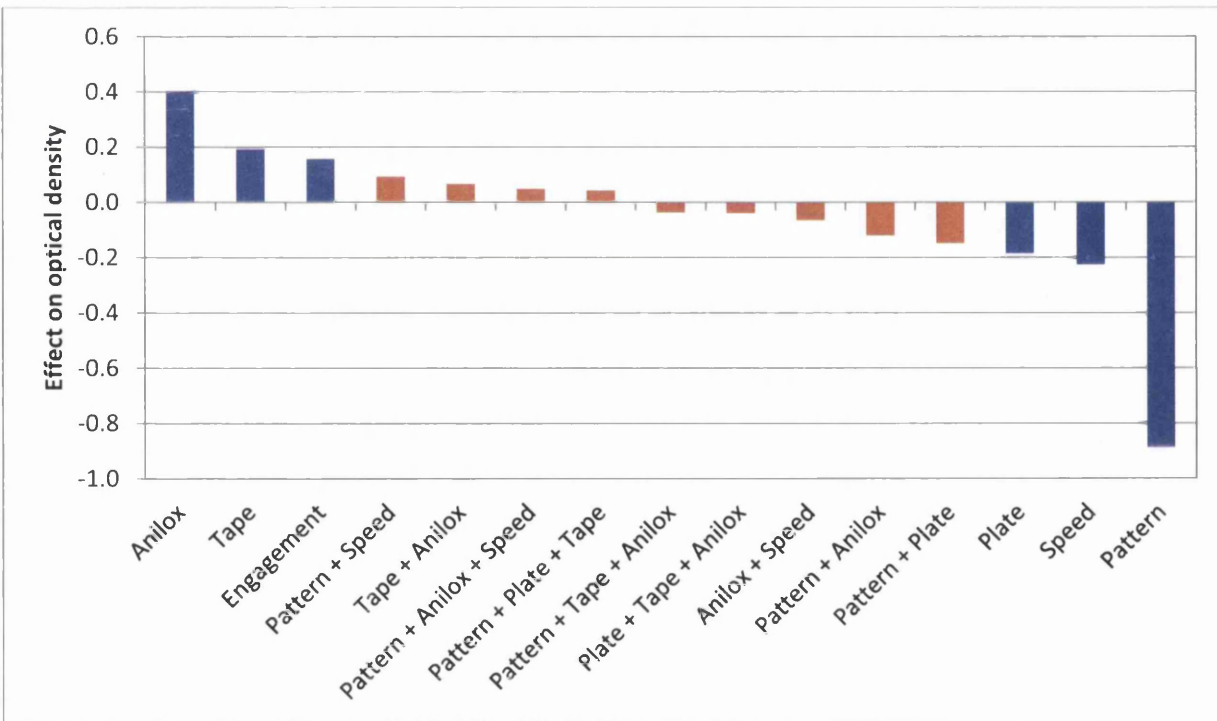


Figure 5.26: The 15 largest main factor and interaction effects on optical density for the example of checker pattern at 45° tilt on the T-Flex 508 (main effects in blue, interaction effects in orange)

In general, all material and process parameters that increased ink transfer from the plate to the substrate or ink squeeze on the substrate increased optical density. More ink provided by the anilox led to higher ink transfer to the plate and then to the substrate where better area coverage was achieved through ink squeeze ($E_D=+0.40$). The slightly harder combination tape compressed less in its core during impact. Thus the printing plate itself had to deform more against the substrate. The contact area of plate and substrate increased and with it the ink squeeze in the printing nip ($E_D=+0.19$). The soft mounting tape on the other hand relieved the printing plate through core compression. This is more important in halftone printing to avoid dot distortion and create sharper printed dots. The interaction of high anilox volume and combination tape increased the effect on optical density through ink squeeze even further ($E_D=+0.07$). The last main factor with positive effect on optical density was the engagement which increased the contact area between the plate and substrate ($E_D=+0.16$), thereby creating higher area coverage and supporting ink squeeze towards more homogenous ink distribution.

Surface patterning had the largest negative influence on optical density ($E_D=-0.89$). On the printing plate, patterned patches had lower area coverage than the reference solid which translated into reduced ink coverage and optical density in the prints. Patterns featuring holes rather than freestanding features, such as the 95%, grid and negative hexagon patterns, fared slightly better

than the others. Due to the interconnectivity of the features, these patches were closer to forming continuous ink films in the print than isolated features which had to connect the separate ink depositions on the substrate through ink squeeze. Since the ink squeeze action is the dominant mechanism for surface patterns in conjunction with UV-curing ink, it can be concluded that the design characteristics of the meso-patterns, namely geometry, area coverage and feature pitch, were not suited to this particular ink type under the printing conditions encountered on the T-Flex 508, which contributed to the pattern failure. To confirm this, a further print trial was conducted where the printing plates were imaged with micro-patterns, and this will be dealt with in Chapter 6.

The negative patterning effect was amplified when including the interaction with the plate material ($E_D=-0.15$), because the pattern area coverage was significantly lower on the solvent-washable AFP-DSH (Figure 5.8) than on the water-washable AWP-DEF (Figure 5.9). Furthermore, the increased surface roughness of AWP-DEF potentially improved its ink-carrying capabilities. Consequently, larger amounts of ink transferred to the plate, hence to the substrate, improving the ink squeeze action and optical density (reduction of optical density with usage of AFP-DSH expressed by $E_D=-0.19$).

The rise in printing speed decreased the optical density ($E_D=-0.23$). One potential cause identified for this was the ink film splitting closer to the substrate at higher speed, thereby reducing the ink film thickness printed (De Grâce and Mangin, 1983). It has also been observed previously that a reduction of ink volume in the anilox cells occurs due to their filling being hampered by hydrodynamics at higher speed, and ink being scooped out of the cell through the wiping action of the doctor blade (Kunz, 1975). Less ink in the cells leads to less ink transferred to the substrate. The negative interaction effect of printing speed and anilox volume ($E_D=-0.06$) implies that the larger anilox volumes were impacted further by the change in speed due to more ink being doctored out of these cells with larger opening. However, there was a positive interaction of speed and surface patterning ($E_D=+0.09$) which meant that the individual reduction in optical density by usage of surface patterning and higher speed was cumulatively less severe. Potentially, while the reference solid was unable to deform sufficiently into the anilox cells containing reduced fluid levels to ink up fully, the pattern features deformed better or dipped into the cells, picking up proportionally more ink. That this beneficial effect had its limit is suggested in the negative interaction of patterning and anilox volume ($E_D=-0.12$). Assuming that the anilox cells with larger opening contain lower ink levels (as discussed above), the pattern features also were increasingly unable to retrieve ink from the depths of the cells and the ink transfer was reduced. However, no trend in the correlation of the

latter two interaction effects and the type of surface pattern could be observed. Furthermore, the magnitude of most interaction effects fell within the noise range identified for the T-Flex 508 ($\Delta D=0.1$) and have to be treated with caution.

Overall there was a good agreement of parameter effects on optical density between the studies on the IGT-F1 and T-Flex 508. The deviant influence of printing speed was attributed to particular differences in the construction of IGT-F1 and T-Flex 508. On the IGT-F1, the ink supply is dependent on the operator and can easily be overdosed. The deflection of the doctor blade due to non-rigid mounting was aggravated by overdosage, thereby allowing the flooding of the anilox roll (cells and land area) with ink. Consequently, this ink swamped the patterned patches on the printing plate, creating higher ink coverage and making meso-patterns a viable option for the improvement of print density. The effect was particularly severe for low-viscosity water-based ink. On the other hand, the ink supply on the T-Flex 508 is consistent through design which renders surface patterning less successful.

A second difference between the printing methods was the anilox specifications. The anilox screen ruling used on the IGT-F1 was 300 and 350 lpi (84.7 and 72.6 μm respectively) which was significantly larger than the nominal pattern size of 50 μm . Pattern features were therefore likely to dip into the anilox cells and pick up more ink on the feature shoulders. On the T-Flex 508 the nominal pattern width on the plate and anilox cell pitch (50.8 μm) were similar. Thus, it is possibly that dot dipping was a less frequent occurrence, reducing ink coverage on the plate and then the print. Furthermore, the anilox volumes investigated on the IGT-F1 (8 and 12 cm^3/m^2) were larger than those on the T-Flex 508 (3.04 and 8.31 cm^3/m^2), thereby facilitating increased ink transfer to the printing plates.

5.2.4 Conclusions

The investigation of eleven meso-patterns was scaled up to near-industrial conditions. The effects of material and process parameters on print quality observed on the T-Flex 508 confirmed the findings of the IGT-F1 study. Using UV-curing ink, the surface patterns failed to create closed ink films on the substrate, because the ink squeeze mechanisms was potentially insufficient due to a lack of ink volume or inappropriate pattern design, notably too large a distance between pattern features or freestanding pattern geometry.

5.3 Closure

A comprehensive investigation of the influence of plate surface patterning on the ink transfer from solid printing patches has been undertaken under laboratory and near-industrial conditions. Meso-patterns with nominal feature sizes of 50 μm were examined for their effect on print quality, namely optical density and print uniformity, in conjunction with different material and process parameters.

For the first time, two functionalities of surface patterns were identified in conjunction with the ink type used. Lower-viscosity water-based ink is carried on the plate surface as well as in the pattern recesses analogous to anilox cells, and the pattern geometry can be used to shift the frequency of printing defects towards improved print uniformity. Higher-viscosity UV-curing ink remains on the pattern features and depends on the ink squeeze across the substrate to create closed ink films. The successful application of this mechanism requires an optimisation of the pattern design to facilitate ink coalescence.

Under the conditions investigated on the T-Flex 508, the meso-patterns failed to create closed ink films. On the IGT-F1, meso-patterns were found to be capable of improving optical density and print uniformity, although both quality criteria were not necessarily obtainable at the same time. The effectiveness of the patterns was highly dependent on material and process parameters, and some parameter combinations had particularly adverse influence on the amount and consistency of the ink transferred. In general, the process parameters were able to affect optical density and print uniformity more than the application of surface patterning, and very specific parameter combinations were required to gain a benefit from patterning. The directions of the parameter effects determined for the IGT-F1 and T-Flex 508 were in agreement with previous knowledge of printing solids and halftones in flexography, and can be employed in the optimisation of printing processes.

Chapter 6 Microcell Patterns on Printing Plates

In the previous chapter two different functionalities of meso-patterns were identified dependent on the ink type used. In conjunction with UV-curing ink, the surface patterns created only partial ink films on the substrate due to a lack of ink coalescence. This was attributed to inadequate pattern design, notably geometry, insufficient area coverage and feature pitch, in order to allow ink coalescence by a squeezing action.

In this chapter the design issues identified for the meso-patterns were addressed in the form of commercial microcell patterns. The microcells have in common that they are made up of small recesses in the surface of the flexographic printing plate analogous to the land areas and cells on the anilox cylinder. Their area coverage and feature frequency is higher than for the meso-patterns, and the recess diameter smaller than the nominal width of the meso-features. This chapter aims to explore the ink transfer functionality of these micro-patterns superimposed on solid printing patches and halftone dots. For this purpose, again, investigations were conducted on a printability tester and industrial-scale printing press. An overview of the two trials is provided below.

MICROCELL PATTERN EFFECT USING A PRINTABILITY TESTER

The IGT-F1 printability tester was used to explore a total of three pattern sets. The plate-imaging was performed using “flat-top” imaging technology on appropriate plate material supplied by MacDermid. In order to establish whether this material behaved fundamentally differently in conjunction with surface patterns, the print trial for meso-patterns was repeated and formed the first pattern set. The second printing plate employed a selection of meso- and four microcell patterns. The particular microcell specifications were chosen by the reproduction house for their claimed successful application in previous industrial print jobs. The last printing plate consisted of four of the most efficient meso-patterns at three different size ratios (50%, 100% and 200%). The shrinkage of meso-patterns by 50% made their dimensions comparable to the ones of microcells and bridged the gap between meso- and micro-patterns in the investigation. Furthermore, this served to gain additional information on the effect of pattern-scaling on print quality.

MICROCELL PATTERN EFFECT USING AN INDUSTRIAL PRINTING PRESS

The study conducted on the T-Flex 508 printing press examined the effects of four microcell patterns under varying printing conditions at a practical commercial scale. “Flat-topped” and “round-topped” solid printing patches and halftones superimposed with microcells were investigated on three different plate types. The quality characteristics that were applied comprised optical density and print uniformity.

6.1 Microcell Pattern Effect using a Printability Tester

The main aim of this study was to establish whether the functionality of microcell patterns is fundamentally different to their meso-scale counterparts. Different meso- and micro- pattern designs were investigated.

6.1.1 Materials, Printing and Print Characterisation

The plate material “Digital Rave” by MacDermid was provided and imaged by SGS Packaging Europe. The key plate properties are listed in Table 6.1. The imaging was performed using MacDermid LUX technology and an imaging resolution of 4,000 dpi. Details of the pattern sets for all three plates are listed in Table 6.2. The first pattern set (Plate 1) is identical to the set of the previous chapter and served to establish whether the different plate materials and imaging technologies in conjunction with surface patterning had an effect on print quality. The second pattern set (Plate 2) compares meso-patterns and microcells. The third pattern set (Plate 3) contains meso-patterns at three different scales, the smallest of which is similar to the micro-patterning and links the two pattern groups investigated. For the illustrations of the meso-patterns refer to Figure 5.2. Specifications of the microcell patterns are provided in Figure 6.1 and Table 6.3. The actual pattern geometries on the printing plates were characterised using WLI. This is illustrated in Appendix A.7 and will be discussed in section 6.1.3.1.

The substrates APCO and Ford as well as the UV-curing ink FlexoCure Gemini and the in-house water-based Newtonian ink were selected again. The material properties are detailed in section 5.1.1.

Table 6.1: Selected properties of plate material used for micro-pattern study on the IGT-F1

Property	MacDermid Digital Rave
Washability	solvent
Surface roughness, R_a	54 nm
Surface roughness, R_z	1.1 μm
Steady-state surface energy	44.6 mN/m
Hardness*	60 Shore A
Thickness	1.7 mm
* hardness according to publication by MacDermid Printing Solutions (2012)	

Table 6.2: Surface patterns of the three printing plates used for micro-pattern study on the IGT-F1

Surface pattern	Nominal pattern dimensions	Plate1	Plate 2	Plate 3
Reference solid	-	√	√	√
Vertical lines	50 μm track/50 μm gap	√	√	
Positive hexagons	50 μm width/25 μm gap	√	√	
Negative hexagons	50 μm width/25 μm track	√	√	
Horizontal lines	50 μm track/50 μm gap	√		
Diagonal lines	50 μm track/50 μm gap	√		
Polka dots	50 μm diameter/100 μm pitch	√		
Chequer (no tilt)	50 μm by 50 μm width	√		
Chequer (45° tilt)	25 μm by 25 μm width			√
	50 μm by 50 μm width	√	√	√
	100 μm by 100 μm width			√
95%	24 μm diameter/95.5 μm pitch			√
	48 μm diameter/191 μm pitch	√	√	√
	96 μm diameter/382 μm pitch			√
Grid	25 μm by 25 μm width/25 μm track			√
	50 μm by 50 μm width/50 μm track	√	√	√
	100 μm by 100 μm width/100 μm track			√
Tiles	50 μm by 25 μm width/12.5 μm gap			√
	100 μm by 50 μm width/25 μm gap	√	√	√
	200 μm by 100 μm width/50 μm gap			√
Microcells	MC 09P_H		√	
	MC 09P_L		√	
	MC 12P		√	
	MC 16P		√	

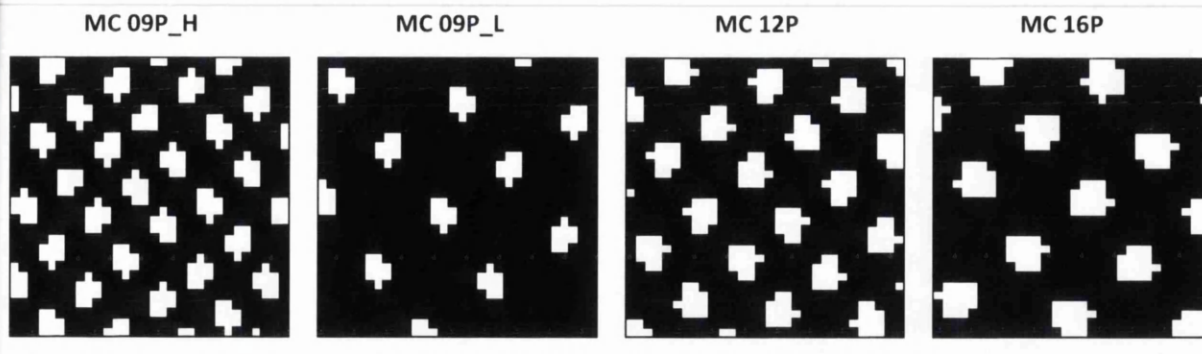


Figure 6.1: Illustrations of microcell patterns (200x magnification)

Table 6.3: Specifications of microcell patterns

Microcell pattern	Nominal size (approx.)	Nominal area coverage (%)
MC 09P_H	19 μm diameter recesses	64.0
MC 09P_L	19 μm diameter recesses	89.9
MC 12P	22 μm diameter recesses	76.0
MC 16P	25 μm diameter recesses	78.4

6.1.2 Printing and Print Characterisation

All three printing plates were subjected to the same full-factorial experimental plan involving five factors (each adjustable on two levels) (Figure 6.2). The same parameter levels (except for the change in plate material) selected for the meso-pattern studies on the printability tester were adopted (refer to Table 5.6). The prints from the 32 experimental points were digitised, and the measurands MGSL (density) and StDev (print uniformity) obtained through the image analysis software. The complete effect data for MGSL and StDev of all surface patterns, as well as the uncertainty of the effects stating their significance, is provided on the CD-ROM attached to this thesis.

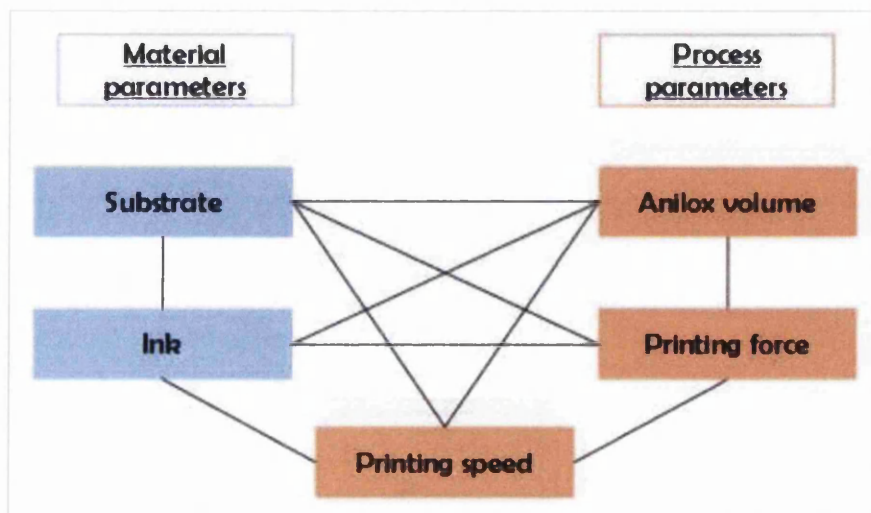


Figure 6.2: Parameters and their potential interactions in micro-pattern study on the IGT-F1

6.1.3 Results and Discussions

6.1.3.1 Plate Characterisation

Using LUX technology, oxygen inhibition of the plate polymerisation was prevented during imaging and the digital designs were transferred to the printing plate at almost perfect fidelity (compare images in Appendix A.7). A slight gain in area coverage of up to 3% was noted for all pattern patches (Plate 1 – Figure 6.3, Plate 2 – Figure 6.4 and Plate 3 – Figure 6.5). Only the microcell patterns MC09P_H and MC12P had slightly higher increases of 6% and 4% respectively. The actual geometrical shapes of the features were maintained on the printing plate within practicability of the imaging process defined by the resolution of the laser creating the imaging mask on the plate.

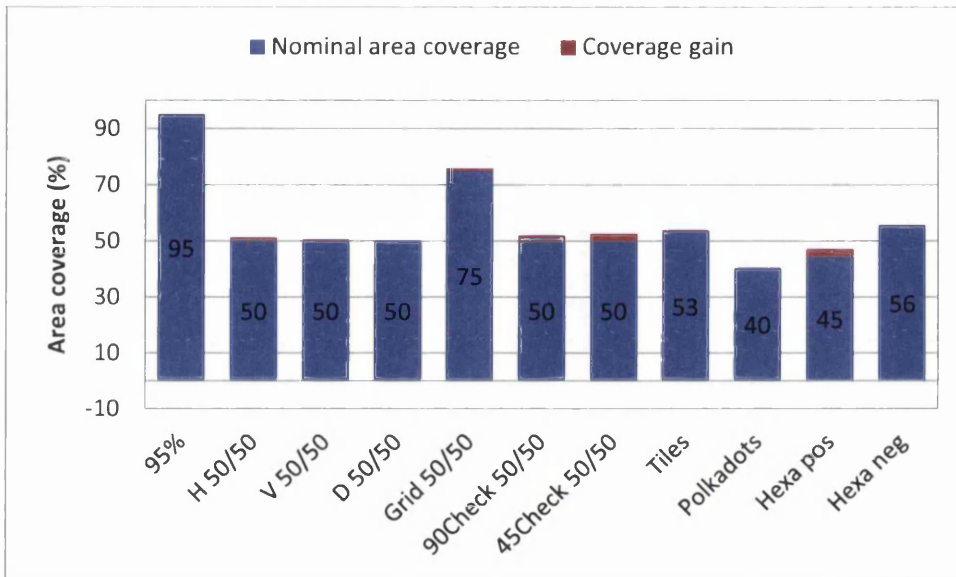


Figure 6.3: Actual area coverage on printing plate and coverage loss compared to the artwork for MacDermid Lux Plate 1

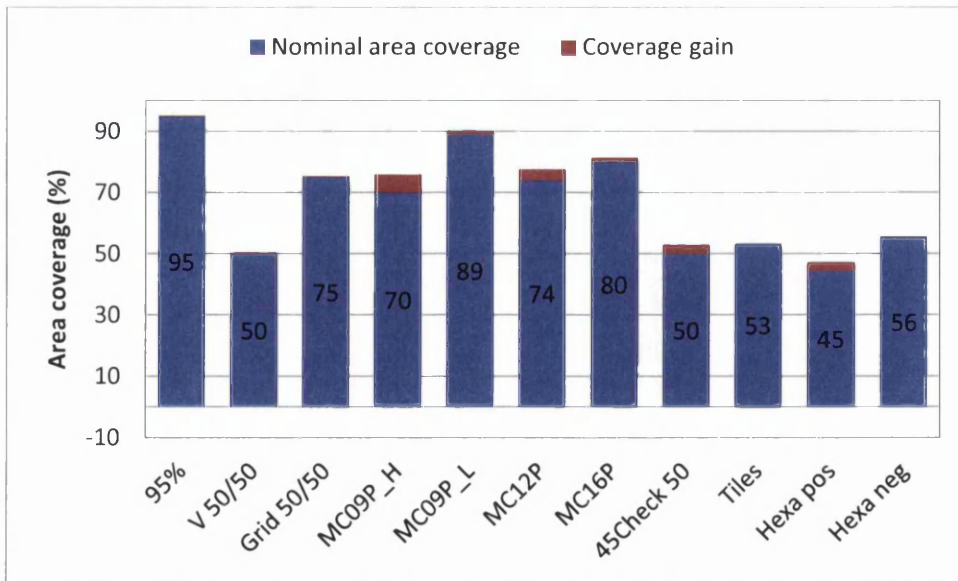


Figure 6.4: Actual area coverage on printing plate and coverage loss compared to the artwork for MacDermid Lux Plate 2

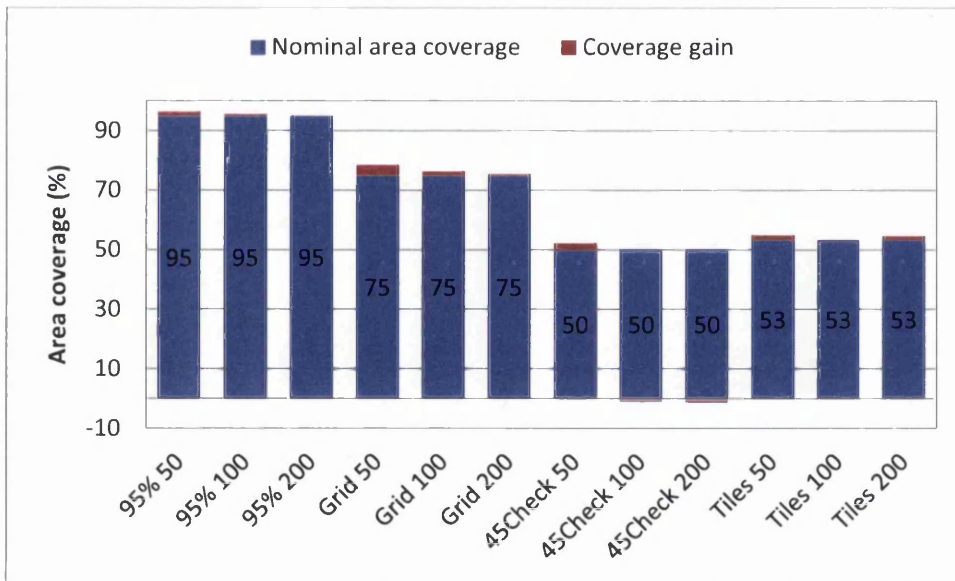


Figure 6.5: Actual area coverage on printing plate and coverage loss compared to the artwork for MacDermid Lux Plate 3

6.1.3.2 Effect of Plate Material and Imaging Technology

For the investigation of the effect of plate material and imaging technology, meso-pattern designs identical to the ones in the previous chapter have been used. Despite the significant differences in plate geometries, the mean MGSL (Figure 6.6) and mean StDev (Figure 6.8) from the experiment were very similar or better for the MacDermid Lux (Plate 1) compared to the Asahi plates. A difference of 10 GSLs within the range observed correlates approximately to a difference of 0.1 in optical density which corresponds to the limit of discernibility for the untrained eye.

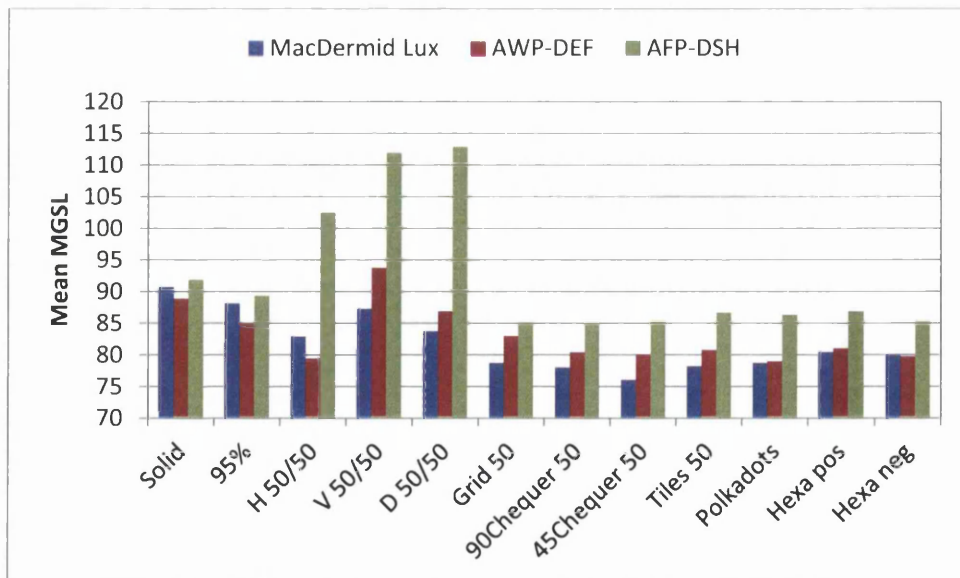


Figure 6.6: Comparison of mean MGSL (averaged over all printing conditions of the entire experimental plan) for MacDermid Lux (Plate 1) and Asahi plates

The pattern fidelity on the MacDermid Lux plate had two advantages with regards to the dual functionality of surface patterns identified in the previous chapter. On the one hand, it led to an increased area coverage which governed the transfer of UV-curing ink. This translated directly to increased amounts of ink supplied to the substrate and improved mean MGSL of the prints for the majority of pattern patches (Figure 6.6). On the other hand, deeper pattern recesses were established (Figure 6.7) which, dependent on cell evacuation, potentially allowed larger volumes of water-based ink to be transferred, thereby creating darker prints. The lack of area coverage and recess volume on the AWP-DEF plate seemed to have been compensated by its higher ink-carrying capabilities, and the mean MGSL for this Asahi material and the MacDermid Lux plate were very similar.

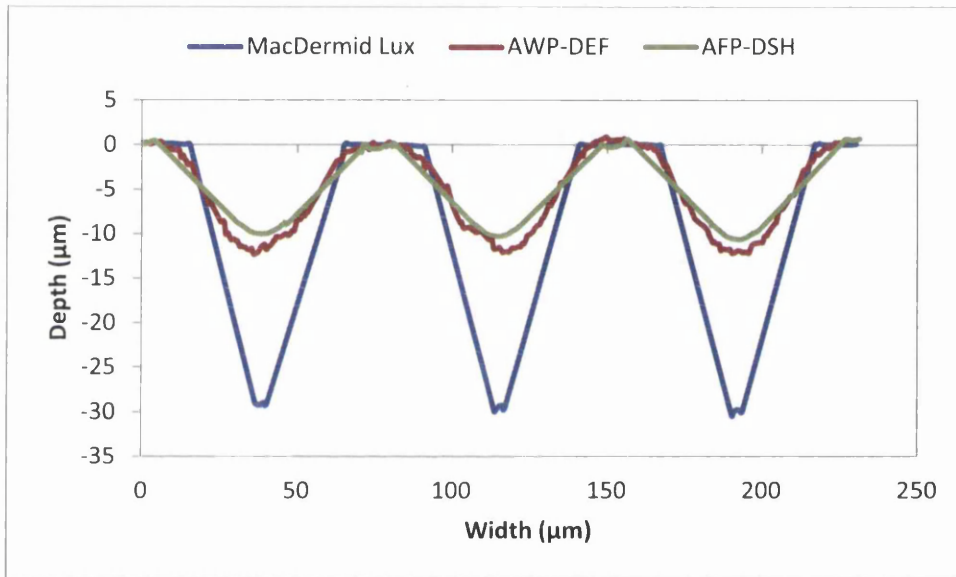


Figure 6.7: Surface profile of negative hexagon pattern on different plate types (missing WLI data on feature shoulders of MacDermid Lux and AFP-DSH plates was interpolated from captured data at peaks and troughs)

The higher mean StDev from the experiment reveals that the MacDermid Lux plate produced less uniform prints than the AWP-DEF material and most patches on the AFP-DSH plate (Figure 6.8). One reason for this might be the bigger ink transfer from the MacDermid Lux plate which aided the evolution of fingering instabilities (refer to Figure 6.19 for examples). Furthermore, larger volumes of ink amplified the contrast of the printed patterns, thereby enhancing the inhomogeneities. This can be quantified in the difference between maximum and minimum GSLs observable for the print samples. Secondly, the printed patterns created with the MacDermid Lux plate were by their nature less uniform. This might be due to the very low surface roughness of the plate which provided few

points to which the receding ink could be pinned in order to create finer filaments during ink film splitting. Thus, the formation of broad, low-frequency fingering patterns was facilitated.

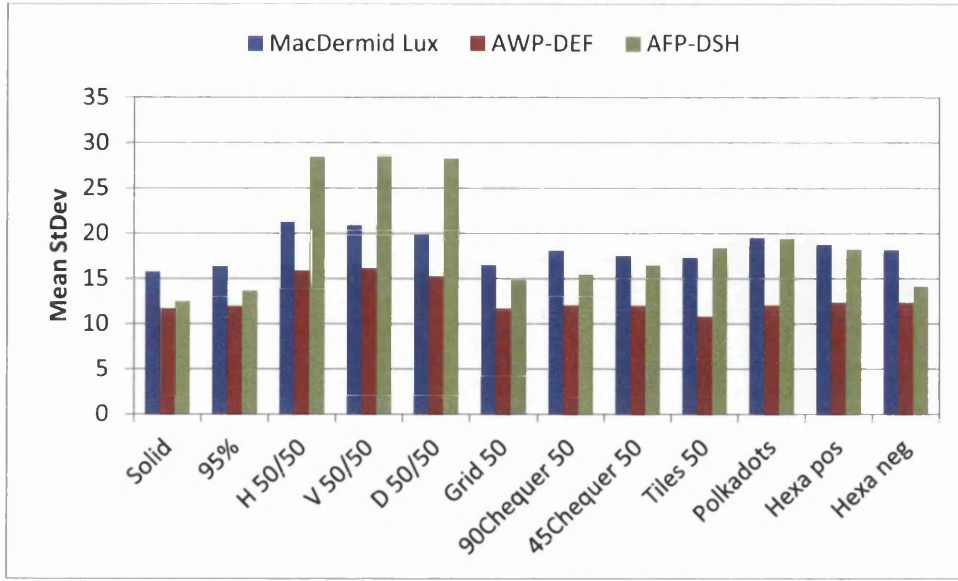


Figure 6.8: Comparison of mean StDev (averaged over all printing conditions of the entire experimental plan) for MacDermid Lux (Plate 1) and Asahi plates

In general the direction and magnitude of the main factor effects were similar on all three plates. Therefore, the parameter effects determined for the Asahi plates on the IGT-F1 in the previous chapter remain applicable for the MacDermid Lux plates. However, the printing force was an exception. On the MacDermid Lux plate, the force had no significant or only a smaller effect on MGSL (Figure 6.9) and StDev (Figure 6.10), when the printing force was changed from 50 to 150N. The effect was positive for some and negative for other printing patches. On the Asahi plates, printing force had a significant negative effect throughout. The Asahi plates suffered from a loss in area coverage and exhibited reduced edge sharpness. This made them more sensitive to deformation under pressure, whereas the MacDermid Lux features retained their geometry and were able to distribute the pressure load better (Anderson and Schlotthauer, 2010). Furthermore, the deformation of the softer MacDermid Lux plate took place within the plate layers rather than at the top of the printing features (Mirle, 1989).

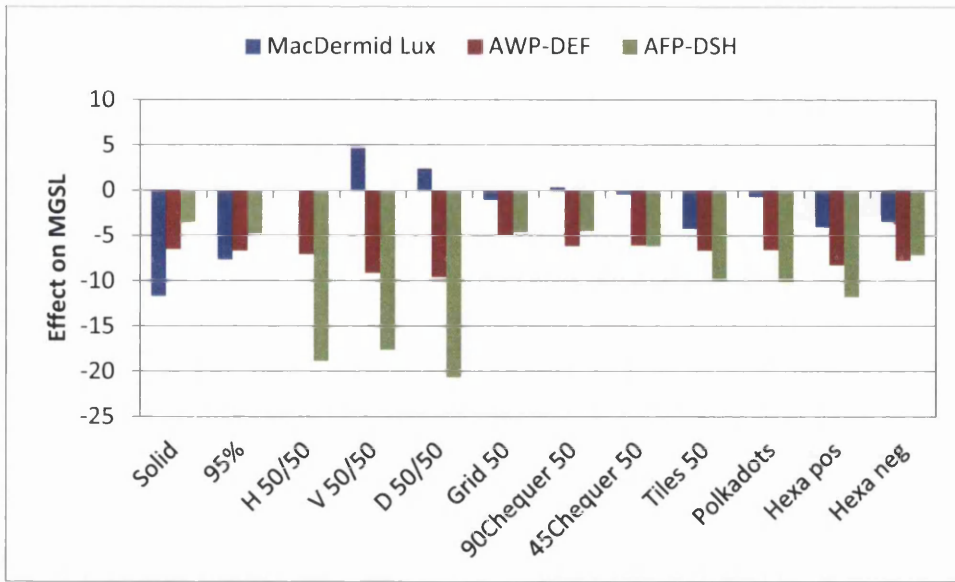


Figure 6.9: Effect of printing force on MGSL for MacDermid Lux (Plate 1) and Asahi plates

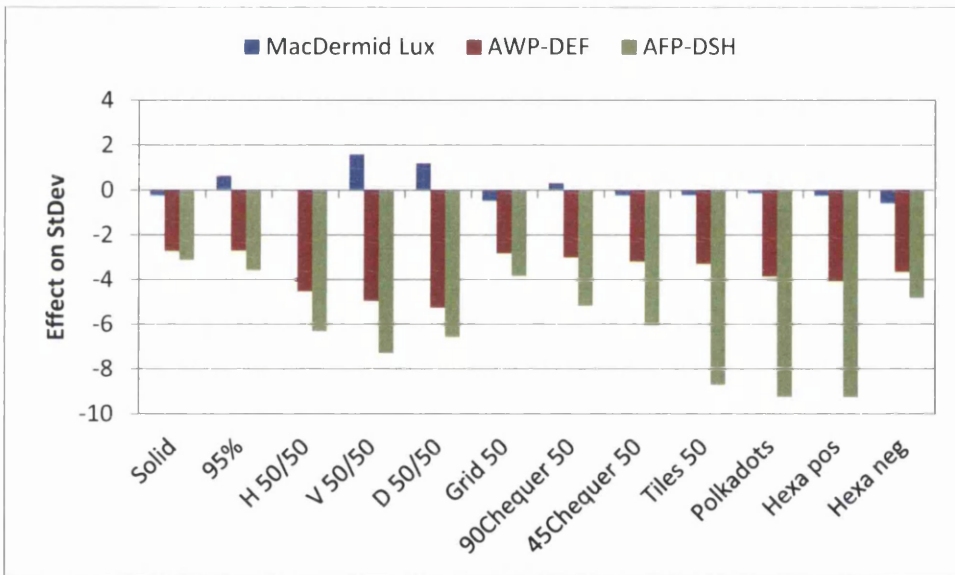


Figure 6.10: Effect of printing force on StDev for MacDermid Lux (Plate 1) and Asahi plates

6.1.3.3 Effect of Microcell versus Meso-patterns

To investigate microcell patterns in comparison with meso-patterns, as well as the plain reference solid, Plate 2 contained seven of the original meso-patterns and four solid printing patches superimposed with microcells (patterns as outlined in Table 6.3). The patches including microcells, which are in essence patterns of recesses analogous to the 95% and negative hexagon meso-patterns, produced lighter prints (Figure 6.11) and had less impact on MGSL (Figure 6.12) than most of the other pattern geometries. There was only a very small number of process parameter combinations for which the microcells achieved higher density.

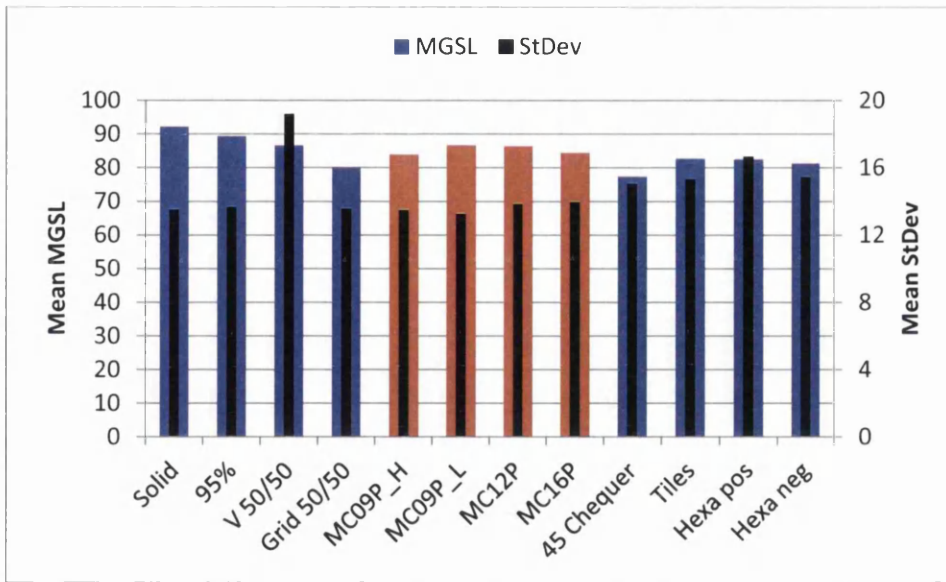


Figure 6.11: Mean MGSL and mean StDev (averaged over all printing conditions of the entire experimental plan) for plain solid reference and all surface patterns on MacDermid Lux (Plate 2) (microcell patterns – orange; meso-patterns – blue)

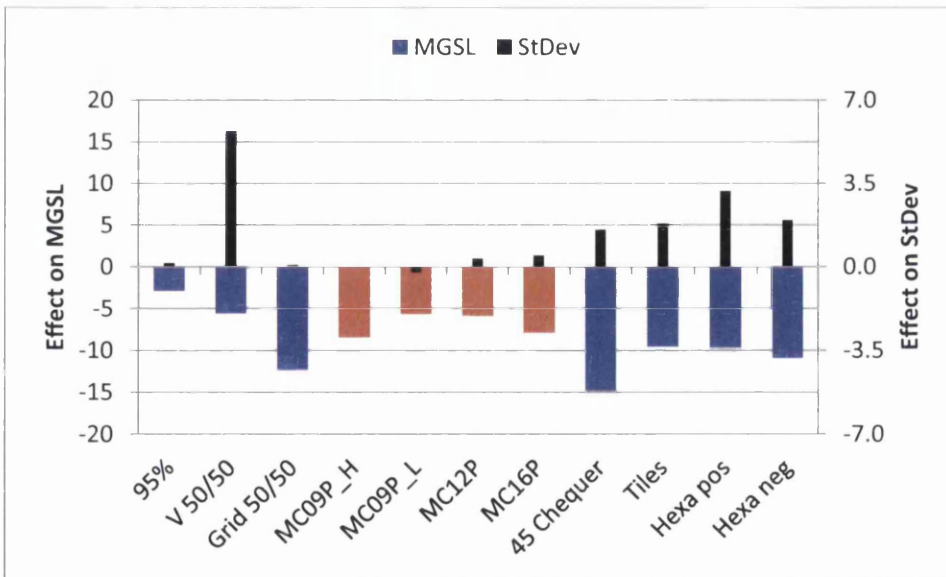


Figure 6.12: Main effect of surface patterning on MGSL and StDev for all surface patterns on MacDermid Lux (Plate 2) (microcell patterns – orange; meso-patterns – blue)

In the previous chapter it could be concluded that meso-patterns act analogous to anilox cells in conjunction with water-based but not UV-curing ink, and the study of micro-patterns corroborates this. Using UV-curing ink which remains on the printing features, the mean MGSL improves with the area coverage of the pattern on the printing plate, as this results in higher area coverage on the prints (Figure 6.13). The ink volume that the pattern recesses can potentially hold is of little consequence with UV-curing ink, because the recesses are not being flooded (Figure 6.14). The opposite can be observed for prints with water-based ink. The lower the pattern area coverage and the larger the recess volume⁷, the darker are the prints. The microcells had significantly higher area coverage (Figure 6.4) than most of the meso-patterns which provided a small advantage for prints with UV-ink. However, they also had a lower recess volume, as illustrated by Figure 6.15, which strongly hampered water-based prints and led to the overall reduced patterning effect on MGSL (Figure 6.12).

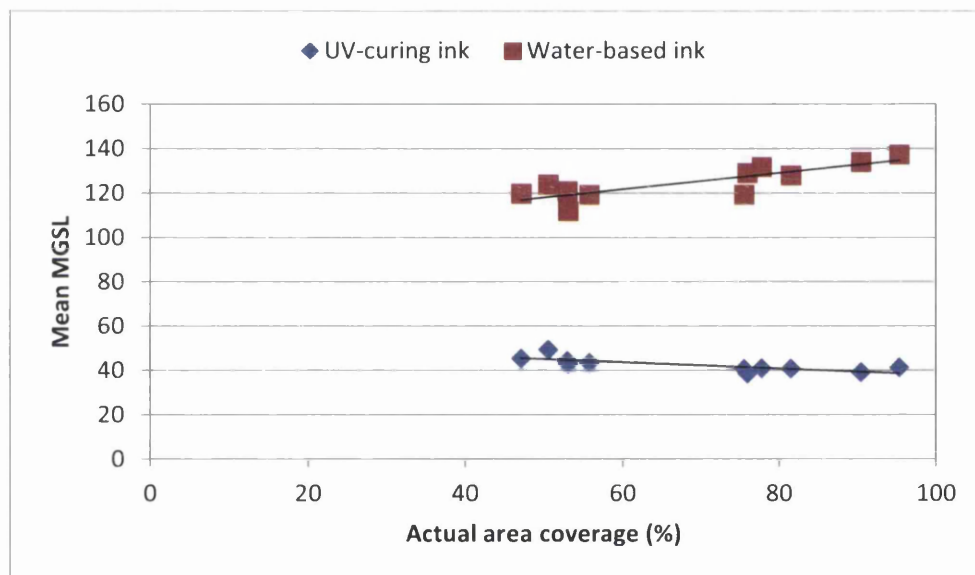


Figure 6.13: Correlation of area coverage on MacDermid Lux (Plate 2) with mean MGSL (averaged over all printing conditions of the entire experimental plan involving the respective ink type)

⁷ The recess volume was estimated assuming conical recesses for the microcell, 95% and negative hexagon patterns, and pyramidal recesses for the grid and chequer patterns (choice informed by WLI data) on a square area of ten millimetres side. The recess depth and width was obtained from the WLI data and examples of recess profiles are shown in Figure 6.15. No volume data was calculated for the tile and positive hexagon patterns which contained freestanding features.

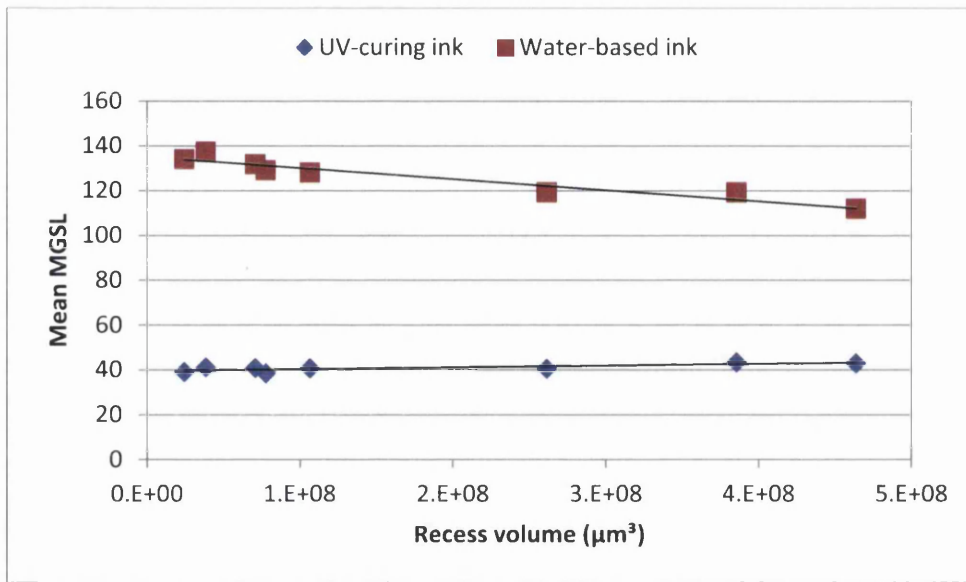


Figure 6.14: Correlation of recess volume on MacDermid Lux (Plate 2) with mean MGSL (averaged over all printing conditions of the entire experimental plan involving the respective ink type) for all surface patterns except V50/50, tiles and positive hexagons

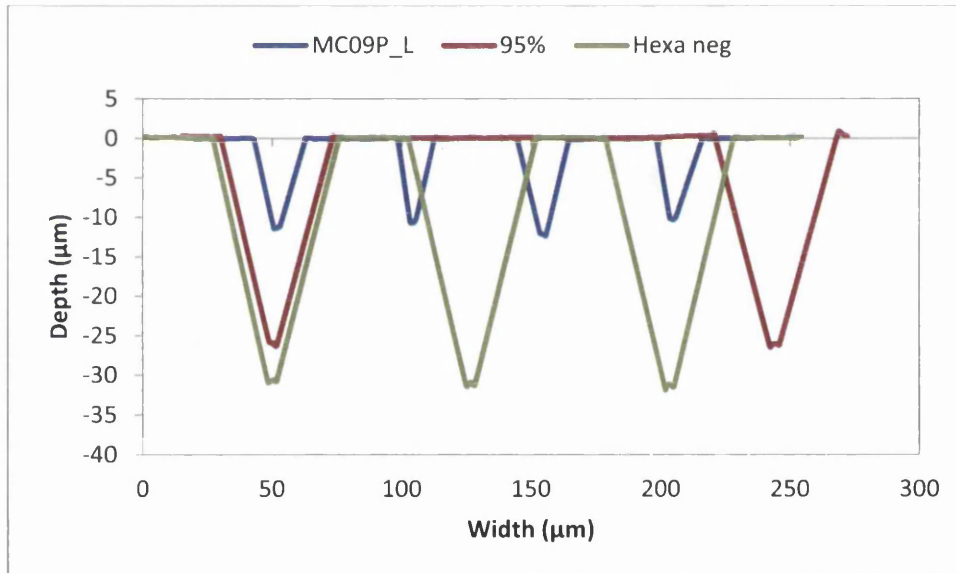


Figure 6.15: Example profiles of selected microcell and meso-patterns featuring recesses

The effect of surface patterning on print uniformity was also highly dependent on the ink type used (refer to section 5.1.4.8). The high opacity of the UV-curing ink did not allow the observation of any fingering instability in the prints featuring closed ink films (Figure 6.16). The only visible printing defects for UV-curing ink were UCAs which remained where the patterns failed to create closed ink films on the substrate. The extent of UCAs was directly dependent on the pattern area coverage, as high area coverage aids the ink film coalescence and thereby print uniformity (Figure 6.17). The observable trend in print uniformity improvement with decreasing recess volume relates directly to

area coverage (Figure 6.18), because the recesses volume is inversely proportional to the area coverage. The microcell patterns led to fewer UCAs in the UV-prints due to their high area coverage, small recess volume and feature pitch. Thus the calculated effect of microcell patterning on print uniformity (Figure 6.12) was governed by the data obtained from prints made with water-based ink featuring fingering instabilities which reduced print uniformity, representing a worst case result.


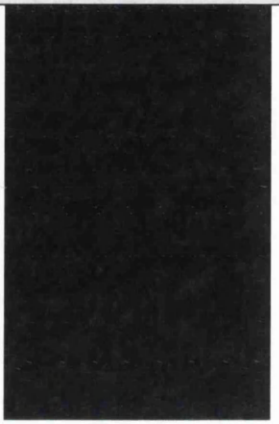
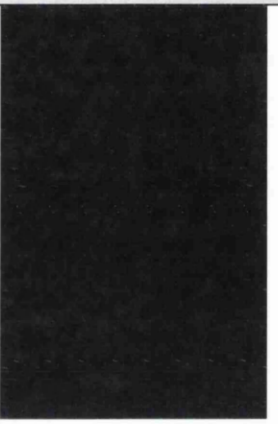
Name	Reference solid	95%	MC09P_L
Area coverage	100%	95.4%	90.5%
			

Figure 6.16: Lack of defects in prints made with UV-curing ink (APCO substrate, MacDermid Lux (Plate 2), speed = 0.2 m/s, force = 50 N, anilox volume = 8 cm³/m²; 7x magnification)

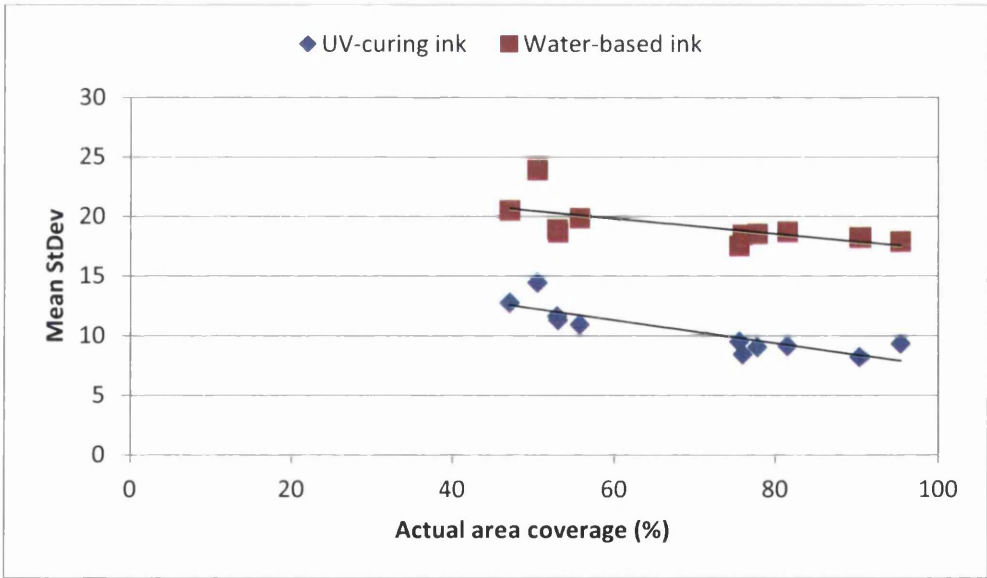


Figure 6.17: Correlation of area coverage on MacDermid Lux (Plate 2) with mean StDev (averaged over all printing conditions of the entire experimental plan involving the respective ink type)

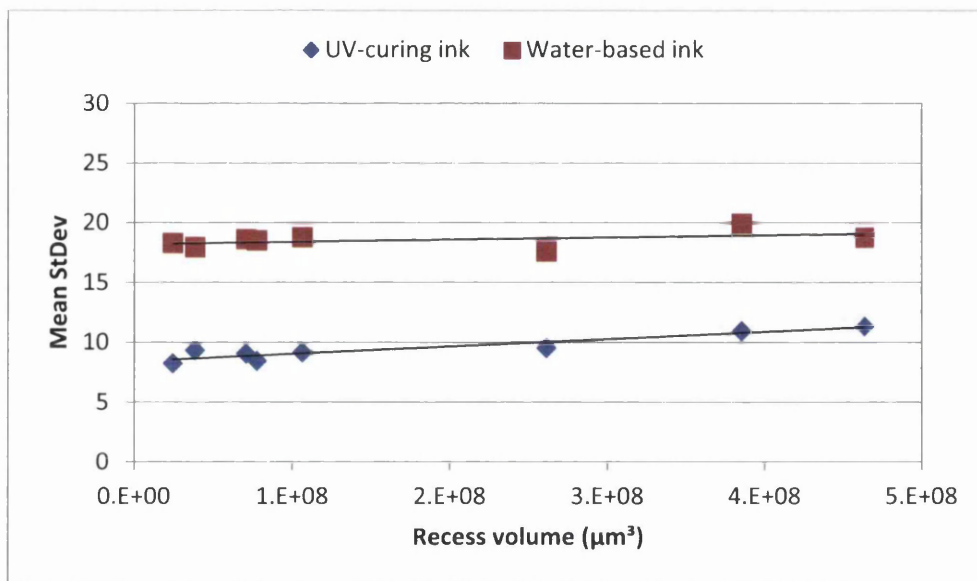


Figure 6.18: Correlation of recess volume on MacDermid Lux (Plate 2) with mean StDev (averaged over all printing conditions of the entire experimental plan involving the respective ink type) for all surface patterns except V50/50, tiles and positive hexagons

Although the microcell patterns did not perform exceptionally by improving the print density of water-based prints, they led to improvements in print uniformity. The patterns MC09P_H and MC09P_L achieved a small negative main factor effect implying more homogeneous prints than the reference solids (Figure 6.12). However, the effects were too small to be recognised as statistically significant. Also not significant was the positive effect of the 95% and grid patterns which, together with the two larger microcell patterns (MC12P and MC16P), had the least detrimental effect on print uniformity. These six patterns have in common that they are made up of holes entirely surrounded by a land area. Thus a trend may be deduced from this factor, although the negative hexagon pattern, which by definition is also a hole pattern, did not fit with this observation. This may be attributed to the larger size of the land area: the negative hexagons have a land area coverage of 55.7%, whereas none of the others fell below 75% (Figure 6.4). This is confirmed by the correlation of area coverage with print uniformity (Figure 6.17). The recess ink had little impact on print uniformity (Figure 6.18).

The demarcation in area coverage was accompanied by a transition in printing defects. The solid reference (100% area coverage), 95% (95.4%) and microcell patterns (90.5% to 76.0%) exhibit defects of viscous fingering (Figure 6.19). The grid pattern (75.5%) showed the transitional formation of small beads on top of the viscous fingers. The negative hexagons and open patterns with freestanding features (55.7% to 47.1%) exhibited extensive beading. It appears that hole patterns are able to counteract the evolution of filaments during ink film splitting which leads to beading. The

transition in fingering patterns might not only be due to effects of area coverage, but also to the difference in scale between microcell and meso-patterns as discussed in the next section.

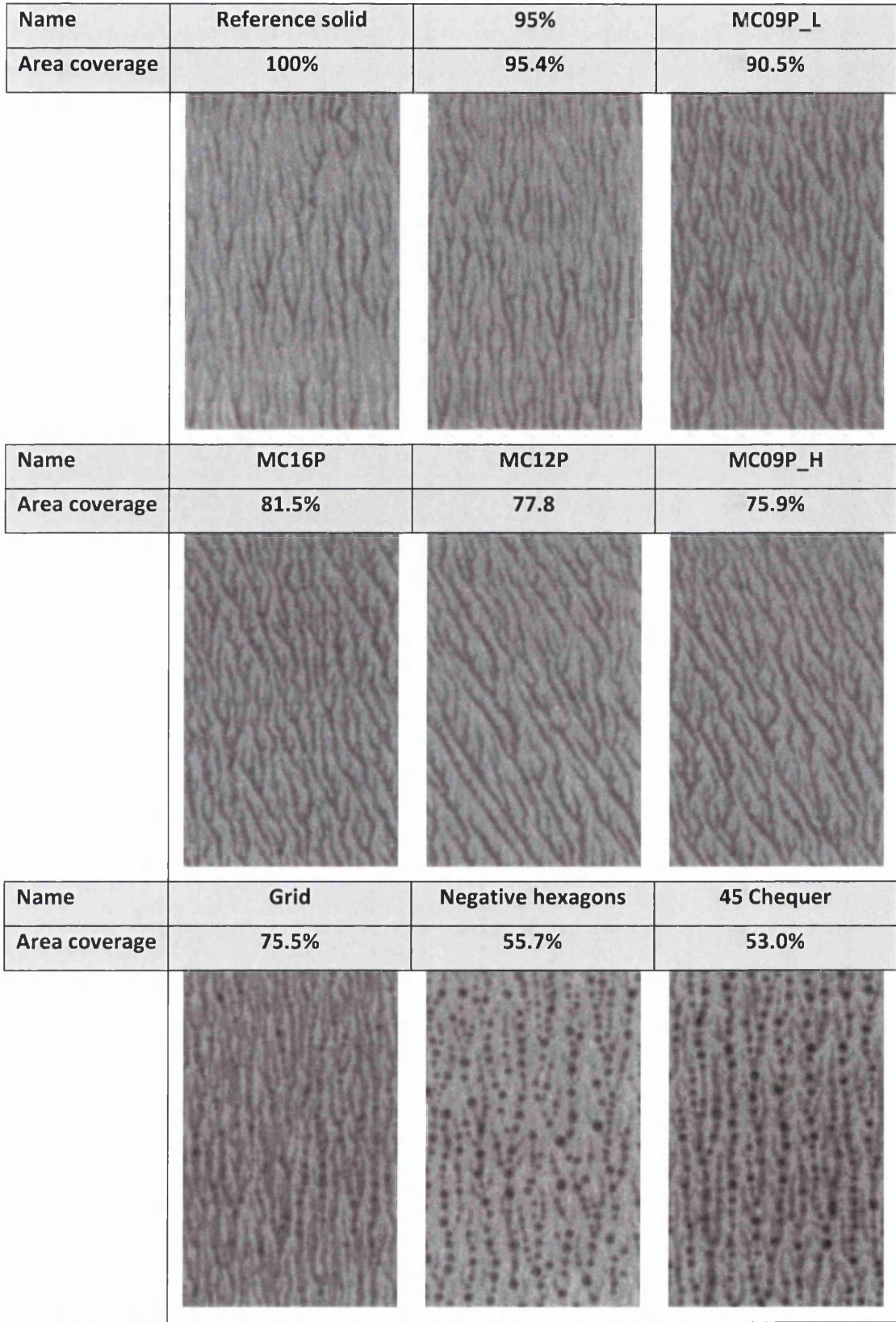


Figure 6.19: Transition of fingering defect regimes with area coverage in descending order (water-based ink on APCO substrate, MacDermid Lux (Plate 2), speed = 0.2 m/s, force = 50 N, anilox volume = 8 cm³/m²; 7x magnification)

6.1.3.4 Effect of Pattern Scaling

In order to bridge the scaling gap between microcell and meso-patterns, this third part of the study, using Plate 3 (patterns as outlined in Table 6.3), investigated four meso-pattern designs at three different scales, the smallest of which was comparable to the size of the microcell patterns. The scaling of the four patterns was adjusted from 100% (original feature size of about 50 μm) to 50% (25 μm) and 200% (100 μm). The proportions of land and recess areas as well as the nominal area coverage were maintained at the three scales (Figure 6.20). The actual area coverage was shown in Figure 6.5.

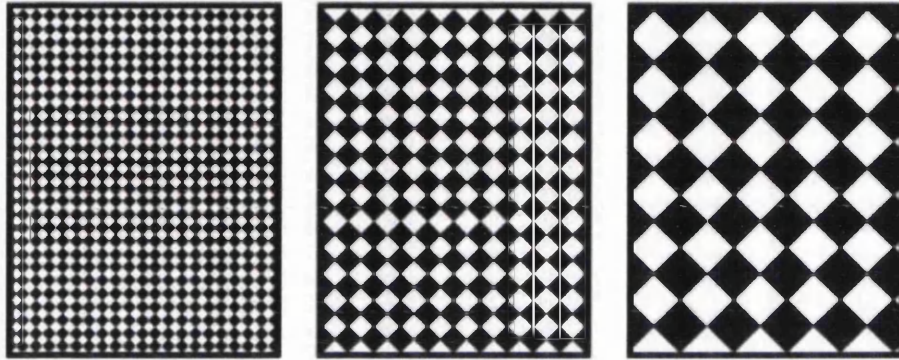


Figure 6.20: Scaling example of chequer meso-pattern designs – (from left to right) 50%, 100% and 200% scaling (50x magnification)

Pattern scaling had an impact on MGSL as well as on StDev (Figure 6.21). The main factor effect of patterning suggests that scaling had no consistent influence on MGSL for three of the four patterns investigated (95%, grid and chequer at 45° tilt) (Figure 6.22). Only for the tile pattern did the magnitude of the patterning effect increase steadily with decreasing feature size. This was directly related to the print uniformity, because smaller patterns resulted in lower StDev and more homogeneous prints. The larger patterns (200% scaling, about 100 μm feature size), as well as the original tile pattern (100% scaling, 50 μm), showed increased value, meaning a deterioration of print uniformity. This observation is very much in agreement with the claims of Samworth (2001), Stolt, Zwadlo and Rozzi (2010) that micro-patterning is required to improve uniformity. The origin of the improvement in print quality can be attributed directly to the two functionalities of surface patterns identified in the previous chapter (refer to section 5.1.4.8)

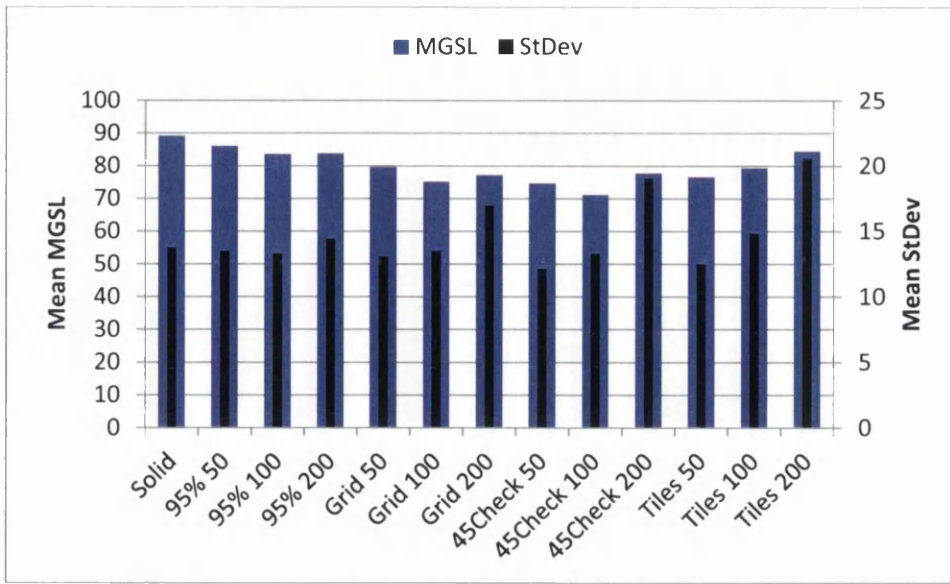


Figure 6.21: MGSL and StDev of entire experimental plan for plain solid reference and all surface patterns on MacDermid Lux (Plate 3) (50/100/200 denoting pattern scale in percent)

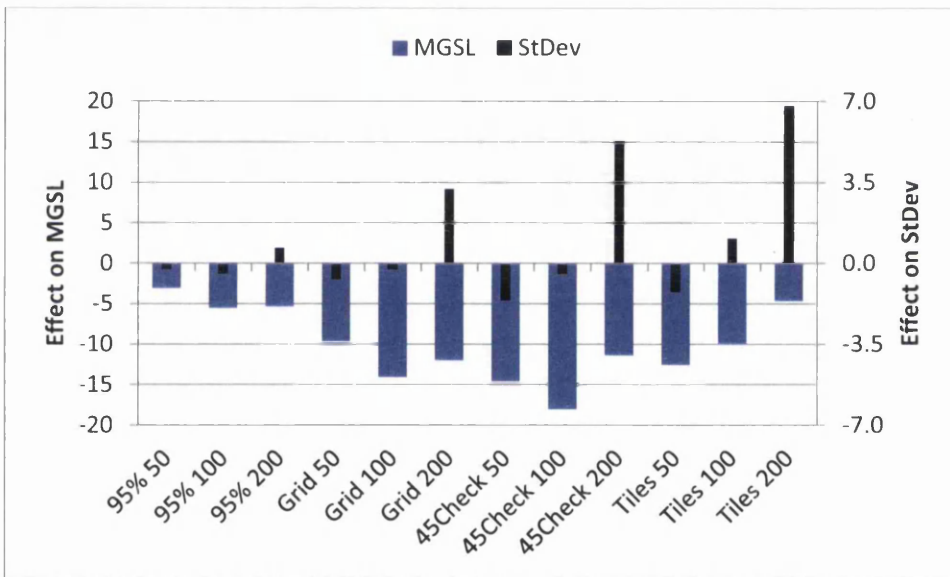


Figure 6.22: Main factor effects of patterning on MGSL and StDev for different pattern scales on MacDermid Lux (Plate 3) (50/100/200 denoting pattern scale in percent)

The printing defects observed for the UV-curing ink are related to the reproduction of the surface patterning from the plate in the prints (Figure 6.23). At the largest scale individual printed elements are discernible for the chequer and tile patterns. This printing defect is due to a lack of ink coalescence between neighbouring features through squeeze action, confirmed by the fact that higher anilox volume and printing pressure facilitated better coalescence. At medium scale an ink film disrupted by small UCAs is created which transforms to a very uniform, closed ink film at the smallest scale caused by the ink squeeze. Figure 6.24 shows the 95% and grid patterns at the largest

scale which exhibit printed patterns of areas with increased ink film thickness. The geometry of these areas corresponds to the non-printing regions of the pattern patches on the printing plate. This suggests that the printing force was of sufficiently high magnitude to squeeze out most of the ink from under the printing features and into the pattern recesses to coalesce.

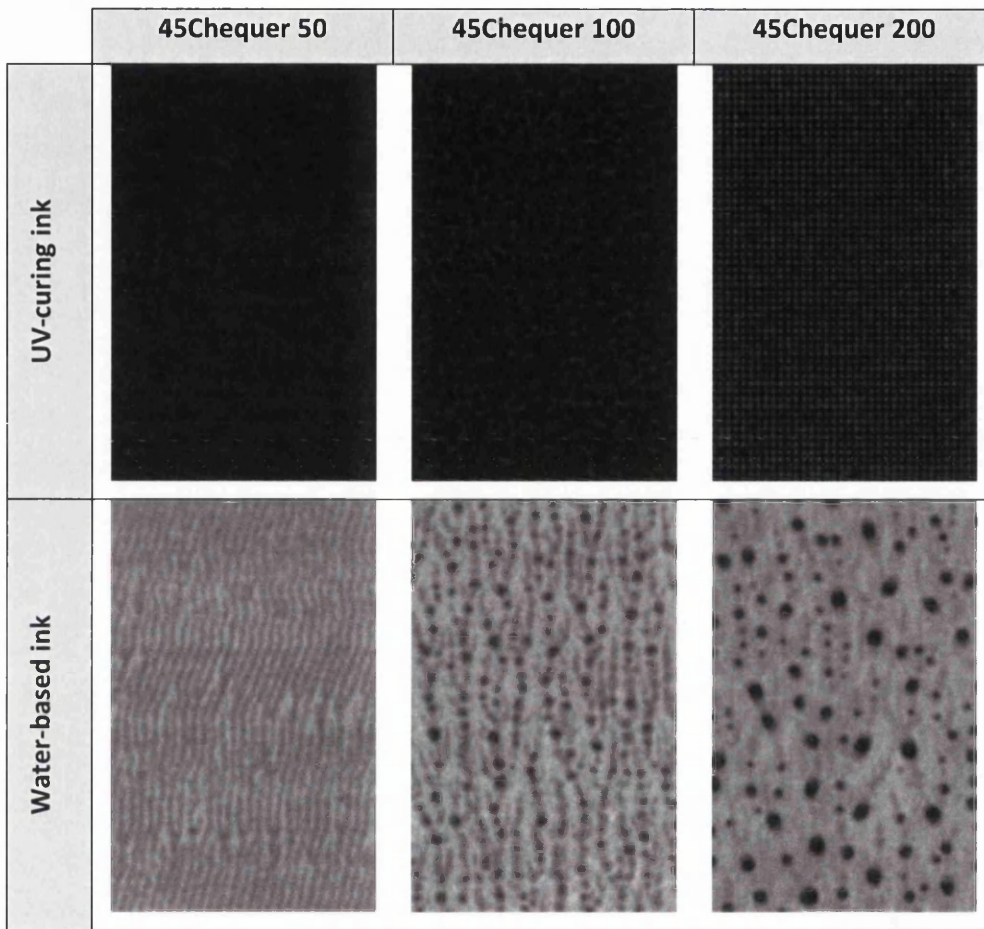


Figure 6.23: Transition of printing defects with pattern scaling for chequer pattern at 45° tilt (50/100/200 denoting pattern scale in percent) (APCO substrate, speed = 0.2 m/s, force = 50 N, anilox volume = 8 cm³/m²; 7x magnification)

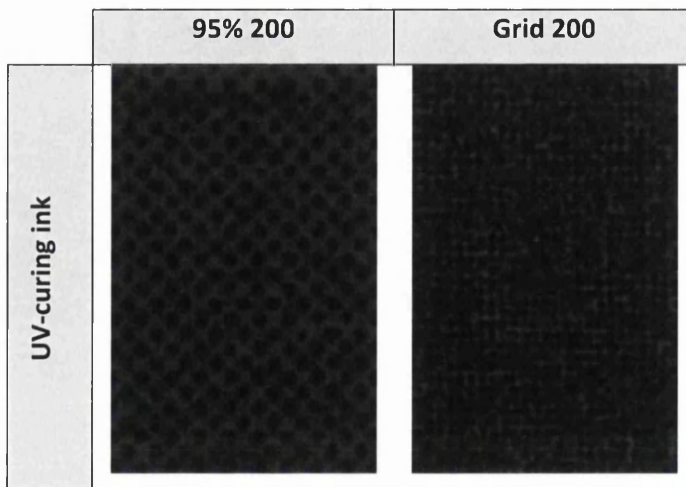


Figure 6.24: Samples indicating ink squeeze at high printing force (200 denoting pattern scale in percent) (APCO substrate, speed = 0.2 m/s, force = 50 N, anilox volume = 8 cm³/m²; 7x magnification)

The print uniformity of water-based ink samples was governed by fingering instabilities which changed appearance with pattern scaling. At large scale the printing defects observed for all patterns were beads. Reducing the pattern scale also changed the bead pattern (size of the actual beads as well as the intervals at which they occurred). Further reduction resolved the beads and the underlying viscous fingering pattern remained. Depending on pattern and printing conditions, the viscous fingers transformed to ribs at the smallest pattern scale. The example provided in Figure 6.23 demonstrates the transition from beads to ribs for the chequer pattern. This suggests that plate features act as anchor points during ink film splitting. Ink filaments pin to the features and cause a local increase in the ink volume deposited after the filament breakup. The smaller the pattern features and the higher the frequency of their occurrence, the more ink filaments are created during film splitting. More and thereby finer filaments result in less obtrusive printing defects. This is in agreement with Griesheimer (2014) who performed initial investigations into the effect of pattern scale on filament formation using halftone dots, and observed that more secondary filaments are created at smaller scale. Furthermore, this mechanism corroborates the findings of the previous section that the microcell patterns of smaller recess diameter and feature pitch have a particularly beneficial effect on print quality.

6.1.4 Conclusions

This investigation formed an extension to the meso-pattern trial conducted on the IGT-F1 and discussed in the previous chapter which sought to determine the effect of different meso-patterns on print density and uniformity. The three more detailed studies in this chapter served to

- verify the parameter effects for meso-patterns created by a “flat-top” imaging technology on a different plate material,
- compare the effectiveness of microcell versus meso-patterns, and
- identify the effect of pattern scaling.

In general, as for the findings on the Asahi plates, all results achieved by the patterns on the MacDermid Lux plates were highly dependent on the combination of experimental parameters used. The MacDermid plates imaged with LUX technology allowed almost perfect fidelity in the transfer of the image information from the artwork to the plate. MacDermid Lux improved the impact of surface patterning on print density because of the increase in the pattern area coverage and recess volume which corroborates the dual functionality of surface patterns depending on ink type used.

A good correlation was found between area coverage and print density for UV-prints as well as recess volume and print density for water-based prints. This applies equally to microcells, micro- and meso-patterns. It is possible that transitions between pattern functionalities take place dependent on pattern design, material and process parameters. The smaller the pattern scale and the shallower the pattern recesses, the more likely the recesses are to be filled with ink independent of ink type.

The print uniformity was determined by pattern geometry, area coverage, feature size and pitch. The creation of closed ink films with UV-curing ink relies on the ink squeeze in the printing nip. Hole patterns, such as microcells, and small feature pitch, as achieved by very small pattern scaling, improve ink coalescence of neighbouring depositions, because the ink has to be displaced over a shorter distance. The appearance of fingering instabilities (ribs, viscous fingers, beads) in water-based prints also profits from lower feature pitch. The pattern features act as anchors for ink filaments during film splitting. The smaller the feature size and pitch, the finer is the ink filamentation and the more uniform the resultant printed ink film. This was confirmed by comparing the prints of different scale meso-patterns. Patterns with lower area coverage, isolated features or large-diameter recesses led to a transition in printing defects to very distinct beads which was attributed to the formation of large filaments pinned to the pattern features during the film splitting process.

6.2 Microcell Pattern Effect using an Industrial Printing Press

The knowledge gained in the study of microcell patterns on the IGT-F1 was explored further on the T-Flex 508. Since the print trial of meso-patterns on the T-Flex 508 failed to produce solid prints (refer to section 5.2.3), it was decided not to repeat an entire stand-alone study for microcells on the press. Instead printing patches containing microcells were included in the test image investigating dot geometry on the T-Flex 508 (refer to Chapter 4).

This setup on the one hand allowed studying the influence of microcell patterns on the optical density and print uniformity produced by halftones and solids under different printing conditions. On the other hand, the influence of imaging technology in conjunction with microcell patterning could be investigated. A previous trial had indicated that the use of MacDermid LUX “flat-top” imaging technology with microcells improved print optical density compared to standard digital technologies (MacDermid Printing Solutions, 2011; Cook, Recchia and Gotsick, 2014). The work in this chapter will be aimed at exploring this independently.

6.2.1 Materials, Printing and Print Characterisation

Detailed information on the experimental order, material and process parameters was provided in Chapter 4. Due to the small number of variable parameters, no experimental plan was required for the execution and analysis of this study. The MacDermid Lux (“flat-topped”)⁸, MacDermid and Asahi plates (both “round-topped”) carried identical test images (Figure 6.25) of which the following elements were relevant for the investigation of microcell patterning:

- Solid patches with
 - microcell patterns MC09P_L, MC09P_H, MC12P and MC16P and
 - in-house patterns Grid (50 µm track and gap) and Chequer (50 µm at 45° tilt);
- Halftone scales in CMYK consisting of
 - 10 area coverages (20, 30, 40, 50, 60, 70, 80, 90, 95, 100%) each at
 - 100 lpi line rulings without microcells and 100 lpi with microcells MC09P_H.

The two meso-patterns were included in the investigation for the purpose of reference and comparison with the previous trial. By default microcells cannot be superimposed on halftone dots below 20% nominal area coverage, so that only halftones of 20% upwards were taken into account for the analysis. The plate features were characterised using WLI and this will be explained in section 6.2.2.1.

⁸ The Kodak plate was excluded from the study, since the proprietary Kodak Flexcel NX imaging technology did not allow the superimposition of microcells in the image.

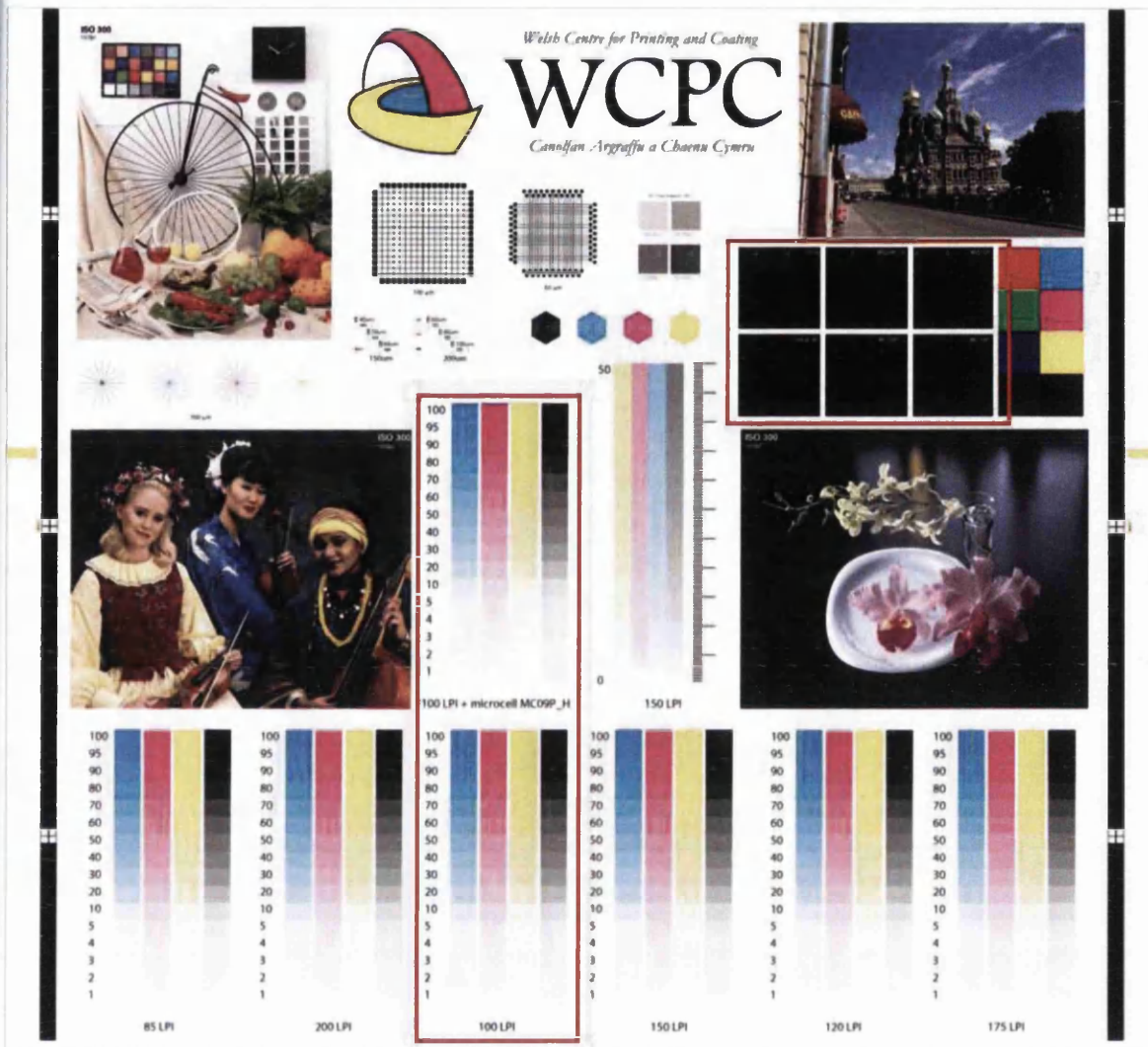


Figure 6.25: Image for microcell trial on the T-Flex 508 (image parts contained in red boxes taken into account for image analysis: red boxes not included in actual image) (0.35x magnification)

The visual inspection of the prints was performed on the Keyence digital microscope. Based on the experiences with meso-patterns reproduced on the T-Flex 508, it was deemed sufficient to determine the optical density of the relevant image elements under investigation by spectrophotometry (eight consecutively printed sheets for each experimental number were measured). Conclusions on print uniformity were drawn from visual and optical density data. Data was obtained for the halftone scales for all four process colours CMYK, but only the analysis of the black prints is presented here due to similarity in the results.

6.2.2 Results and Discussions

The results are presented separately for microcells on solids and halftones. The information obtained from the measurement of optical density is explained in conjunction with observations from print uniformity.

6.2.2.1 Plate Characterisation

The area coverage of patterned solids for the Asahi and MacDermid plate materials was expected to be smaller than the nominal value due to oxygen inhibition during the polymerisation process. On the Asahi plate the three smaller microcells patterns exhibited significant increases in area coverage (Figure 6.26) which was the result of insufficiently cross-linked polymer molecules on the plate surface being eroded during washout. Thus the depth of the microcells was decreased (Figure 6.27) and, taking into account the higher surface roughness of the AWP-DEF material, the area coverage increased. The MC09P_H and MC09P_L microcells were shallow such that peaks and troughs became comparable with surface roughness, thus approximating 100% area coverage. The smoothness of the MacDermid material did not allow the capture of WLI data from the cell shoulders, therefore the area coverage determined was significantly smaller than for the other two plate materials. On the MacDermid Lux plate the surface remained intact and the microcells were distinctive (Figure 6.27). Actual and nominal area coverage almost matched.

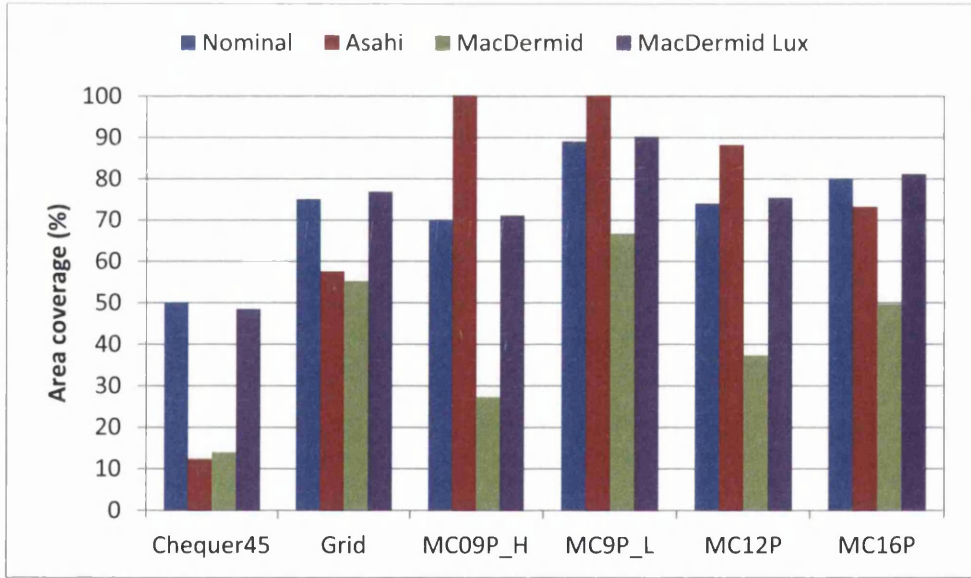


Figure 6.26: Actual area coverage of micro- and meso-patterns on printing plates investigated on the T-Flex 508

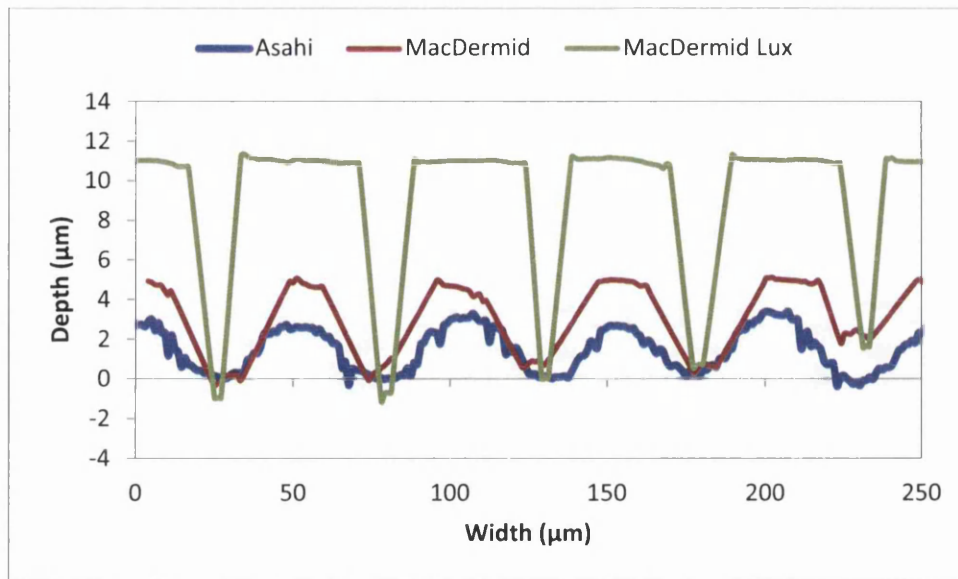


Figure 6.27: Surface profile of solid superimposed with MC09P_L microcell pattern (missing WLI data on microcell shoulders of MacDermid and MacDermid Lux plates was interpolated from captured data at peaks and troughs)

Examples of microcells superimposed on a halftone dot are shown in Figure 6.28. The superimposition of microcells on to halftones had varying effects on dot geometry for the different plate materials (Figure 6.29). On the Asahi plate the masked areas used to create microcells during plate-imaging reduced the oxygen inhibition. Improved polymerisation of the plate surface took place which decreased the removal of plate material during washout. The resultant dot geometry shifted from convex and relatively flat dots to more concave which exhibited the effects of polymer shrinkage⁹. Midtones and shadows exhibited erratic changes in cupping depth due to the number and placement of microcells on the dot. The algorithms in the imaging software align the centre of the microcell array with the centre of the halftone dot. Then the dot surface is progressively filled with cells from the centre outwards to the dot edges. The algorithms prohibit the coincidence of microcell and dot edge in which case no further cells are placed. In this way the distance between the microcell and dot edge varies (Figure 6.28). Microcells placed very close to the dot edge hamper polymerisation, decrease the edge height and thereby reduce the height difference of edge to centre (i.e. cupping depth). The further away from the edge the microcell is located, the better the edge formation and deeper the cupping.

On the two MacDermid plates the microcells had less effect on the cupping (Figure 6.29), because the height difference of cup edge to centre of the dot was created by a narrower rim around the dot circumference which was not wide enough to experience significant changes through microcells

⁹ Detailed explanations of dot top geometries, polymer shrinkage and cupping are provided in section 1.2.1.

placed near the edge. In general, where the interference of microcells with the dot edge could be ruled out, there was a tendency of slightly decreased cupping depths for dots with microcells (independent of imaging technology). The internal tensions, created by polymer shrinkage that led to cupping, were partly released by the breakup of the dot surface with microcells. Less tension was exerted on the dot surface and the cupping reduced.

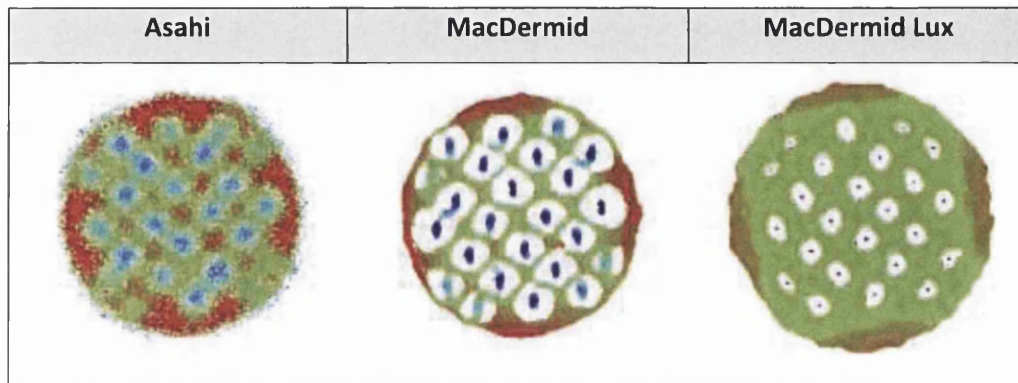


Figure 6.28: Example of microcells superimposed on halftone dots of all three plate types (WLI data – red colour represents raised areas; dot of 70% nominal area coverage, 100 lpi; 150x magnification)

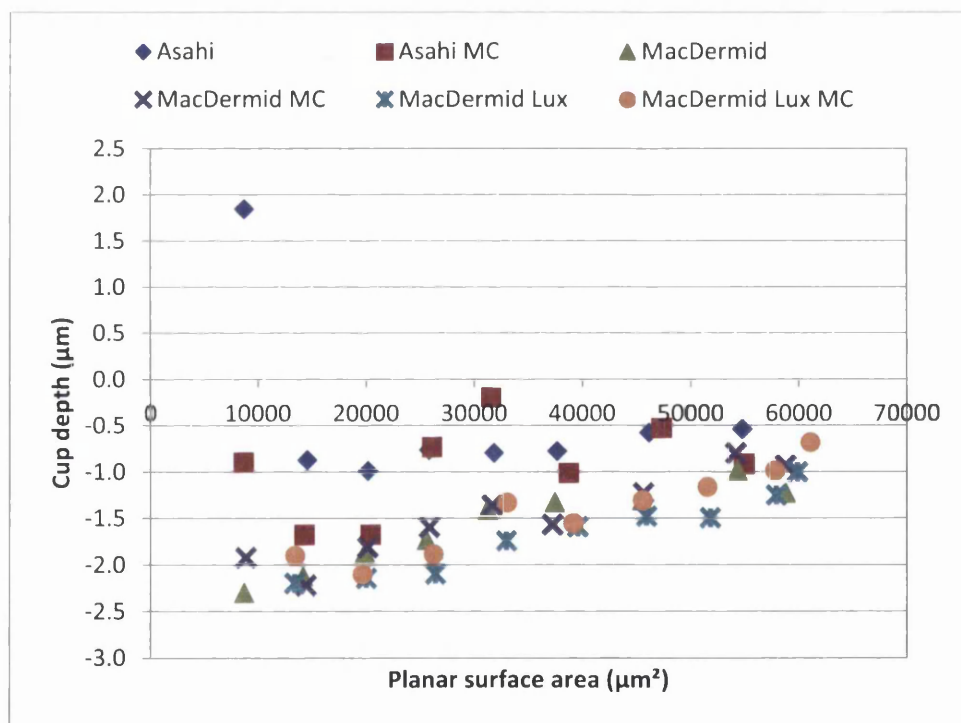


Figure 6.29: Effect of microcells on cup depth of halftone dots on plate ("MC" denotes microcells)

The planar surface area of dots with microcells could not be determined consistently for all plate types. The erosion of the dot surface on the Asahi and MacDermid plates due to oxygen inhibition rendered the WLI data points of microcells, cupping bottom and rim too similar in height, and no clear peak was visible in the height histogram which to use as reference for the separation of the dot

top and shoulder. If the microcells were included in the planar surface area, the area coverage obtained showed no difference between halftones with and without microcells (Figure 6.30) despite their influence on top geometry (Figure 6.29). An exclusion of the microcell area was only possible for the MacDermid Lux plate and showed increasing coverage losses with halftone coverage (Figure 6.31).

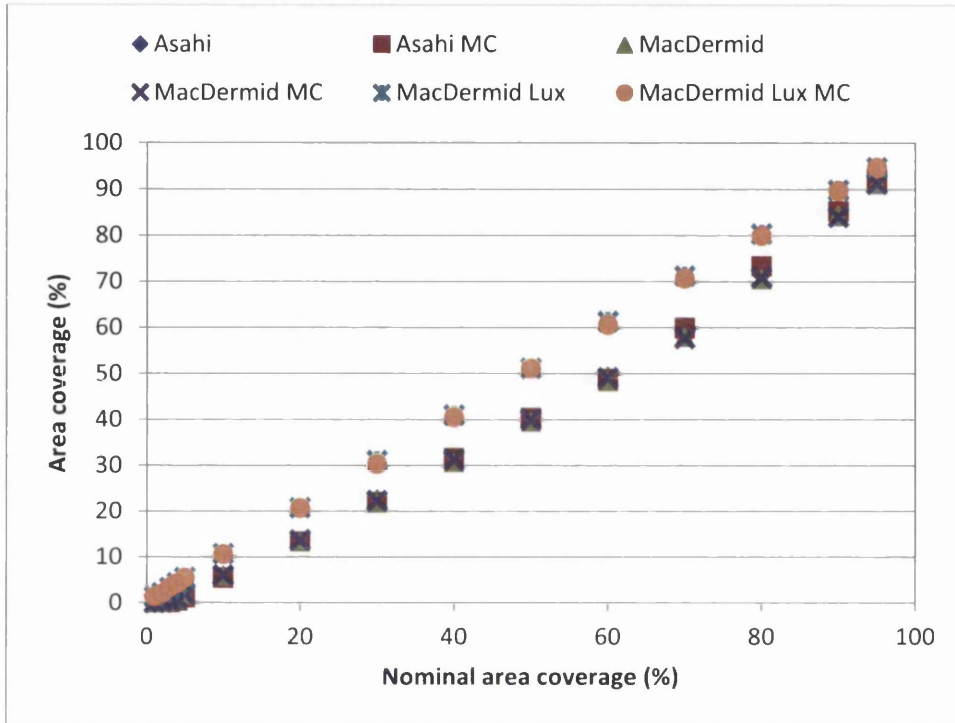


Figure 6.30: Area coverage of halftone dots with and without microcells based on dot edge (MC denoting microcells)

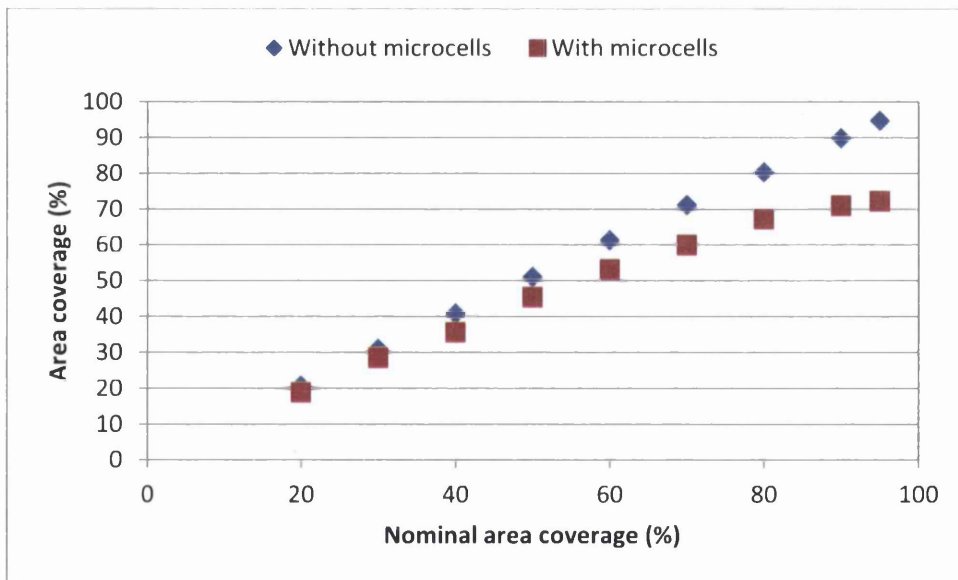


Figure 6.31: Area coverage of halftone dots with and without microcells based on actual data points on MacDermid Lux plates

6.2.2.2 Microcells on Solids

This section details the findings on the effect and functionality of microcell patterns superimposed on solid printing patches. The printing experiment was analysed for optical density (shown in Figure 6.32 to Figure 6.36) and print uniformity (shown in Figure 6.37 to Figure 6.40). The two meso-patterns (grid and chequer at 45° tilt) performed worse than the microcells patterns and reference solid under all printing conditions (refer to Appendix A.10). The reason was the same as for the pattern failure in the meso-pattern trial conducted on the T-Flex 508 and studied in the previous chapter: the area coverage of the patterns and the printing conditions were insufficient to form closed ink films on the substrate. These two patterns were therefore eliminated from the analysis.

Figure 6.32 shows that the optical densities of the plain solids were very similar for all plate types under the given printing conditions providing an equal point of reference. The following graphs (Asahi – Figure 6.33, MacDermid – Figure 6.34, MacDermid Lux – Figure 6.35) display the difference in optical density between the plain solid reference and the microcell patterns (negative values correspond to higher optical density achieved through microcells). A difference of $\Delta D=0.1$ approximates the limit of discernibility for the untrained eye. Within the exploration of process parameters, it was found that for all microcell patterns and plate materials either no significant density difference could be observed between the plain reference solid and microcell patterns, or the solid achieved higher optical densities, because the microcell patterns led to increased UCAs in the prints (refer to Appendix A.10).

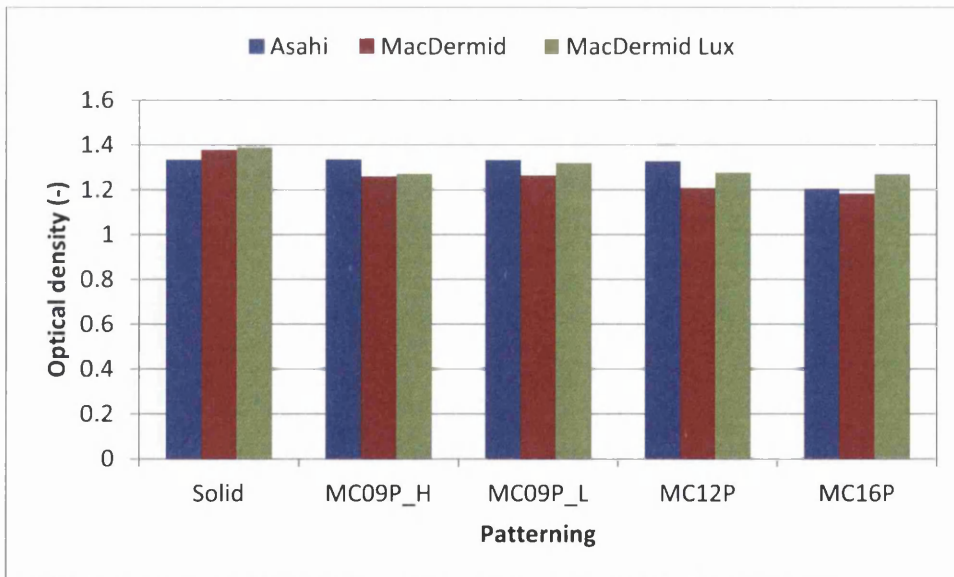


Figure 6.32: Comparison of optical densities for plain solid reference and microcells patches for all plate materials (printing speed of 150 ft/min at 4 thou engagement)

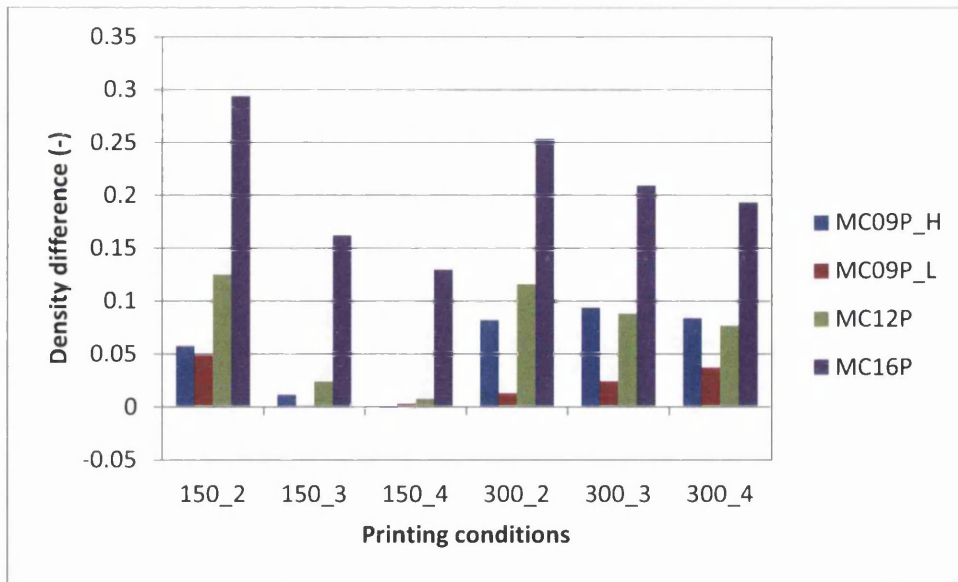


Figure 6.33: Difference in optical density between solids without and with microcells on Asahi plate for different printing conditions (printing conditions: "speed (ft/min)_engagement (thou)")

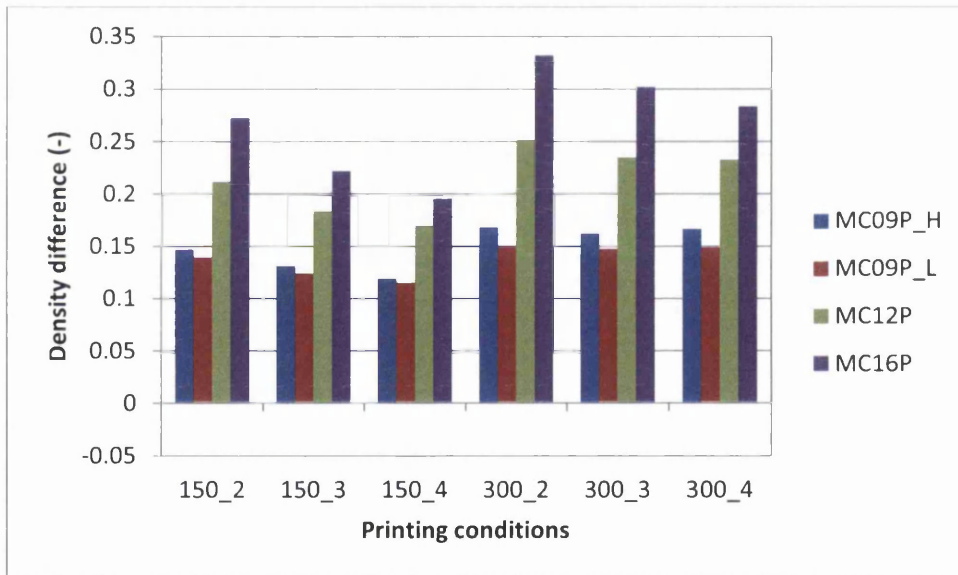


Figure 6.34: Difference in optical density between solids without and with microcells on MacDermid plate for different printing conditions (printing conditions: "speed (ft/min)_engagement (thou)")

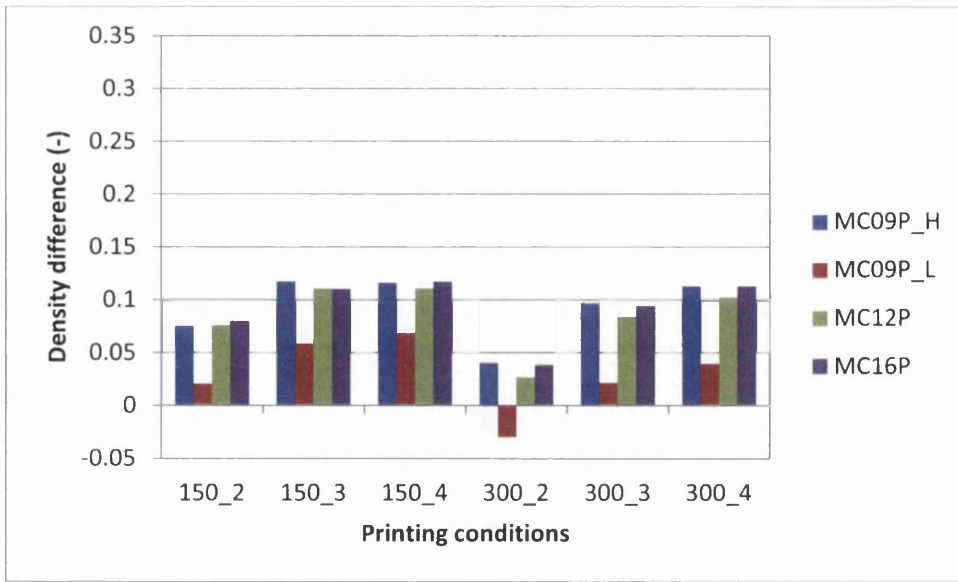


Figure 6.35: Difference in optical density between solids without and with microcells on MacDermid Lux plate for different printing conditions (printing conditions: “speed (ft/min)_engagement (thou)”)

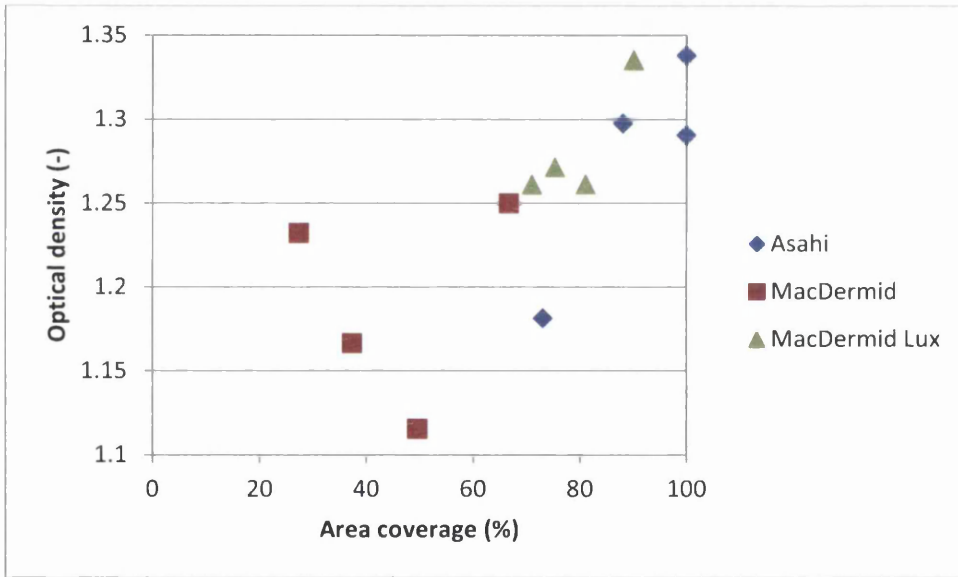


Figure 6.36: Correlation of actual area coverage and optical density for the microcell patterns for all plate materials (printing speed of 150 ft/min at 4 thou engagement)

The correlation of the microcells area coverage on the printing plate and the print optical density confirms the findings from the IGT-F1 study. Since the UV-curing ink is only held on the pattern features, the optical density increases with area coverage (Figure 6.36). The advantage of the Asahi plate was the reproduction of shallow microcells (see Figure 6.27) which made them more likely to be inked up fully by the anilox, thereby achieving higher area coverage in the prints. The slight trend discrepancy in the data of the MacDermid plate is due to the challenges encountered during the determination of the area coverage from WLI data for this material (refer to 6.2.2.1). The true area

coverage might be larger than the determined one, thereby placing the outlying MacDermid data points closer to the range described by the Asahi and MacDermid Lux plates (Figure 6.36).

Figure 6.37 shows prints of the reference solids within which UCAs are present. The discontinuities in the ink film might have been caused by dewetting of the substrate, but the surface energy of the substrate (43.2 mN/m) was sufficiently larger than the ink surface tension (32.4 mN/m) to promote good wetting. It was therefore most likely that the UCAs were caused by air bubbles entrained into the printing nip. The bubbles were trapped during the contact between the plate and substrate, because the non-porous film substrate provided no means by which the air could escape, thereby preventing ink transfer.

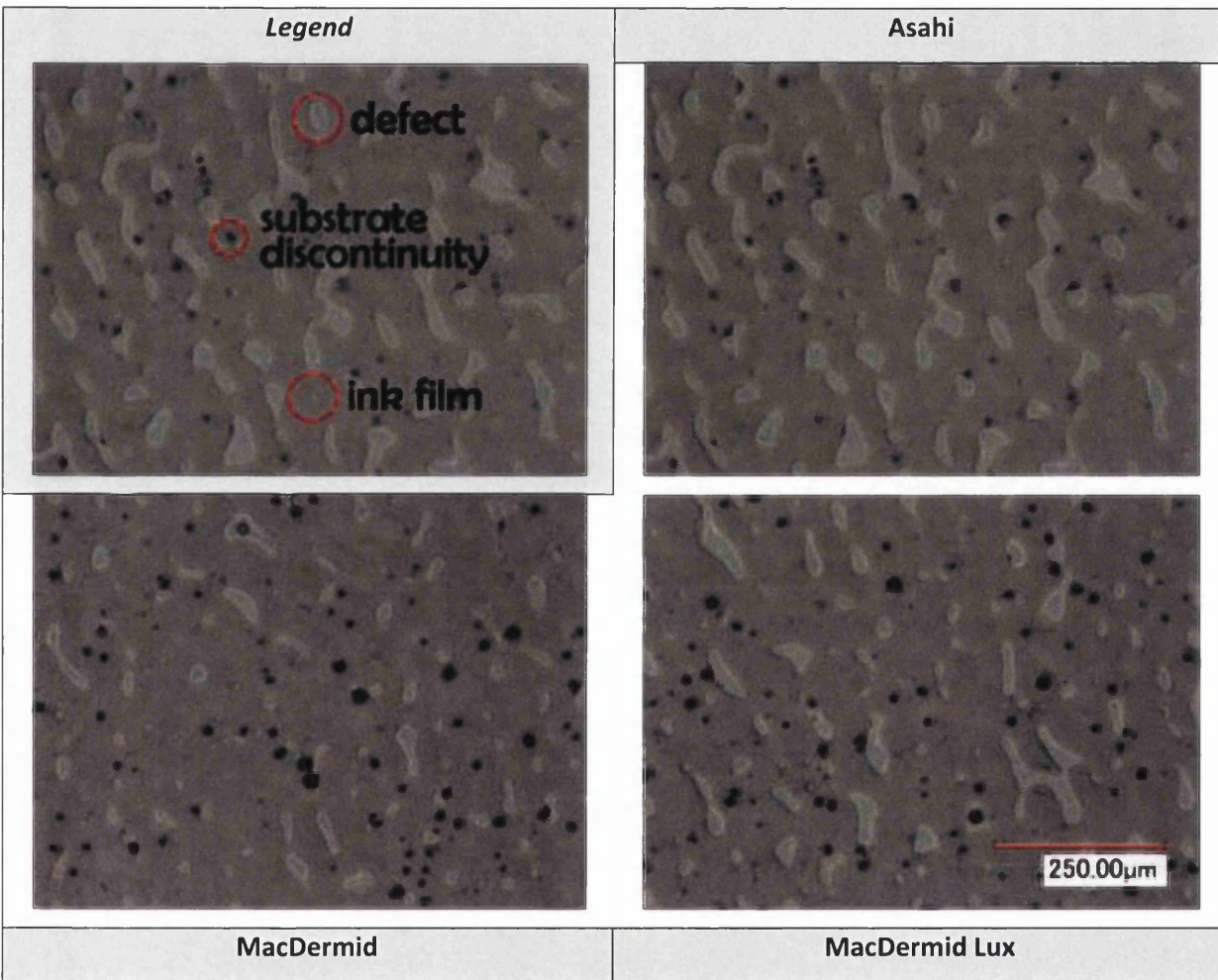


Figure 6.37: Printing defects (UCAs) in printed reference solids caused by air entrapment (printing speed of 150 ft/min, 2 thou engagement)

Although fairly random in size and distribution, the UCAs were distinctive for the different plate materials. The Asahi print stood out from the others, because a more regular pattern was recognisable in the defect distribution. The air bubbles were orientated along lines parallel to the

print direction (Figure 6.38). The average line pitch was 69 μm . This correlates very well with the striae found on the printing plate¹⁰ which were also aligned in print direction at a pitch of about 65 μm (this distance was measured with the plate lying flat and increased slightly through surface expansion during mounting on the round printing cylinder). Both MacDermid plates also exhibited striae, but since these were orientated perpendicular to the print direction, they might not have exerted the same influence on the trapped air bubbles as was observed for the Asahi plate. This raises the question whether the striation patterns can be regarded as surface texturing in their own right, an aspect which was not part of the current research, but merits further investigation.

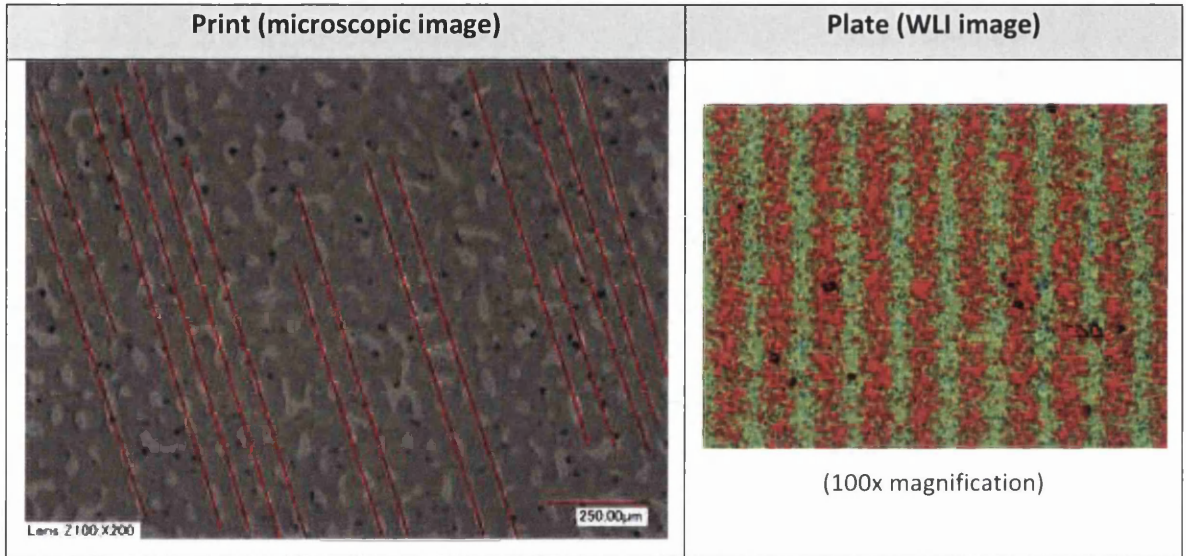


Figure 6.38: Orientation of UCAs in prints along lines similar in frequency to striae on Asahi printing plate (red lines superimposed on microscopic image to highlight alignment of UCAs)

Expanding on the air entrapment model (explained in section 4.4.2.1.2), at low engagement the trapped air bubbles nestle into any free space created by unevenness of the printing plate against the substrate and very irregular UCAs are created in the prints (Figure 6.39). With increasing engagement the UCAs decrease and become more regular in shape and distribution, attributed to the air bubbles being pressed into the remaining caverns between printing plate and substrate which are not closed up fully under pressure. Microcells are thought to constitute such caverns and cause a defined redistribution of the trapped air bubbles in the printing nip (Figure 6.40). The regular frequency of the locations to which the air bubbles are consigned corresponds to the microcell pitch on the plate and this now improves print uniformity. Indications of this additional mechanism were found on all plate materials (Figure 6.41), although it could not be observed in the samples of the trial conducted on the IGT-F1. The effect might have been masked or even completely erased by the

¹⁰ The explanation of the origin of striae is provided in section 4.1. The complete tables of striation images and parameters for all plate types can be found in Appendix A.4.

use of higher-volume anilox rolls on the IGT-F1 (8 and 12 cm³/m²) compared to the T-Flex 508 (3.32 cm³/m²). The lower ink volume supplied would affect the ink distribution and squeeze across printing plate and substrate.

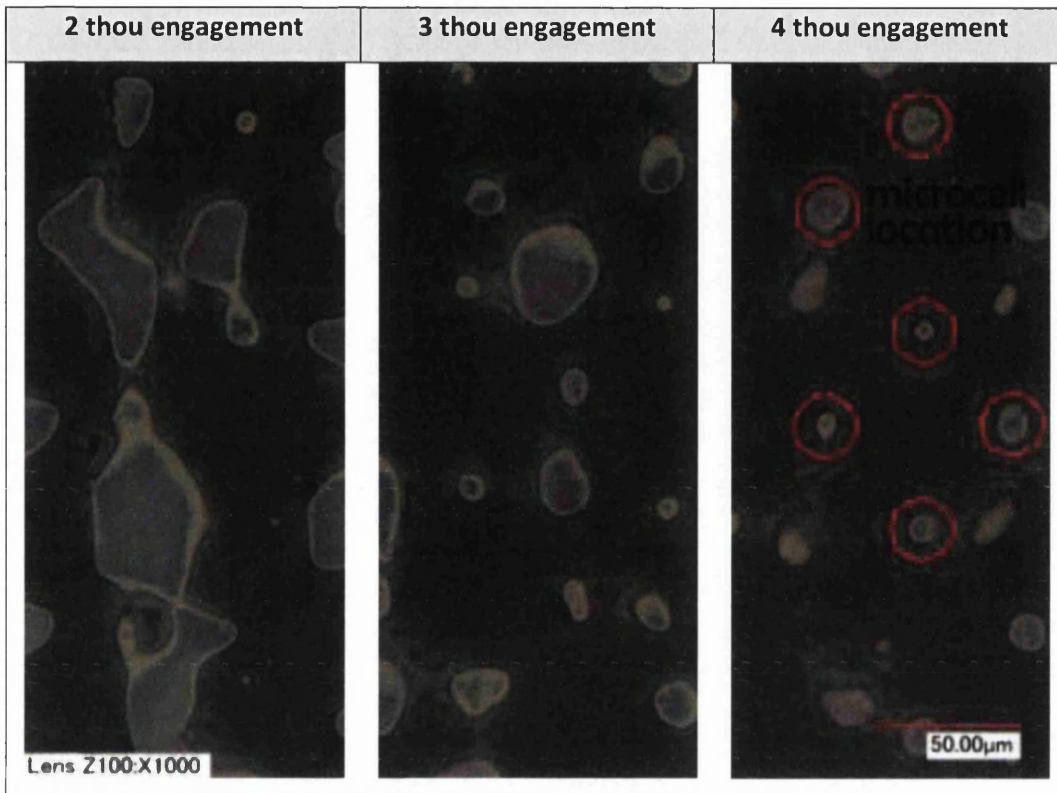


Figure 6.39: Change of size and distribution of UCAs with increasing engagement. At 4 thou engagement the spacing of UCAs in the prints corresponds to intervals of microcells on printing plate. (Asahi plate, MC16P, 150 ft/min)

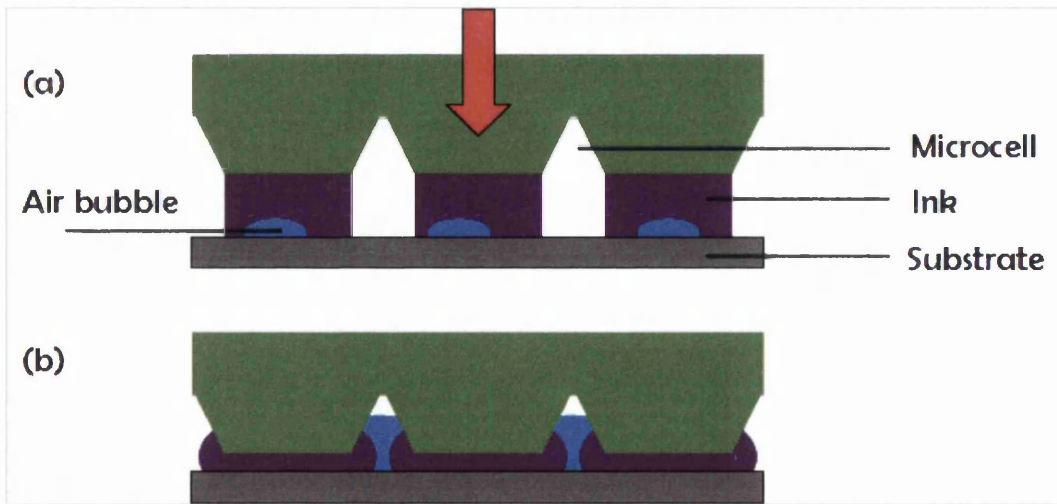


Figure 6.40: Schematic of redistribution of entrapped air bubbles by microcells; (a) air bubbles entrained into printing nip by ink film, and (b) redistribution of entrapped air bubbles into microcells.

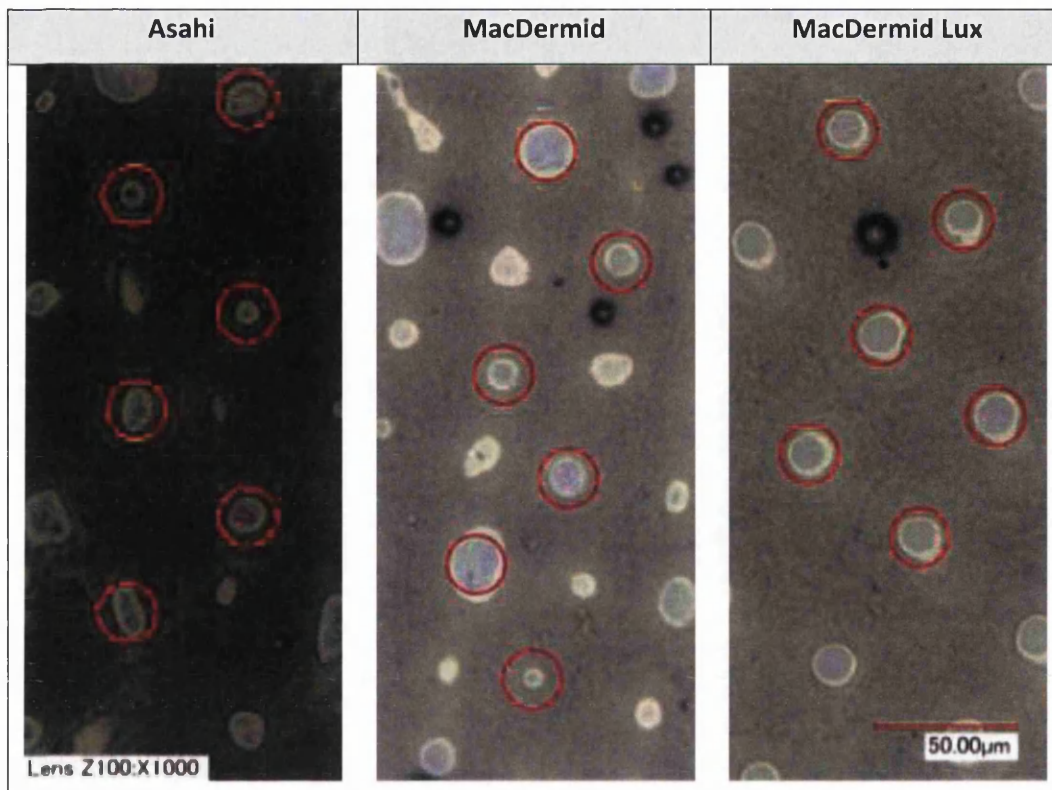


Figure 6.41: Distribution of UCAs in relationship to microcell location on different printing plate materials (red highlight = microcell location) (MC16P pattern, 150 ft/min, 4 thou)

6.2.2.3 Microcells on Halftones

This section details the findings on the effect of microcells superimposed on halftone dots. The printing experiment was analysed for optical density (shown in Figure 6.42 f. and Figure 6.45) and print uniformity (shown in Figure 6.39, Figure 6.44 and Figure 6.46). The ink transfer from halftone dots with microcells followed the same trends with regards to changes in printing speed and engagement as was observed for plain halftones. Figure 6.42 and Figure 6.43 show the difference in optical density between halftones without and with microcells on the Asahi and MacDermid plates (positive values correspond to higher optical density achieved without microcells). The microcells failed to improve ink transfer under any printing condition. A consistent density difference existed for halftones of 20% to 60% nominal area coverage with similar values for all printing conditions. On both plates a maximum difference was achieved for dots of 70% nominal area coverage. The shadows produced a large variety of results depending on plate material and printing conditions.

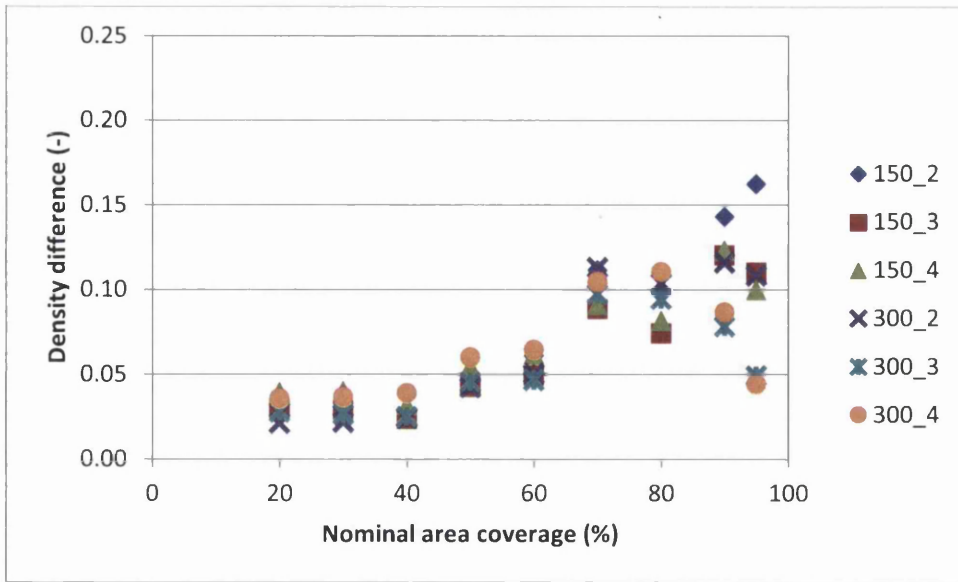


Figure 6.42: Difference in optical density between halftones without and with microcells (Asahi plate) (printing conditions: "speed (ft/min)_engagement (thou)")

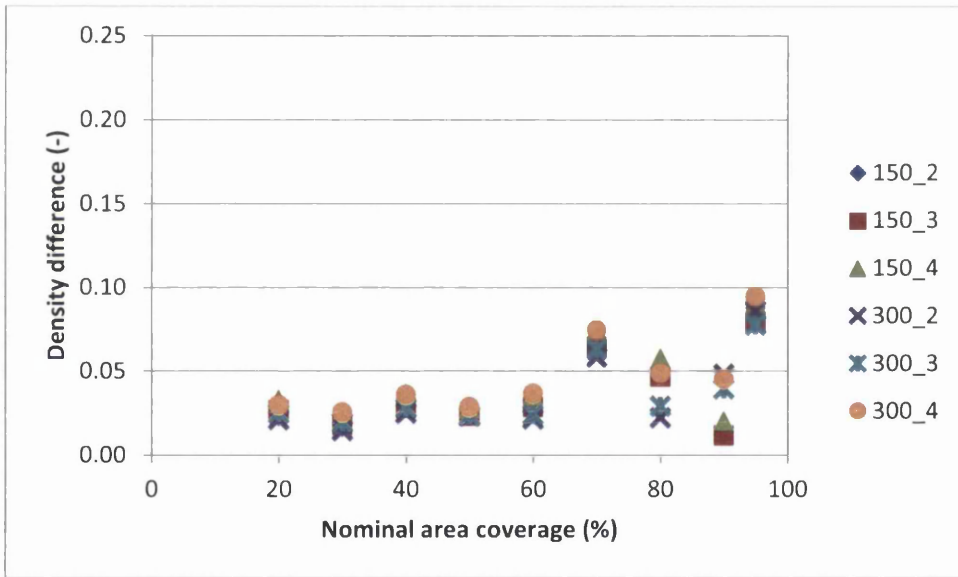


Figure 6.43: Difference in optical density between halftones without and with microcells (MacDermid plate) (printing conditions: "speed (ft/min)_engagement (thou)")

The failure of the microcells on these materials was attributed to two mechanisms. Firstly, the actual cell valleys did not ink up fully when in contact with the anilox. The decrease in ink volume supplied reduced the overall ink spread on the substrate (Figure 6.44). UCAs created by microcells could only be partially closed by ink squeeze. This accounted for the maximum difference in optical density for dots of 70% nominal area coverage which marked the transition between midtones and shadows. Without microcells the ink volume carried by the 70% dots was large so that by ink squeeze the dots joined together on the substrate and a higher optical density was created. The reduction in ink

transfer with microcells allowed no or little joining of printed dots, thereby lowering optical density. Secondly, microcells constituted additional sites at which air could be entrained into the printing nip. The air was not sufficiently redistributed in the shallow microcells of the Asahi and MacDermid plate (see also Figure 6.44), thereby hampering ink transfer, creating UCAs and decreasing optical density.

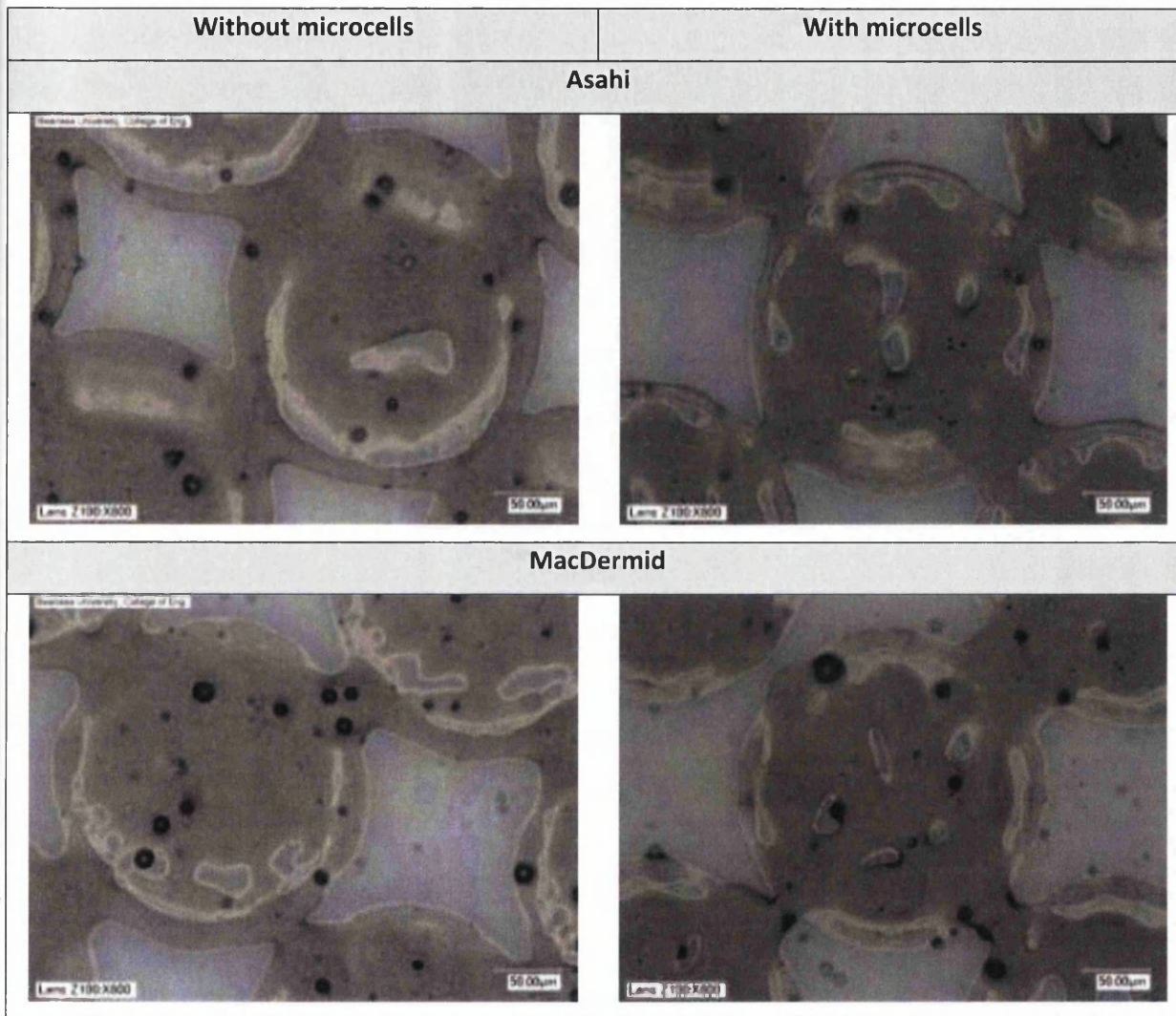


Figure 6.44: Comparison of print uniformity produced by halftone dots imaged without and with microcells on Asahi and MacDermid plate materials (70% nominal area coverage; printing speed of 300 ft/min at 4 thou engagement)

The MacDermid Lux plate was the only one able to improve optical density with the use of microcells (Figure 6.45). For the halftones from 20% to 60% nominal area coverage, the density difference changed continuously exhibiting the benefit of microcells. Between 70% and 80% nominal area coverage the microcells became less effective, before regaining their efficiency at 90% coverage. At 95% the performance becomes reversed and the plain halftone without microcells outperforms its patterned counterpart. This results pattern was repeatable for all printing conditions and may be attributed to several mechanisms.

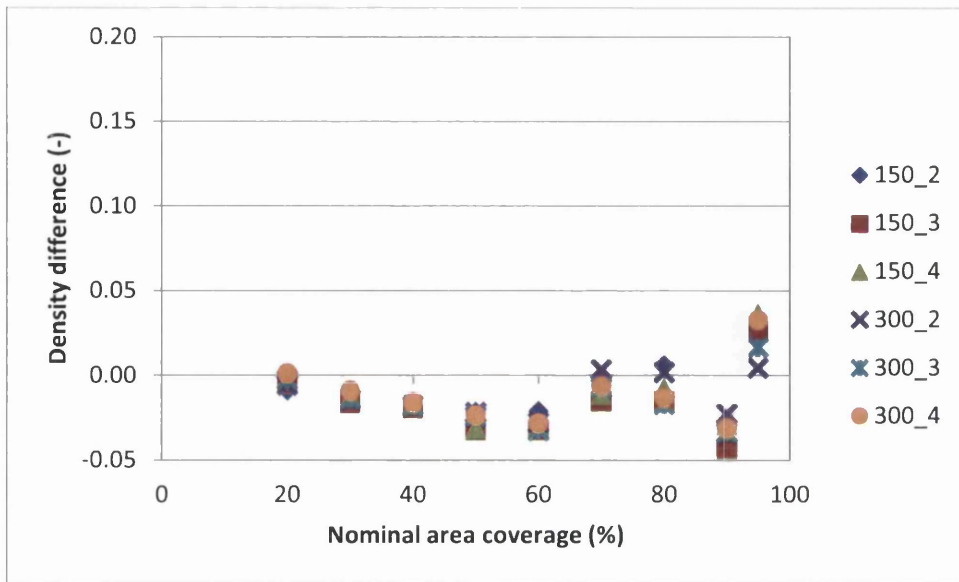


Figure 6.45: Difference in optical density between halftones without and with microcells (MacDermid Lux plate) (printing conditions: "speed (ft/min)_engagement (thou)")

It was shown in section 4.4.2.1.3 that the plain halftones printed by the MacDermid Lux plate suffered from thin residual films around the printed dot perimeter with increasing size (Figure 6.46). Dewetting was identified as one potential cause for these films which did not contribute to the optical density. Halftones with microcells also resulted in residual films, but they were intermittent and less extended (Figure 6.46). The microcells possibly interrupted the dewetting mechanism acting towards the centre of the dot by causing the break-up of the ink film into multiple filaments which locally fixed more ink around the dot perimeter. The effect was an increase in printed area which actually contributed to optical density. This was also observed at 70% and 80% nominal area coverage. However, the net effect was reduced by the overall decrease in ink volume transferred (see above for explanation on 70% dots on Asahi and MacDermid plate).

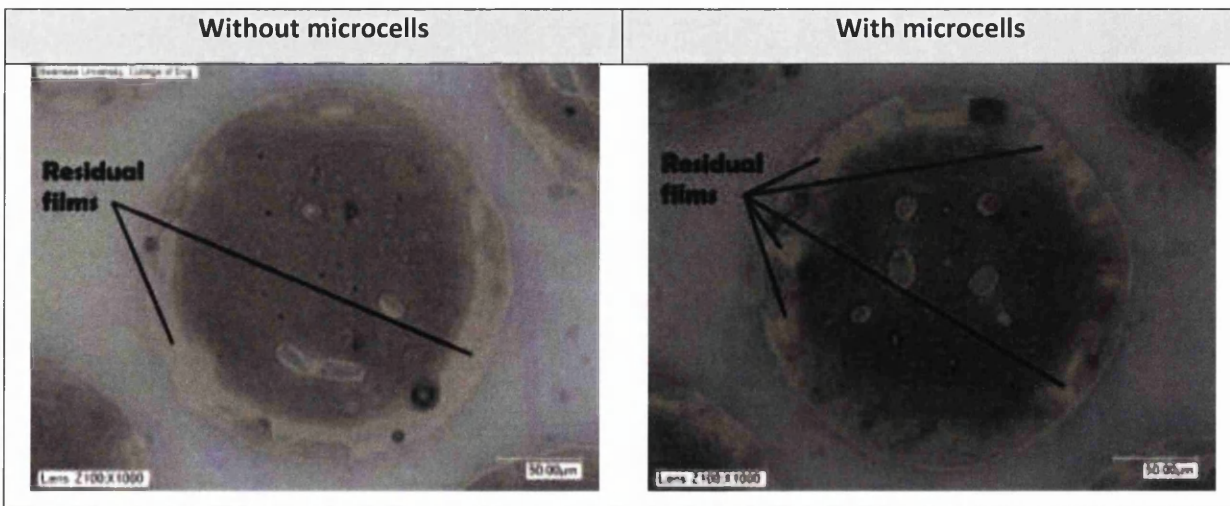


Figure 6.46: Comparison of print uniformity produced by halftone dots without and with microcells on MacDermid Lux plate material (50% nominal area coverage; printing speed of 300 ft/min at 4 thou engagement)

At 90% nominal area coverage the circumference of the non-printing areas and thereby any dewetting edge effects become less significant in comparison with the size of the printed area. UCAs hampering optical density and print uniformity gain importance. Therefore, it is thought that the governing mechanism for print quality improvement changes to the redistribution of entrained air by the microcells. The microcells took up the trapped air in their recesses (Figure 6.40) which led to very small, less visible UCAs and improved optical density. For nominal area coverages higher than 90% this turned into a disadvantage, because the cumulative area of the UCAs caused by entrained air and microcells on patterned surfaces exceeded the area of UCAs caused by entrapped air on plain surfaces.

Overall these findings could be interpreted as supportive of the industrial claim that microcells have to be imaged by “flat-top” imaging technology, because only the “flat-topped” MacDermid Lux plate achieved improved optical densities with microcells. Yet, a direct comparison of the optical densities achieved by the three plate materials with and without microcells (Figure 6.47) shows that there was very little difference between the plate types. It was the plain Asahi halftones which achieved slightly better optical densities than the other plate types. This emphasised again the significance of plate composition and topography over imaging technology and surface patterning.

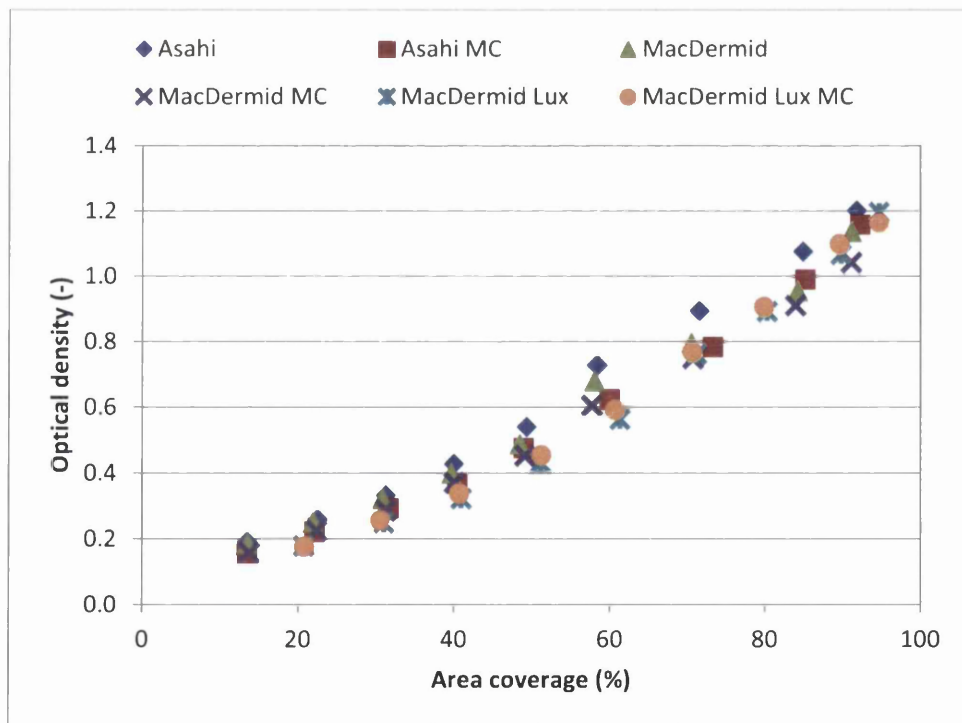


Figure 6.47: Optical densities of halftones without and with microcells for all plate materials (printing speed of 300 ft/min at 4 thou engagement; conditions chosen for highest optical density achieved in print trial)

6.2.3 Conclusions

As for the meso-patterns studied on the T-Flex 508, microcells failed to achieve improved print quality under the given process conditions. It was confirmed that the optical density of solids and halftones was mainly dependent on the area coverage on the printing plate. All microcell patterns decreased area coverage and with it optical density. Of the microcells, the pattern of smallest and least frequent recesses achieved the darker prints. Only for selected midtones on the MacDermid Lux plate were microcells able to achieve higher optical densities than their plain counterparts. This was thought to be caused by microcells preventing the dewetting of the printed dot perimeter.

In the previous chapter it had been identified that UV-curing ink remains on the top of plate features. Ink squeeze across the substrate is required to coalesce ink depositions and create closed ink films. Insufficient ink squeeze results in UCAs, additional to those created by air entrapped in the printing nip. In general, the print uniformity of halftones with microcells was not only hampered by the pattern recesses acting as non-printing area, but also by them constituting additional cavities which allowed air to be entrained into the contact zone. If sealed off by the cupping of the dot top, this air caused further defects of the printed dot.

For the solid printing patches superimposed with microcells an additional mechanism to the already established pattern functionality could be observed. That this had not been apparent on the IGT-F1 might be due to the reduction in available ink volume on the T-Flex 508 affecting the ink distribution on the printing plate and ink transfer. On the T-Flex 508 the microcells improved print uniformity by acting as redistribution sites for the entrapped air. Air bubbles, which would otherwise have caused UCAs in the prints, were shifted into the pattern recesses where they had less adverse effects on optical density and print uniformity.

The industrial call for imaging of microcells with “flat-top” technologies for improved optical density was shown to be unfounded. In the case of solid printing patches the optical density was primarily subject to highest area coverage which was achieved by “flat-” or “round-top” imaging technology depending on pattern. Very little advantage of “flat-top” technology was observed for halftones superimposed with microcells. Under the given combination of material and process parameters employed in this study, the overall best optical densities were achieved by plain printing features as these provided the highest area coverage.

6.3 Closure

A comprehensive study of the influence of microcell patterning on ink transfer of solids and halftones has been undertaken. It showed that microcells, just like micro- and meso-patterns, hold a dual functionality dependent on ink type. An additional mechanism was identified by which microcells act as redistribution sites for air entrained into the printing nip. The relocation of entrapped air into the pattern recesses by a squeeze action decreases the number of UCAs caused by air bubbles in the prints, thereby improving print uniformity. This has not been reported previously.

With regards to the aims of achieving higher optical density and improved print uniformity, surface pattern recommendations can be expressed based on the dual pattern functionalities:-

- Ultimately, plain printing patches achieve the highest print quality with UV-curing ink. The decreased area coverage of surface patterns reduces the ink volume transferred, and pattern recesses create UCAs in the prints. The least detrimental effect on print quality had microcell and other micro-patterns comprising high area coverage, small feature size and pitch, because these provide the best conditions for ink film coalescence under squeeze action.
- Using water-based ink, it is possible to increase ink transfer without significantly deteriorating print uniformity by employing microcells or other hole patterns (independent of recess geometry), as long as the area coverage remains higher than 75%. However, printed patterns in the form of fingering instabilities cannot be avoided entirely.

Several questions concerning the detailed mechanisms of ink transfer to and from the pattern patches remain and merit future exploration. Until then it continues to be advisable for printers to perform a trial run with a selection of surface patterns under production conditions to identify the optimum surface patterning for the respective print job. The guidelines provided above will help to make an informed decision whether any profit might be gained from surface patterning and narrow down the selection of patterns.

Above all, the potential of plate chemistry and topography, two factors which are already an inherent part of the printing process, should not be neglected as their optimisation might hold the key to improvements in print quality beyond the possibilities of surface patterning.

Chapter 7 Conclusions and Recommendations

The market share of flexography in graphic and functional device printing is increasing, but several inherent problems to the printing process are currently setting limits to its expansion, one of which are printing defects caused by interaction with the printing plate. The printing industry addressed the issue by introducing solutions such as “flat-top” imaging technology and surface texturing to printing plates. Selected industrial print trials demonstrated that these innovations are able to resolve some of the issues under particular process conditions. However, the underlying mechanisms were not understood. A review of the literature available revealed a big gap in this subject area and insufficient information transferrable from related research fields. This work has contributed to the body of knowledge by systematically investigating the role of dot geometry and surface patterning on printing plates in ink transfer. The quantification of the dot top geometry presented is the first of its kind.

To achieve this, print trials were conducted under laboratory and near-industrial conditions. Different types of printing plates imaged by standard digital and new “flat-top” imaging technology were employed to investigate ink transfer from varying dot geometries and surface patterns (meso- and micro-scale designs). New procedures to characterise features on the printing plate and in the prints by WLI and image analysis were developed to meet the special requirements of the materials used. During the investigation of dot geometry, the surface area and geometry of the halftone dot was related to the size, volume and uniformity of the printed dots produced under varying printing conditions. The effect of dot uniformity on the validity of selected halftone models was demonstrated. Surface patterning of the printing plate was studied under the aspect of pattern and process parameters affecting optical density and print uniformity.

The following sections contain the conclusions obtained from this research in answer to the knowledge gaps identified in the literature review, as well as recommendations for future work in this field and better industrial practice.

7.1 Conclusions

DOT GEOMETRY

- Previous observations that oxygen inhibition of the standard digital imaging process creates area coverages smaller than nominal were confirmed using Asahi and MacDermid plate materials. The largest losses occurred in the midtones and increased with line ruling. Halftones imaged with “flat-top” imaging technology using a Gaussian laser beam

(MacDermid LUX) had area coverages closest to nominal with only small plate gain in the midtones. SQUAREspot laser beams (Kodak) resulted in intermediate area sizes and a saw tooth-like pattern around the circumference of the halftones, whereas the aforementioned imaging technologies produced circular dots. The geometry of the halftone circumference directly influenced the edge stability of the printed dot. The tooth-like edges of the Kodak halftones produced the least stable dot edges, characterised by intermittent thin residual ink films, which are of particular significance to functional device printing. No indications were found that the ragged edges render the dot more susceptible to fingering instabilities during printing.

- The predominant dot geometry identified on printing plates imaged with standard digital as well as “flat-top” imaging technology was concave, most probably due to a polymer shrinkage mechanism. The new term of cupping was suggested to describe this geometry and a method based on cup depth introduced for its quantification. The cupping depth was found to be more dependent on the composition of the plate material than the imaging technology. The cupping effect is most pronounced in the midtones, which have the largest free bulk volume deformable under tension. Only on the water-washable Asahi plate a transition from convex to concave dot tops took place in the midtones, because the insufficient polymerisation of the dot edges under oxygen inhibition led to their subsequent washout.
- In conjunction with the cupping, a third mechanisms of dot deformation on the printing plate, besides shoulder barrelling and top expansion, was identified: sealing off the ink within the cup at the dot top creates hydraulic pressure which depresses the centre of the dot and causes the cupping brim to fold in on itself. Ink atop the cup brim is displaced outward and into the cup leaving an ink-free annulus on the substrate which is the origin of the halo defect. If air bubbles as well as ink are sealed off inside the cup, the bubbles prevent ink transfer creating UCAs in the prints.
- A rise in printing pressure led to increased dot gain from plate to print due to increased deformation of the halftones on the plate and ink squeeze. The dot gain was smaller for the plates produced by “flat-top” imaging technology, because they experienced less dot shoulder barrelling and thereby increase in printing area under pressure. The standard digital plates resulted in higher dot gain due to enhanced ink-buildup around the dot top facilitated by ink migration down the dot shoulders. For the first time it had been reported that the ink volume transferred is solely dependent on the size of the printed area and not the printing area on the plate. The mean ink film thickness across the printed dots lies

between 0.7 and 0.8 μm for all plate materials. Ink volumes containing printing defects, notably halos, UCAs and unstable geometry of the dot edges, resulted in lower optical densities for halftones. The effect of printing speed could not be observed in isolation, as it was masked by the ink buildup around the halftones.

- Five halftone models were investigated for their precision in predicting halftone reflectance from the actual halftone coverage and solid reflectance on the prints. Retrospective optimisation rendered the Expanded Murray-Davies and Yule-Nielsen models the overall most precise. Beer's Law proved a good fit for small, defect-free halftones as their printed area coverage was the most similar to the one on the printing plate taken into account for the model. The Murray-Davies model, which is most popular in industry, led to increased errors, because it could not account for the deviation in reflectance caused by the printing defects encountered. The Noffke-Seymour model was subject to the same problem, but resulted in further inaccuracies due to the adjustment of the reflectance in the equation for ink film thinning by ink spread which could not be observed in the actual prints. In general, the validity of the halftone models was less dependent on the geometry of the dot top on the plate than the printing defects encountered. The scale of printed halftones was divided into sharp, uniform highlights, and flawed midtones and shadows containing UCAs and thin residual films. Since the halftone models investigated were better in predicting either one or the other, a new approach in the development of halftone models taking into account these different classes of halftones is called for.

SURFACE PATTERNING

- For the first time different functionalities of surface patterns were reported in conjunction with the ink type used. The effect of surface patterning on print quality, notably optical density and print uniformity, is dependent on pattern geometry, area coverage, feature size and pitch, as well as other material and process parameters.
 - Lower-viscosity water-based ink tends to flood pattern recesses which thereby act analogous to anilox cells and increase the ink volume transferred. The higher the recess volume, the more ink can be transferred and the higher the optical density of the prints. However, the recess volume shall not exceed the volume of ink supplied by the anilox, as this would prevent the pattern recesses to be filled completely and cause UCAs in the prints. The appearance of fingering instabilities in the prints can be controlled by the surface pattern parameters. Microcell and other hole patterns

with area coverages above 75% achieved print uniformity comparable to the plain solid, but with improved optical density.

- Higher-viscosity UV-curing ink remains on the pattern features. For the creation of closed ink films in the prints, the most beneficial surface patterns are microcells and other micro-patterns with high area coverage, small feature size and pitch as they aid ink coalescence. Failure to coalesce leads to UCAs in the prints.
- An additional mechanism by which microcell patterns improve optical density and print uniformity on the T-Flex 508 was by acting as redistribution sites for entrapped air bubbles. Air that would otherwise have formed UCAs in the prints and decreased print quality is compressed into the microcells where it has less effect on ink transfer. The smaller the opening of the microcells and the larger the overall area coverage, the better the print quality achieved. Large microcell openings prevented the formation of closed ink films.
- The optical density and print uniformity achieved by surface patterning on the IGT-F1 printability tester was highly dependent on printing conditions, material and pattern parameters. The surface patterning had to be well-matched to the other parameters in order to achieve an improvement in print quality. The optimisation of optical density together with print uniformity was not always possible. In some cases the sole adjustment of IGT-F1 printing conditions achieved better results than the use of surface patterning. In general, an increase in anilox volume, printing force and speed improved optical density and print uniformity.
- Different classes of hydrodynamic instabilities of the Saffman-Taylor type were identified in the printing defects, namely beads, dendrites, viscous fingers and ribs. The transitions between fingering patterns were dependent on printing conditions, material and pattern properties. Surface patterns with extended grooves parallel to the print direction (e.g. chequer tilted at 45°, polka dots and positive hexagons) resulted in more linear dendrites or ribbing along this orientation, whereas surface patterns with grooves of changing direction or orientation other than parallel to the print direction caused highly-branched viscous fingering. In the case of the latter, the pattern geometry controlled emerging finger growth, bifurcation and dominant frequency. The bead pattern atop viscous fingering defects resulted from local dewetting of the ink film and formed the base of filaments during ink film splitting. High-frequency surface patterns, which offered more sites for filament pinning, created finer secondary filaments and more uniform prints.

- The efficiency of surface patterning in combination with flat-top imaging technology differed for solid and halftone prints:
 - For three of four microcell patterns on solid printing patches, “flat-top” imaging technology did not improve the print quality, because it creates deeper, more defined microcells which do not fill up with ink and cause UCAs in the prints. Standard digital technology on the other hand results in rudimentary microcells of only a few micrometres. These are more likely to make complete contact with the anilox cylinder, therefore facilitating increased ink transfer with the feature tops and recesses, while at the same time retaining the capability to act as redistribution sites for entrapped air.
 - In halftone printing, microcells reduced the area coverage on the printing plate and thereby the volume of ink transferred. Furthermore, they acted as additional sources for entrapped air which caused more UCAs. However, microcells imaged by “flat-top” technology achieved an improvement in print quality for highlights and midtones by reducing the residual ink film around printed dots. This was attributed to microcells interrupting the dewetting of the substrate by causing ink to break up into multiple filaments and remain pinned at the dot edge.

7.2 Further Work

DOT GEOMETRY

- WLI was found to be insufficient to capture the full geometry of dot tops and shoulders on the printing plate. An advanced method has to be developed in order to capture the cupping geometry, cup and dot shoulders sufficiently. (section 4.4.1.2)
- Detailed knowledge of the deformation of concave dot tops in the inking and printing nips, as well as the ink transfer to and from different top geometries is currently not available. Since direct observation of the mechanisms is not possible at this size scale, numerical modelling is suggested for the future exploration of these issues. This might also allow the systematic investigation of the origins of printing defects, namely halos and UCAs within dots. (sections 4.4.2.1.1 f.)
- The research question of why halftones on MacDermid, MacDermid Lux and Kodak plates lead to widely different area transfer ratios despite very similar surface geometries remains open. This could be the missing link between the behaviour of “flat-” and “round-top” plates. It might require the implementation of the two processes suggested above as well as

morphological analysis of the respective plate materials to answer the question. (section 4.4.2.2.1)

- A new halftone model which takes into account different classes of printed dots has to be developed. (section 4.4.2.5.2)

SURFACE PATTERNING

- Confirmation of the microcell functionality to redistribute air bubbles entrapped in the printing nip could be obtained by printing against glass and observing the ink film formation from the reverse of the glass with high-speed camera. This might also allow the observation of differences in microcell functionality between patterns imaged by standard digital and “flat-top” imaging technology. (section 6.2.2.2)
- Further exploration of surface pattern functionalities could employ WLI to determine the amount of ink contained within pattern recesses between inking and printing, as well as after printing of the plate. This would provide information on whether the pattern recesses are filled completely or only partially, and how much of the ink is released from the recesses during printing. (section 5.1.4.8)
- Certain striation patterns on the printing surface caused by the laser imaging of the mask layer also exhibited an effect on the redistribution of UCAs. Closer investigation of the striae as potential integrated surface texturing to the imaging process is required. (section 6.2.2.2)
- Halftones with microcell patterning showed less residual films around printed dots which was attributed to microcells preventing dewetting. Confirmation of this mechanism might be obtained by observing the transfer of ink from a sufficiently large model dot with patterned surface in an extensional rheometer or similar apparatus. (section 6.2.2.3)
- The general effect of surface patterning on ink transfer mechanisms might be observable in a radially lifting Hele-Shaw cell of which one plate is replaced by a patterned printing plate. During the opening of the cell, ink filamentation and meniscus destabilisation can be captured by high-speed camera. High-speed recording is also suitable for the direct observation of the printing nip in a printing press (access permitting).

7.3 Industrial Recommendations

- Neither “flat-top” nor standard digital imaging technology can be endorsed fully. Standard digital halftones suffer from tonal value decrease on the plate due to oxygen inhibition of

the imaging process, but the loss can be compensated for during the preparation of the digital data for plate-making. The dot gain from plate to print is large. "Flat-top" technologies produce features closer to nominal size and the dot gain from plate to print is small, varying less under different printing conditions. This stable operation latitude requires a rethink by the printer who tends to regulate ink transfer on the press with the pressure setting. However, "flat-topped" plates result in more printing defects and thereby cannot be synonymous of print quality.

- The terminology of "flat-top" and "round-top" imaging technology is misleading, because dot geometry is independent from imaging technology. The quantification of the dot geometry, e.g. by cup depth, width, volume and rim radius, has to be added to the common measurands of halftone dots, notably dot height, shoulder angle and planar surface area. The method suggested in this work (based on cup depth) could serve as a starting point for the development of an advanced method. An international standard for the characterisation of flexographic printing plates is still missing. Its significance has to be emphasised in the light of these findings.
- Surface patterning is not a panacea for print quality. The effect of the plate's surface patterning on ink transfer is strongly dependent on material and process parameters. In the closure of Chapter 6, guidelines on the use of surface pattern designs for UV-curing and water-based ink were provided which will help to make an informed choice. In order to avoid waste during the print run caused by prints not meeting the quality target, a fingerprint trial should be performed in advance to identify which pattern (if any at all) produces the print quality desired in combination with the printer's most commonly used inks, substrates and press settings. The results can then be referred to for future print runs to select the optimum parameter combinations.
- Fingerprints like this can also serve as reference for the calculation of parameters for halftones models, notably the Expanded Murray-Davies and Yule-Nielsen equation. These models are more accurate than the more widely used Murray-Davies equation.

A Appendix

A.1 Macros for ImageJ

MACRO – PLANAR SURFACE AREA OF ISOLATED PRINTING FEATURES IN IMAGEJ

```
run("Options...", "iterations=1 count=1 black edm=Overwrite");
setBackground(255, 255, 255);
setForegroundColor(0, 0, 0);
while (nImages>0)
{
    setTool ("point");
        waitForUser("Fill area", "Select the NON-ROI and click 'OK'");
            getSelectionCoordinates(xPoints,yPoints);
                x = xPoints[0];
                y = yPoints[0];
            floodFill(x, y);
run("8-bit");
setThreshold(0, 199);
    run("Convert to Mask");
setTool("polygon");
    waitForUser("Select areas", "Select the area to analyse and click 'OK'");
        getSelectionBounds(x,y,width,height);
setKeyDown("alt");
    run("Histogram", "bins=256 x_min=255 x_max=255 y_max=Auto");
    waitForUser("Copy pixel count", "Has the pixel count been copied?");
    run("Close");
    run("Open Next");
}
```

```
run("Options...", "iterations=1 count=1 black edm=Overwrite");
setBackground(255, 255, 255);
setForegroundColor(0, 0, 0);
while (nImages>0)
{
  setTool ("point");
  waitForUser("Fill area", "Select the ROI and click 'OK'");
  getSelectionCoordinates(xPoints,yPoints);
  x = xPoints[0];
  y = yPoints[0];
  floodFill(x, y);
  run("8-bit");
  setThreshold(200, 255);
  run("Convert to Mask");
  setTool("polygon");
  waitForUser("Select areas", "Select the area to analyse and click 'OK'");
  getSelectionBounds(x,y,width,height);
  setKeyDown("alt");
  run("Histogram", "bins=256 x_min=255 x_max=255 y_max=Auto");
  waitForUser("Copy pixel count", "Has the pixel count been copied?");
  run("Close");
  run("Open Next");
}
```

A.2 Screening of Scanning Parameters

This section contains the considerations and tests performed for the screening of scanning parameters. The specifications investigated were scan colour, resolution, temporal stability and consistency, linearity and gamma correction, file format for data storage, and ROI size for image analysis.

A.2.1 Selection of Scan Colour

The main purpose for the digitisation of the prints for this investigation was to use ImageJ as a fast and simple means to gain comparable information on print uniformity and optical density from the image histogram. The scan option of 48-bit colour was immediately discarded as it was questionable whether it is indeed possible for the scanner to discern 281.3 trillion different colours. Furthermore, the large amount of data generated would be very disadvantageous from the practical viewpoint of digital data handling in ImageJ as well as in other computer programmes. This left the scan options of 24-bit colour, 16- and 8-bit greyscale. All three options were investigated in ImageJ, and it became apparent that the software employed certain standard procedures for the generation of the histograms, which was not consistent for all colour options.

ImageJ converted the 24-bit colour image to an 8-bit greyscale image, before the histogram was calculated. Therefore, the resultant histogram had only 256 levels and the advantage of the 16.8 million colour digitisation was lost. Furthermore, the colour channels scanned were RGB. Any image manipulation would take place only within the realm of these channels. This is of less practical significance for the field of printing, since the process colours are CMYK, and any colour analysis, such as spectrophotometry, is more commonly performed for the CMYK than the RGB channels. Thus the long scanning time and large disc space for the digitisation to 24-bit colour images became rarely justifiable.

The histogram of the 16-bit greyscale image was calculated correctly for 65,536 levels, but then was truncated for the graphical display. All levels equal to zero at either end of the histogram were discarded. All the remaining levels and their values were proportionally distributed over 256 bins and displayed as a histogram. By gathering several greyscale levels into one bin, the possibility for later calculations in other software based on the histogram data was forfeited. Although, it was possible to generate the full histogram of 65,536 levels with the help of a macro in ImageJ, this large number of data points could not be handled by every computer programme. For example, Microsoft Office Excel limits the number of data points displayable in a chart to 32,000 within a series.

Finally, the 8-bit greyscale image was resolved in an 8-bit greyscale histogram of 256 levels. This number of data points was small enough to be handled by most computer programmes.

Furthermore, the colour difference between two levels is smaller than what the human eye can easily discern, therefore rendering this approach sufficient for the field of printing.

A.2.2 Selection of Scan Resolution

Digitisation was mainly required for prints investigating surface patterning on printing plates. For the selection of the scan resolution, the smallest feature size expected in the prints had to be taken into account. Assuming a one-to-one transfer of the image from digital file to printing plate to substrate, the smallest printed structures would have had a width of 25 μm (based on the original in-house artwork for plate-imaging). According to the Nyquist-Shannon sampling theorem, the scanning frequency had to be at least twice as high as the largest frequency encountered in the image, in order to reconstruct the original information sufficiently from the sampled data (Unser, 2000). Using this as a reference, the maximum scan width had to be 12.5 μm and the minimum scan frequency 800 lines/cm (approx. 2,000 lpi).

To compare the effect of scan resolution, the same print of six surface pattern patches was scanned at eight different resolutions (500; 1,000; 1,500; 2000; 2500; 3000; 3500; 4000 dpi) and 8-bit greyscale. The GSL histograms were plotted normalised to pixel number, and were almost identical for all scan resolutions. Figure A.1 shows the histograms of the patch “reference solid” which were the most divergent of all patterns. Only the resolution of 500 dpi produced slightly deviating results, thereby prompting the use of at least 1,000 dpi. The relative standard deviation of the MGSL and StDev did not exceed 0.2% and 0.9% respectively for any pattern. A similar observation was made by Stahl (2013) for the Epson Perfection V750 Photo scanner. Above 2,000 dpi the scan time and file size increased considerably. Due to memory restrictions in ImageJ, very large file sizes had to be avoided, and the setting of 2,000 dpi was selected as the scan resolution.

A.2.3 Determination of Temporal Stability and Consistency

A series of scans was performed with the aim of analysing the scanner temporal stability and consistency. The same print containing three pattern patches was scanned at 8-bit greyscale and 2,000 dpi resolution in several test runs, called “a” to “h” (Table A.1). The runs differed in the number of patches captured in each scan, the inclusion of a standard Lanetta paper (a high-gloss coated paper with a black and white half serving as a black-white reference), and the number of consecutive scans. One pattern patch was contained in every scan and was analysed using the MGSL and StDev of the histogram distribution.

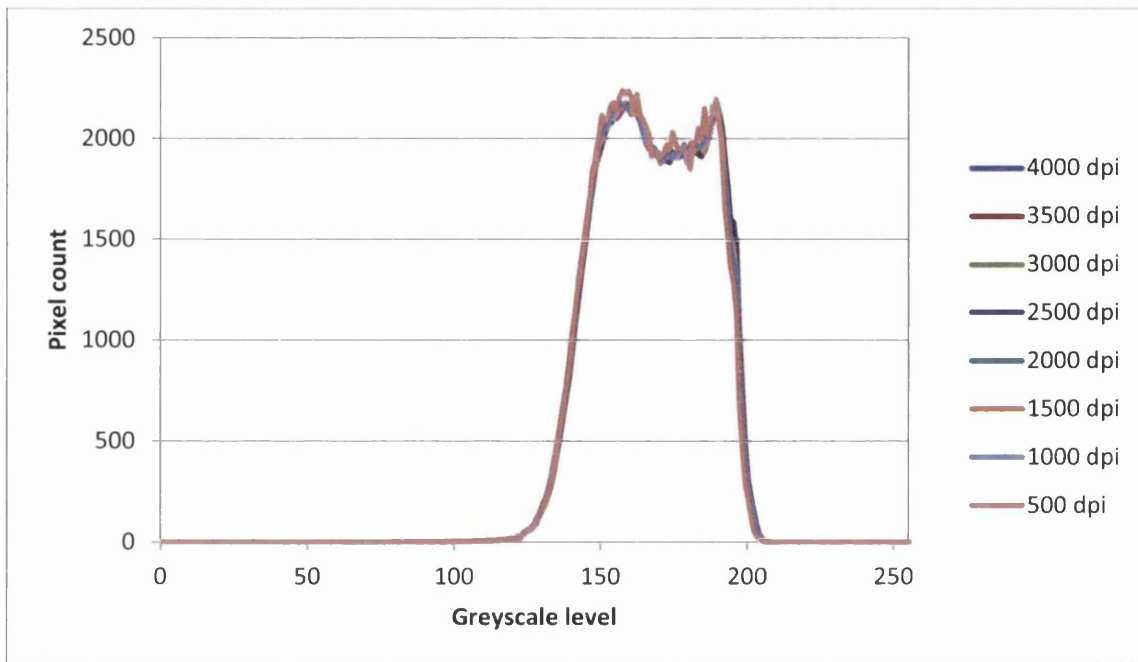


Figure A.1: Normalised histogram of GSL distribution for patch “reference solid” at different scan resolutions

Figure A.2a shows that the MGSL of the scanned image decreased for the first six prints of run “a”. This was attributed to a prolonged warm-up period of the scanner lamp beyond the time which was automatically allocated by the scanner software. After that the MGSL increased continuously in an almost linear fashion for all scan runs. This was not an indicator of scanner instability, but was most likely caused by changes in the printed ink itself. The water-based ink used was an in-house model liquid which contained dye. The pigments in the dye were not lightproof and faded under the continual exposure of the strong scanner lamp, thereby increasing the MGSL. This conclusion was supported by the increasing StDev of the histogram distribution with scan number (Figure A.2b). The only exception to the linear trend was the first scan of each run. It exhibited a larger MGSL than the rest of the run, most likely caused by the lamp cooling down slightly between scan runs. Breaks of about one minute increased the MGSL by half a level and breaks of two minutes by one level (run “h”).

In order to confirm the findings of the water-based ink and exclude fading issues, scan runs were analysed for a UV-curing ink (scan runs “A” to “E” in Table A.1). Figure A.3 shows clearly that the scanner stabilised after the initial warm-up period, and then scanned very consistently, as long as its lamp did not cool down between scans. The cool-down effect became obvious again in the first scan of each print run, as well as in run “E”. During the last run most scans were taken at intervals of 30

seconds. The two scans which were performed about two minutes after the previous scan stood out with slightly higher MGSL. However, the standard deviation within that run was well below 0.2%.

It can be concluded that the scanner was capable of performing very stably and consistently depending on a constant lamp temperature. Practically that required the running of the scanner several times before the actual scanning, and a steady exchanging of samples between scans to avoid too large an influence of the lamp cooling down.

Table A.1: Scan conditions for determination of scanner's temporal stability and consistency

Ink	Run	No. of patches	Reference	No. of scans	Duration
water-based	a	1	-	12	9 min
	b	3	-	16	32 min
	c	1	Lanetta	16	33 min
	d	3	Lanetta	16	53 min
	e	1	-	16	13 min
	f	1	Lanetta	16	32 min
	g	* omitted *			5 min
	h	1	-	12	10 min
UV-curing	A	3	Lanetta	15	54 min
	B	* omitted *			50 min
	C	3	-	15	30 min
	D	1	Lanetta	15	31 min
	E	1	-	15	12 min

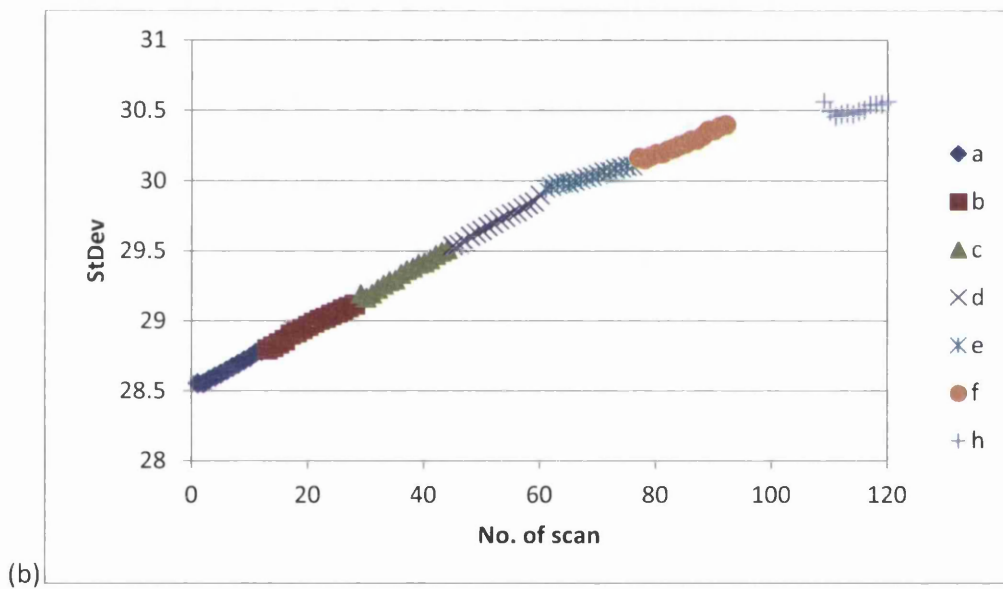
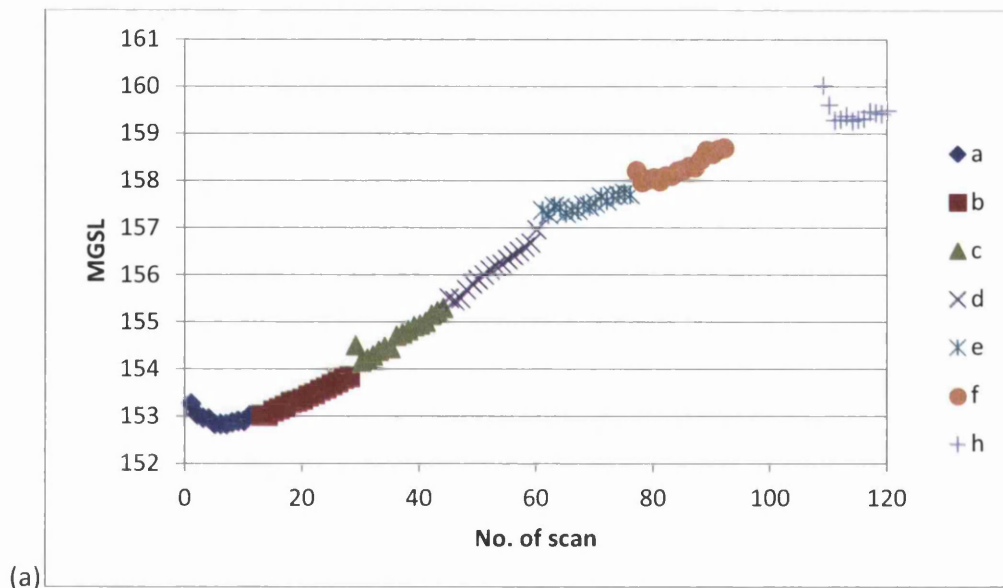
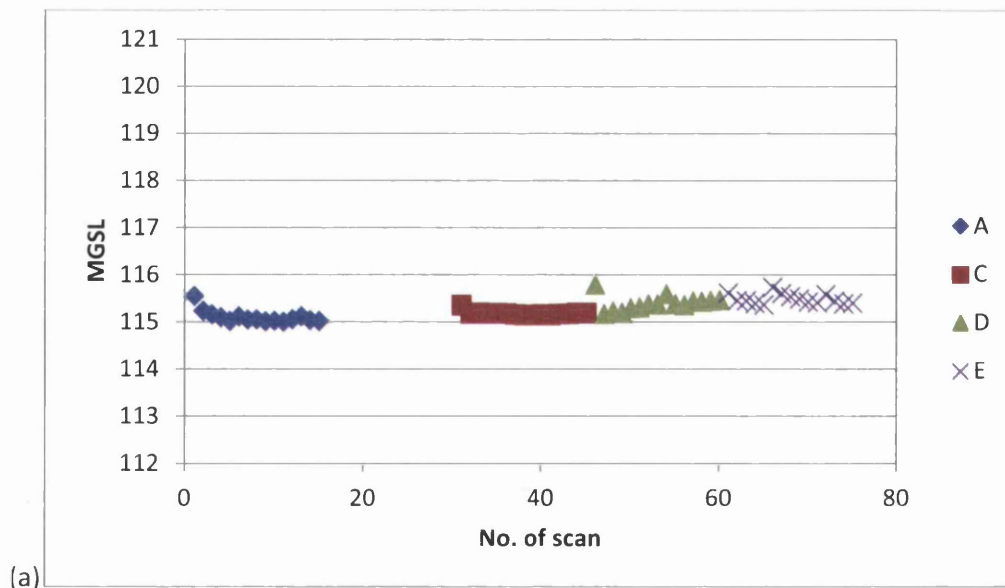
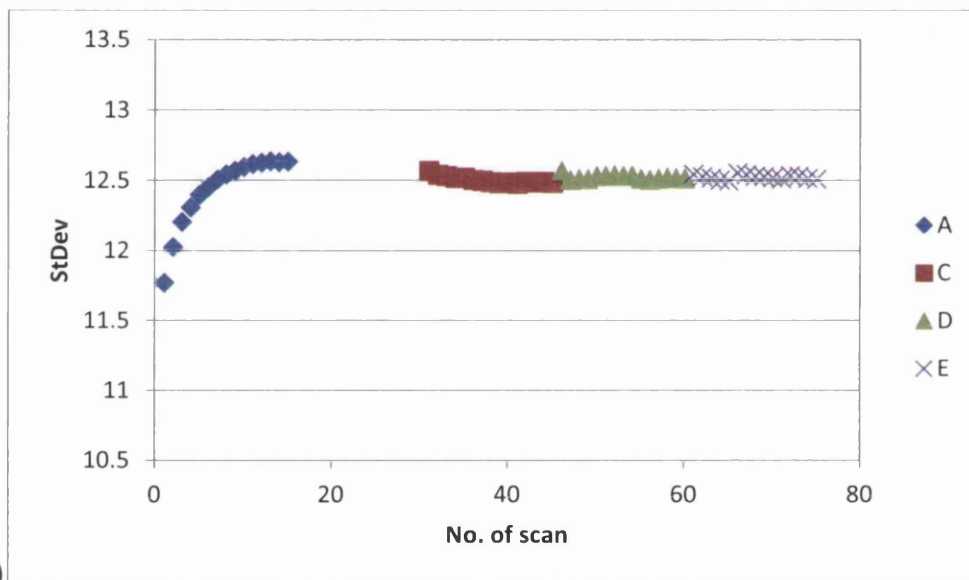


Figure A.2: Water-based ink prints – MGSL (a) and StDev (b) of test scans in consecutive order



(a)



(b)

Figure A.3: UV-curing ink prints – MGSL (a) and StDev (b) of test scans in consecutive order

A.2.4 Determination of Linearity and Gamma Correction

All scans were performed in good faith that if the option “no colour correction” was selected in the scanner software, the scanner would indeed not apply any corrections to the image. However after completing the analysis of the scanned images, the author received a copy of a dissertation (Stahl, 2013) in which similar work had been done, revealing that the scan software applies an algorithm which affects the linearity of the scan system. These automatic non-linearity algorithms (called gamma corrections) serve to adjust the tonal values of an input image to the output medium by taking into account the human eye’s perception (Busch, 2003; Stone, 2003; Urban, 2005).

One possible and simple test for gamma correction and a subsequent restoration of linearity was outlined by Stahl (based on Urban, 2005). A reference greyscale is characterised with a calibrated spectrophotometer (in this work a Gretag Macbeth Spectrolino) and digitised by the scanner under investigation. The grey reference used for this work was a Color Checker Classic (X-Rite, Grand Rapids, MI, USA) with six fields of different GSLs (Figure A.4). The mean greyscale level of each patch determined by scanning and image analysis was then compared to the corresponding relative luminance value, Y (CIE XYZ colour space), obtained through spectrophotometry. The scanner settings tested were “no colour correction” and colour correction with gammas $\gamma=1.0$ (linear); 1.8 and 2.2.

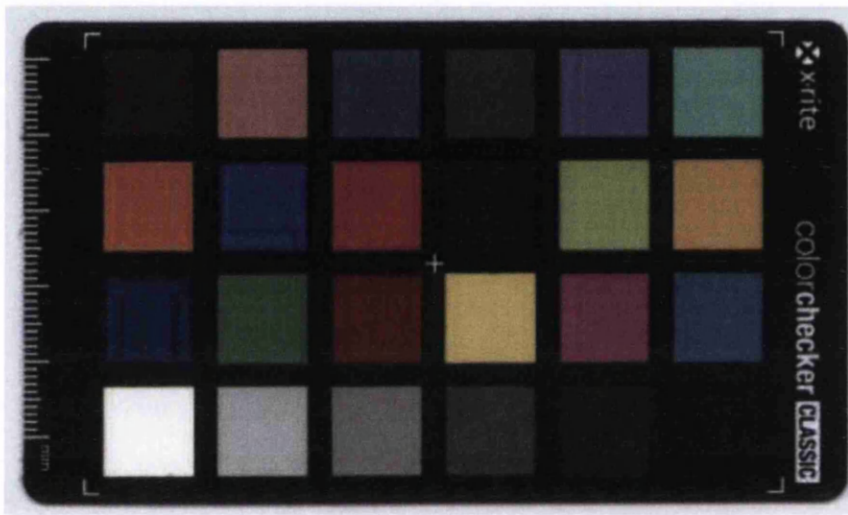


Figure A.4: Reference greyscale (bottom row) as part of the Color Checker Classic

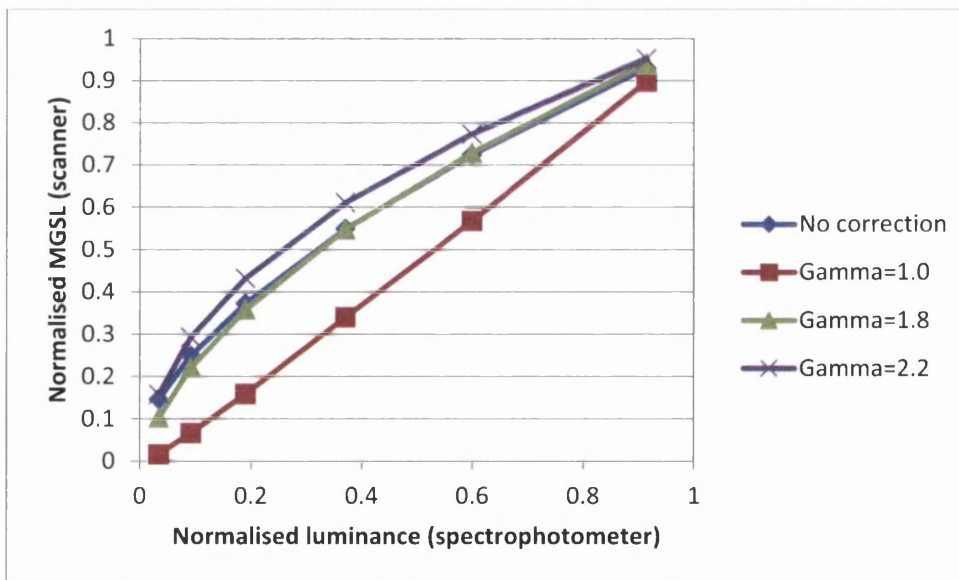


Figure A.5: Comparison of normalised MGSL (determined by scanning) and normalised luminance (obtained by spectrophotometry) showing non-linear manipulation of scanner data using “no colour correction” option

From Figure A.5 it can be seen that the “no colour correction” option actually produces a non-linear graph similar to the one of correction $\gamma=1.8$. This would correspond to the adjustment performed on output to a Macintosh computer screen. This finding had a large impact on this work as all scanned data was only available in non-linear form which rendered all consequent measurands calculated from it unreliable. Since it was not feasible to re-scan the entire data with linear gamma correction, the correction inversion had to be performed on the existing encoded data using the inversed gamma function (based on 8-bit greyscale):

$$GSL_{i,linear} = \left(\frac{GSL_{i,encoded}}{255} \right)^\gamma \cdot 255 \quad \text{Equation A.1}$$

A more detailed analysis of the graphs in Figure A.5 showed that a gamma of $\gamma=1.8$ did not fully correct the non-linearity of the data. This might be attributed to other non-linear influences which affect the encoded data, such as an offset in the analogue-to-digital converter or reduced input signal range of the scanner sensors (Urban, 2005). Gammas within the range of $\gamma=\{1.66, \dots, 1.71\}$ resulted in $R^2=1$. This corresponded to the range in gamma determined by Stahl (2013) for the Epson Perfection V750 Photo ($\gamma=1.68$). For this work a gamma of $\gamma=1.66$ was chosen, as this resulted in a slightly better fit for lighter greyscale values. Once the linear GSLs were restored, they had to be applied to every single histogram that had been recorded.

A.2.5 Selection of File Format

The largest prints to be scanned contained seven bands of 12 pattern patches each. The size of the scanner bed was designed for a maximum document size of 216 by 297 mm. A single sample band made up of 12 pattern patches was about 313 mm long and exceeded these dimensions. Cutting the bands apart and placing them next to each other was not a viable option. Therefore, each scan run included a group of six pattern patches only. The scanned data of the two groupings was then saved within one multi-page compression-free TIFF-file for easier data management. Every page of the file corresponded to a single image level. The different image levels could be viewed separately in Microsoft Windows Photo Viewer, ImageJ and several other computer programmes. A slight disadvantage of multi-page TIFF-files was the increased file size which made it desirable to scan smaller ROIs. However, printed patches occasionally contained contaminations which rendered part of the image unsuitable for image analysis. Therefore tests on scanned sample area were conducted to determine the ROI size.

A.2.6 Selection of ROI Size

The same six pattern patches as for the test of scan resolution were scanned in their entirety in the chosen colour of 8-bit greyscale and 2,000 dpi resolution. Seven different ROI sizes, ranging from 100 mm² to 900 mm², were selected and applied to the scanned images (alignment of ROI centre with centre of scanned patch). The largest ROI size of 25 by 25 mm was selected to be smaller than the patch size (30 by 30 mm) in order to avoid any edge effects (uneven or faulty ink application along the edges of printed features) which could hamper the data collection (Bornemann, 2013; Stahl, 2013). Then the GSL histograms (normalised to pixel number), MGSL and StDev of the histogram distribution were obtained for all ROI sizes and compared with each other.

It was found that the ROI size had only a small impact on the histogram and resulting measurands. The histogram distributions were very similar (Figure A.6). The relative standard deviation of the MGSL was less than 0.9% for all patterns. The relative standard deviation of the StDev was higher with a maximum of 4.0% for one particular pattern. This was due to several contaminations contained within the scanned area which stood out in a darker colour against the rest of the prints and caused slight shifts in the histograms. Depending on the ROI size used, all, part or none of the contaminations were included in the ROI, thereby having varying effects on the results. But it was exactly for this reason that the ROI had to be kept small; in order to be able to avoid measurements on contaminated areas of the prints. Therefore a ROI of 10 by 10 mm (787 by 787 pixels) within a scanned image of 20 by 15mm was chosen for the image analysis in this work.

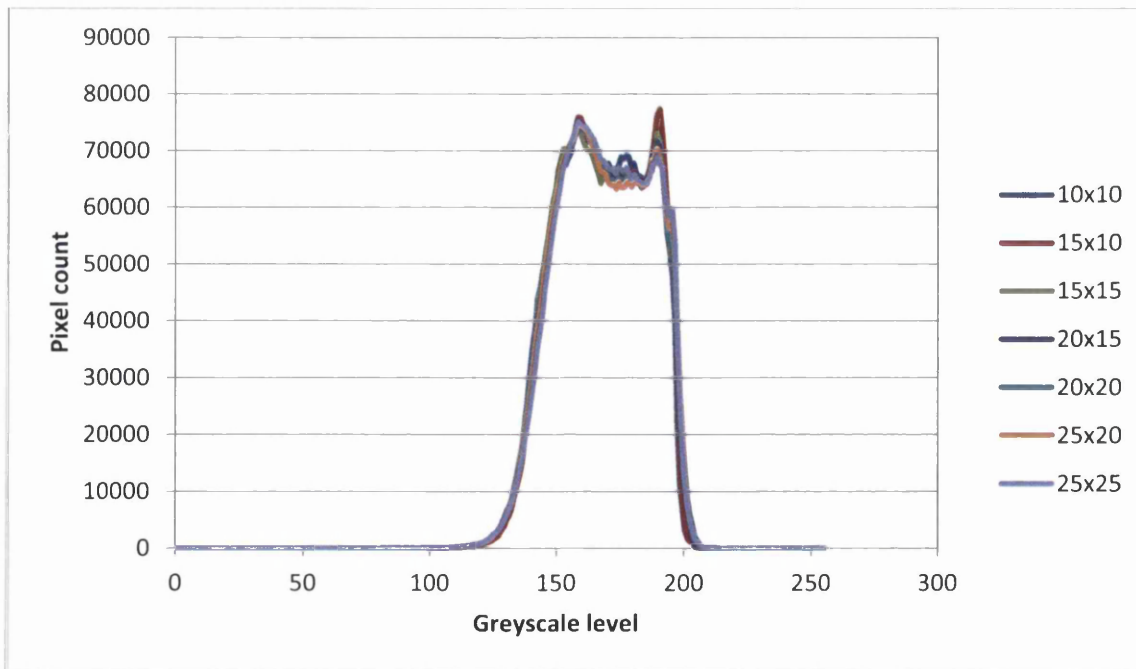


Figure A.6: Normalised histogram of GSL distribution for patch "reference solid" at different ROI sizes (sizes stated in millimetres for x- and y- direction of rectangular ROI)

A.3 Macro - Print Uniformity and Optical Density in Image

```
run("Set Measurements...", " mean standard min skewness kurtosis redirect=None decimal=3");
run("Specify...", "width=787 height=787 x=800 y=600 slice=1 centered");
while (nSlices>0)
{
    waitForUser("Move ROI", "Move ROI and click 'OK'");
    run("Measure");
    run("Histogram", "slice");
    waitForUser("Copy data", "Has the data been copied?");
    run("Close");
    run("Next Slice [>]");
}
```

A.4 Striation of Printing Plate Surface

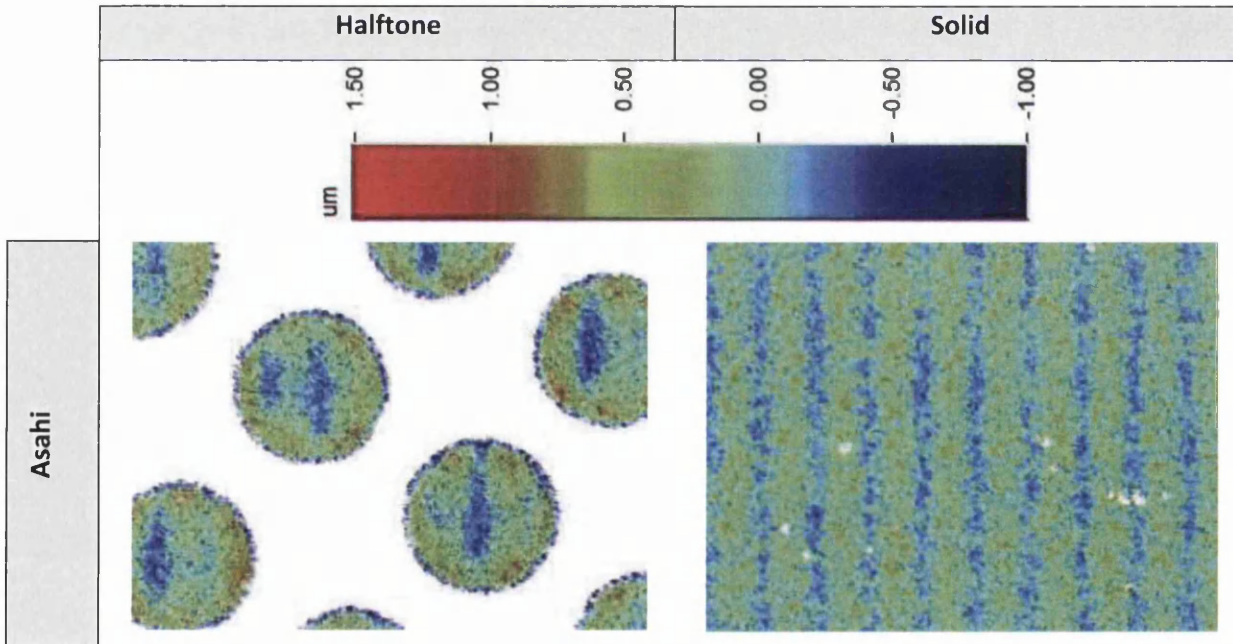


Figure A.7: Comparison of surface striation in halftone dots (50% dot at 100 lpi) and solids on printing plates (110x magnification) (continued on next page)

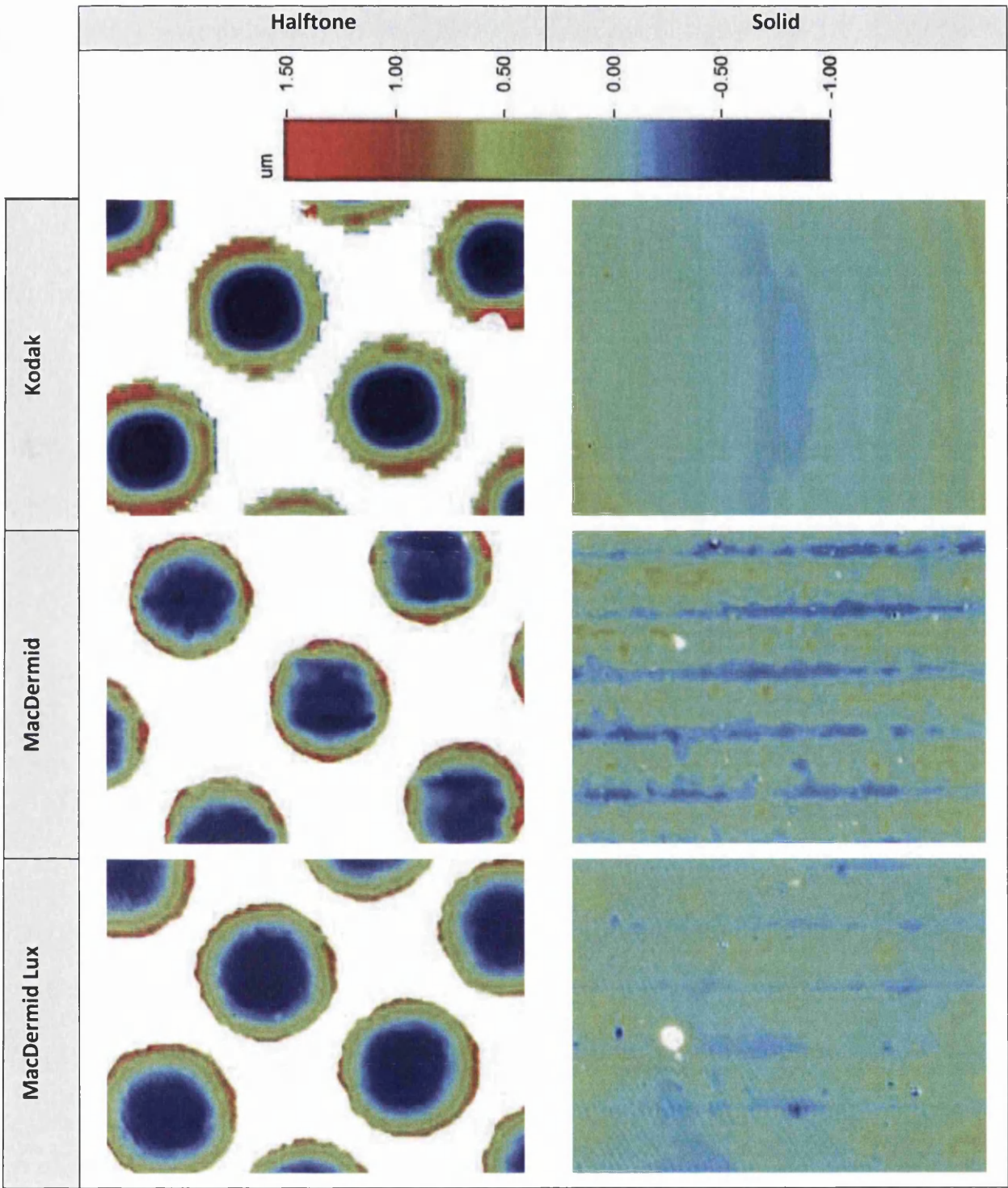


Figure A.7: (continued from previous page)

Table A.2: Distance and depth of striae

Plate type	Distance (μm)	Depth (μm)
Asahi	64.8	0.3
Kodak	-	-
MacDermid	90.0	0.3
MacDermid Lux		
• major striation	90.1	0.1
• minor striation	9.8	0.04

A.5 Area Transfer Ratios

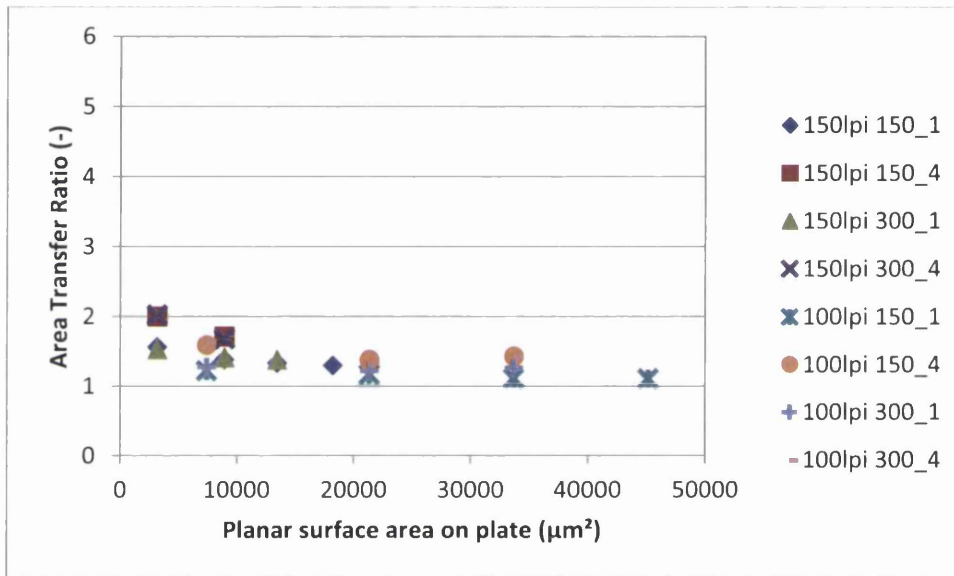


Figure A.8: Comparison of ATRs for line rulings of 150 lpi and 100 lpi for Kodak plate (printing conditions: "speed (ft/min)_engagement (thou)")

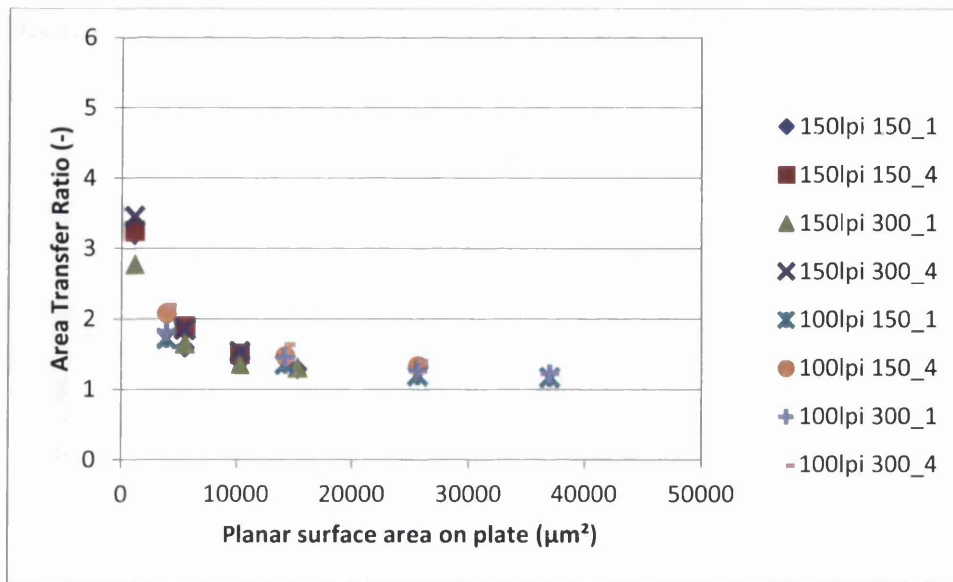


Figure A.9: Comparison of ATRs for line rulings of 150 lpi and 100 lpi for MacDermid plate (printing conditions: "speed (ft/min)_engagement (thou)")

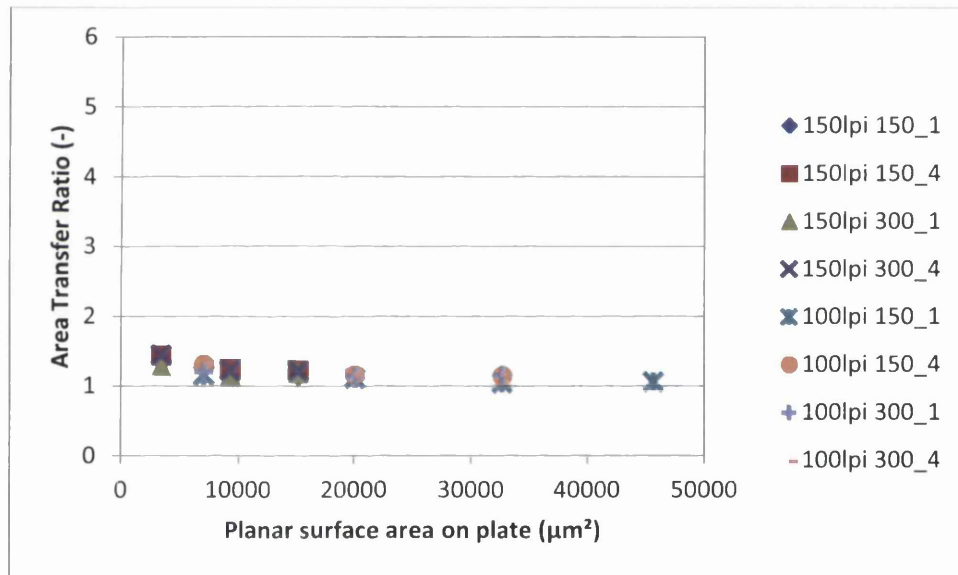


Figure A.10: Comparison of ATRs for line rulings of 150 lpi and 100 lpi for MacDermid Lux plate (printing conditions: "speed (ft/min)_engagement (thou)")

A.6 Volume Transfer Ratios

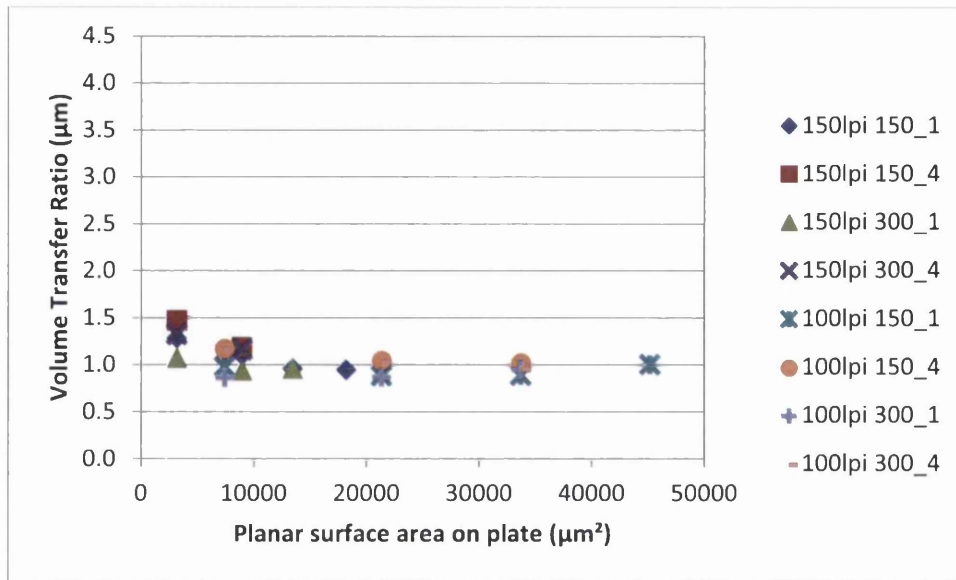


Figure A.11: Comparison of VTRs for line rulings of 150 lpi and 100 lpi for Kodak plate (printing conditions: "speed (ft/min)_engagement (thou)")

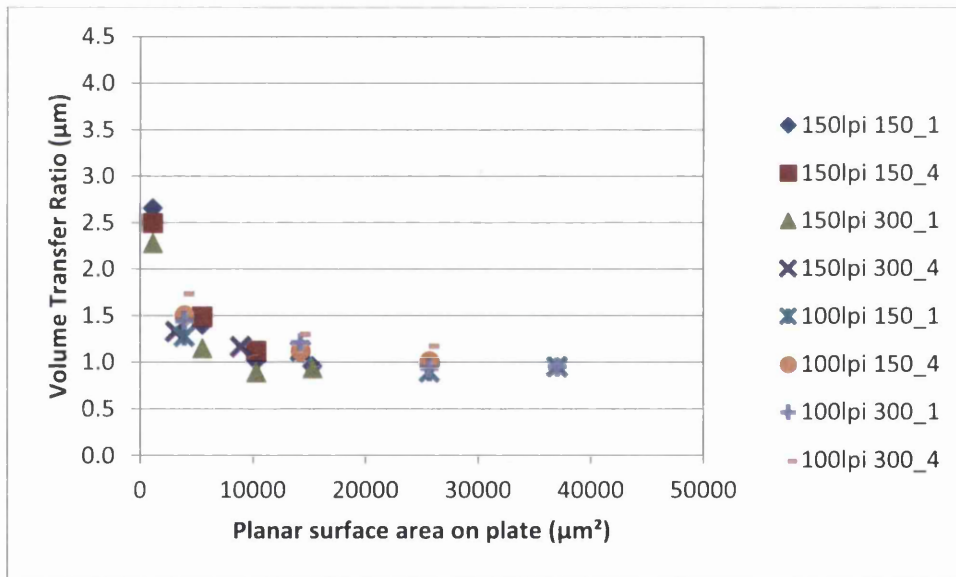


Figure A.12: Comparison of VTRs for line rulings of 150 lpi and 100 lpi for MacDermid plate (printing conditions: "speed (ft/min)_engagement (thou)")

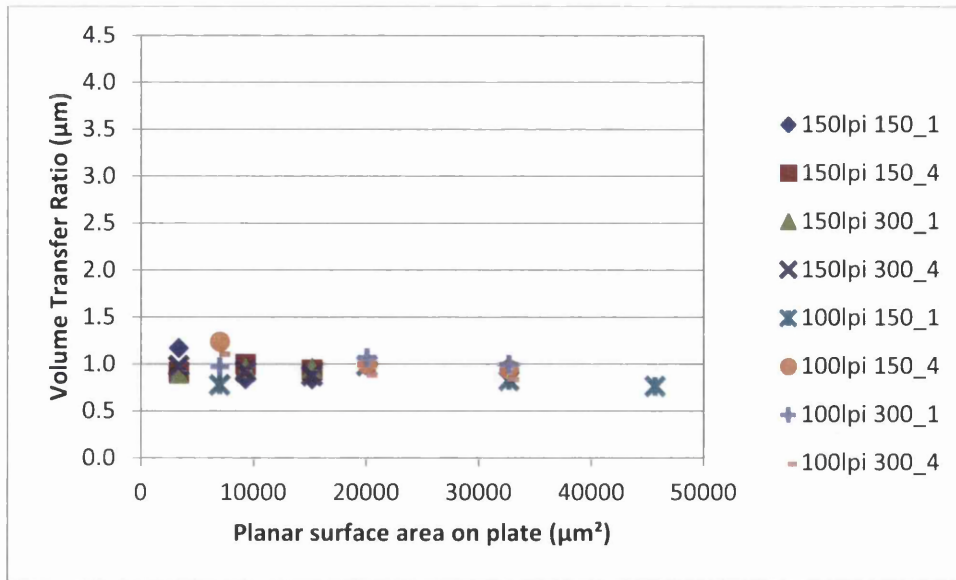

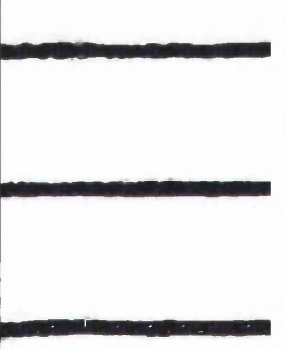



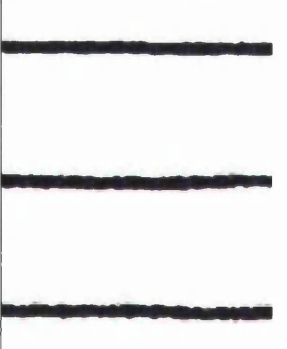
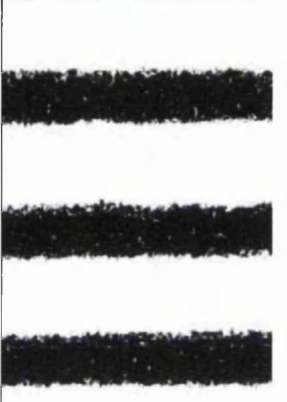


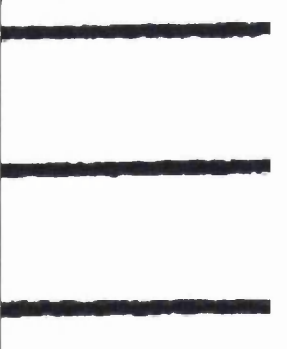
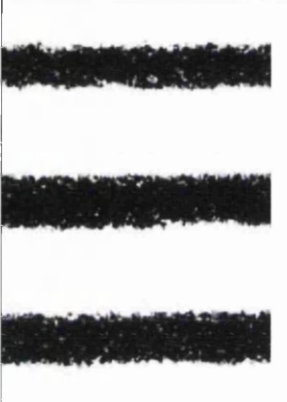

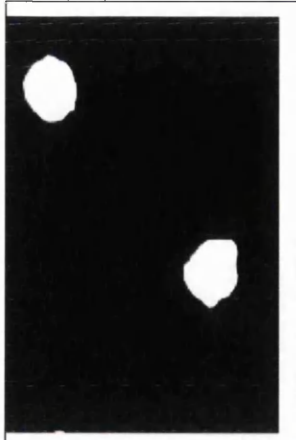
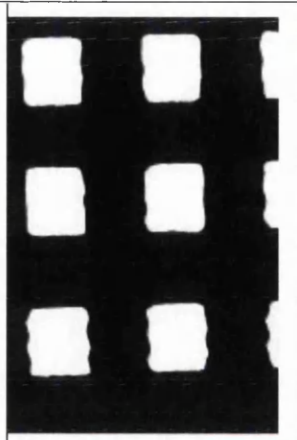
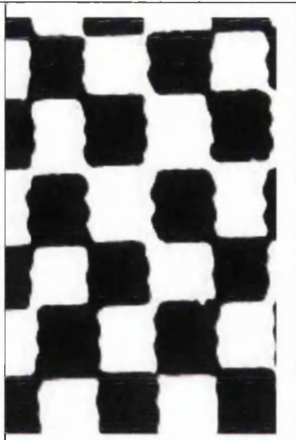
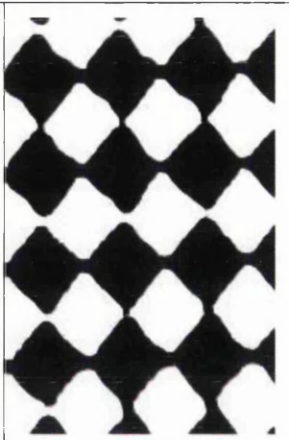
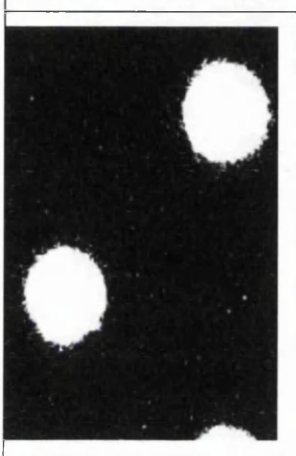
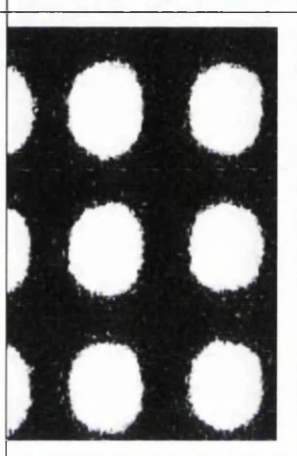
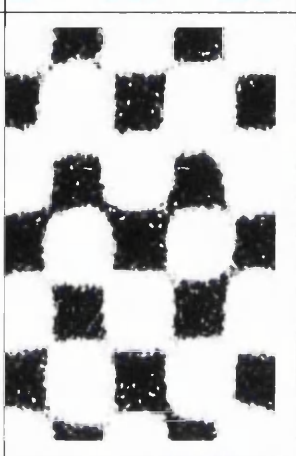
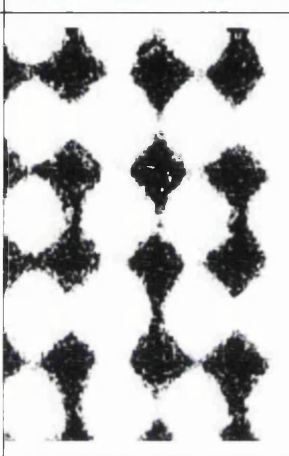
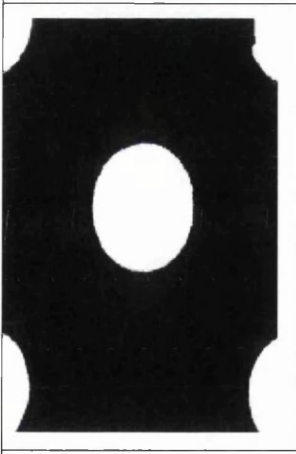
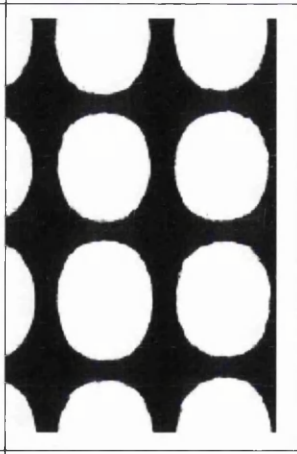
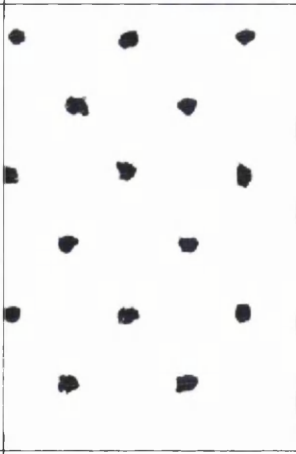
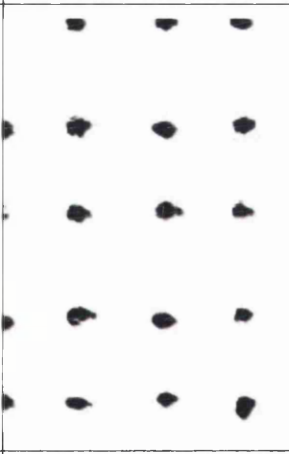
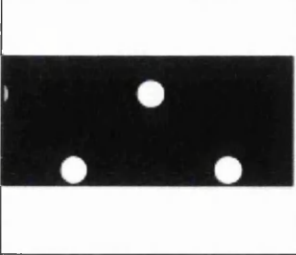
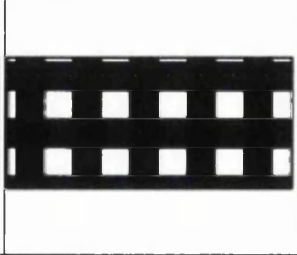
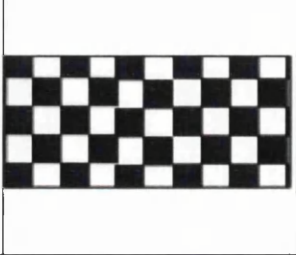
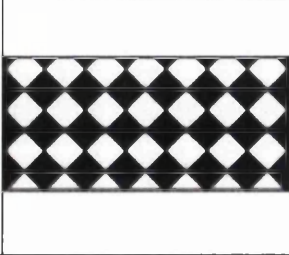


Figure A.13: Comparison of VTRs for line rulings of 150 lpi and 100 lpi for MacDermid Lux plate (printing conditions: "speed (ft/min)_engagement (thou)")

A.7 Plate Characterisation

Figure A.14: Nominal versus actual feature geometries of original image on printing plates for the meso-pattern trials on the IGT-F1 (some images not presented at real angle; 76x nominal pattern magnification; 180x actual sample magnification)

Pattern	Nominal geometry	Actual geometry		
		AFP-DSH	AWP-DEF	MacDermid Lux
Horizontal Lines				
Diagonal Lines				
Vertical Lines				

			
			
			
			
<p>Holes</p>	<p>Grid</p>	<p>Chequer (90° tilt)</p>	<p>Chequer (45° tilt)</p>

Tiles	Polka dots	Positive hexagons	Negative hexagons

A.8 Example of Full Data Set for Main Factor and Interaction Effects

This is the exemplary data set for main factor and interaction effects in the experimental plan investigating the MGSL of the plain solid reference in the meso-pattern study conducted on the IGT-F1 (Table A.3). Positive effects are set in green, negative effects in red; effects that could not be recognised as significant (uncertainty of effect $\Delta E = 0.489$) are marked grey. The nomenclature of factors involved in main factor/interaction effects is: 1 – ink, 2 – substrate, 3 – printing plate, 4 – anilox volume, 5 – printing force, 6 – printing speed.

Table A.3: Exemplary DoE data set of plain solid reference (meso-pattern trial on the IGT-F1)

Mean 0	Main effects						2-factor interaction effects		
	1	2	3	4	5	6	12	13	14
90.375	98.319	-2.540	2.971	-21.943	-5.028	-13.031	-9.237	1.479	-4.665
2-factor interaction effects									
15	16	23	24	25	26	34	35	36	45
-1.987	-11.868	-3.769	-0.199	-2.145	-2.074	-5.570	1.504	-1.192	2.800
2-factor		3-factor interaction effects							
46	56	123	124	125	126	134	135	136	145
4.206	1.354	-5.632	1.552	1.216	-3.560	-4.267	2.586	0.225	0.180
3-factor interaction effects									
146	156	234	235	236	245	246	256	345	346
3.613	2.379	-1.591	-1.494	1.590	-1.242	-1.381	-0.260	-0.183	1.598
3-factor		4-factor interaction effects							
356	456	1234	1235	1236	1245	1246	1256	1345	1346
-1.765	-0.690	-0.165	-2.012	1.721	-0.755	-0.328	-0.656	-0.195	1.684
4-factor interaction effects							5-factor interaction effects		
1356	1456	2345	2346	2356	2456	3456	12345	12346	12356
-1.459	-0.824	1.316	2.593	1.867	0.704	1.885	1.075	2.343	2.187
5-factor interaction effects			6-factor interaction effect			Uncertainty of effects			
12456	13456	23456	123456			ΔE			
0.726	0.939	-0.846	-1.128			±0.489			

A.9 Printing Defects of AFP-DSH Plate

Refer to next page.

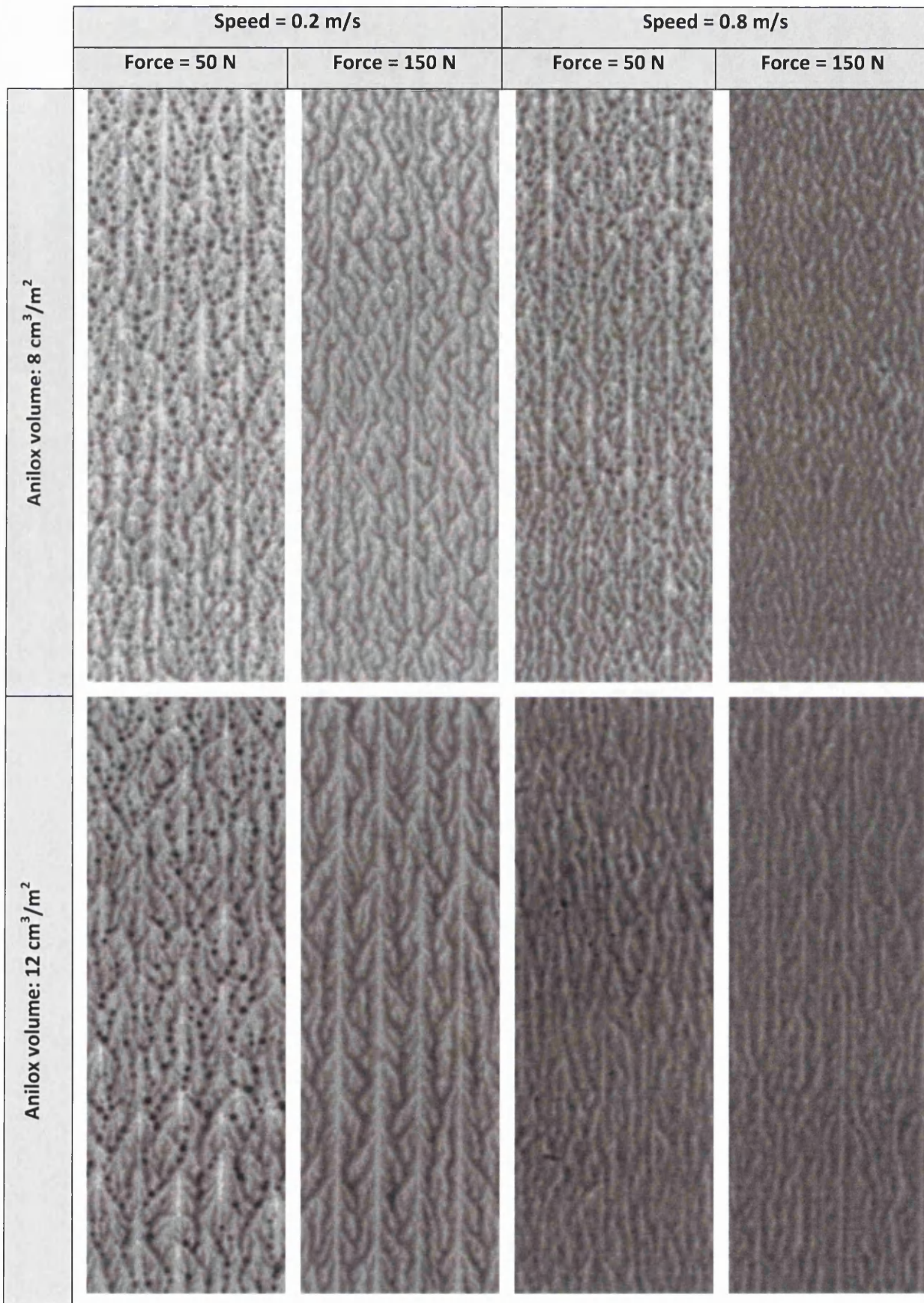


Figure A.15: Chequer pattern without tilt on AFP-DSH plate material. Strong change between fingering defect regimes with printing conditions observed for water-based ink on APCO substrate (7x magnification)

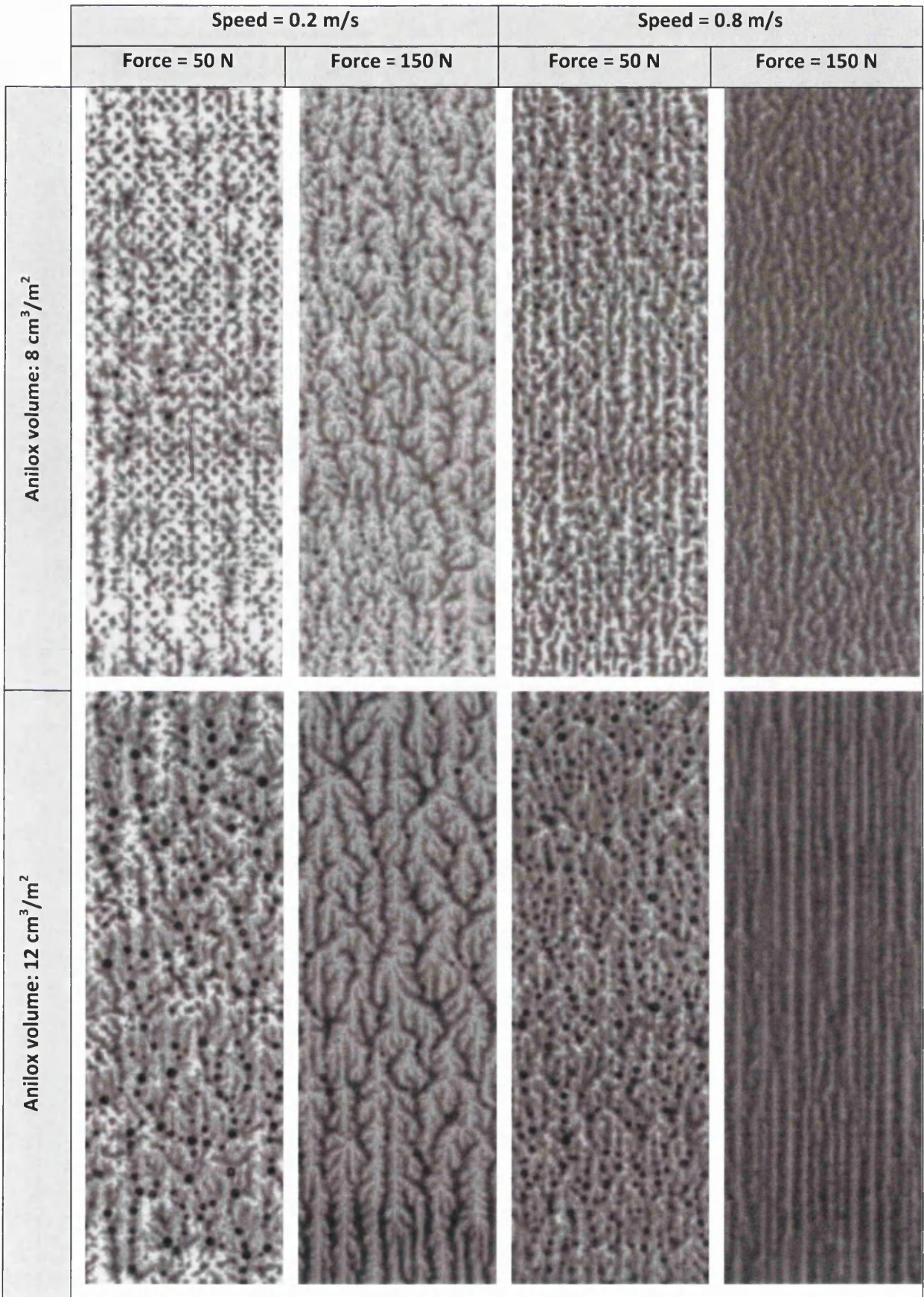
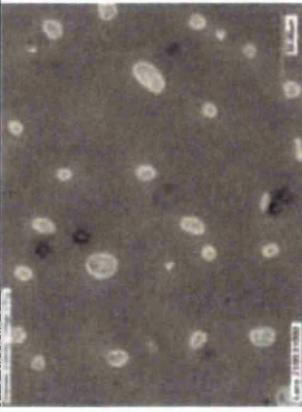
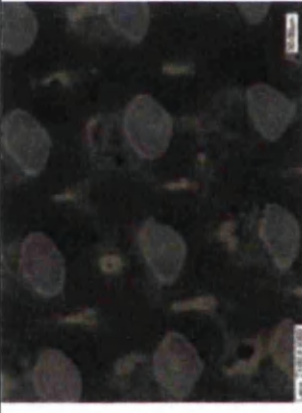

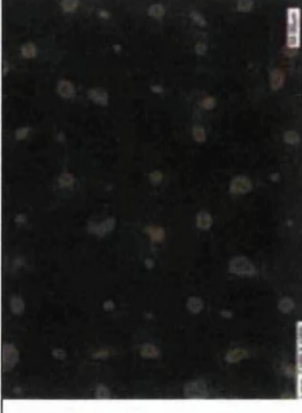
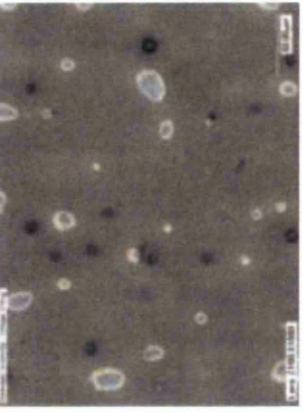
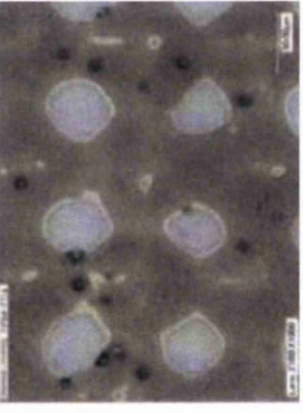
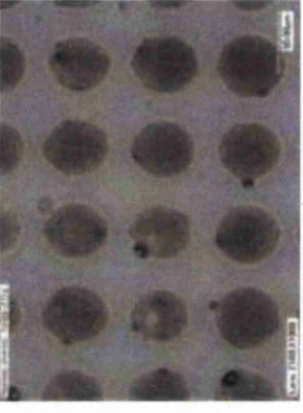
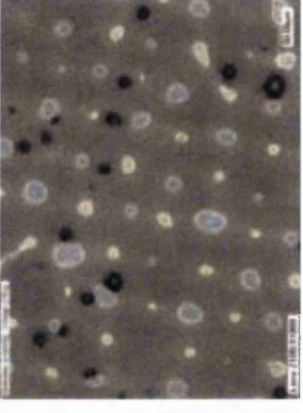
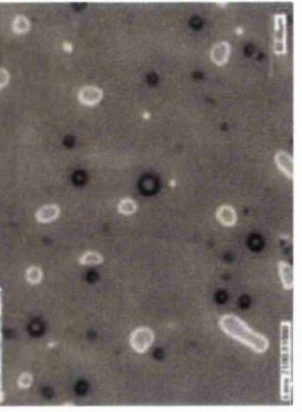
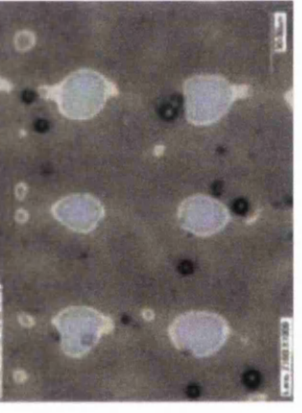
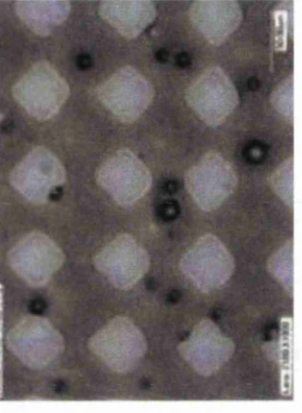
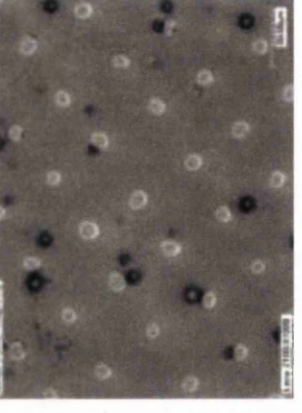


Figure A.16: Polka dot pattern on AFP-DSH plate material. Strong change between fingering defect regimes with printing conditions observed for water-based ink on APCO substrate (7x magnification)

A.10 Print Characterisation

Figure A.17: Failure of meso-patterns to produce closed ink films on the T-Flex 508 (printing speed of 150 ft/min, 4 thou engagement)

	Solid	Grid	Chequer at 45°	MC16P
Asahi				
MacDermid				
MacDermid Lux				

Glossary

Cupping: Top geometry of concave halftone dots which features the centre of the dot top below the top edge.

Dot dipping: Immersion of a dot on the printing plate into the cell of an anilox roll if the cell opening is larger than the dot.

Dot gain, optical: Apparent increase in printed area coverage of halftones due to light gathering.

Dot gain, physical: Increase in printed area coverage of halftones compared to the corresponding area coverage on the printing plate due to plate deformation and ink spreading.

Dot hardness: → *Sharpness*

Dot softness: → *Sharpness*

Doughnut: (Printing defect) printed halftone dots which assume a ring-shape due to lack of ink in their centre.

Halftone: Image element of varying size, shape and pitch into which a printing area is separated (screened) in order to create tonal gradients in the printed image. The smallest, isolated halftones are known as highlights, because they print faint areas. In this work this includes area coverages up to 20%. The halftones in the middle of the range are suitably called midtones. Halftones consisting of conjoint elements and resulting in dark printed areas are referred to as shadows (approximately 75% area coverage and above). Unscreened areas creating 100% area coverage are called solids.

Halo: (Printing defect) ink-free annulus found in printed halftone dots.

Highlight: → *Halftone*

Kiss contact or kiss engagement: Printing press setting at which printing plate and substrate on the impression cylinder just about touch and the mean contact force between them is near enough zero.

Light gathering: Absorption of scattered photons by ink films upon exiting the substrate.

Line ruling: Pitch of halftones.

Meso-pattern: Surface patterning on the printing plate which is made up of recesses or raised features with approximate nominal width of 50 µm; the feature geometry and pitch may vary.

Microcell: Commercial surface patterning of printing plates (EskoArtworks) which is made up of small recesses varying in size and pitch.

Micro-pattern: Surface patterning of printing plate which is made up of recesses or raised features with approximate nominal width of 25 µm or smaller, including microcells; the feature geometry and pitch may vary.

Midtone: → *Halftone*

Oxygen inhibition: Premature termination of a polymerisation reaction by the interference of molecular oxygen from the ambient air with the reagents.

Plate gain: Increase in area coverage of halftones on the printing plate compared to the corresponding area coverage in the digital image design.

Ribbing: (Printing defect) undulating ink film thickness transverse to the print direction, also referred to as “printer’s instability”.

Screen ruling: Pitch of anilox cells.

Shadow: → *Halftone*

Sharpness: Property of halftone dots and ink films describing the angle formed between the top and sides of the feature surface. Perfectly sharp features have right angles. Sharpness is also referred to as hardness in case of ink films. Hard printed dots are characterized by right angles, whereas soft dots feature obtuse angles.

Solid: → *Halftone*

SQUAREspot: Proprietary laser technology by Eastman Kodak which creates a laser beam of uniform lower power with rectangular cross section.

Surface patterning: Secondary design superimposed on ink-transferring areas of a printing plate to create additional surface texturing which is claimed to improve print quality.

Tonal value increase: Difference between the observed area coverage of halftones on the print and the corresponding area coverage on the printing plate. Sum of optical and physical dot gain.

UCA, uncovered area: (Printing defect) randomly occurring small holes in printed ink films.

Viscous fingering: (Printing defect) ramified channels of lower ink film thickness transverse to the print direction, also referred to as “Saffman-Taylor(-like) instability”.

Bibliography

- Abràmoff, M. D., Magalhães, P. J. & Ram, S. J., 2004. Image Processing with ImageJ. *Biophotonics International*, July, 11(7), pp. 36-42.
- Adamson, A. W. & Gast, A. P., 1967. *Physical Chemistry of Surfaces*. New York: Wiley-Interscience.
- Anderson, J., 2009. Don't Overthink It. Flexo platemaking is complex only if you let it become so. *package Printing*, March Volume.
- Anderson, J. & Schlotthauer, E., 2010. *Kodak's Flat Top Dots. The effect of flexo dot shape on plate stress and wear*. s.l.:Kodak.
- Andersson, C., Johnson, J. & Järnström, L., 2009. Ultraviolet-Induced Aging of Flexographic Printing Plates Studied by Thermal and Structural Analysis Methods. *Journal of Applied Polymer Science*, 112(3), pp. 1636-1646.
- Andreas, J. M., Hauser, E. A. & Tucker, W. B., 1938. Boundary tension by pendant drops. *Journal of Physical Chemistry*, 42(8), pp. 1001-1019.
- Arney, J. S., Engeldrum, P. G. & Zeng, H., 1995. A Modified Murray-Davies Model of Halftone Gray Scales. *1995 TAGA Proceedings*. TAGA, pp. 353-363.
- Aspler, J. S., 2004. Print Quality Test Method for Linerboard. In: *2004 TAGA Proceedings*. TAGA, pp. 427-452.
- Banks, W. H. & Mill, C. C., 1954. Some observations on the behaviour of liquids between rotating rollers. *Proceedings of the Royal Society A*, 233(1154), pp. 414-419.
- Barnes, H. A., 2000. *A Handbook of Elementary Rheology*. Aberystwyth: University of Wales, Institute of Non-Newtonian Fluid Mechanics.
- Barros, G. G., 2004. *Optical Topographical Characterisation for Flexographic Printability Assessment*. Karlstad: Karlstad University.
- Barros, G. G., 2006. *Influence of Substrate Topography on Ink Distribution in Flexography*. Karlstad: Karlstad University.
- Barros, G. G., Fahlcrantz, C.-M. & Johansson, P.-Å., 2006. Topographic Distribution of Uncovered Areas (UCA) in Full Tone Flexographic Prints. *TAGA Journal*, 2(1), pp. 43-57.
- Barros, G. G. & Johansson, P.-Å., 2006. Prediction of UnCovered Area occurrence in flexography based on topography - A feasibility study. *Nordic Pulp and Paper Research Journal*, 21(2), pp. 172-179.
- Barros, G. G. & Johansson, P.-Å., 2007. Mottle and ink distribution in full-tone flexography prints on coated linerboard. *Journal of Pulp and Paper Science*, 33(4), pp. 217-226.
- Barrow, M. S. et al., 2003. A study of the tensile properties of liquids in confined spaces using an atomic force microscope. *Proceedings of the Royal Society of London. Series A: Mathematical and Physical Science*, 459(2039), pp. 2885-2908.
- Bassemir, R. W. & Krishnan, R., 1990. Practical Applications of Surface Energy Measurements in Flexography. *FLEXO*, July Issue, n.p.

- Behler, H., 1993. *Die Randstrukturen von Druckpunkten - eine experimentelle Untersuchung der Farbspaltungsströmung*. Darmstadt: Technische Hochschule Darmstadt.
- Ben-Jacob, E. et al., 1985. Experimental Demonstration of the Role of Anisotropy in Interfacial Pattern Formation. *Physical Review Letters*, 55(12), pp. 1315-1318.
- Beynon, D. G., 2007. *Plate to Substrate Ink Transfer in the Flexographic Printing Process*. Swansea: Swansea University.
- Birkenshaw, J. W., 2004. Printing processes. In: R. H. Leach & R. J. Pierce, eds. *The Printing Ink Manual*. 5th edition. Dordrecht: Kluwer Academic Publishers, pp. 14-85.
- Bohan, M. F. J. et al., 2003. Evaluation of Pressures in Flexographic Printing. In: *2003 TAGA Proceedings*. TAGA, pp. 311-320.
- Borbély, Á. & Szentgyörgyvölgyi, R., 2011. The influence of printing pressure on flexographic print quality. In: N. Enlund & M. Lovreček, eds. *Advances in Printing and Media Technology. Proceedings of the 38th International Research Conference*. Darmstadt: iarigai, pp. 87-92.
- Bornemann, N., 2013. *Characterization and Investigation of Large-Area, Ultra-Thin Gravure Printed Layers*. Darmstadt: Technische Hochschule Darmstadt.
- Bornemann, N., Sauer, H. M. & Dörsam, E., 2010. Thin Film Behavior after Ink Transfer in Printing Processes. In: Anonymous. *LOPE-C (Large-area, Organic and Printed Electronics Convention) Proceedings*. Frankfurt a. M., Germany, 31 May-2 June 2010. Frankfurt a. M.: LOPE-C.
- Bornemann, N., Sauer, H. M. & Dörsam, E., 2011. Gravure Printed Ultrathin Layers of Small-Molecule Semiconductors on Glass. *Journal of Image Science and Technology*, 55(4), n.p.
- Bould, D. C., 2001. *An Investigation into Quality Improvements in Flexographic Printing*. Swansea, University of Wales Swansea.
- Bould, D. C., Claypole, T. C. & Bohan, M. F. J., 2004a. An investigation into plate deformation in flexographic printing. *Proceedings of the Institute of Mechanical Engineers Part B: Journal of Engineering Manufacture*, Volume 218, pp. 1499-1511.
- Bould, D. C., Claypole, T. C., Bohan, M. F. J. & Gethin, D. T., 2004b. Tone Gain due to Deformation of the Flexographic Plate. In: Anonymous. *Advances in Printing and Media Technology. 31st International Research Conference*. Copenhagen, Denmark, 5-8 September 2004. Copenhagen: Danish School of Media and Journalism.
- Bould, D. C., Hamblyn, S. M., Gethin, D. T. & Claypole, T. C., 2011. Effect of impression pressure and anilox specification on solid and halftone density. *Proceedings of the Institute of Mechanical Engineers Part B: Journal of Engineering Manufacture*, Volume 225, pp. 699-709.
- Broer, D. J., 1993. Photoinitiated Polymerization and Cross-Linking of Liquid-Crystalline Systems. In: J. P. Fouassier & J. F. Rabek, eds. *Polymerisation Mechanisms*. Barking: Elsevier Science Publishers, pp. 383-443.
- Busch, D. D., 2003. *Mastering Digital Scanning with Slides, Film, and Transparencies*. Boston: Course Technology/Cengage Learning.
- Cassie, A. B. D. & Baxter, S., 1944. Wettability of porous surfaces. *Transactions of the Faraday Society*, Volume 40, pp. 546-551.

- Chadov, A. V. & Yakhnin, E. D., 1988. Influence of roughness on wetting and the transfer of liquid from one solid surface onto the other. *Colloid Journal of the USSR*, 50(4), pp. 771-775.
- Chang, F.-M., Hong, S.-J., Sheng, Y.-J. & Tsao, H.-K., 2010. Wetting Invasion and Retreat Across a Corner Boundary. *Journal of Physical Chemistry C*, January, 114(3), pp. 1615-1621.
- Charlesworth, K., 2008. Flexo turns to flat-top dots. *PrintWeek*, February, Issue 21 February, pp. 29-30.
- Cherry, J. A., 2007. *Ink Release Characteristics of Anilox Rolls*. Swansea: University of Wales Swansea.
- Claypole, T. C. et al., 2008. Flexo printing of fine lines. In: *2008 TAGA Proceedings*. TAGA, pp. 252-266.
- Cook, B., Recchia, D. A. & Gotsick, T., 2014. *Method for improving print performance of flexographic printing elements*. US Patent 8669041.
- Cusdin, G., 1999. Introduction. In: Anonymous. *Flexography: Principles and Practices*. 5th edition. Ronkonkoma: Foundation of Flexographic Technical Association, pp. 1-36.
- Damroth, G. et al., 1996. The effect of UV flexo ink viscosity, anilox cell volume, and press speed on printed density and dot gain. In: *1996 TAGA Proceedings*. TAGA, pp. 86-101.
- Davies, G. R. & Claypole, T. C., 2004. The Effect of Speed on Image Transfer in Rotogravure Printing. In: Anonymous. *Advances in Printing and Media Technology. 31st International Research Conference*. Copenhagen, Denmark, 5-8 September 2004. Copenhagen: Danish School of Media and Journalism.
- de Gennes, P. G., 1985. Wetting: statics and dynamics. *Reviews of Modern Physics*, 57(3, Part 1), pp. 827-863.
- De Grâce, J. H. & Mangin, P. J., 1983. *A Mechanistic Approach to Ink Transfer: Part I: Effect of Substrate Properties and Press Conditions*. In: W. H. Banks Jr, ed. *Advances in Printing Science and Technology. Proceedings of the 17th International Conference of Printing Research Institutes*. London, Plymouth: Pentech Press, pp. 312-332.
- De Grâce, J. H. & Mangin, P. J., 1987. *A Mechanistic Approach to Ink Transfer: Part II - The Splitting Behaviour of Inks in Printing Nips*. In: W. H. Banks Jr, ed. *Advances in Printing Science and Technology. Proceedings of the 19th International Conference of Printing Research Institutes*. London, Plymouth: Pentech Press, pp. 146-161.
- Debeljak, M., Hladnik, A., Černe, L. & Gregor-Svetec, D., 2013. Use of Effect Pigments for Quality Enhancement of Offset Printed Speciality Papers. *Color Research and Application*, June, 38(3), pp. 168-176.
- Decker, C., 1993. New Developments in UV-Curable Acrylic Monomers. In: J. P. Fouassier & J. F. Rabek, eds. *Polymerisation Mechanisms*. Barking: Elsevier Science Publishers, pp. 33-64.
- Dedijer, S. et al., 2012. Flexographic ink composition and its wetting influence on flexo printing plate and printed substrate (PE FOIL). *Papřípar*, 56(4), pp. 24-30.
- Deganello, D. et al., 2011. Level-set method for the modelling of liquid bridge formation and break-up. *Computers and Fluids*, Volume 40, pp. 52-51.
- Della Volpe, C. et al., 2004. The solid surface free energy calculation. I. In defense of the multicomponent approach. *Journal of Colloid and Interface Science*, Volume 271, pp. 434-453.

- DFTA, 2002. Technical comparison of different flexo plate-making processes. *Flexo and Gravure International*, Volume 3, pp. 14-19.
- Dubé, M., Mairesse, F., Boisvert, J.-P. & Voisin, Y., 2005. Wavelet Analysis of Print Mottle. *submitted to IEEE Transactions on Image Processing*.
- Dykes, Y., 1999. Flexographic Printing Plates. In: Anonymous. *Flexography: Principles and Practices*. 5th edition. Ronkonkoma: Foundation of Flexographic Technical Association, pp. 1-60.
- Extrand, C. W., 2005. Modeling of Ultralyophobicity: Suspension of Liquid Drops by a Single Asperity. *Langmuir*, 21(23), pp. 10370-10374.
- Extrand, C. W. & Moon, S. I., 2008. Contact Angles on Spherical Surfaces. *Langmuir*, September, 24(17), pp. 9470-9473.
- Fernando, H. J. S. (Ed.), 2012. *Handbook of Environmental Fluid Dynamics. Volume One: Overview and Fundamentals*. Boca-Raton: CRC Press.
- Fetsko, J. M. & Walker, W. C., 1955. Measurement of Ink Transfer in Printing Coated Paper. *American Ink Maker*, November, 33(11), pp. 38-42/67-69.
- Fioravanti, M., 2003. The future of exposure technology. *Flexo and Gravure International*, Volume 1, pp. 72-74.
- Flexcor, 2012. *Anilox screens*. Available from: < <http://www.flexcor.com.au/html/rollers/rollers.htm> > [11 February 2015]
- Fouché, L. & Blayo, A., 2001. Transfer Characterization of UV Flexo Inks. In: *2001 TAGA Proceedings*. TAGA, pp. 426-443.
- Fowkes, F. M., 1962. Determination of interfacial tensions, contact angles, and dispersion forces in surfaces by assuming additivity of intermolecular interactions in surfaces. *Journal of Physical Chemistry*, 66(2), p. 382.
- Fuh, J. Y. H. et al., 1997. Post-Cure Shrinkage of Photo-Sensitive Material Used in Laser Lithography Process. *Journal of Materials Processing Technology*, Volume 63, pp. 887-891.
- Galton, D. J., 2003. A study of the effects of the process parameters on the characteristics of photochemical flexographic printing plates. *Pigment and Resin Technology*, 32(4), pp. 235-247.
- Galton, D. J., 2004a. Investigation into the Causes for "Mottle". In: *2004 TAGA Proceedings*. TAGA, pp. 409-427.
- Galton, D. J., 2004b. A study of the effects of the process parameters on the flexographic printing problem "dot bridging" - Part I: experimental design and linear run length. *Pigment and Resin Technology*, 33(5), pp. 293-301.
- Galton, D. J., 2005a. Investigation into the Causes for "Mottle". In: *2005 TAGA Proceedings*. TAGA, pp. 202-221.
- Galton, D. J., 2005b. A study of the effects of the process parameters on the flexographic printing problem "dot bridging" - Part II: experimental design and print contrast/density. *Pigment and Resin Technology*, 34(2), pp. 94-100.
- Galton, D. J. & Rosenberger, R. R., 2007. A novel solution for the characterisation of corrugated printing quality. In: *2007 TAGA Proceedings*. TAGA, pp. 403-414.

- Gay, C., 2002. Stickiness - Some Fundamentals of Adhesion. *Integrative and Comparative Biology*, Volume 42, pp. 1123-1126.
- Gibbs, J. W., 1874-1878. On the Equilibrium of Heterogeneous Substances. *Transactions of the Connecticut Academy of Arts and Sciences*, Volume 3, pp. 108-248, 343-520.
- Gilbert, E. D. & Lee, F., 2008. Flexographic Plate Technology: Conventional Solvent Plates versus Digital Solvent Plates. *Journal of Industrial Technology*, 24(3), n.p.
- Girard Leloup, L., 2000. Statistical Analysis of the Possibilities and Limits of Flexographic Process Modelling. In: *2000 TAGA Proceedings*. TAGA, 469-486.
- Good, R. J., 1992. Contact angle, wetting, and adhesion: a critical review. *Journal of Adhesion Science and Technology*, 6(12), pp. 1269-1302.
- Gotsick, T., 2014. *Theoretical and Empirical Models of Print Gain. Analyzing Shoulder Angle and Compression*. Available from < <http://www.flexoglobal.com/blog/2014/01/20/theoretical-empirical-models-of-print-gain/> > [20 November 2014]
- Griesheimer, S., 2013. *Farbspaltungsphänomene von Druckfarben an strukturierten Oberflächen am Beispiel des Flexodrucks*. Darmstadt: Technische Hochschule Darmstadt.
- Gupta, C., Mensing, G. A., Shannon, M. A. & Kenis, P. J. A., 2007. Double Transfer Printing of Small Volumes of Liquids. *Langmuir*, 23(5), pp. 2906-2914.
- Hageman, H. J., 1989. Photoinitiators and Photoinitiation Mechanisms of Free-Radical Polymerisation Processes. In: N. S. Allen, ed. *Photopolymerisation and photoimaging science and technology*. Barking: Elsevier Science Publishers, pp. 1-54.
- Hall, E. L., 1979. *Computer Image Processing and Recognition*. New York: Academic Press.
- Hallberg, E., Odeberg Glasenapp, A. & Lestelius, M., 2005. Quantification of Banding on Printed Currogated Board Using Spatial Frequency Analysis. *Packaging Technology and Science*, Volume 18, pp. 89-95.
- Hamblyn, S. M., 2004. *The Role of the Plate in the Ink Transfer Process in Flexographic Printing*. Swansea: University of Wales Swansea.
- Hargreaves, I., 2004. Ultra-violet and electron-beam curing systems. In: R. H. Leach & R. J. Pierce, eds. *The Printing Ink Manual*. 5th edition. Dordrecht: Kluwer Academic Publishers, pp. 636-677.
- Harri, L., 2009. Microscopic Studies of the Influence of Main Exposure Time on Parameters of Flexographic Printing Plate Produced by Digital Thermal Method. *Microscopy Research and Technique*, Volume 72, pp. 707-716.
- Harri, L. & Czichon, H., 2006. Microscopic Studies of the Influence of Technological Conditions on Technical Parameters of Photopolymer Flexographic Plates. *Microscopy Research and Technique*, Volume 69, pp. 675-683.
- Hecker, K. & Breitung, S., 2013. *Organic and Printed Electronics. Applications, Technologies and Suppliers*. 5th edition. Frankfurt a. M.: VDMA Verlag.
- Hejda, F., Solař, P. & Kousal, J., 2010. Surface Free Energy Determination by Contact Angle Measurements - A Comparison of Various Approaches. In: J. Šafránková & J. Pavlů, eds., *WDS'10 Proceedings of Contributed Papers: Part III - Physics*. Prague: Matfyzpress, pp. 25-30.

- Hejduk, J., 2010. *The Impact of Physical Properties of Rubber Roller Surfaces on the Effectivity of Ink Transfer (Annotation)*. Pardubice: University of Pardubice.
- Hernandez-Sosa, G. et al., 2013. Rheological and Drying Considerations for Uniformly Gravure-Printed Layers: Towards Large-Area Flexible Organic Light-Emitting Diodes. *Advanced Functional Materials*, Volume 23, pp. 3164-3171.
- Hikmet, R. A. M., Zwerver, B. H. & Broer, D. J., 1992. Anisotropic polymerization shrinkage behaviour of liquid-crystalline diacrylates. *Polymer*, 33(1), pp. 89-95.
- Holmvall, M., 2010. *Nip Mechanics, Hydrodynamics and Print Quality in Flexo Post-Printing*. Sundsvall: Mittuniversitetet.
- Holmvall, M. & Uesaka, T., 2007. Nip Mechanics of Flexo Post-Printing on Corrugated Board. *Journal of Composite Materials*, 41(17), pp. 2129-2145.
- Holmvall, M. & Uesaka, T., 2008a. Striping of Corrugated Board in Full-Tone Flexo Post-Printing. *Appita Journal*, 61(1), pp. 35-40.
- Holmvall, M. & Uesaka, T., 2008b. Print Uniformity of Corrugated Board in Flexo Printing: Effects of Corrugated Board and Halftone Dot Deformation. *Packaging Technology and Science*, Volume 21, pp. 385-394.
- Holmvall, M., Uesaka, T., Drolet, F. & Lindström, S. B., 2011. Transfer of a microfluid to a stochastic fibre network. *Journal of Fluids and Structures*, October, 27(7), pp. 937-946.
- Hornschuh, M., 2005. *Diskussion über Probleme im drucktechnischen Alltag. Auszüge aus dem DFTA-Frühjahrs-Symposium*. Available from < <http://www.manfred-hornschuh.de/downloads/gesdok05.pdf>> [29 January 2015]
- Huang, W.-X. et al., 2008. Simulation of Liquid Transfer Between Separating Walls for Modeling Micro-Gravure-Offset Printing. *International Journal of Heat and Fluid Flow*, Volume 29, pp. 1436-1446.
- Hübner, A. C. et al., 2002. High Volume Printing Technologies for the Production of Polymer Electronic Structures. In: Anonymous. *POLYTRONIC 2002. Proceedings of the 2nd International IEEE Conference on Polymers and Adhesives in Microelectronics and Photonics*. Piscataway: IEEE, pp. 172-176.
- Hübner, G., 1991. *Ein Beitrag zum Problem der Flüssigkeitsspaltung in der Drucktechnik*. Darmstadt: Technische Hochschule Darmstadt.
- Järnström, J. et al., 2007. Alternative methods to evaluate the surface energy components of ink-jet paper. *Colloids and*, Volume 294, pp. 46-55.
- Johnson, J., Rättö, P., Lestelius, M. & Järnström, L., 2003. Dynamic Nip Pressure in a Flexographic CI-Printing Press. In: *2003 TAGA Proceedings*. TAGA, pp. 357-374.
- Johnson, J. et al., 2009. Some Properties of Flexographic Printing Plates and Aspects of Print Quality. *Appita Journal*, October-December, 62(5), pp. 371-378.
- Jung, Y. C. & Bhushan, B., 2006. Contact angle, adhesion and friction properties of micro- and nanopatterned polymers for superhydrophobicity. *Nanotechnology*, Volume 17, pp. 4970-4980.
- Kaelble, D. H., 1970. Dispersion-Polar Surface Tension Properties of Organic Solids. *Journal of Adhesion*, Volume 2, pp. 66-81.

Kang, H. R., 1999. *Digital Color Halftoning*. Bellingham, WA: SPIE - The International Society for Optical Engineering.

Kaplanová, M. & Hejduk, J., 2006. Influence of Rubber Surface Tension on Ink Transfer in Flexography. In: Anonymous. *Conference proceedings of Printing Technology SPb '06*. St. Petersburg: St. Petersburg State University of Technology and Design, pp. 59-61.

Kempa, H. et al., 2006. On the applicability of different mass printing methods for the deposition of organic functional materials. In: Anonymous. *OEC-06. Proceedings of the Organic Electronics Conference*. Cambridge: cintelliq.

Kempa, H. et al., 2008. Progress in Mass-Printed Electronics. In: Anonymous. *TPE 08. 3rd International Symposium "Technologies for Polymer Electronics"*. Rudolstadt: TITK (Thüringisches Institut für Textil- und Kunststoff-Forschung e.V.), p. 146 ff.

Kipphan, H. (Ed.), 2001. *Handbook of Print Media*. Berlin, Heidelberg: Springer.

Kodak, 2010. *Kodak DigiCap NX Screening. Achieve higher densities and greater efficiency in flexographic printing*. Rochester: Eastman Kodak Company.

Kodak, 2012. *Accuracy, stability, and repeatability. Kodak SQUAREspot Imaging Technology*. Rochester: Eastman Kodak Company.

Kodak, 2013. *Kodak Flexcel NX System. Anything is possible*. Rochester: Eastman Kodak Company.

Kunz, W., 1975. Ink Transfer in Gravure Process. In: *1975 TAGA Proceedings*. TAGA, pp. 151-176.

Kwok, D. Y., Li, D. & Neumann, A. W., 1994. Evaluation of the Lifshitz-van der Waals/Acid-Base Approach To Determine Interfacial Tensions. *Langmuir*, Volume 10, pp. 1323-1328.

Kwok, D. Y. & Neumann, A. W., 1999. Contact angle measurement and contact angle determination. *Advances in Colloid and Interface Science*, Volume 81, pp. 167-249.

Kwok, D. Y., Ng, H. & Neumann, A. W., 2000. Experimental Study on Contact Angle Patterns: Liquid Surface Tensions Less Than Solid Surface Tensions. *Journal of Colloid and Interface Science*, Volume 225, pp. 323-328.

Laksin, M. & Parris, J., 1997. Optimization of Ink Lay in UV Flexographic Printing. In: *1997 TAGA Proceedings*. TAGA, pp. 861-871.

Leach, R. H. & Pierce, R. J., 2004. The nature of printing ink. In: R. H. Leach & R. J. Pierce, eds. *The Printing Ink Manual*. 5th edition. Dordrecht: Kluwer Academic Publishers, pp. 1-13.

Lindholm, G., Gustafsson, M., Girard Leloup, L. & Vuillermoz, S., 1996. Ink transfer in flexo evaluated by X-ray fluorescence. In: *1996 TAGA Proceedings*. TAGA, pp. 102-117.

Lindner, A., Derks, D. & Shelley, M. J., 2005. Stretch flow of thin layers of Newtonian liquids: Fingering patterns and lifting forces. *Physics of Fluids*, Volume 17, pp. 072107-1 - 072107-13.

Lippold, S. & Podlesny, J., 1998. *WYKO Surface Profilers. Technical Reference Manual*. Tuscon: Veeco Metrology Group.

Liu, F. & Shen, W., 2008. Forced Wetting and Dewetting of Liquids on Solid Surfaces and their Roles in Offset Printing. *Colloids and Surfaces A: Physicochemical Engineering Aspects*, March, 316(1-3), pp. 62-69.

Liu, X. & Guthrie, J. T., 2003. A review of flexographic printing plate development. *Surface Coatings International Part B: Coatings Transactions*, June, 86(2), pp. 91-99.

Liu, X., Guthrie, J. T. & Bryant, C., 2002. A study of the processing of flexographic solid-sheet photopolymer printing plates. *Surface Coatings International Part B: Coatings Transactions*, November, 85(4), pp. 313-319.

Liu, X., Guthrie, J. & Bryant, C., 2004. A Study of the Relevance of Plate Quality and Print Quality to UV Flexographic Folding Carton Printing. *Surface Coatings International Part B: Coatings Transactions*, 87(3), pp. 167-174.

LPC, 2010. *PRIMIR "Benchmarking and Worldwide Market Trends for Flexographic Printing"*. Austin: LPC.

MacDermid Printing Solutions, 2011. *The Effect of MacDermid LUX on the Solid Ink Density. Enhancement of EskoArtworks MicroCell Surface Patterning Technology*. s.l.: MacDermid Printing Solutions.

MacDermid Printing Solutions, 2012. *MacDermid Digital Rave*. s.l.: MacDermid Printing Solutions.

MacPhee, J., 1997. A Unified View of the Film Splitting Process, Part 1. *American Ink Maker*, 75(1), pp. 42-49.

MacPhee, J. & Lind, J. T., 2002. Insight Into the Relationship Between Print Density and Ink Film Thickness. In: *2002 TAGA Proceedings*. TAGA, pp. 479-496.

Mahović Poljaček, S., Cigula, T., Tomašegović, T. & Brajnović, O., 2013. Meeting the Quality Requirements in the Flexographic Plate Making Process. *International Circular of Graphic Education and Research*, Volume 6, pp. 62-69.

Mathes, H., 2011. Flexo troubleshooting. Most common flexo printing issues, Part 1/2/3. *Flexo and Gravure International*, Volume 2/3/4, pp. 12-13/20-22/22-23.

Mathes, H., 2012. Flexo troubleshooting. Most common flexo printing issues, Part 4. *Flexo and Gravure Global*, Volume 1, pp. 10-11.

McCloud, K. V. & Maher, J. V., 1995. Experimental perturbations to Saffman-Taylor flow. *Physics Reports*, Volume 260, pp. 139-185.

Mesic, B., Lestelius, M. & Engström, G., 2006a. Influence of Corona Treatment Decay on Print Quality in Water-borne Flexographic Printing of Low-density Polyethylene-coated Paperboard. *Packaging Technology and Science*, Volume 19, pp. 61-70.

Mesic, B., Lestelius, M. & Engström, G., 2006b. Occurrence and Causes of Uncovered Areas in Water-Borne Flexographic Print on PE-extrusion-coated Packaging Papers. In: Anonymous, *Proceedings of the International Printing and Graphic Arts Conference*. Peachtree Corners: TAPPI.

Mettänen, M., 2010. *Measurement of Print Quality: Joint Statistical Analysis of Paper Topography and Print Defects*. Tampere: Tampere University of Technology.

Meyer, K.-H., Dürholz, R. & Bütterich, K., 1996. *The printing plate as a quality characteristic in the reproduction of the printed image in flexographic printing*. Stuttgart: DFTA Technology Centre at the Technical College of Printing.

Miller, J. C. & Myers, R. R., 1958. A Photographic Study of Liquid Flow in a Roll Nip. *Transactions of the Society of Rheology*, Volume 2, pp. 77-93.

- Miller, S. & Zmetana, S., 2005. *Advanced Prepress Technologies for Flexographic Printing*. Burnaby: Creo Inc.
- Mirle, S. K., 1989. *Studies on Flexography: Characterization of Surface, Compositional and Mechanical Properties of Photopolymer Plates; Printability Experiments and Mathematical Modelling of Flexographic Printing*. Bethlehem: Lehigh University.
- Montgomery, D. C., 2012. *Design and Analysis of Experiments*. 8th edition (International Student Version). Singapore: John Wiley and Sons Singapore.
- Müller, P. H., Neumann, P. & Storm, R., 1979. *Tafeln der mathematischen Statistik*. 3rd, improved edition. Leipzig: VEB Fachbuchverlag Leipzig.
- Murray, A., 1936. Monochrome Reproduction in Photoengraving. *Journal of the Franklin Institute*, June, 221(6), pp. 721-744.
- Myers, R. R., Miller, J. C. & Zettlemyer, A. C., 1959. The Splitting of Thin Liquid Films. Kinematics. *Journal of Colloid Science*, Volume 14, pp. 287-299.
- Naito, I. et al., 2004. Examining the Mechanism of Ink Transfer. In: Anonymous. *Advances in Printing and Media Technology. 31st International Research Conference*. Copenhagen, Denmark, 5-8 September 2004. Copenhagen: Danish School of Media and Journalism.
- Naito, I., Tsuzaki, Y., Ohto, A. & Nitta, Y., 2006. Studies of Ink Trapping III. Direct detection of small air bubbles in ink layer. *Acta Graphica*, 18(1-4), pp. 19-24.
- Nase, J., Derks, D. & Lindner, A., 2011. Dynamic evolution of fingering patterns in a lifted Hele-Shaw cell. *Physics of Fluids*, 23(12), n.p.
- Niggemeier, G., 2002. *Around the Anilox Roller*. Available from <http://www.zecher.com/fileadmin/user_upload/Knowledge/Basics/AniloxBasics/AniloxBasics_ENG.pdf> [12 February 2015]
- Novaković, D., Dedijer, S. & Mahović Poljaček, S., 2010. A Model for Improving the Flexographic Printing Plate Making Process. *Teknički vjesnik*, 17(4), pp. 403-410.
- Oakland, J. S., 1987. *Statistical Process Control. A Practical Guide*. London, Melbourne, Johannesburg, Auckland: Heinemann Professional Publishing.
- Oliver, J. F., Huh, C. & Mason, S. G., 1977. Resistance to Spreading of Liquids by Sharp Edges. *Journal of Colloid and Interface Science*, May, 59(3), pp. 568-581.
- Olsson, R., Yang, L., van Stam, J. & Lestelius, M., 2006. Effects on ink setting in flexographic printing: coating polarity and dot gain. *Nordic Pulp and Paper Research Journal*, 21(5), pp. 569-574.
- Olsson, R., Yang, L., van Stam, J. & Lestelius, M., 2007. Effects of elevated temperature on flexographic printing. In: N. Enlund & M. Lovreček, eds. *Advances in Printing and Media Technology. Proceedings of the 34th International Research Conference*. Darmstadt: iarigai.
- Olszak, A. G., Schmit, J. & Heaton, M. G., 2001. *Interferometry: Technology and Applications*. Available from <http://cmi.epfl.ch/metrology/files/Wyko/DOC3_AN47_Interferometry.pdf>. [27 January 2015]
- Owens, D. K. & Wendt, R., 1969. Estimation of surface free energy of polymers. *Journal of Applied Polymer Science*, August, 13(8), pp. 1741-1747.

Pearson, J. R. A., 1960. The instability of uniform viscous flow under rollers and spreaders. *Journal of Fluid Mechanics*, 7(4), pp. 481-500.

Pearson, M., 1980. n Value for General Conditions. In: *1980 TAGA Proceedings*. TAGA, pp. 415-425.

Pluhar, J., 2004. Die Suche nach dem universellen Material. *Flexo + Tief-Druck*, Volume 5, pp. 103-105.

Poivet, S., Nallet, F., Gay, C. & Fabre, P., 2003. Cavitation-induced force transition in confined viscous liquids under traction. *Europhysics Letters*, April, 62(2), pp. 244-250.

Poivet, S. et al., 2004. Force response of a viscous liquid in a probe-tack geometry: Fingering versus cavitation. *The European Physical Journal E*, Volume 15, pp. 97-116.

Quinn, J. A., Valenzuela, D. P., Micale, F. J. & Lavelle, J. S., 1997. Does the Surface Energy of the Plate Affect Ink Transfer? *CONVERTER e Cartotecnica*, 10(unk.), pp. 135-143.

Rabaud, M., Couder, Y. & Michalland, S., 1991. Wavelength selection and transients in the one-dimensional array of cells of the printer's instability. *European Journal of Mechanics - B/Fluids*, 10 (2 (Suppl.)), pp. 253-260.

Rabel, W., 1971. Einige Aspekte der Benetzungstheorie und ihre Anwendung auf die Untersuchung und Veränderung der Oberflächeneigenschaften von Polymeren. *Farbe und Lack*, 77(10), pp. 997-1006.

Reuter, K. et al., 2007. Influence of process parameters on the electrical properties of offset printed conductive polymer layers. *Progress in Organic Coatings*, 58(4), pp. 312-315.

Roch, F., 2007. *Lecture notes for "Statistische Versuchsplanung", Sommersemester 2007*. Leipzig: Hochschule für Technik, Wirtschaft und Kultur Leipzig, unpublished.

Rosenberger, R. R., 2010. *Method of, and apparatus for, measuring the quality of a surface of a substrate*. US Patent 2010/0231708.

Rousset, E., Baudin, G., Cugnet, P. & Viallet, A., 2001. Screened Offset Plates: A Contact Angle Study. *Journal of Imaging Science and Technology*, 45(6), pp. 517-522.

Sadovnikov, A., Lensu, L., Kamarainen, J.-K. & Kälviäinen, H., 2005a. Quantified and Perceived Unevenness of Solid Printed Areas. In: A. Sanfeliu & M. Lazo Cortés, eds. *Progress in Pattern Recognition, Image Analysis and Applications. Proceedings of the 10th Iberoamerican Congress on Pattern Recognition, CIARP 2005*. Berlin, Heidelberg: Springer-Verlag, pp. 710-719.

Sadovnikov, A. et al., 2005b. Mottling Assessment of Solid Printed Areas and Its Correlation to Perceived Uniformity. In: H. Kälviäinen, J. Parkkinen & A. Kaarna, eds. *Image Analysis. Proceedings of the 15th Scandinavian Conference, SCIA 2007*. Berlin, Heidelberg: Springer-Verlag, pp. 409-418.

Sadovnikov, A., Lensu, L. & Kälviäinen, H., 2007. Automated Mottling Assessment of Colored Printed Areas. In: H. Kälviäinen, J. Parkkinen & A. Kaarna, eds. *Image Analysis. Proceedings of the 15th Scandinavian Conference, SCIA 2007*. Berlin, Heidelberg: Springer-Verlag, pp. 621-630.

Saffman, P. G., 1986. Viscous Fingering in Hele-Shaw cells. *Journal of Fluid Mechanics*, Volume 173, pp. 73-94.

Saffman, P. G. & Taylor, G. I., 1958. The penetration of a fluid into a porous medium or Hele-Shaw cell containing a more viscous liquid. *Proceedings of the Royal Society of London. Series A: Mathematical and Physical Science*, 245(1242), pp. 312-329.

- Samworth, M., 2001. *Flexographic Printing Plate Having Improved Solids Rendition*. US Patent 6,213,048.
- Samworth, M., 2009. *Printing Plates Containing Ink Cells in Both Solid and Halftone Areas*. US Patent 7,580,154.
- Samworth, M. & Cadogan, P., 2007. *Method of Controlling Ink Film Thickness on a Printing Plate*. US Patent 2007/0002384.
- Sauer, H. M., Bornemann, N. & Dörsam, E., 2011. Viscous fingering in functional flexo printing: an inevitable bug?. In: Anonymous. *LOPE-C (Large-area, Organic and Printed Electronics Convention) Proceedings*. München, Germany, 28-30 June 2011. München: LOPE-C.
- Savage, M. D., 1984. Mathematical Model for the Onset of Ribbing. *AIChE Journal*, November, 30(6), pp. 999-1002.
- Selli, E. & Bellobono, I. R., 1993. Photopolymerization of Multifunctional Monomers: Kinetic Aspects. In: J. P. Fouassier & J. F. Rabek, eds. *Polymerisation Mechanisms*. Barking: Elsevier Science Publishers, pp. 1-32.
- Seymour, J., 2013a. *Noffke-Seymour Halftone Model*. Personal communication, 11 January 2013.
- Seymour, J., 2013b. *The color of a bunch of dots, Part 4*. Available from <<http://johnthematguy.blogspot.co.uk/2013/07/the-color-of-bunch-of-dots-part-4.html>> [5 January 2015]
- Seymour, J. & Noffke, P., 2012. A Universal Model for Halftone Reflectance. In: *2012 TAGA Proceedings*. TAGA, pp. 1-40.
- Shibanov, V., 2012. Flat top dot technology spreads! *Flexo and Gravure Global*, 1(1), pp. 6-7.
- Sievers, W., 2011. *Curing of photo-curable printing plates with flat tops or round tops by variable speed exposure*. US Patent 2011/0104615.
- Sinha, S. & Tarafdar, S., 2009. Viscous Fingering Patterns and Evolution of Their Fractal Dimension. *Industrial and Engineering Chemistry Research*, Volume 48, pp. 8837-8841.
- Spelt, J. K., Moy, E., Kwok, D. Y. & Neumann, A. W., 1996. The Theory of Surface Tension Components and the Equation of State Approach. In: A. W. Neumann & J. K. Spelt, eds. *Applied Surface Thermodynamics*. New York: Marcel Dekker, pp. 293-332.
- Spelt, J. K. & Neumann, A. W., 1987. Solid Surface Tension: The Equation of State Approach and the Theory of Surface Tension Components. Theoretical and Conceptual Considerations. *Langmuir*, 3(4), pp. 588-591.
- Stahl, S., 2013. *Einfluss der Druckform und der Fluidviskosität auf die Schichtdicke von im Tiefdruck hergestellten Funktionsschichten und deren Charakterisierung*. Darmstadt: Technische Hochschule Darmstadt.
- Stahl, S., Sauer, H. M. & Dörsam, E., 2012. Investigation in the homogeneity of gravure printed polymer films for printed electronics. In: N. Enlund & M. Lovreček, eds. *Advances in Printing and Media Technology. Proceedings of the 39th International Research Conference*. Darmstadt: iarigai, pp. 47-51.
- Stolt, P., Zwadlo, G. L. & Rozzi, W. A., 2010. *Enhanced Relief Printing Plate*. US Patent 2010/0143841.

- Stone, M. C., 2003. *Field Guide to Digital Color*. Natick: A K Peters/CRC Press.
- Takimoto, Y., 1993. Comparative Advantages and Drawbacks of Radical and Cationic Polymerization in UV Curing. In: J. P. Fouassier & J. F. Rabek, eds. *Polymerisation Mechanisms*. Barking: Elsevier Science Publishers, pp. 269-299.
- Taylor, J. H. & Zettlemoyer, A. C., 1958. Hypothesis on the Mechanism of Ink Splitting During Printing. *TAPPI*, December, 41(12), pp. 749-757.
- Theopold, A., Neumann, J., Massfelder, D. & Dörsam, E., 2012. Effects of solvents on flexographic printing plates. In: N. Enlund & M. Lovreček, eds. *Advances in Printing and Media Technology. Proceedings of the 39th International Research Conference*. Darmstadt: iarigai, pp. 159-167.
- Thompson, B., 1998. *Printing Materials: Science and Technology*. Leatherhead: Pira International.
- Tian, D., Song, Y. & Jiang, L., 2013. Patterning of controllable surface wettability for printing techniques. *Chemical Society Reviews*, 42(12), pp. 5184-5209.
- Tomašegović, T., Mahović Poljaček, S. & Cigula, T., 2013a. Surface properties of flexographic printing plates related to UVC post-treatment. *Journal of Print and Media Technology Research*, 2(4), pp. 227-233.
- Tomašegović, T., Mahović Poljaček, S. & Cigula, T., 2013b. Impact of Screen Ruling on the Formation of the Printing Elements on the Flexographic Printing Plate. *Acta Graphica. Journal for Printing Science and Graphic Communication*, 24(1-2), pp. 1-12.
- Tóth, T. et al., 2011. Suspension of Water Droplets on Individual Pillars. *Langmuir*, Volume 27, pp. 4742-4748.
- Unser, M., 2000. Sampling - 50 Years After Shannon. *Proceedings of the IEEE*, April, 88(4), pp. 569-587.
- Urban, P. M., 2005. *Metamere und multispektrale Methoden zur Reproduktion farbiger Vorlagen*. Hamburg: Technische Universität Hamburg-Harburg.
- Valdec, D., Zjakić, I. & Milković, M., 2013. The influence of variable parameters of flexographic printing on dot geometry of pre-printed printing substrate [sic]. *Teknički vjesnik*, 20(4), pp. 659-667.
- van Oss, C. J., Chaudhury, M. K. & Good, R. J., 1988. Interfacial Lifshitz-van der Waals and Polar Interactions in Macroscopic Systems. *Chemical Reviews*, 33(6), pp. 927-941.
- Vlachopoulos, G., 2009. *Phenomena Affecting Ink Transfer in Offset Printing*. Swansea: Swansea University.
- Voß, C., 2002. *Analytische Modellierung, experimentelle Untersuchungen und dreidimensionale Gitter-Boltzmann Simulation der quasistatischen und instabilen Farbspaltung*. Wuppertal: Bergische Universität Gesamthochschule Wuppertal.
- Walker, W. C. & Fetsko, J. M., 1955. A Concept of Ink Transfer in Printing. *American Ink Maker*, December, 33(12), pp. 38-44, 69-71.
- Weichmann, A., 2002. *Method of Varying the Ink Density of the Full Tone in Offset Printing Within a Rotary [sic] Printing Machine*. US Patent 2002/0152911.
- Wenzel, R. N., 1936. Resistance of solid surfaces to wetting by water. *Industrial and Engineering Chemistry*, 28(8), pp. 988-994.

- Whyman, G., Bormashenko, E. & Stein, T., 2008. The rigorous derivation of Young, Cassie-Baxter and Wenzel equations and the analysis of the contact angle hysteresis phenomenon. *Chemical Physics Letters*, 450(4-6), pp. 355-359.
- Wyatt, F. C., 2004. Flexographic inks. In: R. H. Leach & R. J. Pierce, eds. *The Printing Ink Manual*. 5th edition. Dordrecht: Kluwer Academic Publishers, pp. 547-598.
- Wyble, D. R. & Berns, R. S., 2000. A Critical Review of Spectral Models Applied to Binary Color Printing. *Color Research and Application*, 25(1), pp. 4-19.
- Yule, J. A. C., 1943. Theory of the Halftone Process. III. Dot Size and Halftone Density. *Journal of the Franklin Institute*, November, 236(5), pp. 473-487.
- Yule, J. A. C. & Neilsen, W. J., 1951. The Penetration of Light into Paper and its Effect on Halftone Reproduction. In: *1951 TAGA Proceedings*. TAGA, pp. 65-76.
- Yusof, M. S., Ahmad Zaidi, A. M., Claypole, T. C. & Gethin, D. T., 2007. The Effects of Printing Plate on the Reproduction of Fine Solid Line Printing in Flexography. In: Anonymous. *Printing Future Days 2007. Proceedings of the 2nd International Student Conference*. Chemnitz: Institute for Print and Media Technology at Technische Universität Chemnitz, pp. 214-218.
- Zaleski, M., Schaeffer, W. D. & Zettlemoyer, A. C., 1971. An Extended Application of the Walker-Fetsko Ink Transfer Equation. In: W. H. Banks Jr., ed. *Advances in Printing Science and Technology. Proceedings of the 11th International Conference of Printing Research Institutes*. London, Plymouth: Pentech Press, pp. 175-184.
- Zang, Y. H., 1992. Asymmetric splitting and ink transfer: a new ink transfer model. In: Anonymous. *Proceedings of the 6th International Printing and Graphic Arts conference*. Peachtree Corners: TAPPI, pp. 103-112.
- Żenkiewicz, M., 2007a. Comparative study on the surface free energy of a solid calculated by different methods. *Polymer Testing*, Volume 26, pp. 14-19.
- Żenkiewicz, M., 2007b. Methods for the calculation of surface free energy of solids. *Journal of Achievements in Materials and Manufacturing Engineering*, September, 25(1), pp. 137-145.
- Zettlemoyer, A.C. & Myers, R. R., 1960. The Rheology of Printing Inks. In: F. R. Eirich, ed. *Rheology. Theory and Application. Volume 3*. New York, London: Academic Press, pp. 145-188.
- Zhang, L., Yun Zhang, M. & Ping Yang, J., 2011. Development and Comparison of Models for Predicting Printing Quality in Flexographic Printing. *Advanced Materials Research*, Volume 174, pp. 231-234.
- Zumbrum, M. A., Wilkes, G. L. & Ward, T. C., 1993. Characterization of the Dynamic Mechanical and Dielectric Properties of UV- and EB-Cured Coatings. In: J. P. Fouassier & J. F. Rabek, eds. *Polymerisation Mechanisms*. Barking: Elsevier Science Publishers, pp. 101-151.